



**HAL**  
open science

## Process development and scale-up for low-cost high-efficiency kesterite thin film photovoltaics

Laura Vauche

► **To cite this version:**

Laura Vauche. Process development and scale-up for low-cost high-efficiency kesterite thin film photovoltaics. Micro and nanotechnologies/Microelectronics. Université d'Aix Marseille, 2015. English. NNT: . tel-01314175

**HAL Id: tel-01314175**

**<https://theses.hal.science/tel-01314175>**

Submitted on 10 May 2016

**HAL** is a multi-disciplinary open access archive for the deposit and dissemination of scientific research documents, whether they are published or not. The documents may come from teaching and research institutions in France or abroad, or from public or private research centers.

L'archive ouverte pluridisciplinaire **HAL**, est destinée au dépôt et à la diffusion de documents scientifiques de niveau recherche, publiés ou non, émanant des établissements d'enseignement et de recherche français ou étrangers, des laboratoires publics ou privés.



Distributed under a Creative Commons Attribution 4.0 International License

UNIVERSITÉ d'AIX-MARSEILLE

ÉCOLE DOCTORALE 353

UMR CNRS 7334

IM2NP Institut Matériaux Microélectronique Nanosciences de Provence

Thèse présentée pour obtenir le grade universitaire de docteur

Discipline : SCIENCES POUR L'INGENIEUR : MECANIQUE, PHYSIQUE, MICRO ET  
NANOELECTRONIQUE  
Spécialité : Micro et Nanoélectronique

**Laura VAUCHE**

## **Process development and scale-up for low-cost high-efficiency kesterite thin film photovoltaics**

Directeur de thèse : **Marcel PASQUINELLI**  
Encadrants : **Thomas GOISLARD DE MONSABERT,**  
**Pierre-Philippe GRAND, Salvador JAIME.**

Soutenue le 27/11/2015 devant le jury :

<b>Daniel LINCOT</b> , CNRS-IRDEP	Rapporteur
<b>Henri MARIETTE</b> , CEA-INAC	Rapporteur
<b>Gilles DENNLER</b> , IMRA Europe	Examineur
<b>Pierre-Philippe GRAND</b> , EDF	Examineur
<b>Ian FORBES</b> , Northumbria University (UK)	Invité
<b>Thomas GOISLARD DE MONSABERT</b> , NEXCIS	Invité
<b>Salvador JAIME</b> , NEXCIS	Invité
<b>Marcel PASQUINELLI</b> , Aix Marseille Université	Directeur de thèse

# Contents

<b>Acknowledgements</b>	<b>v</b>
<b>Work done in conjunction with others</b>	<b>vii</b>
<b>Acronyms</b>	<b>ix</b>
<b>Constants and values</b>	<b>xi</b>
<b>Résumé (French)</b>	<b>xiii</b>
Contexte général . . . . .	xiv
Électro-dépôt du précurseur . . . . .	xv
Formation de l'absorbeur par traitement thermique . . . . .	xviii
Optimisation de la cellule . . . . .	xix
Conclusions: Kesterite — une approche industrielle . . . . .	xxii
<b>I Introduction</b>	<b>1</b>
I.1 Photovoltaics . . . . .	2
I.1.1 Basics . . . . .	2
I.1.2 Technologies . . . . .	7
I.1.3 Historical . . . . .	9
I.1.4 Perspectives . . . . .	10
I.1.5 Material considerations . . . . .	12
I.2 Kesterite properties . . . . .	16
I.2.1 Properties of kesterite materials . . . . .	16
I.2.2 Kesterite fabrication processes . . . . .	17
I.2.3 Challenges for high-efficient kesterite devices production . . . . .	21
I.3 Objectives and Structure . . . . .	27
<b>II Electrodeposition</b>	<b>29</b>
II.1 Basics . . . . .	31
II.1.1 Advantages of electrochemical processes . . . . .	31
II.1.2 Electrodeposition principle . . . . .	31
II.1.3 Operating parameters during electroplating . . . . .	35
II.2 Experimental approaches . . . . .	38
II.2.1 ED for thin films solar cells . . . . .	38
II.2.2 Kesterite fabrication routes . . . . .	38
II.2.3 Electrodeposition of Cu, Sn and Zn: an industrial approach . . . . .	43
II.2.4 Desired precursor properties for high-efficient kesterite devices . . . . .	49
II.3 Experimentals . . . . .	52
II.3.1 Substrates . . . . .	52
II.3.2 Chemistry . . . . .	52
II.3.3 Process conditions . . . . .	53
II.3.4 Low-temperature annealing of metallic stacks . . . . .	55
II.3.5 Material and bath characterization . . . . .	55
II.4 Results and discussion . . . . .	56
II.4.1 Chemistry: Lifetime and stability . . . . .	56

II.4.2	Process and material optimization . . . . .	60
II.5	Discussion and Conclusions . . . . .	68
<b>III</b>	<b>Absorber formation</b>	<b>69</b>
III.1	Background . . . . .	71
III.1.1	The annealing process . . . . .	71
III.1.2	Kesterite annealing strategies in literature . . . . .	72
III.1.3	Challenges in kesterite absorber manufacturing . . . . .	77
III.2	Experimentals . . . . .	81
III.2.1	Substrates . . . . .	81
III.2.2	Precursors . . . . .	81
III.2.3	Optional Se capping layer . . . . .	81
III.2.4	Annealing systems . . . . .	82
III.2.5	Characterization of the absorber material . . . . .	85
III.2.6	Device fabrication and characterization . . . . .	86
III.3	Results . . . . .	88
III.3.1	Sulfurization in NEXCIS system . . . . .	88
III.3.2	Selenization in NEXCIS system . . . . .	93
III.3.3	Selenization in IRDEP systems . . . . .	96
III.3.4	Selenization in IREC system . . . . .	101
III.4	Conclusions . . . . .	108
<b>IV</b>	<b>Device optimization</b>	<b>109</b>
IV.1	Kesterite surface treatments . . . . .	111
IV.1.1	Background . . . . .	111
IV.1.2	Experimentals . . . . .	113
IV.1.3	Results . . . . .	114
IV.2	Buffer optimization . . . . .	120
IV.2.1	Background . . . . .	120
IV.2.2	Experimentals . . . . .	123
IV.2.3	Results . . . . .	124
IV.3	Front contact optimization . . . . .	129
IV.3.1	Background . . . . .	129
IV.3.2	Experimentals . . . . .	130
IV.3.3	Results: Implementation of metal contacts . . . . .	130
IV.4	Conclusions . . . . .	131
IV.4.1	Optimal parameters for high-efficient kesterite devices . . . . .	131
IV.4.2	Optimum processes . . . . .	133
<b>V</b>	<b>Conclusions</b>	<b>135</b>
V.1	PV technologies perspective . . . . .	136
V.2	Cost per energy unit - Example of CIGS . . . . .	137
V.2.1	Definition of the industrial line . . . . .	137
V.2.2	Production costs . . . . .	138
V.3	Kesterite — an industrial approach . . . . .	139
V.3.1	Low-cost processes . . . . .	139
V.3.2	High efficiency . . . . .	142
V.4	Perspective . . . . .	143
	<b>Appendix</b>	<b>144</b>
<b>A</b>	<b>Photovoltaics perspectives</b>	<b>145</b>
A.1	PV in general . . . . .	145
A.2	Part of thin film technologies . . . . .	146
<b>B</b>	<b>Characterization methods</b>	<b>147</b>
B.1	Hull cell . . . . .	147

## CONTENTS

---

B.2	Composition analysis . . . . .	151
B.2.1	ICP . . . . .	151
B.2.2	XRF and RSD . . . . .	151
B.3	Bandgap determination . . . . .	153
<b>C</b>	<b>Safety classifications: risk phrases</b>	<b>155</b>
	<b>Bibliography</b>	<b>159</b>
	<b>List of Publications</b>	<b>181</b>
	<b>List of Figures</b>	<b>183</b>
	<b>List of Tables</b>	<b>187</b>

# Acknowledgements

I have really appreciated these three years of learning and research and would like to thank several people who have helped me on the way towards this dissertation. Firstly, I would like to express my deepest gratitude to my supervisors for giving me this opportunity and mentoring me over the last years:

I would like to thank Dr Salvador Jaime, for his constant support especially in the tough times, for many fruitful discussions and excellent guidance for the development of this research work. His constructive suggestions and advice, based on deep scientific knowledge and high exigence standard, were always very helpful and appreciated. I have learn a lot from him and this thesis would not have been the same without him.

I am grateful to Dr Pierre-Philippe Grand, first for accepting me as a PhD student, but also for his kind support, helpful discussions and precious advice during this work. I want to thank him for the ideas and suggestions, and for the time spent in supervising my work, reading and commenting my reports, presentations and thesis.

I am also very grateful to Dr Thomas Goislard, for his help and enthusiasm. His comments and discussions, especially for the evaluation of opto-electronic measurements, really helped.

I would like to thank Prof. Marcel Pasquinelli for giving me the opportunity to join the IM2NP lab, for his support, availability, kindness, for his help and for the time spent in reading my works.

Furthermore, I would like to thank Prof. Daniel Lincot, head of the Institut de Recherche et Développement sur l'Énergie Photovoltaïque (IRDEP) and Dr Henri Mariette, head of Nanophysics and Semiconductors - NPSC group at CEA-CNRS for being part of the jury as rapporteurs, Dr Ian Forbes, reader in the Department of Physics and Electrical Engineering, at Northumbria university and Dr Gilles Dennler, head of Energy and Environment Department at IMRA Europe for accepting to be part of the PhD committee. Thank you for your time and consideration.

I would like to thank all members of NEXCIS, for their support and teamwork throughout the past years. In particular I would like to acknowledge: Aurélie Laparre for her help with the electrodeposition and characterizations, for her kindness and for making me feel welcome at NEXCIS; Cédric Broussillou for his valuable advice and helpful discussions; Céline Plomion for her suggestions for the Introduction of the thesis; Denis Fouchier for his work on kesterite as an intern; Jérôme Dubois for his precious help with the annealings, for his kindness, constant support and helpful discussions; Lisa Risch for being such a nice co-worker, for all her huge help inside and outside the lab: all the kesterite discussions, a rock solid enthusiasm and energy, and for proof reading many of my works including the thesis, I don't have enough words to thank you; Luc Barberis for his help with the bath characterization; Monika Arasimowicz for sharing her kesterite and PhD expertise and her love of tea and chocolate; Noémie Pascal for her help with the annealings and characterizations and her motivation; Sylvie Bodnar for her advice with annealings and for proof-reading; Philippe De Gasquet for his kindness and help with the electrodeposition set-up. I also would like to thank my co-workers from Chemistry and Electrodeposition department Adrien Falourd, Alexis Sorba, Kim Nguyen, Laurent Tillet, Louise Cazilhac, Philippe Guillon, Stéphanie Anthérieu, Tristan Pic for their kind help with characterization, CdS depositions and various lab and office issues. I am also grateful to NEXCIS Sputtering team for all the work to provide me with molybdenum substrates and for depositing the ZnO and the front contact onto my absorber layers, to NEXCIS

Characterization team for characterizing my samples and for the help with the various analytical tools and to NEXCIS Back-end team for scribing and metal contacts deposition on my always too small samples. Good luck to all for you for the future.

It has also been a great pleasure for me to contribute to the European Union SCALENANO and INDUCIS and the French NovaCEZ projects, and to learn from and collaborate with some of the best thin-film solar cell laboratories in Europe. Financial support from the above-mentioned projects is also gratefully acknowledged.

I am very grateful to Alejandro Pérez-Rodríguez and Edgardo Saucedo for receiving me in the Solar Energy Materials and Systems group at IREC (Barcelona) for a few months. I would like to thank all the group members (monas) for being excellent company at work and for answering all my questions patiently. Especially, many thanks to Haibing Xie, Marcel Placidi, Markus Neuschitzer, Moises Espindola-Rodríguez and Simon Lopez-Marino for the fruitful discussions and their help with the processing of my devices; to Yudania Sánchez for her great help and for performing the buffer layer depositions; to Dioullé Sylla for her kind help with SEM and XRD; to Florian Oliva, Mirjana Dimitrievska, Victor Izquierdo-Roca, Xavier Fontané for the help with Raman measurements; and to Andrew Fairbrother, Cristina Insignares, Rokas Kondrotas, Stephan Van Duren for discussions and support.

I would like also to thank Sébastien Delbos and Romain Bodeux, for receiving me a few weeks at IRDEP (Paris) and letting me use the annealing systems, and for their kindness and helpful discussions.

I would like to thank Alexandre Crossay, Diego Colombara and Philip Dale from the University of Luxembourg for the collaboration, for the exchange of samples and ideas over the last years and for the valuable discussions.

Many thanks to my colleagues at IM2NP for the great company: especially to Carmen Ruiz for her help with the PL and with the electrical characterizations; to Dario Cozza for the kesterite and non-kesterite discussions, but also to Adrien Bou, Fatima Bencheikh, François Thierry and Miriam Carlberg for the good times in Aix and Marseille, Antonin Moreau for his advice, Etienne Quiniou for taking care of my poster and all the others.

I am also grateful to all the people from here and from other parts of Europe I have met during exchanges, Kesterite workshops and conferences for fruitful discussions, inspiration and really good times. Many thanks to Alex Carrete, Jose Marquez Prieto (Pepe), Rémi Aninat, Tetiania Olar (Tania) for the discussions and great company.

Last but not least, I would like to thank my family and friends for being such great people, for their moral support and patience during my studies. Many thanks to my Aix friends, who really helped me to enjoy the three years here, especially Maria Riquez (Padre), la famiglia (Alex, Babeth, Carlos, Dario, Diego, Stefy, Vins), my successive roommates Marion, Nico, Clément and Elsa; NEXCIS interns (Avril, Florian, Mathieu and the others), NEXCIS and ST taekwondo partners for the great kicks, ST PhD students (Anthony (x2), Bertrand, Dino, Nicolas) and last but not least, the Sunset. A lot of thanks to my friends from everywhere (special thanks to le club de la loose Audrey, Magali and Stéphanie); to my sister Marina and my parents; and to Gabriel for their great and unconditional support and love throughout the tough times.

Merci, Thank you, Gracias, Gràcies, Grazie, Dank, Danke, Podziękowanie.

# Work done in conjunction with others

The work presented in this thesis was carried out by the author, with the following exceptions:

## Process

1. Substrates. All the Mo- or Cu/Mo-coated soda-lime glass substrates were provided by NEXCIS Sputtering department.
2. Precursors. The electrodeposition of Cu/Sn/Zn precursor was carried out by Aurélie Laparre and by the author.
3. Thermal treatments. The deposition of a Se capping layer and the annealings in CC-NEXCIS annealing system (*Chapter 3*) were carried out by Jérôme Dubois. The thermal treatments in IC- and CC-IRDEP annealing systems (*Chapter 3*) were carried out by Jérôme Dubois and by the author.
4. Wet chemical etching. At NEXCIS, KCN etchings were performed by Louise Cazilhac and Alexis Sorba. At IRDEP, KCN etchings were carried out by Valerie Bockelee, Laurent Michely and Nicolas Loones. At IREC, the etchings were performed by the author at the exception of  $(\text{NH}_4)_2\text{S}$  etching solutions preparation which were prepared by Haibing Xie or Yudania Sánchez.
5. Buffer layer deposition by chemical bath deposition (CBD). At NEXCIS, the CdS layers were deposited either by Louise Cazilhac and Alexis Sorba. At IRDEP, the CdS depositions were carried out by Valerie Bockelee, Laurent Michely and Nicolas Loones. At IREC the CdS,  $\text{In}_2\text{S}_3$  and ZnS buffers layers were deposited by Yudania Sánchez.
6. Transparent conductive oxide (TCO) deposition by sputtering. The TCO window layers and front contacts were deposited either by NEXCIS Sputtering department, by Benoît Roman at IRDEP or by Haibing Xie, Marcel Placidi, Markus Neuschitzer, Moises Espindola-Rodriguez or Simon López-Marino at IREC.
7. Scribing. At NEXCIS scribing and metal contact deposition were performed by the Back-end department. At IRDEP the metallic grid used in Chapter 4 was deposited by Fabien Tsin with a process developed by Torben Klinkert and Myriam Paire.

## Characterization

1. The ICP and titration analysis were carried out by Stéphanie Anthérieu, Luc Barberis, Louise Cazilhac, Aurélie Laparre and Tristan Pic from NEXCIS Chemistry department. Sn(IV) titration method was developed by Luc Barberis.



2. XRF, XRD, SEM analysis realized at NEXCIS were carried out by the author, Aurélie Laparre, Jérôme Dubois, Denis Fouchier, Noémie Pascal and Monika Arasimowicz. XRD at IRDEP was performed by Romain Bodeux. SEM+EDX images of full devices in *Chapter 4* were taken at HZB by Lisa Risch with the help of Stephan Van Duren.
3. The GDOES analysis were carried out at NEXCIS by Aurélie Laparre, Laurence Pacpiack, Noémie Pascal, Marine Annibaliano and Ophélie Rogée. The secondary ion mass spectrometry measurements were performed by STMicroelectronics. The Tof-SIMS measurements were performed by Biophy Research.
4. The Raman spectroscopy measurements with the 785 nm laser in *Chapter 3* and *4* were carried out at IREC by the author or by Lisa Risch with the help of Xavier Fontané, Florian Oliva and Victor Izquierdo-Roca and analyzed by Lisa Risch. The Raman spectroscopy measurements in *Chapter 3* and *4* realized with the 457.9 nm laser were performed and analyzed at IREC by Mirjana Dimitrievska.
5. The J-V and EQE measurements of the 9.1% record device were realized at NEXCIS and IM2NP by Thomas Goislard de Monsabert and Vincent Roue, respectively.

The evaluation of all the results was carried out by the author.

# Acronyms

<b>ALD</b>	atomic layer deposition
<b>AM</b>	air mass
<b>ARC</b>	anti reflective coating
<b>ASD</b>	ampere per square decimeter
<b>AZO</b>	aluminium doped zinc oxide
<b>CB</b>	conduction band
<b>CBD</b>	chemical bath deposition
<b>CBO</b>	conduction band offset
<b>CC</b>	confined chalcogen
<b>CIGS</b>	$\text{CuIn}_x\text{Ga}_{1-x}(\text{S,Se})_2$
<b>CMR</b>	carcinogenic, mutagenic and toxic for reproduction
<b>CP</b>	chalcogen in precursor
<b>CVD</b>	chemical vapor deposition
<b>CZTS</b>	$\text{Cu}_2\text{ZnSnS}_4$
<b>CZTSe</b>	$\text{Cu}_2\text{ZnSnSe}_4$
<b>CZTSSe</b>	$\text{Cu}_2\text{ZnSn}(\text{S,Se})_4$
<b>ED</b>	electrodeposition
<b>EDX</b>	energy dispersive X-ray spectroscopy
<b>EQE</b>	external quantum efficiency
<b>GDOES</b>	glow discharge optical emission spectroscopy
<b>IC</b>	independent chalcogen
<b>ICP</b>	inductively coupled plasma
<b>ICP-OES</b>	inductively coupled plasma/optical emission spectroscopy
<b>ITO</b>	indium tin oxide
<b>LS</b>	light soaking
<b>MSE</b>	mercury-mercurous sulfate electrode
<b>NHE</b>	normal hydrogen electrode
<b>PL</b>	photoluminescence
<b>PV</b>	photovoltaic
<b>PVD</b>	physical vapor deposition
<b>QACs</b>	quaternary ammonium compounds
<b>RSD</b>	relative standard deviation
<b>RTP</b>	rapid thermal processing
<b>SCE</b>	saturated calomel electrode
<b>SEL</b>	stacked elemental layers
<b>SEM</b>	scanning electron microscopy
<b>SIMS</b>	secondary ion mass spectroscopy
<b>SLG</b>	soda-lime glass

**TCO** transparent conductive oxide

**XRD** X-ray diffraction

**XRF** X-ray fluorescence

**VB** valence band

**VTD** vapor transport deposition

# Constants and values

## Units

$A$	area	$\text{m}^2$
$\alpha$	absorption coefficient	$\text{cm}^{-1}$
$c$	concentration	$\text{mol/L}$
$E$	electrode potential	V
$E$	photon energy	eV
$E_g$	bandgap	eV
$E^\circ$	standard electrode potential	V
$e$	thickness	nm
FF	fill factor	%
$I$	current	A
$J$	current density	$\text{A/m}^2$
$J_{\text{SC}}$	short-circuit current density	$\text{A/m}^2$
$\lambda$	wavelength	nm
$L_n$	minority carrier diffusion length	$\mu\text{m}$
$m$	weight	g
$M$	atomic weight	$\text{g/mol}$
$\mu$	mean	-
$n$	material amount	mol
$n$	ideality factor	
$\eta$	current efficiency	%
$\eta$	power conversion efficiency	%
$P$	power	W
$\varphi$	overpotential	V
$Q$	charge	C
$R$	resistance	$\Omega$
$R_S$	series resistance	$\Omega.\text{cm}^2$
$R_{\text{SH}}$	shunt resistance	$\Omega.\text{cm}^2$
$\rho$	density or volumic mass	$\text{kg/m}^3$
$\sigma$	standard deviation	-
$t$	time	s
$T$	temperature	K
$\theta$	diffraction angle	$^\circ$
$V$	voltage	V
$V_{\text{OC}}$	open-circuit voltage	V
$W$	space charge region width	$\mu\text{m}$
$z$	charge coefficient on metal ion	-

## Constants

$c$	Light's speed	$2.998 \times 10^8 \text{ m} \cdot \text{s}^{-1}$
$F$	Faraday	$96485 \text{ C} \cdot \text{mol}^{-1}$
$h$	Planck's constant	$6.626 \times 10^{-34} \text{ J} \cdot \text{s}$
$k_B$	Boltzmann's constant	$6.617 \times 10^{-5} \text{ eV} \cdot \text{K}^{-1}$
$q$	Absolute value of electron charge	$1.602 \times 10^{-19} \text{ C}$
$R$	Gas constant	$8.31446 \text{ J} \cdot \text{K}^{-1} \cdot \text{mol}^{-1}$

## Values

$\rho_{Cu}$	Copper density	8920 kg/m <sup>3</sup>
$\rho_{Sn}$	Tin density	7290 kg/m <sup>3</sup>
$\rho_{Zn}$	Zinc density	7134 kg/m <sup>3</sup>
$M_{Cu}$	Copper molar mass	63.55 g/mol
$M_{Sn}$	Tin molar mass	118.71 g/mol
$M_{Zn}$	Zinc molar mass	65.409 g/mol

# Résumé - Développement de procédés pour des cellules photovoltaïques kesterite en couches minces à haut rendement et bas coût

## Contents

---

Contexte général . . . . .	xiv
Électro-dépôt du précurseur . . . . .	xv
Formation de l'absorbeur par traitement thermique . . . . .	xviii
Optimisation de la cellule . . . . .	xix
Conclusions: Kesterite — une approche industrielle . . . . .	xxii

---

## Contexte général

### Le photovoltaïque

Dans un contexte général d'augmentation de la demande énergétique et de préoccupation croissante face au réchauffement climatique et à la limitation des ressources naturelles, l'utilisation d'énergie solaire devrait augmenter. L'Agence Internationale de l'Energie prévoit différents scénarios pour la production d'énergie en 2050, correspondant à une hausse de la température globale entre 6°C (scénario conservateur) et 2°C (déploiement accéléré des énergies renouvelables) [1]. En suivant ces prévisions, on estime entre 200 GW et 7.3 TW la puissance photovoltaïque installée en 2050 pour la génération d'électricité. La prévision de 200 GW n'est pas réaliste car en 2014, la puissance photovoltaïque (PV) installée dans le monde a déjà dépassé les 175 GW [2, 3].

Le marché est actuellement dominé par les cellules solaires en silicium cristallin (c-Si) dont les procédés de fabrication ont été directement inspirés de la micro-électronique. Cependant, le procédé de purification, cristallisation et découpe du silicium est gourmand en énergie, et donc en coût. La recherche de nouveaux matériaux à coûts de fabrication réduits a conduit au développement des cellules solaires dites de seconde et troisième générations. Les technologies à base de couches minces, comprenant le diséléniure de cuivre gallium et indium ou chalcopyrite  $\text{CuIn}_x\text{Ga}_{1-x}(\text{S,Se})_2$  (CIGS) et le tellurure de cadmium CdTe partagent aujourd'hui le marché avec le silicium. Leur fort coefficient d'absorption leur permettent d'absorber une importante partie du spectre solaire sur une épaisseur de deux microns seulement (contre 200 microns pour le silicium).

L'avenir des différentes technologies PV dépend évidemment de leur rendement de conversion photovoltaïque et de leur coût (ces deux paramètres peuvent être ramenés au coût par watt) mais aussi de la disponibilité des ressources. En effet, la rareté et le prix de certains matériaux sont une limite au déploiement du PV à grande échelle (de l'ordre du terawatt). L'argent (utilisé pour les contacts des cellules Si), l'indium, le gallium (pour le CIGS) et le tellurium (pour le CdTe) font partie des matériaux critiques [4–6]. Le développement d'une nouvelle technologie couche mince à base d'éléments abondants et de préférence non toxiques permettrait de soulager la demande en matériaux critiques. À cet égard, les composés de la famille des kesterites,  $\text{Cu}_2\text{ZnSnS}_4$  (CZTS),  $\text{Cu}_2\text{ZnSnSe}_4$  (CZTSe),  $\text{Cu}_2\text{ZnSn}(\text{S,Se})_4$  (CZTSSe) sont des candidats prometteurs. Le zinc et l'étain sont 278 et 28 fois moins cher et les quantités produites 16000 et 360 fois plus importantes que l'indium, respectivement [7, 8].

### La kesterite

La kesterite réunit les propriétés nécessaires pour être utilisée comme absorbeur en couche mince dans des cellules solaires:

- un dopage intrinsèque de type p [9, 10];
- un coefficient d'absorption élevé ( $> 10^4 \text{ cm}^{-1}$  [11]), permettant d'absorber le spectre solaire avec quelques microns d'épaisseur seulement;
- des bandgaps directs (1.0 eV pour le CZTS à 1.5 eV pour le CZTSe [11, 12]), proches de la valeur idéale pour des cellules solaires à une jonction. Le ratio soufre sur sélénium permet d'ajuster le bandgap.

La structure cristalline la plus stable pour les composés  $\text{Cu}_2\text{ZnSn}(\text{S,Se})_4$  (CZTSSe) est la structure kesterite, qui correspond à une alternance de couches contenant des cations Cu et Zn ou Cu et Sn.

Les cellules solaires ne contiennent pas seulement une couche de kesterite (semiconducteur de type p) mais aussi une couche dopée n afin de former une jonction p-n, ainsi que des contacts arrière et avant pour la collecte du courant. La structure des dispositifs à base de kesterite est calquée sur le CIGS. La majorité des laboratoires et entreprises utilisent la structure suivante: verre silico-sodocalcique aussi nommé verre sodo-calcique (SLG)/contact arrière Mo/absorbeur CZTSSe/couche

tampon CdS/oxide de zinc non-dopé (i-ZnO)/oxide de zinc dopé à l'aluminium (AZO) ou oxide d'indium dopé à l'étain (ITO), comme illustré en Figure 2.

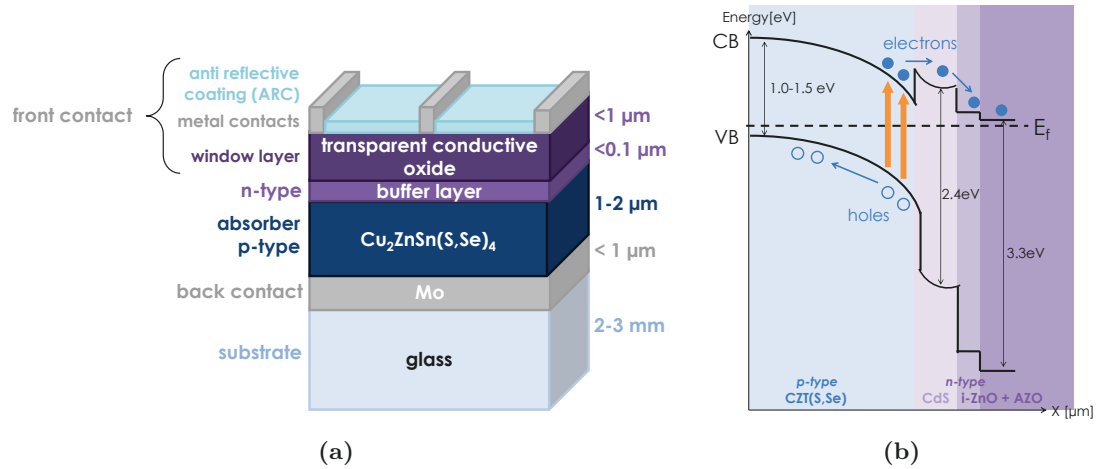


**Figure 2:** (a) Représentation schématique et (b) diagramme de bandes de la structure d'un dispositif photovoltaïque à base de kesterite.

L'absorbant peut être déposé en une étape ou en deux étapes, en utilisant des procédés sous vide ou atmosphériques.

Les procédés sous vide de pulvérisation cathodique, évaporation et co-évaporation ont déjà prouvé leur utilité pour la fabrication de CIGS à haute performance. Ces techniques sont également utilisées pour la fabrication de kesterite, avec des rendements dépassant les 10% [13–15].

Les techniques de dépôt atmosphériques sont avantageuses par rapport aux techniques sous vide : les équipements nécessaires sont moins chers, les dépôts peuvent être réalisés sur substrats flexibles et de grande taille, tout en permettant des cadences de production plus élevées, une utilisation plus efficace des matières premières à des températures de procédé réduites [16]. Parmi ces techniques, on peut citer les méthodes de dépôt direct de solution à la surface d'un substrat (dépôt d'une couche ou impression) [17], l'électrodépôt [18, 19], le dépôt par bain chimique ou CBD [20], etc.

Actuellement, les rendements record de conversion photovoltaïque pour la kesterite (12.7%) sont obtenus avec des procédés de fabrication à base d'hydrazine [21–26]. Bien que considérée comme un solvant idéal car ne contenant ni carbone ni oxygène, l'hydrazine est toxique et explosive. D'autres solvants tels que le DMSO permettent également la production de cellules solaires à base de kesterite avec des rendements supérieurs à 10% [27, 28]. L'électrodépôt est également une approche industrielle attractive : température ambiante, solutions non-toxiques à bas coût et longue durée de vie. Des rendements de 7 à 8% ont été obtenus pour le CZTS [29, 30] et le CZTSe [31, 32].

## Électro-dépôt du précurseur

### Approche industrielle

L'électro-dépôt permet le dépôt d'une couche sur une surface par un procédé électrochimique, et implique l'échange d'électrons entre une électrode solide et des ions ou molécules en solution. Il existe trois stratégies principales pour la fabrication de kesterite par électro-dépôt : le co-dépôt des métaux Cu-Sn-Zn, le dépôt d'un quaternaire CZTS ou CZTSe, ou l'électrodépôt d'un empilement de couches élémentaires, toutes ces stratégies étant suivies d'un traitement thermique.

D'un point de vue industriel, le dépôt par empilement est préférable aux co-dépôts car les conditions de dépôt et l'électrolyte peuvent être ajustés indépendamment pour chaque élément, ce qui permet



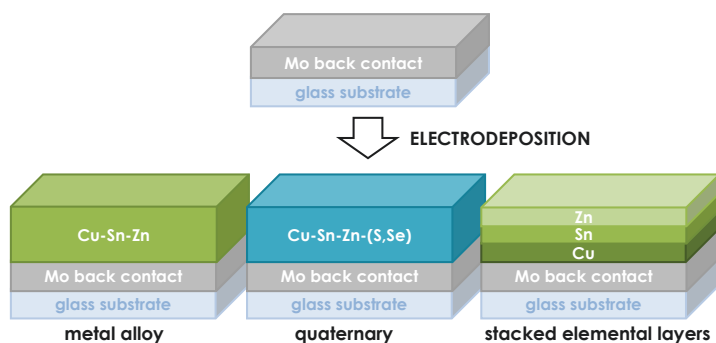


**Figure 3:** Représentation schématique des stratégies d'électrodépôt de kesterite utilisées dans la littérature.

de déposer une couche uniforme sur une grande surface, et d'avoir un procédé plus robuste et flexible. L'utilisation de bain chimiques commerciaux pour l'électrodépôt est souhaitable car d'une part ces chimies sont concentrées, permettant d'éviter les problèmes de transport de masse, et d'autre part les additifs présents dans ces bains permettent de contrôler la morphologie, la stabilité de l'électrolyte ainsi que les propriétés mécaniques de couches déposées. Les bains chimiques doivent être compatibles avec le substrat, stables, avoir une longue durée de vie et permettre un dépôt rapide à température ambiante. Les composants du bain doivent être abondants, peu cher et non toxiques. Les bains choisis sont décrits dans la Table 1.

**Table 1:** Composition et prix des bains chimiques choisis pour l'électrodépôt de Cu, Sn et Zn.

Bain	Composition et concentration requise	Prix du composant	Prix du bain par L	Prix par m <sup>2</sup> déposé
<b>Acid Copper Sulfate</b> <i>Microfab SC</i>	Make-up (CuSO <sub>4</sub> , Cu: 27 – 30 g/L; H <sub>2</sub> SO <sub>4</sub> : 150 – 170 g/L) Additives (MD: 6 – 9 mL/L; LO: 1 – 4 mL/L)	34 €/L 120 €/L	34.8 €	2.17 €
<b>Acid Tin Sulfate</b> <i>Stannostar GSM</i>	SnSO <sub>4</sub> , Sn: 20 – 25 g/L H <sub>2</sub> SO <sub>4</sub> : 155 – 175 g/L Additive GSM smoothing agent: 30 mL/L	32.6 €/kg 28.4 €/L	1.6 €	0.12 €
<b>Alkaline Zinc</b> <i>Enthobrite NCZ 5001</i>	Zincate solution (Zn(OH) <sub>4</sub> <sup>2-</sup> , Zn: 12 – 20 g/L) NaOH Additive A: 8 – 15 mL/L Additive B: 0.25 – 2 mL/L	3.4 €/L 9.0 €/L 4.3 €/L	1.3 €	0.23 €

Les concentrations en métaux, acide, base et additifs sont analysées par différentes méthodes (ICP, titrage, cellule de Hull). Lorsque les niveaux sont bas, des produits chimiques (par exemple sulfate de cuivre, sulfate d'étain, soude) sont ajoutés afin de maintenir les concentrations proches de leur niveau initial. Les dépôts sont effectués selon le procédé décrit en Figure 4. Les couches successives de Cu, Sn et Zn sont déposées sur des substrats de molybdène (600 nm) sur verre sodio-calcique (SLG) (3 mm) de taille 15 × 15 cm<sup>2</sup>, recouverts d'une couche initiale de Cu.

L'équipement utilisé pour l'électrodépôt est constitué d'un réacteur de 50 L contenant l'électrolyte, d'un système d'agitation, d'un système de filtration, d'un porte-échantillon muni d'un voleur de courant, d'une anode ainsi que d'une source de courant extérieure et de bains de rinçage.

## Résultats

Les bains de cuivre et de zinc sont stables sur plus d'un an, leur durée de vie semble donc être suffisante pour une application industrielle. Le bain d'étain, par contre, n'est pas stable car Sn(II) a tendance à s'oxyder, ce qui se traduit par une diminution de la concentration en Sn(II) et la formation de colloïdes dans le bain. L'ajout d'agent flocculant permet de faire précipiter le Sn(IV)

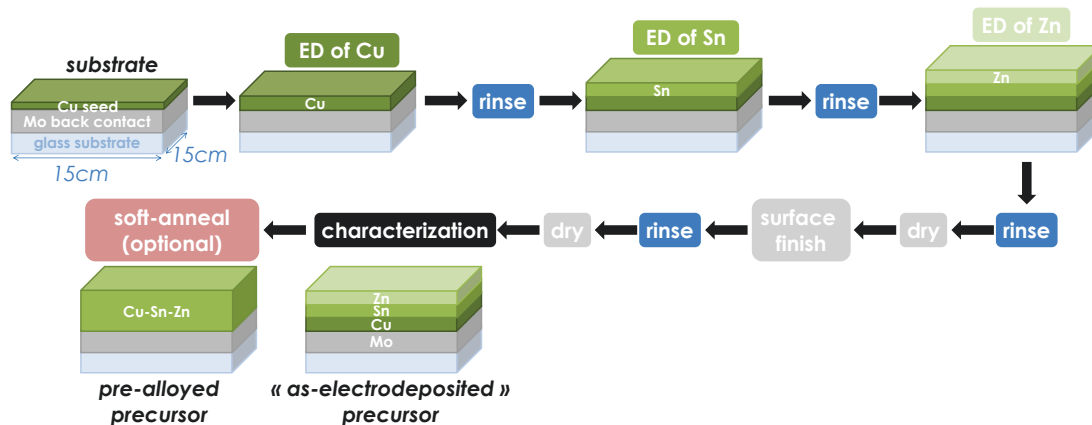


Figure 4: Vue générale du procédé d'électrodépôt de Cu/Sn/Zn.

et de régénérer le bain en Sn(II), allongeant ainsi sa durée de vie. Idéalement, le bain d'étain devrait se baser sur une chimie plus stable, mais qui soit également compatible avec un procédé industriel.

Les bains de Cu, Sn et Zn utilisés permettent le dépôt d'un empilement Cu/Sn/Zn en 2.5 à 5 minutes (vitesses de dépôt de 120 à 350 nanomètres par minute), de composition et d'épaisseur désirée par ajustement des durées de dépôt. De plus les couches déposées recouvrent intégralement les couches inférieures et sont uniformes sur  $15 \times 15 \text{ cm}^2$ : le coefficient de variation de l'épaisseur de chaque couche est inférieur à 5%.

Juste après le dépôt, le profil de composition est conforme à l'ordre de dépôt: Cu/Sn/Zn, et le précurseur est composé de Cu, Sn et Zn élémentaires. Rapidement après dépôt (quelques heures à quelques jours), le zinc migre vers l'arrière et forme avec le cuivre l'alliage  $\epsilon\text{-CuZn}_5$ , jusqu'à disparition du zinc élémentaire. Après quelques mois de vieillissement naturel (température et atmosphère ambiantes) l'alliage  $\gamma\text{-Cu}_5\text{Zn}_8$  se forme. Un traitement thermique basse température dans une étuve (atmosphère ambiante,  $200 \text{ }^\circ\text{C}$ , "pre-alloying") permet la formation d'alliages Cu-Sn et Cu-Zn, et surtout la stabilisation du précurseur. En effet, le zinc migre là aussi vers l'arrière du précurseur pour former l'alliage  $\text{Cu}_5\text{Zn}_8$ , et l'étain réagit avec le cuivre pour former l'alliage  $\text{Cu}_6\text{Sn}_5$ , et ce précurseur allié est stable. Les évolutions du précurseur sont représentées en Figure 5.

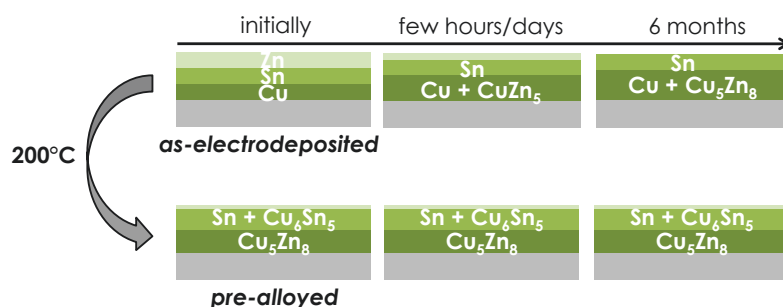


Figure 5: Représentation schématique en coupe du précurseur, juste après électro-dépôt ou après traitement thermique basse température, ainsi que leur évolution naturelle.

Finalement, l'électro-dépôt de précurseur de kesterite par empilement Cu/Sn/Zn est compatible avec un procédé industriel (dépôt rapide sur des grandes surfaces avec des produits non-toxiques), permet de contrôler la composition Cu-Sn-Zn et d'obtenir des couches uniformes.

## Formation de l'absorbeur par traitement thermique

### Principe et challenges

La conversion du précurseur métallique Cu-Sn-Zn en semiconducteur CZTS, CZTSe ou CZTSSe est réalisée par un traitement thermique en présence de chalcogène (S et/ou Se). La plupart des mécanismes réactionnels proposés dans la littérature incluent la formation de composés binaires Cu-S(e), Sn-S(e) et ZnS(e) aux températures intermédiaires (300 – 400 °C) puis la formation de kesterite aux alentours de 500 °C. Le soufre ou le sélénium nécessaire peut être apporté par l'atmosphère réactionnelle et/ou déposé sur le précurseur préalablement. Il existe différents types de traitement thermiques:

- Chalcogène confiné (CC). Le chalcogène est confiné avec le précurseur lors du traitement thermique. Le système de boîte graphique est le système de traitement thermique confiné le plus utilisé pour la formation de kesterite [33–35]. Cependant, des vapeurs peuvent s'échapper de la boîte graphite [36]. Les systèmes fermés étanches tels qu'une ampoule ou tube de quartz scellés [29–31, 37] permettent d'obtenir des pressions partielles en chalcogène plus élevées, mais présentent un risque de surpression.
- Source de chalcogène indépendante (IC). Le chalcogène est apporté par une source extérieure, que ce soit des vapeurs de S(e) venant d'une source solide évaporée dans une chambre séparée (four à 2 ou 3 zones [32, 38]) ou le gaz H<sub>2</sub>S(e) [15].
- Chalcogène déjà inséré dans le précurseur (CP). Un traitement thermique sur une plaque chauffante peut être suffisant lorsque S(e) est déjà présent dans le précurseur, notamment dans le cas de précurseurs obtenus par dépôt de solution, encre ou nano-particules [21, 23–25, 39].

Dans tous les cas, des cellules avec des rendements supérieurs à 8% ont été obtenues. Les systèmes boîte graphite et four à 2 ou 3 zones sont les plus utilisés dans la littérature, et sont étudiés dans cette thèse. Les systèmes de traitements thermiques peuvent également être classés par leur gamme de pression utilisée (vide ou atmosphérique) et vitesse de chauffe (procédé thermique rapide (RTP) ou standard). Les systèmes utilisés dans cette thèse sont décrits en Table 2.

**Table 2:** Systèmes de traitement thermiques, incluant des systèmes à chalcogène confiné (CC) et à source de chalcogène indépendante (IC)

Nom (Institution)	Chalcogène mg	Atm	Pression mbar	$T$ °C	Rampe °C/min	$t$ min	$A$ cm <sup>2</sup>
CC-NEXCIS	S (100)	Ar	7 – 500	500 – 600	RTP: 120 – 600	0 – 10	15×15
IC-IRDEP	Se (500-5500)	N <sub>2</sub>	985	500 – 610	RTP: 180 – 400	3	2.5×2.5
CC-IRDEP	Se (20-70)	Ar	1013	550	40	15	2.5×2.5
CC-IREC	Se (50); Sn (5)	Ar	1.5 + 1000	300 – 400 + 550	20	15 + 30	5×5

La formation de kesterite est soumise à de nombreux challenges. La volatilité des éléments, non seulement S et Se, mais aussi SnS, SnSe et Zn, représente un sérieux obstacle au contrôle de la composition et à l'homogénéité de la couche de kesterite [40]. Des pertes d'étain [27, 41–45] et de zinc [44, 46, 47] sont fréquemment constatées lors des traitements thermiques. Les pertes en Sn peuvent être compensées par l'ajout de poudre SnS(e) [41], de Sn [48, 49], ou d'une couche recouvrante de SnSe<sub>2</sub> [50] (approche thermodynamique). Effectuer le traitement thermique avec une pression d'inerte élevée est aussi une solution pour réduire la perte des espèces volatiles [36] (approche cinétique). Non seulement la composition est difficilement contrôlée du fait de la volatilité des espèces, mais en plus la région du diagramme de phase où la kesterite est la seule phase à exister est très étroite, ce qui signifie que la présence de phases secondaires est très probable. En général, les meilleurs rendements sont obtenus pour des compositions de type pauvre en cuivre, riche en zinc, où seule la phase secondaire ZnS(e) devrait exister en plus de la kesterite.

---

## Résultats

Des couches de CZTS et de CZTSe sont produites avec les différents systèmes de traitement thermique (Table 2). Lors du traitement thermique d'échantillons  $15 \times 15 \text{ cm}^2$  dans le système CC-NEXCIS, de faibles pressions de gaz inerte sont nécessaires à la bonne répartition des vapeurs de chalcogène. Dans ces conditions, les composés sont très volatils et le contrôle de la composition devient très difficile. Dans le cas d'une sulfuration (le chalcogène utilisé est le soufre), les traitements thermiques très rapides ( $10 \text{ }^\circ\text{C/s}$ , 3 min) mènent à une perte de Zn alors que des traitements thermiques rapides ( $10 \text{ }^\circ\text{C/s}$ , 9 min) entraînent une perte en SnS. Dans le cas d'une sélénisation (le chalcogène utilisé est le sélénium), l'ajout d'une couche de Se directement sur le précurseur permet d'améliorer l'uniformité de la couche CZTSe et de limiter les pertes en Sn, seule une perte de Zn est observée. Lorsque les traitements thermiques sont effectuées à des pressions d'inerte plus élevées (atmosphérique), comme par exemple dans les systèmes CC-IRDEP et IC-IRDEP, une perte d'étain est également constatée. Lors du traitement thermique dans le système CC-IREC, la saturation en SnS(e) dans l'atmosphère réactionnelle par ajout de Sn(s) permet limiter les pertes d'étain et de contrôler la composition des absorbeurs.

**Table 3:** Résultats principaux pour les différents systèmes de traitement thermique.

Nom	Matériau	Pertes ?	Uniformité (RSD)	Meilleur rendement %	Morphologie de l'absorbeur	Emplacement de l'excès en Zn	Bandgap eV
CC-NEXCIS	CZTS	Zn, Sn	<20	2.4	petits grains/gros grains	avant et arrière	1.68
CC-NEXCIS	CZTSe	Zn	<6	5.4	petits grains/gros grains	avant et arrière	1.0 – 1.1
IC-IRDEP	CZTSe	Sn	<5	5.5	gros grains/gros grains	uniforme	0.95 – 1.0
CC-IRDEP	CZTSe	Sn	<6	5.3	petits grains/gros grains	arrière	0.95 – 1.0
CC-IREC	CZTSe	no	<4	6.0	gros grains	avant	1.0 – 1.1

Finalement, des performances similaires sont obtenues avec tous les systèmes de traitement thermique étudiés (entre 5.3 et 6.0% pour des cellules CZTSe). Lorsqu'on a des pertes de composés volatils pendant le traitement thermique, la morphologie de l'absorbeur est souvent endommagée (trous, perte d'adhérence au contact arrière), ce qui augmente la résistance série et diminue les performances. Si la composition n'est pas contrôlée de manière précise, la présence de phases secondaires est très probable. En effet, même dans la gamme de composition où les meilleures cellules sont obtenues (pauvre en cuivre, riche en zinc), les phases ZnSe, SnSe et SnSe<sub>2</sub> sont détectées. Ces phases secondaires, souvent situées à la surface de l'absorbeur, nuisent aux performances des cellules. Il est donc important d'optimiser l'interface entre l'absorbeur et la couche tampon. Les absorbeurs recuits dans le système CC-IREC, plus uniformes et dont il est plus facile de contrôler la composition, sont utilisés par la suite.

## Optimisation de la cellule

Les procédés typiquement utilisés pour la formation d'une jonction p-n dans les cellules solaires CIGS sont le décapage chimique KCN et le dépôt par bain chimique d'une couche de CdS. Ces deux procédés sont également utilisés pour la kesterite.

### Décapage

L'impact des phases secondaires dépend de leur nature (bandgap, concentration) mais aussi de leur emplacement dans l'absorbeur. Lorsqu'elles sont situées à l'hétérointerface, elles contribuent fortement à la réduction du  $V_{OC}$  [51]. En conséquence, il est très important de réussir à enlever les phases secondaires de la surface. Le décapage chimique, où l'échantillon est immergé dans une solution, permet de traiter la surface de l'absorbeur et peut contribuer 1) au nettoyage de la surface en enlevant les oxydes, 2) au retrait sélectif des phases secondaires, 3) à la passivation de la surface. Dans la littérature, KCN permet principalement d'enlever les phases Cu-S(e) mais

agit aussi sur les phases à base d'étain et sur les oxides [52, 53].  $(\text{NH}_4)_2\text{S}$  a été proposé pour le décapage des phases Sn-S(e) [54], et  $\text{KMnO}_4 / \text{H}_2\text{SO}_4 + \text{Na}_2\text{S}$  pour le ZnSe [55]. Dans ce travail, ces deux derniers décapages ont été appliqués seuls ou combinés sur des absorbeurs pauvres en cuivre. Les analyses SEM, spectroscopie Raman, XRD et de composition XRF montrent que les phases secondaires ZnSe et Sn-Se sont éliminées de la surface avec succès. Les cellules à base d'absorbeurs riches en Sn, initialement à faible performance ( $<2\%$ ) ont vu leur rendement augmenter énormément (+160%) après décapage, confirmant l'influence négative des phases Sn-Se sur la performance des cellules. Les cellules à base d'absorbeurs riches en Zn ont initialement de meilleures performances que celles à base d'absorbeurs riches en Sn, ce qui montre que les phases ZnSe sont moins néfastes que les phases Sn-Se. Cependant, les paramètres opto-électroniques ont été améliorés après décapage, démontrant que ZnSe a également un effet négatif sur la performance. Les cellules à base d'absorbeurs très riches en Zn n'ont pas vu leurs performances s'améliorer car le décapage a créé des trous dans l'absorbeur. Sans décapage, le meilleur rendement obtenu était de 6.0% pour un absorbeur de composition optimum ( $0.70 < \text{Cu}/(\text{Zn}+\text{Sn}) < 0.85$  and  $1.00 < \text{Zn}/\text{Sn} < 1.25$ ). Après décapage combiné de  $\text{KMnO}_4 / \text{H}_2\text{SO}_4 + \text{Na}_2\text{S} + (\text{NH}_4)_2\text{S}$ , le rendement a été augmenté à 7.6%. Par la suite ce décapage combiné est systématiquement appliqué aux absorbeurs.

## Couche tampon

Une couche tampon n est ensuite déposée afin de former la jonction p-n. Le CdS, un semiconducteur de bandgap 2.3 – 2.6 eV [56, 57] est typiquement déposé par bain chimique (CBD) car cette méthode permet d'obtenir une couche conforme très fine de CdS par un dépôt à basse température. Le dépôt est basé sur la libération lente d'ions  $\text{Cd}^{2+}$  et  $\text{S}^{2-}$  dans un bain aqueux alcalin et leur précipitation sur des substrats présents dans le bain. Le cadmium peut être fourni par différents précurseurs de cadmium tels que  $\text{Cd}(\text{SO}_4)$  [57–59],  $\text{Cd}(\text{NO}_3)_2$ ,  $\text{CdCl}_2$ ,  $\text{CdI}_2$  ou  $\text{Cd}(\text{CH}_3\text{COO})_2$  [57], influençant les propriétés de la couche de CdS. Différentes couches de CdS sont déposées à l'IREC sur les absorbeurs décapés. Toutes les cellules présentent des rendements supérieurs à 7%, avec des facteurs de forme (FF) similaires. Cependant, les cellules qui ont le meilleur courant de court-circuit ( $J_{\text{SC}}$ ) ont le pire voltage à circuit ouvert ( $V_{\text{OC}}$ ) et vice-versa. Les cellules présentant les meilleurs  $J_{\text{SC}}$  ont été préparées avec des CdS plus fins (cinétique de dépôt très lente ou durée de dépôt très rapide), ce qui permet d'augmenter l'absorption du courant dans la région de longueur d'onde 400 – 520 nm où le CdS absorbe. Les cellules préparées avec des CdS plus épais ont un  $J_{\text{SC}}$  réduit mais leur  $V_{\text{OC}}$  est très élevé. Toutes les cellules ont les courbes I-V déformées en cas d'illumination avec de la lumière rouge (photons de faible énergie, longueur d'onde au dessus de 600 nm) et les courbes sous illumination et dans le noir se croisent. Ces comportements sont fortement réduits après exposition continue à de la lumière, suggérant la présence de défauts photosensibles jouant sur la barrière de potentiel entre l'absorbeur et la couche tampon. Le meilleur rendement obtenu par variation de la couche tampon est de 8.5%. L'ajout de contacts métalliques fins pour la collection du courant permet d'améliorer le  $J_{\text{SC}}$  (+10%) et d'obtenir une cellule CZTSe de 9.1%, un record pour les cellules de kesterite produites par électro-dépôt.

D'autres couches tampons ( $\text{In}_2\text{S}_3$  et ZnS), qui représentent des alternatives sans cadmium au CdS, ont également été déposées par CBD sur les mêmes absorbeurs. De par leur bandgap (bandgap indirect pour  $\text{In}_2\text{S}_3$  et bandgap de 3.6 eV pour le ZnS), ces couches tampons permettent une amélioration de la génération du courant aux faibles énergies. Cependant les rendements de conversion photovoltaïques sont nettement inférieurs à leur homologues à base de CdS, avec un maximum de 4.5% pour une cellule à base de  $\text{In}_2\text{S}_3$  et de 1.1% pour une cellule à base de ZnS. Les  $V_{\text{OC}}$  observés sont très élevés (jusqu'à 490 mV), parmi les plus élevés reportés pour des cellules de kesterite CZTSe, mais des densités de courant et facteurs de formes très bas limitent les rendements. La mauvaise collection du courant peut être expliquée par différentes raisons: recombinaison des porteurs de courant à l'interface, défauts photosensibles, et alignement de bandes non favorable.

## Conclusion

Comme prévu, les meilleurs rendements sont obtenus pour des absorbeurs de composition pauvre en cuivre riche en zinc, plus précisément  $0.70 < \text{Cu}/(\text{Sn}+\text{Zn}) < 0.85$  and  $1.00 < \text{Zn}/\text{Sn} < 1.25$ . Les  $J_{\text{SC}}$  sont plus faibles dans ce travail que dans la littérature (Tables 5 et 4), probablement car le contact avant n'est pas optimisé (pas de contacts métalliques, pas de couche anti-réflexion (ARC)). Cependant les  $V_{\text{OC}}$  sont très élevés comparés aux  $V_{\text{OC}}$  reportés dans la littérature, ce qui peut être du à un bandgap plus élevé<sup>1</sup>, et/ou à une interface optimisée par décapage et optimisation de la couche tampon. Le déficit en  $V_{\text{OC}}$  étant un des principaux facteurs de limitation de performance dans les cellules à base de kesterite, l'obtention de  $V_{\text{OC}}$  élevés dans ce travail est à noter.

**Table 4:** Paramètres opto-électroniques des cellules  $\text{Cu}_2\text{ZnSnSe}_4$  (CZTSe) devics dans ce travail.

<sup>a</sup> (iii) Décapage par  $\text{KMnO}_4 / \text{H}_2\text{SO}_4 + \text{Na}_2\text{S} + (\text{NH}_4)_2\text{S}$ .

<sup>b</sup> Cellule avec des contacts métalliques.

Décapage	Couche tampon	Cu/Zn+Sn	Zn/Sn	$\eta$ %	$V_{\text{OC}}$ mV	$E_g$ eV	$E_g/q \cdot V_{\text{OC}}$ V	$J_{\text{SC}}$ mA/cm <sup>2</sup>	FF %
(iii) <sup>a</sup>	CdS 4 (45 min)	0.80	1.20	9.1 <sup>b</sup>	421	-	-	34.2	64.6
(iii)	CdS 3	0.75	1.18	8.5	446	1.06	0.61	30.8	62.1
(iii)	CdS 2	0.75	1.18	8.2	466	1.09	0.62	26.1	67.3
(iii)	CdS 4 (45 min)	0.74	1.25	8.2	425	1.05	0.62	30.9	62.7
(iii)	CdS 5 (0.5 min)	0.80	1.17	8.1	413	1.02	0.61	33.4	58.5
(iii)	CdS 5 (7 min)	0.78	1.15	7.5	442	1.04	0.60	29.1	58.1
(iii)	CdS 5 (7 min)	0.66	1.11	6.8	457	1.06	0.60	28.2	52.5
(iii)	$\text{In}_2\text{S}_3$ 6 (40 min)	0.78	1.12	4.5	483	-	-	24.0	38.6

**Table 5:** Paramètres opto-électroniques des cellules  $\text{Cu}_2\text{ZnSnSe}_4$  (CZTSe) devics dans la littérature.

<sup>a</sup> (i) Décapage  $\text{KMnO}_4 / \text{H}_2\text{SO}_4 + \text{Na}_2\text{S}$ .

Méthode de dépôt	Décapage	ARC	Cu/(Zn+Sn)	Zn/Sn	$\eta$ %	$E_g$ eV	$V_{\text{OC}}$ mV	$E_g/q \cdot V_{\text{OC}}$ V	$J_{\text{SC}}$ mA/cm <sup>2</sup>	FF %
co-évap	-	$\text{MgF}_2$	0.85	1.04	11.6 [13]	1	423	0.58	40.6	67.3
sputtering	KCN	$\text{MgF}_2$	0.83	1.2	10.4 [15]	1	394	0.61	39.7	66.4
co-évap	-	-	-	-	9.8 [60]	1	380	0.62	37.6	68.9
sputtering	KCN	$\text{MgF}_2$	0.7	1	9.7 [61]	1	408	0.59	38.9	61.4
co-évap	-	$\text{MgF}_2$	0.86	1.15	9.2 [62]	0.96	377	0.58	37.4	64.9
co-évap	-	$\text{MgF}_2$	-	1.3	8.9 [63]	1	385	0.62	42.6	54.3
sputtering	(i) <sup>a</sup>	-	0.77	1.21	8.2 [34]	1.02	392	0.63	32.4	64.4
ED	KCN	-	-	-	8.0 [32]	1.02	390	0.63	35.3	58
co-évap	KCN	-	-	-	7.5 [64]	-	356	-	35.4	60
sputtering	KCN	-	-	-	7.5 [65]	-	432	-	30.5	56.8
ED	NaCN	$\text{MgF}_2$	-	-	7.0 [31]	1.1	369	0.73	32.4	58.5

Des variations de bandgap sont également observées dans les cellules réalisées dans le cadre de ce travail, avec une augmentation du bandgap lorsque le ratio  $\text{Cu}/(\text{Zn}+\text{Sn})$  diminue. Les hauts bandgaps obtenus pour les absorbeurs très pauvres en cuivre peuvent contribuer à l'augmentation du  $V_{\text{OC}}$ . Différentes hypothèses ont été proposées pour expliquer cette variation, telles que la formation de défauts  $[\text{Zn}^{2+} + V_{\text{Cu}}]$  [10], l'échange des cations Cu et Zn (kesterite désordonnée [66]) et la formation de phases secondaires riches en cuivre avec un bandgap plus faible.

En conclusion, les procédés et les conditions nécessaires pour l'obtention de hauts rendements ont été identifiés : a) la composition de l'absorbeur, qui régit l'abondance et la nature des phases secondaires; b) la ségrégation des phases secondaires à la surface pour qu'elles puissent être décapées; c) l'identification de ces phases secondaires; d) des procédures de décapage adaptées, qui peuvent

<sup>1</sup>La détermination du bandgap fait l'objet d'incertitudes, voir Annexe B.

éventuellement passiver la surface de l'absorbeur; e) l'optimisation de la couche tampon, un compromis entre l'amélioration de courant et l'amélioration du voltage et finalement f) l'optimisation du contact avant, où la collection du courant est améliorée par l'ajout de contacts métalliques et la génération du courant par couche anti-réfléctive. Les améliorations réalisées dans le cadre de ce travail sont résumées dans la Figure 6.

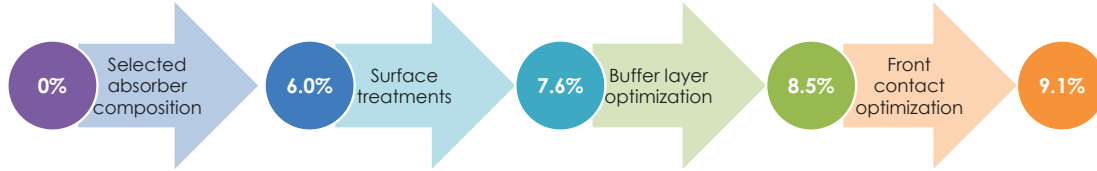


**Figure 6:** Résumé de l'évolution des performances des cellules kesterite: optimisation de différentes étapes.

## Conclusions: Kesterite — une approche industrielle

Le système photovoltaïque idéal serait basé sur des modules à haut rendement et à bas coût. Le potentiel à long terme des différentes technologies dépend également des matériaux utilisés et de la fiabilité de la technologie.

**Table 6:** Comparaison des technologies PV silicium, couches minces CIGS and kesterite en fonction de leur rendement, coût, disponibilité matériaux et fiabilité: évaluation de leur potentiel à long terme. <sup>a</sup> Les rendements sont extraits de [16, 26, 67–72] et <sup>b</sup> les coûts de [73–78].

Technologie	Rendement $\eta$ (%) <sup>a</sup> Meilleure cellule (Module commercial)	Coût module <sup>b</sup> €/Wp	Limitation matériaux	Fiabilité
c-Si	25.6 (16 – 21.5)	0.45 – 0.65	électrode Ag	ok
CuIn <sub>x</sub> Ga <sub>1-x</sub> (S,Se) <sub>2</sub> (CIGS)	21.7 (12 – 15.5)	0.44 – 0.54	In	données requises
Cu <sub>2</sub> ZnSn(S,Se) <sub>4</sub> (CZTSSe)	12.7 (n/a)	n/a	ok	inconnue

- **Haut rendement.** Actuellement, les cellules solaires à base de silicium offrent de meilleurs rendements que leurs homologues couches minces. Cependant les rendements des principales technologies couches minces (CIGS, mais aussi le CdTe) ont atteint des hauts niveaux dans les dernières années, démontrant leur pertinence pour la conversion d'énergie à échelle industrielle. D'ici 2019, on s'attend à ce que les rendements moyens des modules commerciaux atteignent 17% (Si) et 15% (couches minces) [79]. Toute nouvelle technologie doit dépasser les 10% de rendement à court terme et 15% de rendement à moyen terme pour réussir à entrer le (pré)marché [16]. Pour l'instant le rendement maximum des kesterite n'est que de 12.7%.
- **Bas coût.** Les coûts de production des cellules à base de silicium ont énormément diminué entre 2010 et 2013 et ont atteint un niveau stable depuis 2014. Des réductions de coûts supplémentaires nécessiteraient une diminution de quantité de Si et de son coût de purification. Les coûts des cellules solaires couches minces, actuellement assez proches de ceux des cellules solaires silicium, peuvent encore être réduits significativement, par l'utilisation de procédés à haut débit de production et bas coûts. Le coût de production de CIGS est estimé entre 0.34 et 0.54€/Wp. Différents paramètres sont pris en compte, entre autres:

1. Taille de l'usine et emplacement. Passer d'une usine de 100 MW à 1 GW permettrait d'économiser environ 0.03 à 0.04\$/Wp, et un emplacement bon marché peut faire économiser 5 centimes supplémentaires [76, 80].

2. Procédé. Les modules CIGS performants sont généralement produits par évaporation sous vide ou par pulvérisation cathodique suivie de traitement thermique en présence de  $\text{H}_2\text{Se}$ . Ces deux procédés ont un débit de production, utilisation de matériau relativement faibles et nécessitent un haut niveau de vide. Des procédés à bas coûts doivent permettre des dépôts rapides sur de grandes surfaces, avec un équipement simple. Par exemple, l'électrodépôt permet une réduction de  $0.04\text{€}/\text{Wp}$  [77].
  3. Rendement du module. Une augmentation de rendement de 12.8 à 14% permettrait d'économiser  $0.04\text{€}/\text{Wp}$  [77], et de 13 à 16%  $0.08\text{€}/\text{Wp}$  [80]. Les différences de rendement entre les meilleurs cellules et les modules sont dues à des propriétés intrinsèques (aire, épaisseur de la couche fenêtre, contacts) mais aussi à des problèmes d'uniformité.
- **Matériaux non-toxiques, abondants, et disponibles.** Malgré les réserves importantes de silicium (deuxième élément le plus abondant dans la croûte terrestre), le développement des cellules Si peut être limité par les réserves d'argent (Ag), utilisé pour former le contact électrique avant (type n). Si l'utilisation d'argent dans les contacts est réduite, il n'y a pas d'autre limitation matérielle au déploiement des cellules Si. Dans le cas des technologies couches minces, des pénuries d'indium (In), un matériau peu abondant aux prix instables, pourrait limiter le développement et le prix des modules CIGS. La kesterite, en revanche, est composée de matériaux abondants tels que le cuivre, l'étain, le zinc et le soufre, et ne devrait pas rencontrer de restriction majeure.
  - **Fiabilité et longévité.** Les cellules solaires à base de silicium ont démontré leur fiabilité. Dans le cas de couches minces, il y a moins de données disponibles. Le CIGS a un comportement métastable, mais qui conduit à l'amélioration des performances. L'encapsulation des modules pour les préserver des dégradations liées à l'humidité semble être l'enjeu principal. Pour l'instant, le comportement de la kesterite n'est pas connu et devra être étudié avant une éventuelle commercialisation.

Les kesterites doivent donc atteindre de plus haut rendements, tout en étant produites à bas coûts. Comparés au procédés sous vide, l'électrodépôt a de nombreux avantages. Le bas coût du procédé d'électrodépôt a été confirmé par l'analyse de Broussillou et al. pour la production de CZTS et CIGSSe (Figure 7).

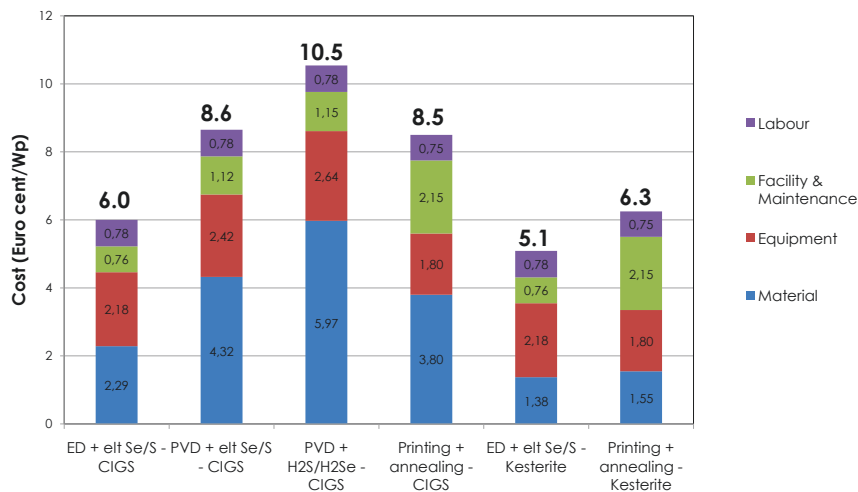


**Figure 7:** Comparaison des coûts de production des absorbeurs  $\text{CuIn}_x\text{Ga}_{1-x}(\text{S,Se})_2$  (CIGS) et  $\text{Cu}_2\text{ZnSn}(\text{S,Se})_4$  (CZTSSe) par ED, PVD procédés d'impression [81]. Estimation pour un rendement module de 14%. Les procédés d'impression sont plus coûteux que l'électrodépôt car le prix des encres en particulier les nanoparticules est assez élevé.

Dans ce travail, le développement d'un procédé d'électrodépôt compatible avec l'industrie a été étudié. La capacité à produire un film de composition et d'épaisseur contrôlées et uniformes,



tout en répondant aux exigences de sécurité, vitesse de dépôt, et bas coût a été démontrée avec succès. Les systèmes de traitement thermique utilisés présentent différents degrés de compatibilité avec un procédé industriel. Un procédé RTP à pression atmosphérique avec Se ou S élémentaire est préférable d'un point de vue du coût, correspondant à la description du système IC-IRDEP. Cependant des problèmes d'uniformité et de reproductibilité du procédé ne nous permettent pas de conclure quand à sa pertinence pour un procédé industriel. La mise à échelle industrielle des procédés utilisés dans ce travail reste sujet à question. Le système CC-IREC, qui n'est pas le procédé idéal en terme de compatibilité avec l'industrie (une étape sous vide, vitesse de chauffe lente) est le système qui permet le contrôle de la composition le plus précis (un challenge majeur lors de la fabrication de kesterite), et a donc été choisi pour les études portant sur l'optimisation de rendement. En effet, l'addition de Sn(s) dans la chambre réactionnelle a été utile pour limiter les pertes d'éléments volatils, donc améliorer le contrôle de la composition et réduire la présence de phases secondaires. Les phases secondaires ZnSe et Sn-Se qui peuvent avoir une influence négative sur la performance des cellules, sont décapées par la combinaison de  $\text{KMnO}_4 / \text{H}_2\text{SO}_4 + \text{Na}_2\text{S} + (\text{NH}_4)_2\text{S}$ . Même si ce décapage comprend plus d'étapes que le KCN typiquement utilisé pour le CIGS, les produits utilisés sont moins toxiques, donc préférables. Des couches tampons alternatives sans cadmium ont été étudiées, mais les meilleures performances sont obtenues avec le CdS. Son épaisseur peut être variée afin d'avoir un compromis entre des bons courants et des bons voltages. Finalement, un rendement de 9.1% a été obtenu, ce qui représente un nouveau record de rendement pour la kesterite préparée par électrodépôt. Cependant le rendement est toujours faible comparé au CIGS et CdTe. Davantage de R&D, notamment sur 1) la compréhension des interfaces et défauts, 2) les propriétés chimiques et électriques de la jonction p-n, 3) la compréhension des fluctuations de potentiel électrostatique, du désordre Cu-Zn, 4) le dopage extrinsèque (Na, K, Li, O et autres) ou la substitution isoélectronique (Ge, Si) est nécessaire pour atteindre de plus hauts niveaux de rendement. Si les rendements de 15 – 18% sont obtenus avec des procédés industriels à bas coûts, la kesterite pourrait prétendre à une part de marché significative entre 2020 et 2030 [16].

# Chapter I

## Introduction

### Contents

---

I.1	Photovoltaics . . . . .	<b>2</b>
I.1.1	Basics . . . . .	2
I.1.1.1	Sunlight . . . . .	2
I.1.1.2	Solar cells . . . . .	3
I.1.1.3	I-V curve . . . . .	5
I.1.2	Technologies . . . . .	7
I.1.3	Historical . . . . .	9
I.1.4	Perspectives . . . . .	10
I.1.4.1	Energy generation scenarios . . . . .	10
I.1.4.2	Which PV technologies to ensure the electricity generation? . . . . .	11
I.1.5	Material considerations . . . . .	12
I.1.5.1	Resources availability . . . . .	12
I.1.5.2	The case of CIGS: indium and gallium . . . . .	13
I.1.5.3	Comparison of metal quantity for CIGS and CZTSSe . . . . .	14
I.2	Kesterite properties . . . . .	<b>16</b>
I.2.1	Properties of kesterite materials . . . . .	16
I.2.1.1	Kesterite semi-conductor properties . . . . .	16
I.2.1.2	Crystalline properties . . . . .	16
I.2.2	Kesterite fabrication processes . . . . .	17
I.2.2.1	Vacuum deposition methods . . . . .	20
I.2.2.2	Non-vacuum deposition methods . . . . .	20
I.2.3	Challenges for high-efficient kesterite devices production . . . . .	21
I.2.3.1	Kesterite fabrication and challenging process control . . . . .	23
I.2.3.2	Bulk properties: defects and passivation . . . . .	25
I.2.3.3	Interface optimization . . . . .	26
I.3	Objectives and Structure . . . . .	<b>27</b>

---

The United Nations predict a world population growth from 7.1 billion in 2013 to 9.6 billion by 2050 [82]. Both population growth and increasing standards of living for many people in developing countries will cause strong growth in energy demand. Facing a growing global electricity demand and increasing concerns about climate change and finite energy sources, the development of renewable and non-polluting power sources is of crucial importance [1]. In order to face this growing demand we mainly use uranium and fossil fuels (petrol, natural gas and coal). The use of the latest leads to greenhouse effect gas and other pollutants' emission in the atmosphere. These energy resources are not renewable, so they are going to run out and become more and more expensive. Solar energy is the source of nearly all energy on the earth under different forms. Fossil fuels are essentially stored solar energy through photosynthesis from millions of years ago. More sustainable alternative energy sources also take their origins from solar energy:

- Biomass converts the sun's energy into fuel, which can then be used for heat, transportation or electricity.
- Wind energy, used for hundreds of years to provide mechanical energy or transportation, uses air currents that are created by solar heated air and the rotation of the earth. Today wind turbines convert wind power into electricity.
- Hydropower depends on the water cycle. The sun, which drives the water cycle, heats water in oceans and seas. Water evaporates as water vapour into the air and returns as rain to the Earth to provide water in dams.
- Photovoltaic (PV) is a simple and elegant method of harnessing the sun's energy. PV devices (solar cells) are unique in the sense that they directly convert the incident solar radiation into electricity.

A wide range of photovoltaic (PV) technologies allow to convert solar energy into electricity. Wafer-based first-generation crystalline silicon solar cells share the market with thin-film based second-generation solar cells (including  $\text{CuIn}_x\text{Ga}_{1-x}(\text{S,Se})_2$  (CIGS) and CdTe), which have a great potential for cheaper manufacturing costs. However, the future deployment of PV technologies at terawatt scale may be restrained by the availability and price of elements such as silver for c-Si solar cells or indium, gallium, tellurium for thin film CIGS and CdTe [4–6]. By contrast, the production of earth-abundant kesterite compounds  $\text{Cu}_2\text{ZnSnS}_4$  (CZTS),  $\text{Cu}_2\text{ZnSnSe}_4$  (CZTSe) and  $\text{Cu}_2\text{ZnSn}(\text{S,Se})_4$  (CZTSSe) would be less impacted by element availability considerations. Thin film kesterite layers are a promising candidate for the next generation of sustainable and competitive solar cells, and their development has accelerated in the last years.

## I.1 Photovoltaics

### I.1.1 Basics

In this section, a quick overview of photovoltaics basics is given. More information and detailed explanations can be found in references [83–85].

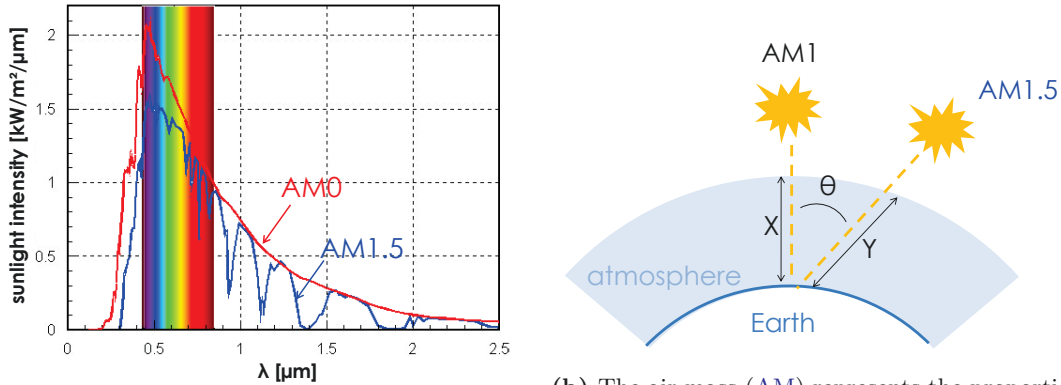
#### I.1.1.1 Sunlight

Light may be viewed as consisting of particles of energy, called photons. A **photon** is characterized by either a wavelength, denoted by  $\lambda$  or equivalently an energy, denoted by  $E$ . There is an inverse relationship between the energy of a photon ( $E$ ) and the wavelength of the light ( $\lambda$ ) given by the equation:

$$E = \frac{hc}{\lambda} \tag{I.1}$$

where  $h$  is Planck's constant ( $6.626 \times 10^{-34} \text{ J}\cdot\text{s}$ ) and  $c$  ( $2.998 \times 10^8 \text{ m}\cdot\text{s}^{-1}$ ) is the speed of light. The above inverse relationship implies that light consisting of high energy photons (such as “blue” light) has a short wavelength. Light consisting of low energy photons (such as “red” light) has a

long wavelength. When dealing with “particles” such as photons or electrons, a commonly used unit of energy is the electron-volt (eV) rather than the joule (J). An electron volt is the energy required to move an electron across an electric potential difference of one volt,  $1 \text{ eV} = 1.602 \times 10^{-19} \text{ J}$ .



(a) A comparison of solar radiation outside the Earth’s atmosphere (AM0) with the amount of solar radiation reaching the Earth itself (AM1.5).

(b) The air mass (AM) represents the proportion of atmosphere that the light must pass through before striking the earth relative to its overhead path length, and is equal to  $Y/X$ .

**Figure I.1:** Solar radiation at the earth’s surface. Adapted from [84].

Sunlight is a spectrum of photons distributed over a range of energy. The total power emitted from the sun is composed not of a single wavelength, but of many wavelengths and therefore appears white or yellow to the human eye. **Solar radiation** at the earth’s surface is dependent on the path length which light takes through the atmosphere. A standard spectrum and power density has been defined for radiation at the earth’s surface, noted AM1.5 and of value  $1 \text{ kW/m}^2$ , which corresponds to a distance travelled through the atmosphere 50% greater than when the sun is exactly overhead (air mass of 1.5). The standard spectrum at the Earth’s surface is called AM1.5G, (the G stands for global and includes both direct and diffuse radiation) or AM1.5D (which includes direct radiation only). AM1.5G spectrum is represented in Figure I.1.

When the sunlight’s photons hit the solar cells, they are absorbed by semiconductor materials, which are the solar cells main constituents. Solar cells working principle is based on P-N junction, formed by joining n-type and p-type semiconductor materials.

### I.1.1.2 Solar cells

**Semiconductors** are made of individual atoms bonded together in a regular, periodic structure (the crystal lattice) and weakly bonded electrons. The energy of these electrons is described by the electronic band structure, as shown in Figure I.2. The **bandgap** ( $E_g$ ) is the energy separating the lower energy band (valence band, VB) and the higher energy band (conduction band, CB).

Semiconductors are defined by their unique electric conductive behavior, somewhere between that of a metal (conductor) and an insulator. When all the electrons are in their bound state, i.e. the lower energy band, there is no conduction, the semiconductor behave as an insulator. When the bandgap energy is met — by thermal excitation or by an incoming photon — an electron can break free from its bound state (valence band) and is excited into a free state (conduction band). The space left behind by the electron appears as a positive charge moving through the crystal lattice. This empty space is commonly called a **hole**, and is similar to an electron, but with a positive charge. Current conduction in a semiconductor occurs through the movement of free electrons and holes, collectively known as **charge carriers**. In a semiconductor, at room temperature significant numbers of electrons can be excited to cross the bandgap, therefore enabling the conduction.

The optical **absorption coefficient** ( $\alpha$ , in  $\text{cm}^{-1}$ ) determines how far into a material the light of a particular wavelength penetrates before it is absorbed. In a material with a low absorption coef-

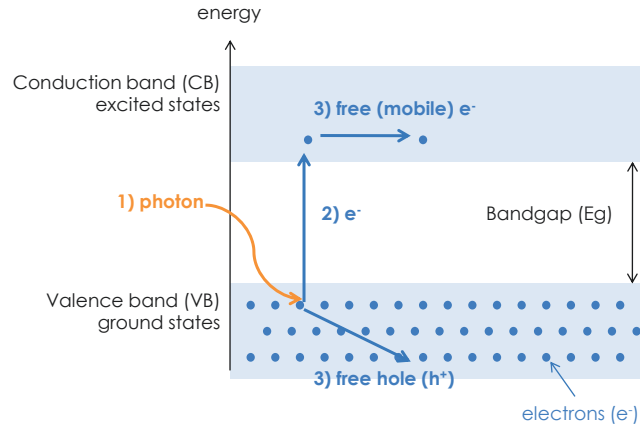


**Figure I.2:** Schematic of a semiconductor electronic band structure. 1) An incoming photon has an energy larger than the bandgap energy. 2) An electron from the valence band is pumped to the conduction band, creating a hole where the electron was formerly bound. 3) The electron in the conduction band and the hole in the valence band are free to move and to participate to conduction. Adapted from [83,84].

ficient, light is only poorly absorbed, and if the material is thin enough, it will appear transparent to that wavelength. For solar cells, the thickness of semiconductor material necessary to absorb the light ranges from  $10^{-8}$  to  $10^{-4}$  m. Light of energy below the bandgap does not have sufficient energy to excite an electron from the valence band into the conduction band, and is not absorbed. Absorption of photons of energy above the bandgap into a semiconductor allows to generate charge carriers.

After their generation, the charge carriers recombine, i.e. the electron loses energy and re-occupies the energy state in the valence band, unless they are separated by the **p-n junction**. A p-n junction is formed by joining n-type and p-type semiconductor materials. N-type (n for negative) semiconductors have extra electrons and the p-type (p for positive) extra holes. The type (n or p) of the semiconductor is determined by **doping**, which can be realized by addition of extra atoms (extrinsic doping) or by intrinsic defects. The Fermi-Dirac distribution  $f(E)$  gives the probability that (at thermodynamic equilibrium) an electron will occupy a state having a determined energy:

$$f(E) = \frac{1}{e^{\frac{E-E_f}{k_B T}} + 1} \quad (\text{I.2})$$

where  $k_B$  is Boltzmann's constant ( $6.617 \times 10^{-5}$  eV · K<sup>-1</sup>),  $T$  the absolute temperature in kelvin (K) and  $E_f$  the Fermi level in electron-volt (eV), located inside the bandgap for a semiconductor. In p-type semiconductors, because of the high hole concentration, the Fermi level is close to the valence band, while in n-type semiconductors the Fermi level is close to the conduction band. When joining p- and n-type semiconductors, at equilibrium, their Fermi levels match on the two sides of the junction, as shown in Figure I.3, and an internal electric field allow the carriers separation. Therefore the electrons are swept to the n-type side of the junction. Similarly, holes are swept to the p-type side.

In a solar cell, the carriers are then collected at the two sides of the p-n junction, as shown in Figure I.4. For instance, in the figure, the carriers are generated in the p-type material. The electrons are swept towards the surface of the solar cell, which becomes negatively charged, while the holes are collected at the backside, which becomes positively charged.

The difference in the amount of electric charge carriers between the negative and positive contacts creates a difference in electric potential. Upon contacting an external load, electrons will flow from the negative contact through the load to the positive contact in order to recombine with the holes, creating an electric current.

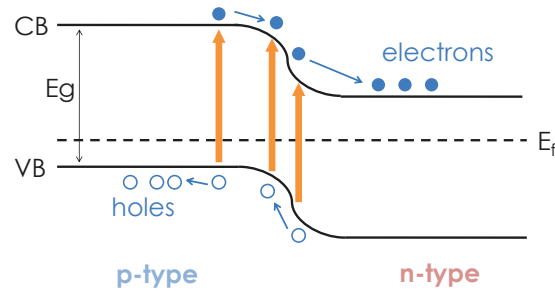


**Figure I.3:** P-N junction band diagram under illumination: illustration of solar cell working principle.

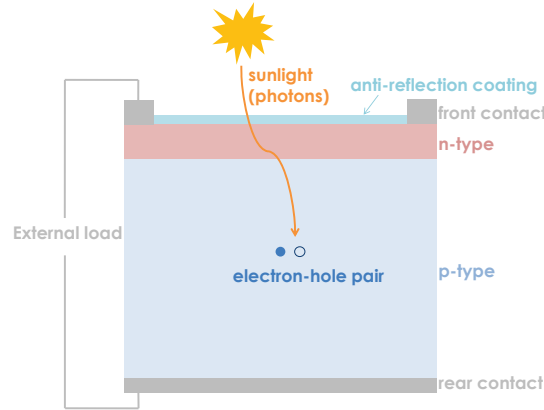


**Figure I.4:** Schematic of a solar cell. Adapted from [84].

In summary, when the solar cell is exposed to sunlight of sufficient energy, the incident solar photons are absorbed by the atoms, generating carriers in the semiconductor. The carriers are separated by the p-n junction and collected at the contacts of the solar cell, generating an electric current. The measure of a solar cell performance will be given by the power conversion efficiency extracted from the current-voltage (I-V) curve.

### I.1.1.3 I-V curve

The I-V curve of a solar cell is the superposition of the light-generated current with the I-V curve of the solar cell diode in the dark. Without illumination, a solar cell has the same electrical characteristics as a diode. Under illumination, the current of a solar cell is expressed by:

$$J = J_L - J_0(e^{qV/nkT} - 1) \quad (\text{I.3})$$

where  $J_L$  is the light generated current ( $\text{A}/\text{m}^2$ ) and

$$J = J_0(e^{qV/nkT} - 1) \quad (\text{I.4})$$

is the diode equation, with  $J$  the current density flowing through the diode in amperes per square meter ( $\text{A}/\text{m}^2$ ),  $J_0$  is the dark saturation current density ( $\text{A}/\text{m}^2$ ), which is the diode leakage current density in the absence of light and is a measure of recombination in the cell.  $V$  is the applied voltage (V),  $q$  the absolute value of electron charge ( $1.602 \times 10^{-19}$  C),  $k_B$  is Boltzmann's constant and  $T$  the temperature (K).  $n$  is the ideality factor, a number typically between 1 and 2, which is a measure of the junction quality and the type of recombination in a solar cell. When there are no external inputs such as light or applied voltage, the net current from the device is zero. The I-V curve of a solar cell under illumination is represented in Figure I.5.

Measuring the I-V curve of a solar cell allows to measure its performance. Dividing the power

generated by the solar cell by the power of the incident light, one obtains the solar to electric conversion efficiency, or **power conversion efficiency**  $\eta$  of the solar cell in %:

$$\eta = \frac{P_{max}}{P_{in}} \times 100 \quad (\text{I.5})$$

where  $P_{max}$  is the power extracted from the solar cell (W) and  $P_{in}$  the power of the incident light (W). Power generated by the solar cell, which is the current times the voltage, shown in Figure I.5, is given by the equation:

$$P_{max} = I_{mp}V_{mp} \quad (\text{I.6})$$

where  $I_{mp}$  and  $V_{mp}$  are the current (A) and voltage (V) of a solar cell for which the maximum power is generated.

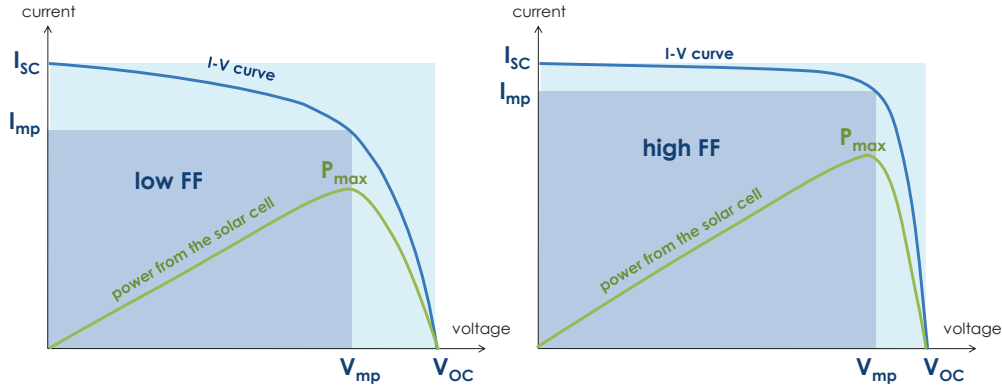


**Figure I.5:** I-V curve of a solar cell under illumination, adapted from [84]. On the left a solar cell with low FF, at the right one exhibiting high FF are shown.

Other important parameters for defining the performance of a solar cell are  $I_{SC}$ ,  $V_{OC}$  and FF.  $I_{SC}$  is the **short-circuit current**, the current through the solar cell when the voltage across the solar cell is zero (i.e., when the solar cell is short circuited), and the largest current which may be drawn from the solar cell.  $I_{SC}$ , which is created by the generation and collection of light-generated carriers, depends on many factors:

- Area of the solar cell. To remove the dependence of the solar cell area, it is more common to list the short circuit current density ( $J_{SC}$ ) in  $A/cm^2$  rather than the short-circuit current. The cell characteristics are then traced in a J-V curve;
- Number of incoming photons;
- Spectrum of the incident light. Brighter sunlight causes more electrons to be generated in the semiconductor resulting in more current. For most solar cell measurement, the spectrum is standardized to the AM1.5 spectrum;
- Optical properties (absorption and reflection) of the solar cell;
- Collection probability of the solar cell, which depends mainly on the surface passivation and the minority carrier lifetime.

$V_{OC}$  is the **open-circuit voltage**, the maximum voltage at zero current. Open-circuit voltage is a measure of the amount of recombination in the device and cannot exceed the bandgap energy. FF, the **fill factor**, is defined as the ratio of the maximum power from the solar cell to the product of  $V_{OC}$  and  $I_{SC}$ .

$$FF = \frac{I_{mp} \times V_{mp}}{I_{SC} \times V_{OC}} \quad (\text{I.7})$$

Graphically, the FF is the area of the largest rectangle fitting inside the IV curve, shown in Figure I.5 by the darker area. Different FF values will have a great influence on the solar cell performance.

Finally, the power generated by the solar cell  $P_{max}$  (W) can be written in functions of these three parameters:

$$P_{max} = I_{SC}V_{OC}FF \quad (\text{I.8})$$

FF, in theory, depends on the  $n$  ideality factor, a measure of the junction quality and series resistance of a solar cell, but in practice the FF will be lower due to the presence of parasitic losses.

The key impact of the parasitic resistances is to reduce the fill factor. Series resistance in a solar cell has three causes: firstly, the movement of current through the solar cell; secondly, the contact resistance between the metal contact and the semiconductor; and finally the resistance of the top and rear metal contacts. Resistive effects in solar cells reduce its efficiency by dissipating power in the resistances. They are included in the solar cell circuit model as a **series resistance** and a parallel **shunt resistance**, as shown in Figure I.6.

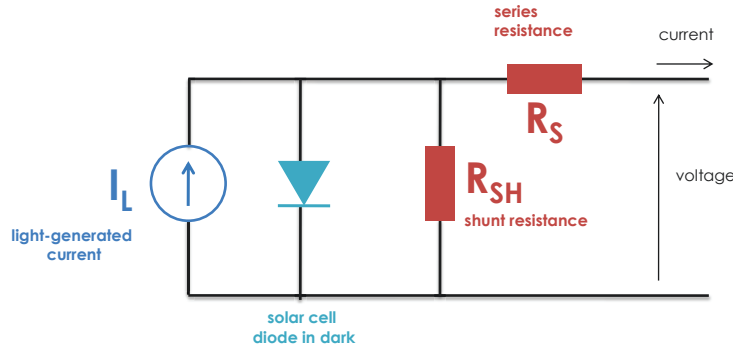


**Figure I.6:** Solar cell circuit with parasitic resistances.  $I_L$  is the light generated current, the diode represents the solar cell characteristics in dark,  $R_S$  and  $R_{SH}$  represent the resistive effects. Adapted from [84].

Since the value of resistance will depend on the area of the solar cell, when comparing the resistance of solar cells which may have different areas, a common unit for resistance is in  $\Omega \cdot \text{cm}^2$ . An excessively high series resistance ( $R_S$ ) may reduce the short-circuit current. Low shunt resistance ( $R_{SH}$ ) causes power losses in solar cells by providing an alternate current path for the light-generated current. Such a diversion reduces the amount of current flowing through the solar cell junction and reduces the voltage from the solar cell.

For practical applications, several solar cells are interconnected and encapsulated into units called **photovoltaic (PV) modules**, which is the product usually sold to the customer. Additional resistances due to the connection between the cells may appear and further limit the module performance.

## I.1.2 Technologies

A wide and steadily growing range of PV technologies using different types of materials are available on the market today, as listed in Table I.1. PV technologies are usually classified into three generations, depending on the basic material used and their level of commercial maturity.

The first-generation of PV systems use the wafer-based crystalline silicon (c-Si) technology, either single crystalline Si (sc-Si) or multi-crystalline Si (mc-Si) and gallium arsenide GaAs. Today, silicon based PV is the dominant technology (more than 80% of the market share, as shown in Table I.2) partially due to the maturity of the silicon industry, with more than 160 GW of PV modules already produced [87]. However, production of first-generation cells is expensive and demands a high energy input for purifying, crystallizing and sawing the single silicon wafer. Due



**Table I.1:** PV Technologies. Efficiency data are extracted from Green et al. (2015, [69]) and thickness from Abermann (2013, [16]) except when mentioned.

Material	Best cell $\eta$ (%)	Best module $\eta$ (%) ( $A$ ( $\text{cm}^2$ ))	Absorber thickness ( $\mu\text{m}$ )
<b>Commercial</b>			
<b>1<sup>st</sup> generation</b>			
Multicrystalline silicon (mc-Si)	20.8	18.5 (14661)	180-250
Monocrystalline silicon (sc-Si)	25.6	22.9 (778)	180-250
<b>2<sup>nd</sup> generation</b>			
Cadmium telluride thin film (CdTe)	21.5	18.6 [86]	2.0-5.0
Chalcopyrite thin film ( $\text{CuIn}_x\text{Ga}_{1-x}(\text{S,Se})_2$ (CIGS) )	21.7 [70]	17.5 (808) / 15.7 (9703)	2.0-3.0
Amorphous silicon (a-Si/nc-Si)	12.7	12.3 (14322)	0.2-0.35/1.0-2.0
<b>Non commercial or less than 1% market share</b>			
Gallium arsenide GaAs	28.8	24.1 (858.5)	
Multijunction InGaP/GaAs/InGaAs (MJ)	37.9	36.7 [87]	$\approx 10$
Kesterite thin film (CZTSSe)	12.7 [26]	11 (14) [14]	1.5-5.0
Dye-sensitized solar cell (DSSC)	11.9		$\approx 10$
Perovskite	20.1		
Organic (OPV)	11.1	8.7 (802)	0.03-0.2

**Table I.2:** Commercial PV Technologies. <sup>a</sup> The market share is given related to total 2014 worldwide PV production [87].

Material	Commercial module $\eta$ (%)	Module price €/W <sub>p</sub>	Market share <sup>a</sup> %	Cumulative production MW
<b>1<sup>st</sup> generation</b>				
mc-Si	15 - 15.5 [68]		55	
sc-Si	16 - 21.5 [16, 67, 68]	0.45 - 0.65 (2015, [75, 78])	35.5	$10^5$ (2013, [87])
<b>2<sup>nd</sup> generation</b>				
CdTe	13 [68]	0.58 (2013, [78])	4	$10^4$ (2012, [68])
CIGS	12 - 15.5 [68, 71, 72]	0.44 - 0.54 (2012-2015 [73-77])	3.5	$10^3$ (2012, [68])
a-Si/nc-Si	10 [87]		2	

to an indirect bandgap, the absorption coefficient of Si is around  $10^3 \text{ cm}^{-1}$ , which means that 200 microns thick silicon wafers are required to absorb the light [83].

The motivation of second and third generation technologies is the same: to decrease the module costs compared to the dominant Si technology. Currently, only the second-generation of PV systems have reached a significant part of the PV market. Second-generation PV systems are based on thin-film technologies, allowing an economic use of active materials and a highly automated processing. Thin-film technologies use semiconductors with absorption coefficients over  $10^4 \text{ cm}^{-1}$ , enabling absorber layers to be only micrometers thick. The low thickness releases some of the constraints on material quality, since electrons hole pairs are generated close to the charge separating p-n junction. Furthermore thin-films can be mounted on glass or flexible substrates. Monolithic integration, the automatic built-in-connection of individual solar cells, reduces manufacturing costs (eliminates expensive labor for manual connection) and increases durability (eliminates stress-prone manual connections of individual solar cells). Three main families are distinguished here: 1) amorphous (a-Si) and micromorph silicon (a-Si/  $\mu\text{c-Si}$ ) cells; 2) Cadmium-Telluride (CdTe) cells; and 3) CIGS cells. The kesterite compounds  $\text{Cu}_2\text{ZnSnS}_4$  (CZTS),  $\text{Cu}_2\text{ZnSnSe}_4$  (CZTSe) and  $\text{Cu}_2\text{ZnSn}(\text{S,Se})_4$  (CZTSSe) have many similar properties with CIGS and can be seen as their emerging cousin technology.

Third-generation PV systems include various technologies such as tandem cells, concentrating PV (CPV), dye-sensitized solar cells (DSSC), solid state DSSCs such as perovskite, organic PV (OPV), novel concepts such as quantum dots [88]. In tandem cells, efficiency can be increased merely by adding more cells of different band gap to a stack [89]. In CPV, expensive and efficient multi-

junction (MJ) solar cells receive a high intensity of sunlight focused by concentrators made of lenses or mirrors. Perovskite solar cells have attracted much attention in the last years due to their high power conversion efficiency. PV technologies based on organic and polymeric materials also appear promising for photovoltaic applications, but their stability is currently insufficient to consider a commercial use. Some third (or next-) generation concepts are based on principles that overpass the calculations of Shockley and Queisser (SQ) concerning the thermodynamic efficiency limit for a single-junction cell [90]. A quantum dot is a nanocrystal made of semiconductor materials that is small enough to exhibit quantum mechanical properties. Novel concepts include the intermediate band solar cell, the multi-exciton generation solar cell and the hot carrier solar cell [83]. Third generation systems include technologies that are still in a demonstration phase or have not yet been widely commercialized, as well as novel concepts under development.

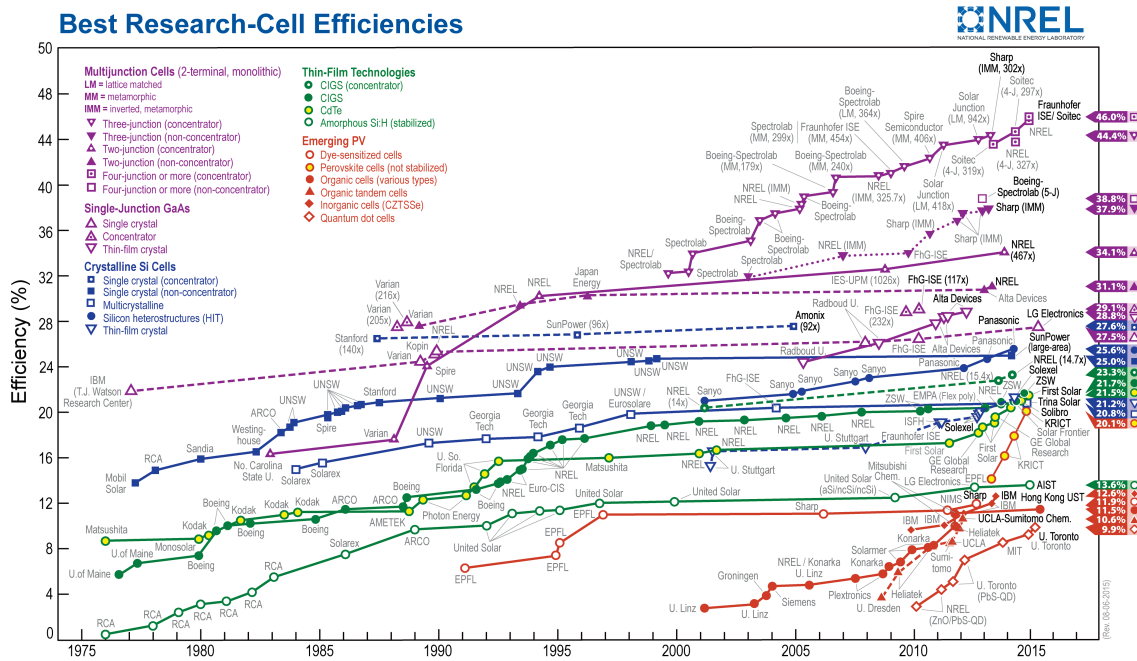


**Figure I.7:** Best laboratory solar cell efficiencies. This plot is courtesy of the National Renewable Energy Laboratory, Golden, CO [91].

Best efficiencies reached by the different technologies at laboratory scale are also represented in Figure I.7. Best crystalline solar cells achieve 25% efficiency, best thin film solar cells 21%, and organic and emerging solar cells typically reach between 9 and 20%.

### I.1.3 Historical

In 1839, Becquerel observed a physical phenomenon allowing light-electricity conversion. However, it is only in 1954 that the first practical photovoltaic device was demonstrated by Bell Laboratories, with a 6% efficient silicon cell in 1954 [92]. Research and development of photovoltaics received its first major boost from space industry in the 1960s which required a power supply separate from “grid” power for satellite applications [83]. It was finally the oil crisis in the 1970s that focused the world’s attention on the desirability of alternate energy sources for terrestrial use. Small scale transportable applications (such as calculators and watches) were utilized and remote power applications began to benefit from photovoltaics. In the 1980s research into silicon solar cells paid off and solar cell efficiencies began to increase: 20% efficiency was reached in 1985. Over the next decade, the photovoltaic industry experienced steady growth rates and today solar cells are recognized not only as a means for providing power and increased quality of life to those who do not have grid access, but they are also a means of significantly diminishing the impact of environmental damage caused by conventional electricity generation in advanced industrial countries. Solar PV is

now a mainstream and mature technology: since 2010, the world has added more solar PV capacity than in the previous four decades. New systems were installed in 2013 at a rate of 100 megawatts (MW) of capacity per day. Total global capacity exceeded 175 gigawatts (GW) in 2014 [1, 3, 93], as shown in Figure I.8.

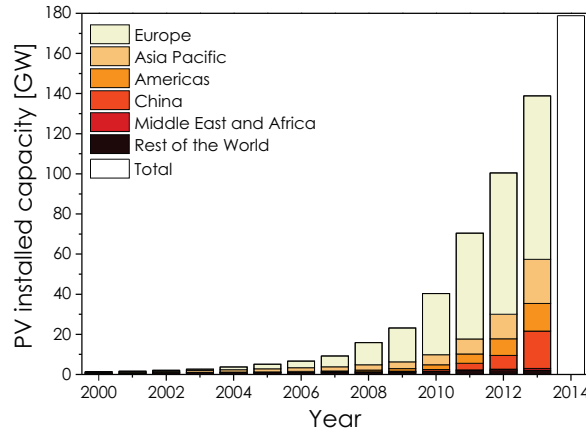


**Figure I.8:** Global cumulative installed solar photovoltaic capacity, 2000-2014. Adapted from [94] for 2000-2013 period and updated with 2014 data [2, 3].

## I.1.4 Perspectives

### I.1.4.1 Energy generation scenarios

The world’s energy demand is predicted to reach 28 terawatts by 2050. As the earth receives about 10,000 times more energy from the sun than the global energy consumption, using solar energy conversion as a significant part of energy production is a clear necessity. A Massachusetts Institute of Technology (MIT) study [95] reports the enormous potential and great importance of solar energy as a tool to reduce global CO<sub>2</sub> emissions. According to this study, solar electricity generation is one of “very few low-carbon energy technologies” with the potential to grow to very large scale. “As a consequence, massive expansion of global solar-generating capacity to multi-terawatt scale is a very likely and essential component of a workable strategy to mitigate climate change risks.” The choice of energy generation sources that will be used in the next years will affect the global climate. Different energy generation scenarios are envisaged by the the International Energy Agency (IEA) for 2050 [1]:

- The 6 °C Scenario (6DS) is a conservative scenario in which current trends continue. It projects that energy demand would increase by more than two-thirds between 2011 and 2050. Associated CO<sub>2</sub> emissions would rise even more rapidly, pushing the global mean temperature up by 6 °C.
- The 2 °C Scenario (2DS) offers a vision of a sustainable energy system implying reduced greenhouse gas and carbon dioxide (CO<sub>2</sub>) emissions.
- The high-renewables Scenario (hi-Ren) is based on 2DS scenario, with lower deployment of carbon capture and storage (CCS) and nuclear power, because of their respective slower progress and persistent increased costs since 2012. The hi-Ren exhibits an optimistic deployment of renewable energy sources.

The Figure I.9 shows the different energy sources that are used to generate electricity today (2011) and that will be used in 2050. Solar PV technologies (in yellow in the figure) are predicted to account for 1% to 16% of the global electricity production in 2050, depending on the scenario. According to the recent report “Tracking clean energy progress 2014” (IEA, [96]), renewable power, including PV, is already on track to meet 2DS targets in 2025, even if sustained deployment and

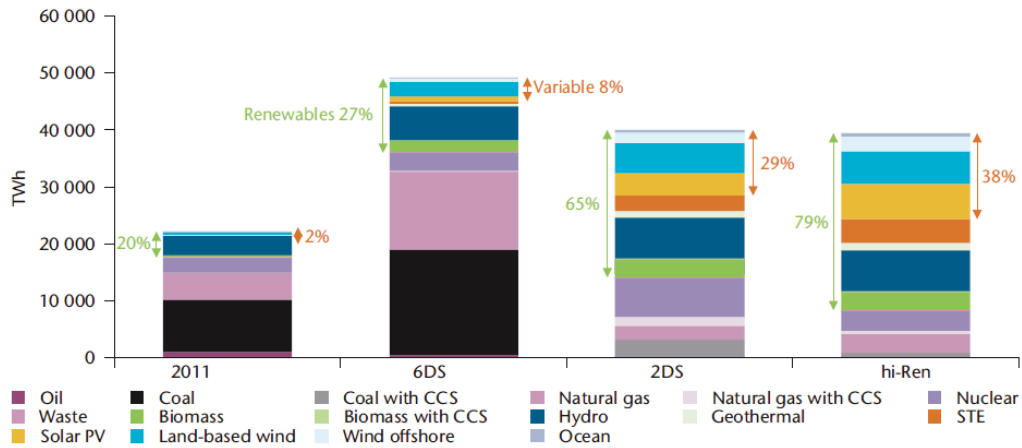


**Figure I.9:** Global electricity mix in 2011 and in 2050, according to Energy Technology Perspectives (ETP) published in 2014 by the International Energy Agency (IEA) [1].

policies are required. The Table I.3 summarizes the possible global PV contribution to the 2050 electric generation mix, for the lower PV deployment scenario (6DS) and the higher PV deployment scenario (hi-Ren). In the best case, PV will contribute to 16% of the total electricity generation by 2050, accounting for annual 6400 TWh.

**Table I.3:** Photovoltaics in the global electricity mix in 2050.

IEA scenario [1]	Low PV deployment (6DS)	High PV deployment (hi-Ren)
Total annual electricity demand (TWh)	50 000	40 000
PV Contribution	1%	16%
Annual electricity generated by PV (TWh)	500	6 400

How much installed PV capacity is needed in order to generate such a quantity of electricity by 2050? The detailed calculation is presented in *Annex A*. Depending on the capacity factor of a PV module (the ratio of its actual output over a period of time, to its potential output when operating at full capacity continuously over the same period), 200 GW<sup>1</sup> to 7.3 TW of worldwide installed PV peak capacity will be needed in order to generate 500 to 6400 TWh. For comparison, the IEA Technology Roadmap for Solar photovoltaic energy predicts 4674 GW in 2050 following the hi-Ren scenario [1]. Assuming a power conversion efficiency ( $\eta$ ) between 10 and 20%, the surface covered by PV needed for 200 to 7300 GW capacity is between 1000 to 73000 square kilometers.

#### I.1.4.2 Which PV technologies to ensure the electricity generation?

In order to compete with established technologies, the new product has to deliver further benefits. One of the most important competitive advantages of thin films is the potential for low-cost production, due to the economic use of active materials and the highly automated processing. Thin film PV technologies are currently competing with the incumbent crystalline silicon technologies [97]. At the same time novel 3<sup>rd</sup> generation technologies will find their way towards commercialization. In 2011, thin film technologies exhibited significant lower prices than crystalline silicon, as shown in Figure I.10a, and were expected to account for a large market share (20 – 30%) over the next decades [6,98]. A technology shift scenario — from 1<sup>st</sup> to 2<sup>nd</sup> and to 3<sup>rd</sup> generation technology — was envisaged by several PV sector road-maps [98], as shown in Figure I.10b.

<sup>1</sup>200 GW is not a realistic prevision as already more than 175 GW have been installed by end 2015.

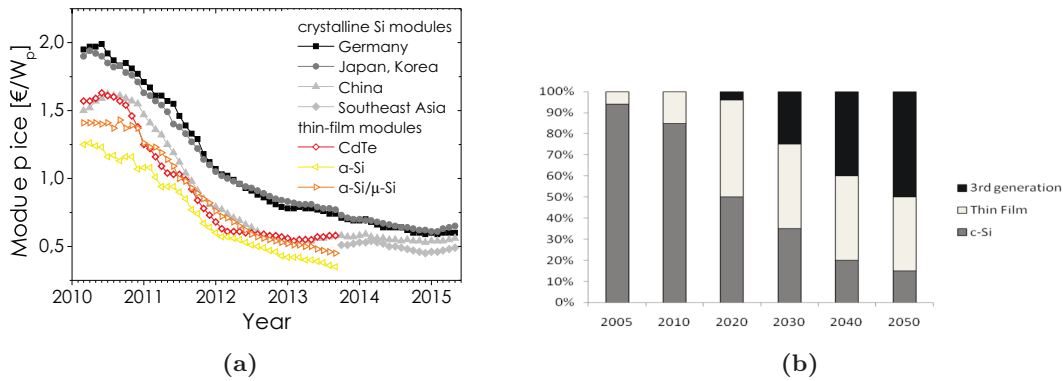


**Figure I.10:** PV Outlook: (a) Module price evolution between 2010 and 2015 (data from [78]) and (b) Changes in PV technologies market share, as predicted in 2011, Figure by Candelise et al. [98].

However, in the last years the price of silicon modules dropped drastically, as shown in Figure I.10a. This decrease is mainly explained by reductions in module and inverter prices (84% decrease of module prices between 2008 and 2014, reaching 0.65 \$/Wp), but also by important manufacturing improvements relative to Chinese government subsidies and excess capacity in the Chinese solar module industry [95,99]. One of the consequences is a facilitated deployment of PV technologies in general, by reducing the gap between electricity generated by solar energy and electricity generated by conventional energy supply. Another consequence is a reconsideration of the expected market shares of the different PV technologies. The cost advantage of thin films over silicon technologies is reduced, limiting its competitiveness. In 2014, the thin films accounted for 9% of the PV market [87], as shown in Table I.1. In the future, which technologies are going to make their way towards market is an open question.

## I.1.5 Material considerations for terawatt level deployment of photovoltaics

### I.1.5.1 Resources availability

Each PV commercial technology contains one or more critical elements, such as silver for c-Si contacts, indium and gallium for  $\text{CuIn}_x\text{Ga}_{1-x}(\text{S,Se})_2$  (CIGS), tellurium for CdTe and silver and indium for thin-film silicon [4–6]. The availability of Ag, In, Ga, Te is limited, and the associated cost pressure might limit the future deployment of these technologies. The sustainability of PV production is therefore a real question, and the development of a new PV technology based on abundant and preferably non-toxic elements would alleviate the pressure on all PV technologies in term of resources. In the USA, the Massachusetts Institute of Technology (MIT) [95] strongly recommends that a large fraction of federal resources available for solar R&D focuses on environmentally benign, emerging thin-film technologies that are based on earth-abundant materials. In this respect, kesterite materials ( $\text{Cu}_2\text{ZnSn}(\text{S,Se})_4$ ) seem a promising candidate for the development of a new PV technology. For comparison, the Table I.4 shows the price and availability of thin-film CdTe, CIGS and CZTSSe main components.

Metals such as cadmium, gallium, indium, selenium, and tellurium are recovered as byproducts from the production of other metals. The supply of these elements relies to a great extent on mining ores for the production of aluminum, copper, and zinc. Furthermore, indium and gallium are considered by the European Union as “critical raw materials” due to the supply risk associated with their economic importance [100]. In contrast, most of the kesterite elements (Cu, Sn, Zn and S) are not dependent on other metals production.

**Table I.4:** World production from primary sources and price of refined metals for byproduct commodities at the end of the year 2014, adapted from [7]. Data is taken from U.S. Geological Survey 2015 [8]. <sup>a</sup> Prices for cadmium, indium, selenium, and tellurium are averages for 2014. Prices for gallium are at the end of 2014. All prices are rounded to the nearest dollar and are reported in dollars per kilogram. Prices may vary based on numerous factors that include contractual agreements, size of inventories, and specifications of the metals traded.

Byproduct	Primary metal	World refinery production Metric tons	Price of refined metal <sup>a</sup> \$/kg
<b>Cadmium (Cd)</b>	Zinc	22200	1.9
<b>Gallium (Ga)</b>	Aluminium, Zinc	170	240
<b>Indium (In)</b>	Zinc	820	695
<b>Selenium (Se)</b>	Copper	> 2300	60
<b>Tellurium (Te)</b>	Copper	> 95	117
	<b>Copper (Cu)</b>	18 700 000	7.4
	<b>Sulfur (S)</b>	72 400 000	< 0.2
	<b>Tin (Sn)</b>	296 000	24.1
	<b>Zinc (Zn)</b>	13 300 000	2.5

### I.1.5.2 The case of CIGS: indium and gallium

Production of indium tin oxide (ITO) accounts for most of the global indium consumption. ITO thin-film coatings are primarily used for electrical conductive purposes in a variety of flat-panel displays — most commonly liquid crystal displays (LCDs). Other indium end uses include alloys and solders, electrical components and semiconductors, as well as research. Indium’s price volatility (Figure I.11 [101]) and various associated supply concerns have spurred the development of ITO substitutes [8, 102]. The main concern for future CIGS mass production is focused on the indium price volatility — from 300 to 1000€/kg in a less than two years, as can be seen in the Figure I.11. The viability of CIGS solar cells deployment at larger (terawatt) scale is questioned. Indium prices may be fundamental to the cost effectiveness and successful deployment of thin film PV [98].

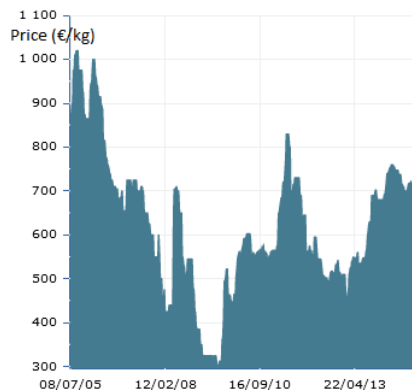


**Figure I.11:** Indium prices according to London stock exchange 2005-2015 [101].

Despite an increasing global gallium demand — GaAs is used for smartphones, GaN for LEDs and many other applications (defense, cable television transmission, commercial wireless infrastructure, power electronics and satellite markets) — gallium prices have kept decreasing for more than 2 years. Indeed, the gallium production in China increased significantly, making the global production exceeding the consumption. However, as Ga is a by-product of other minerals, only

a small percentage of gallium contained in bauxite and zinc resources is potentially recoverable, making the estimation of gallium reserves difficult [8].

### I.1.5.3 Comparison of metal quantity for CIGS and CZTSSe

Table I.5 provides rough estimates of the amounts of mineral materials used in CIGS and CZTSSe of thin-film photovoltaic cells sufficient to produce annually 880 GW, based on 2014 prices and production (Table I.4). Detailed calculations and hypotheses can be found in *Annex A*.

**Table I.5:** Metals required to produce CIGS or CZTSSe cells with a peak capacity of 880 GW, adapted from [7] with 2015 data [8].

Hypotheses: Calculation for metal requirements assumed to be linear and based on a 2-micrometer ( $\mu\text{m}$ ) thickness cell. The combination, amounts, and efficiency of materials used in photovoltaic cells can vary; the amounts and combinations listed in this table are not representative of all technologies. Estimates for material requirements should be considered with caution.

For CIGS, we use  $\text{CuIn}_{0.6}\text{Ga}_{0.4}(\text{Se}_{0.9}\text{S}_{0.1})_2$  with 15% module efficiency. In 2015, module power conversion efficiencies of 13.8% (Solar Frontier mass production [71]) and 15.5% (Miasolé flexible production [72]) are announced for CIGS.

For CZTSSe  $\text{Cu}_2\text{ZnSn}(\text{S}_{0.25}\text{Se}_{0.75})_4$  with 10% module efficiency (Cell record at 12.6% in 2015 [25]).

Metal	Quantity $10^6$ kilograms	Percentage of 30 years estimated world refinery production	Value of contained metal Millions of dollars
Copper	13.7	<0.01	100
Indium	14.9	60	10 333
Gallium	6.0	118	1 440
Selenium	30.7	45	1 847
Sulfur	1.4	<0.01	0.3
Copper	17.6	<0.01	130
Zinc	9.0	<0.01	20
Tin	16.4	0.18	396
Selenium	32.8	47	1 966
Sulfur	4.4	<0.01	0.9

These estimations show that the deployment of CIGS may be severely restrained by the prices of indium and by the production and availability of indium<sup>2</sup>, gallium and selenium. Kesterite components Cu, Sn, Zn or S show no availability restriction and lower prices than In and Ga. However the CZTSe and CZTSSe materials might also be restrained by selenium availability. The total world production of Se reported in Table I.11 is underestimated, because Australia, China, Iran, Kazakhstan, Mexico, the Philippines, and Uzbekistan are known to produce refined selenium, but their output is not reported, and information is inadequate for the formulation of reliable production estimates [8]. As a consequence, the percentage of world production needed in Table I.4 is overestimated and should be considered with caution. In the table, calculations are made considering a S/(S+Se) ratio of 25%, but kesterite can also be developed with 100% sulfur (CZTS).

In summary, the production of CZTS kesterite thin films is not dependent on element availability. Even if CZTSe and CZTSSe materials might depend on Se availability, their production is free from In price volatility risks. All the kesterite materials are of great interest for large scale PV deployment and can be seen as the next generation of thin film solar cells. In addition, kesterite materials are also interesting for tandem solar cells. Stacked with another earth-abundant material

<sup>2</sup>Stamp et al. reported that if indium is only co-produced with zinc at the current indium extraction efficiency, it will be difficult to provide enough indium to support rising CIGS solar cell implementation, especially if demand from other products increases as well. Dependency on zinc may be reduced but these developments will likely require indium prices above 1000 \$/kg, which will affect the cost of CIGS modules [103].

such as Si or the emerging perovskite solar cells [104], the power conversion efficiency can be improved by optimizing the two band-gaps of the stack so as to absorb a different part of the solar spectrum [89].



## I.2 Kesterite: a promising candidate for low-cost mass production of thin film solar cells

The kesterite materials  $\text{Cu}_2\text{ZnSnS}_4$  (CZTS),  $\text{Cu}_2\text{ZnSnSe}_4$  (CZTSe) and  $\text{Cu}_2\text{ZnSn}(\text{S},\text{Se})_4$  (CZTSSe) have attracted growing interest over the last years due to their potential for the low-cost mass production of thin film solar cells. Over 12% efficient kesterite devices were recently demonstrated by Kim et al. with a CZTSSe solar cell exhibiting 12.7 % [26] record power conversion efficiency.

### I.2.1 Properties of kesterite materials

#### I.2.1.1 Kesterite semi-conductor properties

The kesterite compounds fulfill the main requirements in order to compete with more established thin film technologies:

- Intrinsic doping (p-type conductivity [9, 10]);
- High optical absorption coefficients ( $> 10^4 \text{ cm}^{-1}$ ), as shown in Figure I.12 [11], allowing to absorb the light with a few microns thin layer;
- Direct bandgaps (1.0 eV for CZTSe, 1.5 eV for CZTS [11, 12]) close to the ideal value for single junction solar cells [90]. The sulfur-to-selenium ratio, or  $\text{S}/(\text{S} + \text{Se})$ , determines the band gap of CZTSSe;
- Including earth-abundant Zn and Sn which are produced in quantities 16 000 and 360 times larger than In, it allows the mass production of thin film devices (previously discussed in section page 13).

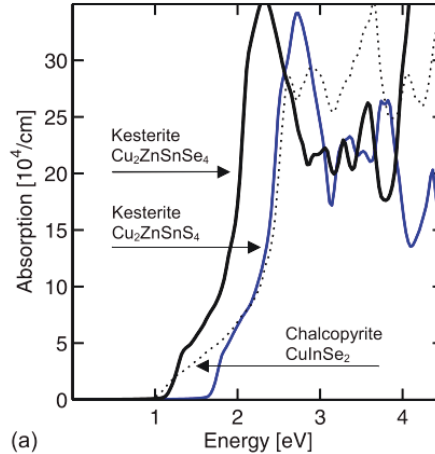


**Figure I.12:** Absorption coefficients [11] of CZTS (blue solid line) and CZTSe (black solid line). For comparison, the absorption coefficient of chalcopyrite CISE is also presented (dotted line).

#### I.2.1.2 Crystalline properties

Kesterite compounds can be thought of as being derived from  $\text{CuInSe}_2$  (CIS) by isoelectronic replacement of the indium atoms with equal numbers of zinc and tin atoms. The mineral kesterite belongs to the  $\text{A}_2^{\text{I}}\text{B}^{\text{II}}\text{C}^{\text{IV}}\text{X}_4^{\text{VI}}$  compound family (with  $\text{A}=\text{Cu}$ ,  $\text{B}=\text{Zn}$ ,  $\text{Fe}$ ,  $\text{C}=\text{Sn}$  and  $\text{X}=\text{S}$ ,  $\text{Se}$ ). For  $\text{A}_2^{\text{I}}\text{B}^{\text{II}}\text{C}^{\text{IV}}\text{X}_4^{\text{VI}}$  compounds two main tetragonal structure types are known from literature: the kesterite type structure (space group I-4, no. 82) and the stannite type structure (space group I-42m, no. 121). As for the chalcopyrite type compounds, it is the mineral for which the structure type was determined in first place that gives the name of the structure. In both

structures, the kesterite type and the stannite type, the cations are located on tetrahedral sites but their distributions on planes perpendicular to the  $c$ -axis are not the same. Specifically, the kesterite structure consists of two alternating cation layers each containing Cu and Zn or Cu and Sn, whereas in the stannite structure, a layer of Cu alternates with a layer of Zn and Sn [6,105,106]. It is now generally accepted that CZTS as well as CZTSe (single crystals, powder, and thin films) crystallize in the kesterite-type structure (represented in Figure I.13), but with a Cu/Zn disorder (referred to as “disordered kesterite”). This disorder causes a high concentration of  $\text{Cu}_{\text{Zn}}$  and  $\text{Zn}_{\text{Cu}}$  antisite defects, even in stoichiometric compounds [107].

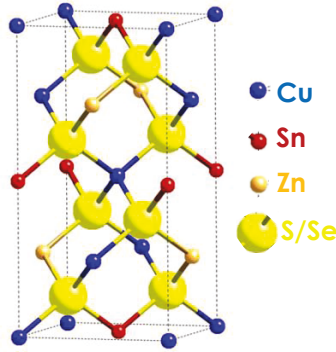


**Figure I.13:** Kesterite crystalline structure (space group  $\bar{I}4$ , no. 82) [105] is the more stable form for  $\text{Cu}_2\text{ZnSn}(\text{S},\text{Se})_4$  compounds.

## I.2.2 Kesterite fabrication processes

The solar cell device structure does not only include the absorber material (CZT(S,Se) is a p-type semiconductor) but also a n-type material to create the p-n junction, and back and front contacts to collect the current, as described in Figure I.4 page 5. Due to the similarity between CZTSSe and  $\text{CuIn}_x\text{Ga}_{1-x}(\text{S},\text{Se})_2$  (CIGS) materials, kesterite-based solar cells typical structure derives from CIGS’s structure. A full description of a CIGS fabrication process can be found in reference [108]. The majority of research laboratories and companies use the following device structure : soda lime glass substrate/Mo back contact/CZTSSe absorber/CdS buffer/i-ZnO/aluminium doped zinc oxide (AZO) or indium tin oxide (ITO) window layer. Thin film modules are usually monolithically integrated, in this case process steps are interspersed with patterning steps to form a series connected module as described by Powalla et al. [109]. Otherwise a metallic grid is applied on the transparent conductive oxide (TCO) [110]. The device structure is represented in Figure I.14.

Thin films need to be deposited on a substrate. Typically a 2 or 3 mm thick glass substrate is used, but thin film solar cells can also be deposited on flexible substrates [111–114]. Molybdenum is typically employed as a back contact for CIGS solar cells because a thin layer of  $\text{MoS}(\text{e})_2$  forms between the Mo layer and the absorber, creating an ohmic contact. The n-type partner in the p-n junction of CIGS solar cells consists of a buffer layer followed by a non-doped layer of ZnO (i-ZnO). A commonly used buffer layer is CdS, but since this layer contains the toxic cadmium (Cd) it is also common to use alternative materials such as  $\text{In}_2\text{S}_3$  and  $\text{Zn}(\text{O},\text{S})$  [115]. On top of these n layers an Al-doped ZnO (AZO) or Sn-doped  $\text{In}_2\text{O}_3$  (ITO) layer is deposited to carry the current. An additional anti-reflective coating can be deposited to reduce reflection losses. Metal contacts can be added to improve the current collection.

In order to reach a high deployment, kesterite based thin film solar cell technologies should be easily manufacturable at low costs and high throughput. Deposition techniques are usually classified as vacuum and non-vacuum processes. Typically, the Mo back contact and i-ZnO, AZO or ITO window layers are deposited by sputtering, a vacuum technique, while the buffer layer is deposited by chemical bath deposition (CBD).

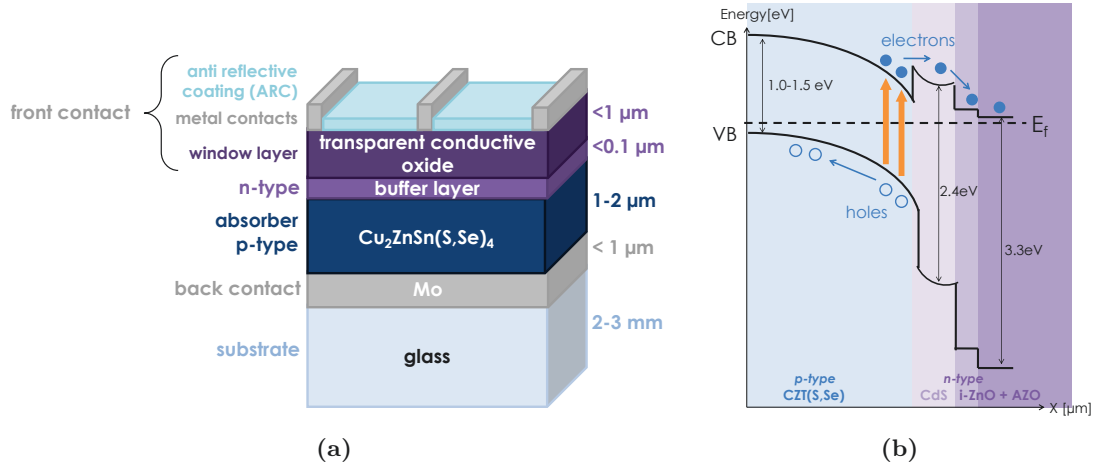


**Figure I.14:** (a) Schematic representation and (b) band diagram of a kesterite-based device structure.

The absorber layer can be grown using vacuum and non-vacuum techniques in one-step or two-step processes. In one-step processes, all elements are incorporated simultaneously, while for two-step processes, the elements are first deposited at ambient or near-ambient temperature, followed by an annealing step. The chalcogen can be incorporated into the precursor or during the annealing step. Two-step processes allow the use of fast and low-cost techniques for precursor deposition. Most of the groups use two-step processes. Table I.6, adapted from Fella et al. [116], compiles a selection of kesterite solar cell devices with conversion efficiency over 7% obtained by different research groups and companies<sup>3</sup>. Recent years have seen dramatic improvements in the performance of kesterite devices. Devices of comparable performance (>8%) are fabricated by a number of different techniques. As research of kesterites continues, start-up companies are emerging whilst several thin film CIGS companies are expanding their knowledge to CZTSSe based solar cell devices. The companies are based in the USA, in Europe or in Japan. Solar Frontier (Japan) combines sputtered precursor stacks followed by sulfurization and selenization [123, 124] and demonstrates 11% sub-module efficiency on an aperture area of 14.0 cm<sup>2</sup> [14].

<sup>3</sup>High efficient devices (not shown in this table) have also been obtained by alloying CZTS, CZTSe or CZTSSe with germanium (Ge): 6.8% [117], 8.4% [118], 9.1% [119], 10.0% [120], 10.2% [121] or cadmium (Cd): 9.2% [122].

**Table I.6:** Selection of CZTS, CZTSe and CZTSSe solar cell devices with conversion efficiency over 7%. The used fabrication methods are two-step processes (deposition followed by annealing), except for NREL.

<sup>a</sup> IMEC = Interuniversity Microelectronics Centre, Belgium (BEL);

<sup>b</sup> NREL = National Renewable Energy Laboratory (USA);

<sup>c</sup> CNU = Chonnam National University, Korea (KOR);

<sup>d</sup> IREC = Catalonia Institute for Energy Research, Spain (ESP);

<sup>e</sup> DGIST = Daegu Gyeongbuk Institute of Science & Technology, Korea (KOR);

<sup>f</sup> CSU = Central South University, China (CHN);

<sup>g</sup> IRDEP = Institute of Research and Development on Photovoltaic Energy, France (FRA);

<sup>h</sup> CEA = Alternative Energies and Atomic Energy Commission, France (FRA);

<sup>i</sup> ZSW = Centre for Solar Energy and Hydrogen Research Baden-Württemberg, Germany (DEU);

<sup>j</sup> UCLA = University of California-Los Angeles (USA);

<sup>k</sup> KIST = Korea Institute of Science and Technology, Korea (KOR).

Method	Institute or <i>Company</i>	Material	Area (cm <sup>2</sup> )	Eff (%)	V <sub>OC</sub> (mV)	J <sub>SC</sub> (mA/cm <sup>2</sup> )	FF (%)	Ref
<b>Vacuum</b>								
Co-evaporation	IBM (USA)	CZTSe	0.43	11.6	423	40.6	67.3	[13]
Sputtering	<i>Solar Frontier</i> (JAP)	CZTSSe	14	11	516	34.1	63	[14, 123, 125]
DC-sputtering	IMEC <sup>a</sup> (BEL)	CZTSe	0.52	10.4	394	39.7	66.4	[15, 61]
One-step co-evaporation	NREL <sup>b</sup> (USA)	CZTSe	0.419	9.8	380	37.6	68.9	[60, 62]
Co-sputtering	<i>AQT Solar</i> (USA)	CZTSSe	-	9.3	-	-	-	[126]
Sputtering	<i>Solar Frontier</i> (JAP)	CZTS	14	9.2	708	21.6	60	[124, 125, 127]
DC-sputtering	CNU <sup>c</sup> (KOR)	CZTSSe	0.43	9.2	455	32.1	63	[128]
Sputtering	Ewha Womans Univ. (KOR)	CZTSSe	0.185	9.1	420	35.6	60.7	[129]
DC-sputtering	Nankai Univ. (CHN)	CZTSe	0.345	8.7	418	36.2	57.6	[130]
Co-sputtering	Academy of Sciences (CHN)	CZTS	0.5	8.6	625	21.8	63	[131]
Co-evaporation	IBM (USA)	CZTS	-	8.4	661	19.5	65.8	[132]
DC-sputtering	IREC <sup>d</sup> (ESP)	CZTSe	0.25 - 1	8.2	392	32.4	64.4	[34]
Sputtering	Northumbria Univ. (GBR)	CZTSe	0.09	8.1	434	31.2	59.6	[133]
Reactive (H <sub>2</sub> S) DC-co-sputtering	Uppsala Univ. (SWE)	CZTS	0.5	7.9	667	19.6	60	[33, 134]
Co-evaporation	Luxembourg Univ. (LUX)	CZTSe	0.5	7.5	356	35.4	60	[64]
DC- and RF-sputtering	DGIST <sup>e</sup> (KOR)	CZTS	-	7.5	632	19.3	61.6	[135]
Sputtering	National Tsing Hua Univ. (TWN)	CZTSSe	0.4	7.4	430	29.8	57.3	[136]
DC-sputtering	CSU <sup>f</sup> (CHN)	CZTSSe	-	7.2	439	27.9	59.2	[137]
RF-co-sputtering	IRDEP <sup>g</sup> (FRA)	CZTSe	0.1	7.1	390	30.7	59.8	[38, 138]
RF-sputtering + evaporation	CEA <sup>h</sup> (FRA)	CZTSSe	0.5	7.0	376	34	55	[139, 140]
DC- and RF-sputtering	Dongguk Univ. (KOR)	CZTSSe	0.538	7.0	470	25.2	59	[141]
<b>Non-vacuum</b>								
Spin-coating: solution + particle	IBM (USA)	CZTSSe	0.42	12.7	466	38.9	69.8	[25, 26, 142]
Spray-coating: molecular inks	Univ. of Washington (USA)	CZTSSe	0.43	11.3	449	37	-	[45, 143]
Spin-coating: solution	EMPA (CHE)	CZTSSe	0.3	11.2	479	36.5	63.8	[28, 144]
Doctor-blade: solution	ZSW <sup>i</sup> (DEU)	CZTSSe	0.25	10.3	471	31.6	69.6	[27, 145, 146]
Ink-printing: NPs	<i>Solezant Corp</i> (USA)	CZTSSe	0.24	9.9	457	32.6	66.1	[147]
Doctor-blade: NPs	Purdue Univ. (USA)	CZTSSe	0.48	9.0	404	35.1	63.7	[148, 149]
Spray-coating: NPs	<i>IMRA</i> (FRA)	CZTSSe	0.25	8.6	460	30.9	60	[39, 150]
Spin-coating: solution	UCLA <sup>j</sup> (USA)	CZTSSe	0.12	8.6	435	32.5	61.0	[151, 152]
Spin-coating: NPs	<i>Dupont</i> (USA)	-	0.39	8.5	451	29	64.9	[153]
Monograins	<i>Crystalsol</i> (EST)	CZTSSe	-	8.4	703	17.8	61.3	[111, 154–157]
Spin-coating: sol-gel	CSU <sup>f</sup> (CHN)	CZTSSe	0.45	8.3	451	31.7	57.7	[158]
ED	Osaka University (JAP)	CZTS	0.05	8.1	705	18	63.2	[30, 159]
ED	KIST <sup>k</sup> (KOR)	CZTSe	0.45	8.0	390	35.3	58	[32]
Spin-coating: solution	Academy of Sciences (CHN)	CZTSe	0.3558	8.0	408	33.4	58.8	[35, 160]
Spin-coating: solution	Academy of Sciences (CHN)	CZTSSe	0.425	7.3	436	34.0	49.5	[161]
ED	IBM (USA)	CZTS	-	7.3	567	22	58	[29]
Spin-coating: NPs	Yonsei Univ. Seoul (KOR)	CZTSSe	0.21	7.2	505	24.6	57.8	[162]
ED	East China Normal Univ. (CHN)	CZTS	0.2	7.1	614	21.8	55.5	[37]
Ink-printing: NPs	<i>Solezant Corp</i> (USA)	CZTSSe	25	7.1	-	-	-	[147]
ED	IBM (USA)	CZTSe	0.45	7.0	369	32.4	58.5	[31]

### I.2.2.1 Vacuum deposition methods

For decades, vacuum-based techniques have been the standard for high-quality semiconductor fabrication for a range of applications from microelectronics to PV. The most popular of these techniques are sputtering and evaporation, both of which have proven useful for CZTSSe deposition [163].

Sputtering — historically the first approach used for kesterite film and device fabrication (Ito et al., 1988 [164]) — has been one of the more extensively studied routes to CZTSSe films [46, 165, 166]. Sputtering is based on bombarding a source target of the material to be deposited (e.g. the component metals or metal chalcogenides) with energetic particles, for example argon plasma, and redepositing the ejected species on a substrate.

Co-evaporation, an one-step process, has been important for CIGS technology development and commercialization, achieving top performance devices [108]. Co-evaporation involves heating the various source materials (e.g. the various individual component elements), typically in a high-vacuum environment, by means such as resistive or electron beam heating to produce vapors that are then condensed on a substrate. However, for CZTSSe, this approach has encountered significant challenges, especially in its classical configuration where the substrate is maintained at high temperature while delivering precisely controlled elemental fluxes. Indeed, in addition to the typically volatile Se and S in chalcopyrite absorbers, Sn re-evaporation is also observed during CZTSSe deposition [50, 167].

Sequential evaporation and annealing route, a two-step process, has also proven successful in the preparation of high-performance devices [13].

Best efficiencies for vacuum methods are reported in Table I.6, and the associated morphologies are represented in Figure I.15.

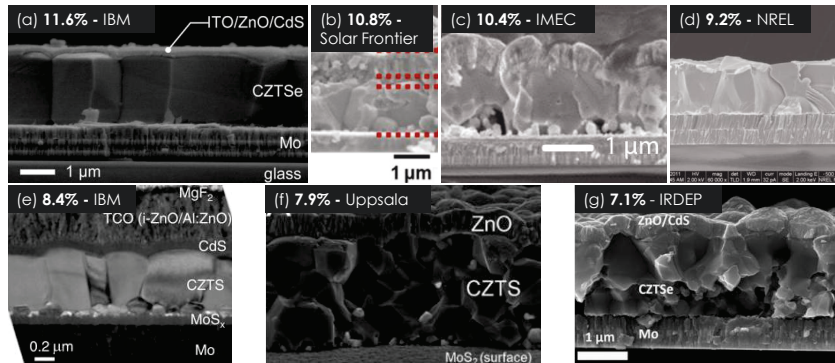


**Figure I.15:** SEM cross sectional images of vacuum-processed kesterite-based solar cells: (a) [13], (b) [123], (c) [15], (d) [62], (e) [132], (f) [33], (g) [38]. Detailed I-V informations are listed in Table I.6.

The absorbers fabricated by vacuum methods exhibit different grain sizes, with small grains possibly associated with the presence of secondary phases. In some of the absorbers voids between the absorber layer and the back contact are also observed, but no clear relationship between the morphology and the performance can be drawn.

### I.2.2.2 Non-vacuum deposition methods

Compared to evaporation or sputtering techniques that require vacuum conditions, non-vacuum deposition methods exhibit numerous advantages. Indeed, solution-based methods demand lower equipment costs, are suitable for large area and flexible substrates, and offer higher throughput, more efficient material usage and lower temperature processing [16]. For instance, the estimated

CIGS absorber cost in a 500 MW manufacturing plant is decreased from 8.6 to 6.0 € cents per watt peak when using electrodeposition (ED)-based processes instead of sputtering [77]. Reviews of non-vacuum methods for kesterite fabrication [16], especially solution [17,168], nanocrystals [169], and electrodeposition routes [18,19] have been written over the last years.

Direct solution coating (DSC) methods are two-step processes which consists in coating a layer of precursor-containing solution at the surface of a substrate followed by annealing. Direct solution coatings include spin-, spray-, dip-, knife- (or doctor blading) and curtain-coating, as well as printing techniques such as ink-jet, flexography and gravure [17]. Since 2010, record power conversion efficiencies for kesterite materials were obtained by IBM via a hydrazine wet chemical approach [21–26]. Hydrazine ( $N_2H_4$ ) is a carbon- and oxygen-free compound that can be considered as an ideal solvent because it dissolves metal chalcogenides and elemental chalcogens (sulfur and selenium) and excludes the introduction of any detrimental impurity elements by decomposing cleanly into  $N_2$ ,  $NH_3$ , and  $H_2$ . Another important feature of hydrazine is its strong reducing action that prevents any metal oxidation. However, hydrazine is highly toxic and explosive, and all of its processing requires inert atmosphere and handling inside a glove box. Scale-up of a process involving such a hazardous material poses serious problems. Other solvents may be used for direct solution coatings such as water and organic solvents (alcohols, DMF, DMSO). The presence of organic solvents and/or additives often imply the presence of a carbon-rich small grains layer in the absorber between the active layer and the Mo substrate, as observed in Figure I.16 for many absorbers. An optimization of annealing parameters allow to reduce the size of this fine grain layer and to get higher efficiencies. 10.3% [27] and 11.2% [28] CZTSSe devices have been recently demonstrated with DMSO solvent.

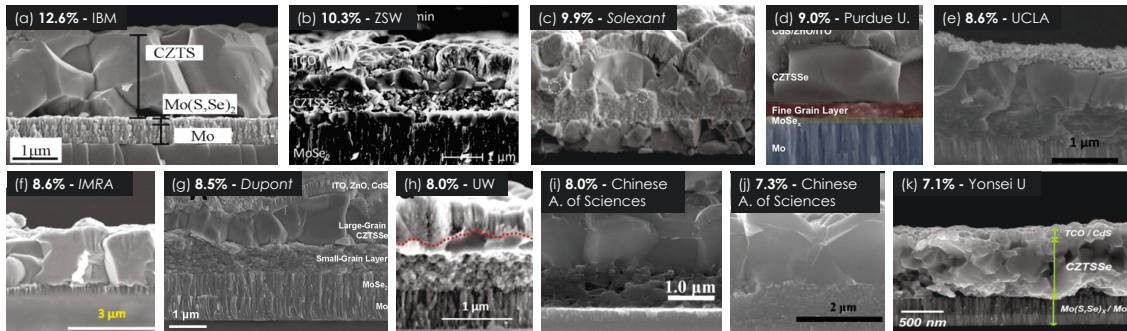


**Figure I.16:** SEM cross sectional images of solution-processed kesterite-based solar cells: (a) [25], (b) [27], (c) [147], (d) [149], (e) [152], (f) [150], (g) [153], (h) [143], (i) [161], (j) [35], (k) [162]. Detailed I-V informations are listed in Table I.6.

Other solution-based techniques for kesterite include chemical bath deposition (CBD) [20,170], electrodeposition (ED) and spray pyrolysis [171–173]. Electrodeposition is an attractive industrial approach for large-scale application and one that is well-established in the electronics industry. ED can be realized at room temperature using non-toxic and low-cost metallic salt solutions, which have long bath lifetimes and a high metal using ratio ( $> 90\%$ ), thus avoiding waste of resources. Electrodeposited kesterite based solar cells, a high potential candidate for reaching terawatt scale deployment [174], reach efficiencies as high as 8.0 % for CZTS [30] and CZTSe [32]. Noticeably, 7.0 % CZTSe [31] and 7.3 % CZTS [29] devices were obtained from large area electrodeposited precursors. Electrodeposited kesterite’s morphology, represented in Figure I.17, presents grains of different size, similarly to kesterite obtained by competing vacuum and non-vacuum techniques, and small grains probably due to the presence of secondary phases.

### I.2.3 Challenges for high-efficient kesterite devices production

The research in kesterite materials is still in its early years and many issues remain to be understood in order to increase their performance. Enormous progress in kesterite device fabrication and a

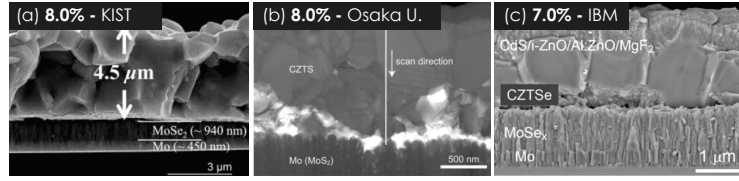


**Figure I.17:** SEM cross sectional images of ED-processed kesterite-based solar cells: (a) [32], (b) [30], (c) [31]. Detailed I-V informations are listed in Table I.6.

better understanding of the physical properties of the material have been achieved in the last years. Reviews about progress and challenges to be overcome were regularly published during this thesis (2012: [6, 12, 168], 2013: [16, 167, 169, 175, 176], 2014: [177], 2015: [178]).

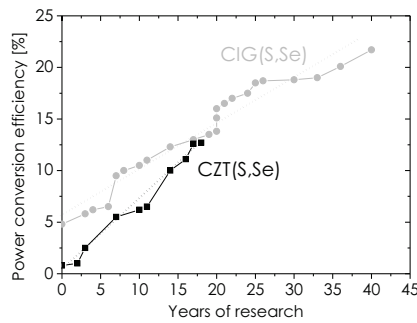


**Figure I.18:** CIGS and CZTS power conversion efficiency trend.

Figure I.18 shows the evolution of kesterite and CIGS best power conversion efficiencies versus the number of research years. The efficiency of kesterite devices have improved faster than CIGS, benefiting from the processes and methods already developed for CIGS. However, the performance of CZTSSe devices still trails that of CIGS, largely due to manufacturing issues and a deficit in the open-circuit voltage ( $V_{OC}$ ), as shown in Figure I.19. In order to contribute significantly to photovoltaic manufacturing, kesterite solar cells should reach higher performance levels.

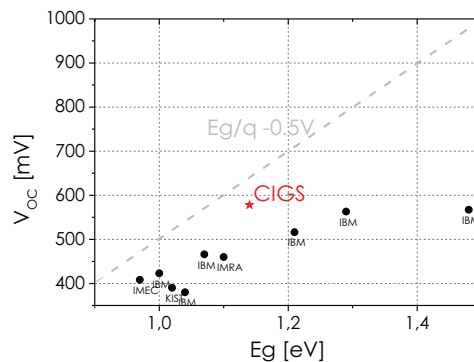


**Figure I.19:**  $V_{OC}$  vs bandgap, adapted from [179]. The dotted line is the  $E_g/q - 0.5$  V line that indicates a nominally good  $V_{OC}$  for thin film solar cells (See [85] page 22, [180] page 365). The star point represents the data of the reference CIGS cell. Black points are kesterite devices, with data from [32, 61, 150, 179].

There have been numerous hypotheses for what is presently limiting the device  $V_{OC}$ . Open-circuit voltage losses are recombination losses. These can be grouped into two broad categories:

a high degree of disorder and/or compensating defects in the CZTSSe bulk, and a non-optimized device structure: a non-ohmic back contact and/or a poorly optimized interface with the buffer layer [181, 182].

### I.2.3.1 Kesterite fabrication and challenging process control

Until now, only Zn-rich and Cu-poor materials ( $\text{Cu}/(\text{Zn} + \text{Sn})=0.80 - 0.85$ ,  $\text{Zn}/\text{Sn}=1.1 - 1.2$ ) resulted in high efficiency devices [6, 10, 177, 179]. There have been several hypotheses for why this off-stoichiometry is required to obtain high efficiencies.

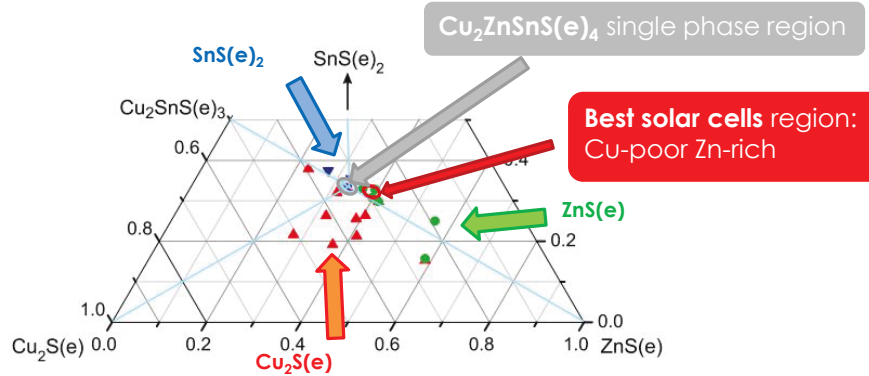


**Figure I.20:** Section of the phase diagram with the kesterite single phase existence region (gray ellipse), the region where the best solar cells are made (red ellipse) and various secondary phases observed in literature, adapted from [176].

The phase diagrams of CZTS and CZTSe exhibit a narrow region of single phase stability [183, 184], much narrower than for CIGS. It is assumed that the phase diagram is essentially the same for the selenide and the sulfide compounds. A slight excess of Cu, Zn or Sn results in the co-precipitation of kesterite and secondary phases. The phase diagram in Figure I.20 shows the main secondary phases observed in literature,  $\text{Cu}_2\text{S}(\text{e})$ ,  $\text{SnS}(\text{e})_2$  and  $\text{ZnS}(\text{e})$ <sup>4</sup>. The ternary phases  $\text{Cu}_2\text{SnS}(\text{e})_3$  and the secondary phase  $\text{SnS}(\text{e})$  may also be observed. The band gap of a secondary phase gives a first estimation of how detrimental the secondary phase will be to the solar cell performance. If the secondary phase has a lower band gap as the absorber it will limit the open circuit voltage of the solar cell [176]. The bandgaps of the secondary phases are described in Table I.7.

In addition, many of the phases are conductive and can shunt the device when present in the film.

- The low bandgap ternary  $\text{Cu}_2\text{SnSe}_3$  has been observed to reduce the efficiency, fill factor and open-circuit voltage of CZTSe devices [192].
- The highly conductive  $\text{Cu-S}(\text{e})$  secondary phases are exceptionally detrimental to device performance [126, 193].
- Sn-based phases are less detrimental than  $\text{Cu-S}(\text{e})$  but may cause severe shunting and performance loss, as observed for  $\text{SnSe}_2$  [138].

Approaching zinc-rich and copper-poor compositions favors the precipitation of wider bandgap  $\text{ZnS}(\text{e})$ , which is not expected to trap electrons or holes, at the expense of the more conductive phases, thereby preventing a shunt mechanism. However, the effect of the secondary phases also depends on their location. The presence  $\text{SnSe}_2$  secondary phase at the absorbers' surface has a strong negative impact on the device performance [138, 193], but certain little amount and even distribution of  $\text{SnSe}_2$  can be beneficial to increase the short circuit-current and device efficiency [194].  $\text{ZnS}(\text{e})$  secondary phases block the current when located at the surface of the absorber [195,

<sup>4</sup>The notation S(e) is used here to describe both S and Se-based compounds.



**Table I.7:** Kesterite main secondary phases and their bandgaps.

Phase	Bandgap (eV)	Reference
<b><i>CZTSe</i> 1.0</b>		
Cu <sub>2</sub> SnSe <sub>3</sub>	0.7 – 0.9	[176, 185, 186]
Cu <sub>2</sub> Se	1.2 – 2.2	[176, 186]
Cu <sub>2-x</sub> Se		
CuSe	2.2	[186]
SnSe	indirect: 0.9; direct: 1.3	[176, 186]
SnSe <sub>2</sub>	indirect: 0.9; direct: 1.0 – 1.7	[36, 186]
ZnSe	2.6 – 2.9	[176, 186, 187]
<b><i>CZTS</i> 1.5</b>		
Cu <sub>2</sub> SnS <sub>3</sub>	0.9 – 1.35	[176, 178, 188]
Cu <sub>2</sub> S	1.0 – 1.2	[176, 178]
Cu <sub>2-x</sub> S		
CuS	1.8 – 2	[189]
SnS	indirect: 1.0 – 1.3; direct: 1.0 – 1.8	[36, 176, 189, 190]
SnS <sub>2</sub>	2.2 – 2.5	[176, 178, 191]
Sn <sub>2</sub> S <sub>3</sub>	0.85	
ZnS	3.5 – 3.7	[176, 189, 191]

[196] but have shown to be harmless when located at the back contact, even in large amounts [124, 193, 195]. In general, secondary phases are more detrimental when present at the absorber/buffer layer interface [51].

Cu-S(e) and Sn-S(e) secondary phases can be identified using XRD [138, 193, 194, 197–200] and/or green-excitation wavelength (514 or 532 nm) Raman spectroscopy [44, 49, 138, 199, 201, 202]. XRD is the more sensitive technique for detecting the binary tin phases (SnSe and SnSe<sub>2</sub>) in kesterites [193]. However, due to close lattice constants, it is very difficult to discriminate Cu-Sn-S(e) and ZnS(e) secondary phases from kesterite CZTS(e), especially when present in low amount, as shown by Berg et al. [203]. In addition Fairbrother et al. [204] have shown that ZnS films thinner as 1400 nm are barely detectable by Raman scattering spectroscopy under standard excitation conditions (514 nm). The use of multiple-wavelength Raman analysis can help to discern secondary phases from kesterite, for instance by using resonant conditions: 325 nm UV-excitation for ZnS [172, 202, 204, 205], 457.9 nm for ZnSe [44, 49, 202, 206]. RT-PL (room temperature photoluminescence) has also been used to detect the presence of ZnSe [206]. Chemical-composition-related techniques with depth-dependent resolution (secondary ion mass spectroscopy (SIMS), glow discharge optical emission spectroscopy (GDOES), energy dispersive X-ray spectroscopy (EDX) in combination with SEM) offer the possibility of obtaining indications of the presence of secondary phases in an indirect manner [36]. For instance the presence of Zn-rich regions can give an indication on the presence of ZnS(e) secondary phases.

Another common issue generally encountered during process optimization involves the volatility upon heating of Sn and Zn materials, which makes compositional control a challenge during film fabrication [41, 207, 208]. Chalcogen (S and/or Se) partial pressures during the annealing step also have an influence on the absorber’s properties and MoS(e)<sub>2</sub> layer’s growth and should be controlled with care [63].

### I.2.3.2 Bulk properties: defects and passivation

**P-type doping by intrinsic point defects formation** The kesterite structure allows the formation of several types of point defects which make discrete energy levels appear, allowing p-type doping. As in CIGS, doping is obtained by stoichiometry variations and not by extrinsic doping. According to Chen et al. [10], the  $\text{Cu}_{\text{Zn}}$  antisite is the dominant point defect in stoichiometric  $\text{Cu}_2\text{ZnSnS}_4$  and  $\text{Cu}_2\text{ZnSnSe}_4$ . Its ionization level is deeper than that of  $\text{V}_{\text{Cu}}$ , but its high population can still produce a significant hole concentration, determining the intrinsic p-type conductivity and making n-type doping difficult. Under Cu poor and Zn rich conditions ( $\text{Cu}/(\text{Zn} + \text{Sn}) < 0.8$ ),  $\text{V}_{\text{Cu}}$  becomes dominant and contributes to p-type conductivity, which reflects the situation in the real solar cells with low  $\text{Cu}/(\text{Zn} + \text{Sn})$  ratio and high efficiency.

**Detrimental deep level** Some studies suggest that copper may preferentially occupy tin lattice sites as the copper content increases; the  $\text{Cu}_{\text{Sn}}$  point defect is expected to contribute to a detrimental deep level in CZTSSe [10]. Under copper-poor conditions, this detrimental effect is avoided.

**Defect clusters** The frequently observed non-stoichiometry in quaternary kesterites results from the easy formation of self-compensated defect clusters [10,209], such as  $[\text{V}_{\text{Cu}} + \text{Zn}_{\text{Cu}}]$ ,  $[\text{Zn}_{\text{Sn}} + 2 \text{Zn}_{\text{Cu}}]$  and  $[2 \text{Cu}_{\text{Zn}} + \text{Sn}_{\text{Zn}}]$ .  $[\text{V}_{\text{Cu}} + \text{Zn}_{\text{Cu}}]$ , expected in copper-poor zinc-rich compositions, may lead to the formation of the least detrimental secondary phases, the high bandgap Zn-S(e).  $[2 \text{Cu}_{\text{Zn}} + \text{Sn}_{\text{Zn}}]$  clusters induce electron-trapping states in the absorber material, and are thus detrimental for solar cell performance. Their easy formation and high population even in near-stoichiometric  $\text{Cu}_2\text{ZnSnS}_4$  and  $\text{Cu}_2\text{ZnSnSe}_4$  degradate the efficiency of solar cells with  $\text{Cu}/(\text{Zn} + \text{Sn})$  and  $\text{Zn}/\text{Sn}$  ratios near unity, therefore a rather Zn-rich and Cu-, Sn-poor conditions are required to prevent their formation and improve solar cell performance. This explains the empirical observation that Cu-poor and Zn-rich condition is crucial for high solar cell efficiency.

The dominant compensating  $[\text{Cu}_{\text{Zn}} + \text{Zn}_{\text{Cu}}]$  defect cluster is predicted to have low formation energy independent of composition, and is likely to cause for Cu/Zn disorder in the kesterite crystal structure [10,107]. Significant disorder of Cu and Zn atoms in the Cu/Zn sublattice is expected for all compositions and may have consequences for kesterite solar cells performance. A reversible Cu/Zn disorder have been reported for CZTS [210,211], CZTSe [66] and CZTSSe [212], as shown in Figure I.21. The bandgap energy being affected by the order/disorder transition [66], a precise control and understanding of this phenomenon is needed. Also, a local Zn enrichment

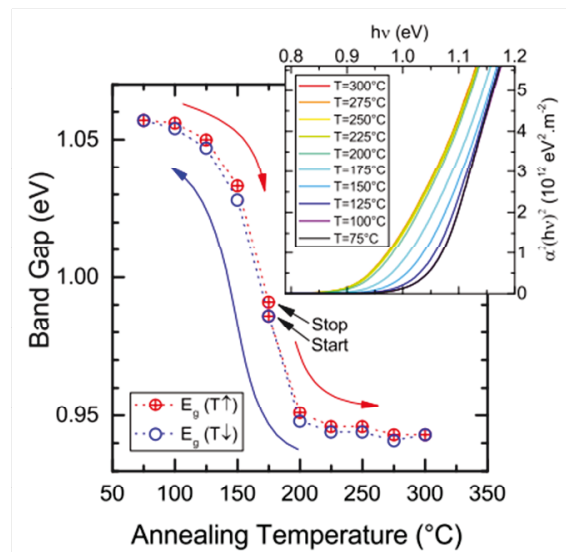


**Figure I.21:** Cu-Zn order-disorder in CZTSe, with a transition critical temperature of 200°C. [66]

inherently implies a local segregation of donor defects, whereas local copper enrichment implies local segregation of acceptors. Thus, assuming these defects are ionized, the density of charged defects [ $\text{Cu}_{\text{Zn}} + \text{Zn}_{\text{Cu}}$ ] in the semiconductor fluctuates along with the compositional fluctuations. These charge fluctuations cause electrostatic potential fluctuations of the conduction and valence bands. Compositional fluctuations of this type can cause band tailing in kesterite [177] and be one of the reasons for the limited  $V_{\text{OC}}$ .

**Band tailing** The formation of band-edge tail states in CZTSSe solar cells, which may be more severe than in CIGS [213], can be an explanation for the limitation of performance. In addition, band tailing may be facilitated by a lower dielectric constant as  $\epsilon_r \approx 6.7$  for CZTS and  $\epsilon_r \approx 8.5$  for CZTSe, while CIGS's dielectric constant is around 12 [11, 214]. Band tailing induces a redshift and broadening of photoluminescence (PL) peak compared to the bandgap  $E_g$  extracted from external quantum efficiency (EQE), and a slower decay in EQE [213]. In what extent this phenomenon contributes to the  $V_{\text{OC}}$  deficit is still an open question.

**Sulfur and selenium** Considering material availability, pure-sulfur kesterite is desirable. Indeed, it is demonstrated that the deployment of solar cells based on Cu, Zn, Sn and S meets no restrictions, while the availability of Se may be limited (page 14). However, comparing predicted defects, deeper defects, and/or higher defect densities in CZTS are expected to cause more severe band tailing and performance losses as in CZTSe [10]. Electron-trapping caused by [ $2 \text{Cu}_{\text{Zn}} + \text{Sn}_{\text{Zn}}$ ] in  $\text{Cu}_2\text{ZnSnSe}_4$  is much weaker than in  $\text{Cu}_2\text{ZnSnS}_4$ . Isolated deep donor defects such as  $\text{Sn}_{\text{Zn}}$  and  $V_{\text{Se}}$  have a lower population in CZTSe than in CZTS. Today, higher efficiencies are obtained with pure-selenide CZTSe devices (11.6% [13]) compared to pure-sulfur CZTS solar cells (9.2% [124]). Still, the highest efficiencies are achieved with selenium-rich mixed CZTSSe compound (12.7% [26]), with a band gap of 1.13 eV. This band gap is lower than the band gap predicted by Shockley-Queisser (1.34 eV) to produce the highest-efficiency devices under AM 1.5 G illumination [90], but CZTSSe compounds with higher sulfur concentration and “optimal” band gap typically display lower efficiencies and worse  $V_{\text{OC}}$  deficits.

### 1.2.3.3 Interface optimization

**Back contact** In high-efficiency CZTSSe devices, an interfacial  $\text{Mo}(\text{S},\text{Se})_2$  layer is always present between the Mo and the CZTSSe. This interfacial layer is believed to be important for film adhesion and also for ensuring ohmic contact with CIGS. However, it may not be true that this contact is ohmic for all CZTSSe materials [182]. In some cases, when CZTSSe device efficiency is low, devices display low fill factor values and high series resistance. In addition a decomposition reaction between Mo and kesterite have been reported to occur at the back contact [33].

**p-n junction** Voltage limitation in kesterite devices may be related to the recombinative character of the CZTSSe/CdS hetero-junctions. The conduction band alignment of CdS/CIGS is “spike-like” with a desired band offset of 0.2 – 0.3 eV, which facilitates the high efficiency of a CIGS solar cell, especially for high  $V_{\text{OC}}$ . It is one of the key factors for high-performance solar cells using a buffer/absorber heterojunction combination. The type of conduction band offset (CBO) in the case of CdS/CZT(S,Se) and other buffers based cells is under investigation [215]. In addition, a spike-like conduction band alignment of kesterite absorbers with a CdS buffer layer can also be the origin of fill factor and current-reducing distortions in current–voltage curves, such as light/dark curve crossover, or an s-like curve shape for long wavelength monochromatic illumination (red kink) if light-dependent defect states are present in the buffer layer [34]. Further investigations are needed in order to optimize the buffer/absorber junction interface.

## I.3 Objectives and Structure

The main objective of this thesis is to develop high-efficient kesterite materials using fabrication processes that are compatible with industry requirements (low-cost mass production). Kesterite based solar cells reach “high” efficiencies ( $>8\%$ ) with a wide range of deposition techniques. ED and other solution techniques such as DSC, CBD and spray pyrolysis are expected to offer lower manufacturing costs than vacuum-based methods. However, this assumption still needs to be proven as several other factors such as final module efficiency, process robustness, energy consumption, price of raw materials, and safety considerations will certainly have a decisive impact on the technology deployment and final cost. This thesis investigates the suitability of electrodeposition of copper, tin and zinc followed by annealing for future industrial implementation. This report consists of three experimental chapters and a discussion chapter. The experimental chapters begin with an introduction to the relevant literature and theory that is utilized in the experimental work. After the results are presented, they are discussed in the light of the available literature, and finally conclusions are drawn. The different chapters will correspond to the process aspects to be considered in order to accomplish the objective:

- *Chapter 2*: the development of an industrially-compatible electrodeposition route to fabricate Cu-Sn-Zn precursors. The success of this objective is judged by the ability to produce a film of controlled, uniform composition which can be varied as required, compliant with industry requirements such as safety, high throughput and low cost.
- *Chapter 3*: the choice of an efficient annealing route to convert the precursor into a kesterite film; either with sulfur or selenium, in order to achieve complete conversion and demonstrate the correct phase and suitable properties for a thin film device, with the maximum uniformity.
- *Chapter 4*: the optimization of the device efficiency by improving the interface: wet chemical etching, device structure.

Finally, *Chapter 5* will summarize the challenges to overcome and possible solutions in order to enable an industrial fabrication process for high efficient kesterite based solar cells.



# Chapter II

## Electrodeposition of precursor

### Contents

---

II.1	Basics . . . . .	<b>31</b>
II.1.1	Advantages of electrochemical processes . . . . .	31
II.1.2	Electrodeposition principle . . . . .	31
II.1.2.1	The electrodeposition cell . . . . .	31
II.1.2.2	Faraday's laws . . . . .	33
II.1.2.3	Electrode potential . . . . .	33
II.1.2.4	Overpotential . . . . .	34
II.1.3	Operating parameters during electroplating . . . . .	35
II.1.3.1	Current distribution . . . . .	35
II.1.3.2	Electrolyte . . . . .	35
II.1.3.3	Agitation . . . . .	36
II.1.3.4	Uniformity . . . . .	36
II.1.3.5	Electrodeposition method . . . . .	37
II.2	Experimental approaches . . . . .	<b>38</b>
II.2.1	ED for thin films solar cells . . . . .	38
II.2.2	Kesterite fabrication routes . . . . .	38
II.2.2.1	Cu-Sn-Zn metal alloy deposition route . . . . .	39
II.2.2.2	Cu-Zn-Sn-S or Cu-Zn-Sn-Se quaternary deposition route . . . . .	40
II.2.2.3	SEL route . . . . .	41
II.2.2.4	Comparison of kesterite electrodeposition routes . . . . .	42
II.2.3	Electrodeposition of Cu, Sn and Zn: an industrial approach . . . . .	43
II.2.3.1	Industry specifications . . . . .	43
II.2.3.2	Copper electrodeposition . . . . .	44
II.2.3.3	Tin electrodeposition . . . . .	45
II.2.3.4	Zinc electrodeposition . . . . .	47
II.2.3.5	Summary: choice of electrolytes . . . . .	48
II.2.4	Desired precursor properties for high-efficient kesterite devices . . . . .	49
II.3	Experimentals . . . . .	<b>52</b>
II.3.1	Substrates . . . . .	52
II.3.2	Chemistry . . . . .	52
II.3.2.1	Electrolyte composition . . . . .	52
II.3.2.2	Electrolyte concentration control and replenishment . . . . .	53
II.3.3	Process conditions . . . . .	53
II.3.4	Low-temperature annealing of metallic stacks . . . . .	55
II.3.5	Material and bath characterization . . . . .	55
II.4	Results and discussion . . . . .	<b>56</b>

II.4.1	Chemistry: Lifetime and stability . . . . .	56
II.4.1.1	Copper . . . . .	56
II.4.1.2	Tin . . . . .	56
II.4.1.3	Zinc . . . . .	59
II.4.1.4	Conclusions on electrolytes' lifetime and stability . . . . .	59
II.4.2	Process and material optimization . . . . .	60
II.4.2.1	Initial deposition parameters: preliminary work . . . . .	60
II.4.2.2	Evolution of deposition parameters over time . . . . .	61
II.4.2.3	Uniformity of the Cu/Sn/Zn precursor . . . . .	62
II.4.2.4	Morphology of Cu, Sn and Zn deposits: adherence and defaults . . . . .	63
II.4.2.5	Composition profile and phases . . . . .	64
II.4.2.6	Low-temperature annealing . . . . .	64
II.5	Discussion and Conclusions . . . . .	<b>68</b>

---

In this chapter, we evaluate the potential of electrodeposition (ED) for low-cost synthesis of kesterite materials. Suitability of ED for the deposition of good quality thin film precursors will be examined, in addition to its compatibility with industry regarding process robustness, cost of ownership (direct and indirect costs) and safety considerations.

## II.1 Basics

### II.1.1 Advantages of electrochemical processes

Electrochemistry applies where a charge transfer is involved at an electrified interface between electronic and ionic conductors. There is a common agreement among scientists that electrochemically based processes will be of increasing importance in the future to meet the economic and social challenges resulting from urgent demands of low-grade raw materials' utilization, energy savings, and protection of the environment [216]. The main advantages of electrochemical processes are:

- Compatibility with environment. Development of industrial processes to meet the requirements of sustainable development has become a major issue. Electrochemistry offers promising approaches due to its environmental compatibility and use of electron as a “clean reagent”;
- Versatility. The electrochemical processes involve direct or indirect reactions, are applicable to a large variety of media: gases, liquids and solids, concentrated or diluted, and allow the treatment of small to large volumes (microliters up to millions of liters);
- Energy efficiency. Lower temperature is required than their nonelectrochemical counterparts processes. Optimized electrode structure and cell design allow to minimize power losses caused by inhomogeneous current distribution, voltage drop and side reactions;
- Amenability to automation. The system variables such as electrode potential and cell current are suitable for a facilitated process automation and control;
- Cost effectiveness. Cell and equipment are generally simple and inexpensive.

### II.1.2 Electrodeposition principle

In this section, generalities about electrodeposition are first approached. More informations can be found in references [216–218].

#### II.1.2.1 The electrodeposition cell

Electroplating or electrodeposition is the deposition of a coating on a surface by an electrochemical process, and involves the exchange of electrons between a solid electrode and ions or molecules dissolved in solution. Within the bulk of the electrodes the current is carried by the movement — also called drift — of electrons, and within the bulk of the solution an equal current is carried by the drift of ions. At the electrode/solution interface, the current is supported by transfer of electrons between the electrode and the species in solution. The electron-transfer reactions are oxidation-reduction reactions. A reduction can usually be described by the equation:



where Ox is the oxidized species,  $z$  the number of electrons exchanged during the redox reaction and Red is the reduced species. In ED, oxidized species present in a solution, the electrolyte, are reduced at the surface of a substrate to form a metal layer. This process essentially consists of:

- An electrically conducting substrate such as a metallic surface or another substrate. On insulating or highly-resistive substrates, a thin metal film (i.e. several tens of nanometers) called seed layer has to be applied first. This substrate is contacted with the current source and is the negative terminal (cathode).



- An electrolyte or plating solution containing the metal ions that will be deposited in the form of salts, supporting chemicals such as acids and salts and eventually additives. A large background concentration of ions is provided to ensure good electrical conductivity in the solution.
- A counter electrode: anode, which can be constituted of the metal being plated: a sacrificial or dissolvable anode; or of a conducting material which serves to complete the circuit: an inert, permanent or insoluble anode. When the reduced species is a metal, the positive electrode (the anode) may consist of the same metal. In this way, the anode dissolves by oxidation, the concentration of metal ions remains constant.
- An external controllable current or voltage source, with means of conveying this current to the plating tank.

The electrochemical cell is illustrated for the case of reduction of a metal ion into a metal atom in Figure II.1. Since the electrodeposited material is itself conductive, the reaction will continue while the potential difference or applied current is maintained. The concentration of metal ions in the solution will gradually decrease while they are consumed, unless they are replenished.

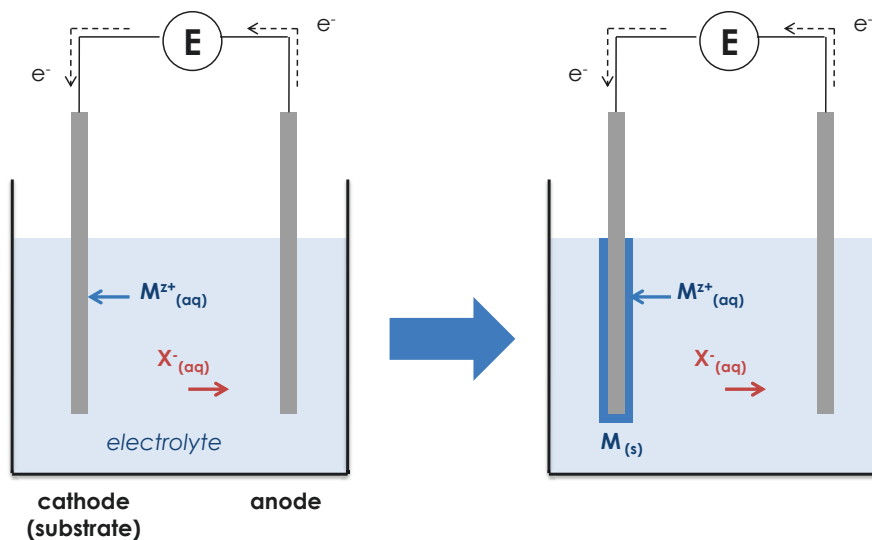


**Figure II.1:** Scheme of a two-electrode electrochemical cell for the reduction of metal ion into a metal atom, i.e.  $M_{(aq)}^{z+} + ze^{-} \rightarrow M_s^0$ . On the right, the deposited metal layer is growing on the substrate.

The reaction path of electrodeposition usually includes the following steps [219]:

1. Mass transfer of reactive species from electrolyte to electrode surface, which depends on the forced convection (hydrodynamic conditions) and diffusion (depending on temperature, nature and concentration of the electroactive species);
2. Charge-transfer step at the surface;
3. Various chemical reactions, such as breaking up the bond with the ligand (when there is one). These reactions can occur before or after step 2;
4. Surface reactions, such as incorporation into the substrate (adsorption), chemical and electrochemical reactions between species, crystallization.

Any step can be rate determining, and the slowest one determines the total reaction rate. The electrolyte concentration influences the time constant of all these steps, because the concentration is a critical factor in all time constants of chemical reactions.

### II.1.2.2 Faraday's laws

The background of electrodeposition processes is the Faraday's laws that connect the amount of electricity and mass of reacted material. Faraday's first and second laws of electrolysis state that the amount of a material deposited on an electrode is proportional to the amount of electricity used. Faraday's laws can be written as:

$$Q = I\Delta t = znF \quad (\text{II.2})$$

where  $Q$  is the amount of charge in coulomb (C),  $I$  the current in ampere (A),  $t$  the time in second (s),  $z$  is the charge on the depositing ion or change in oxidation state,  $n$  the amount of metal deposited in mole (mol),  $F$  is Faraday's constant ( $96485 \text{ C} \cdot \text{mol}^{-1}$  which corresponds to the amount of electric charge carried by 1 mol).

The ideal thickness of the deposit,  $e$ , can be solved by:

$$e = \frac{m}{\rho A} = \frac{Mn}{\rho A} = \frac{M}{\rho A} \times \frac{I\Delta t}{zF} \quad (\text{II.3})$$

where  $m$  is the weight of the deposit in gram (g),  $\rho$  is the density of the metal in gram per cubic meter ( $\text{g}/\text{m}^3$ ),  $A$  is the area of deposition in square meters ( $\text{m}^2$ ), and  $M$  is the atomic weight (g/mol). Faraday's laws give a theoretical prediction of electrodeposition in an ideal situation. However, for real applications, Faradic losses may occur when electrons or ions participate in unwanted reactions. Current that does not contribute to the electrodeposition process is considered wasted. These losses are under the form of heat and/or chemical byproducts. The current efficiency  $\eta$  is a fraction, usually expressed as a percentage, of the current passing through an electrolytic cell (or an electrode) that accomplishes the desired chemical reaction:

$$\eta = \frac{m_{act}}{m_{Faraday}} \times 100 \quad (\text{II.4})$$

where  $m_{act}$  is the weight of metal actually deposited and  $m_{Faraday}$  is the corresponding weight to be expected from Faraday's laws if there is no side reaction.

### II.1.2.3 Electrode potential

The probability of an electrochemical reaction happening is evaluated as electrode potential, the electrical potential difference between an electrode and a reference electrode. In the equilibrium state, the reactions that release electrons (anodic) and the reactions that consume electrons (cathodic) have equal rates. The system is in a dynamic equilibrium state and no net reaction occurs. For example, when a metal is immersed into a solution containing ions of that metal, equilibrium is set up between the tendency of the metal to enter solution as ions and the opposing tendency of the ions to lose their charge and deposit on or in the metal, written as:  $\text{M}_{(aq)}^{z+} + ze^- = \text{M}_s^0$ . The standard electrode potential or oxidation/reduction potential, noted  $E^\circ$ , corresponds to a determined standard rate at 0.1 MPa,  $25^\circ\text{C}$ , ideal solution of 1.0 mol/L and equilibrium potential of any other state. The standard electrode potentials can be found in tables [220]. Under non-standard conditions, the equilibrium potential is given by the Nernst equation:

$$E_{eq} = E^\circ + \frac{RT}{zF} \ln \frac{c_R}{c_O} \quad (\text{II.5})$$

where  $R$  is the gas constant ( $8.31446 \text{ J} \cdot \text{K}^{-1} \cdot \text{mol}^{-1}$ ),  $T$  the temperature in kelvin (K),  $F$  is Faraday's constant and  $c_R$ ,  $c_O$  the concentrations of reduced and oxidized species. Therefore the actual  $E_{eq}$  depends on the concentration of the species in the solution which depends on the pH or the addition of complexing agents. The potential can be modified by adjusting the pH and the complexing agents concentration.

For example,  $E_{eq} = -0.76$  volts for zinc. But, when zinc is complexed with cyanide:  $\text{Zn}^{2+} + 4(\text{CN})^- \longrightarrow [\text{Zn}(\text{CN})_4]$  the electrode potential shifts to approximately  $-1.1 \text{ V}$  [218]<sup>1</sup>.  $E^\circ$  of

<sup>1</sup>When complex ion reactions are involved:



$\text{Cu}^{2+}/\text{Cu}$ ,  $\text{Sn}^{2+}/\text{Sn}$  and  $\text{Zn}^{2+}/\text{Zn}$  redox couples along are given in Figure II.2, along with some oxidation-reduction reactions involving water ( $\text{H}^+/\text{H}_2$  and  $\text{O}_2/\text{H}_2\text{O}$ ).

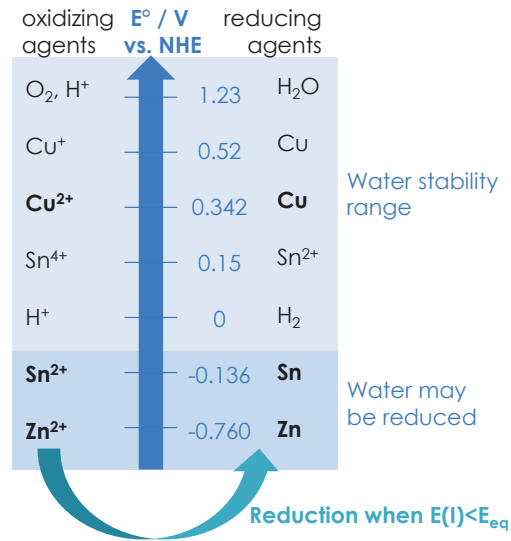


**Figure II.2:** Standard reduction potentials of different elements in aqueous solution vs. NHE [220].

Hydrogen evolution, a cathodic reaction, involves  $\text{H}^+/\text{H}_2$  and is expressed by the reactions:



Evolution of oxygen at the anode, involving  $\text{O}_2/\text{H}_2\text{O}$ , is expressed by the reactions :



At the potential needed to reduce  $\text{Zn}^{2+}$  to  $\text{Zn}$  (lower than -0.76 V in standard conditions), other species in presence such as  $\text{H}^+$  are going to be reduced as well into  $\text{H}_2$ , representing a waste in electricity and a reduction in the current efficiency of the process. Modulation of  $E_{eq}$  by an adequate electrolyte formulation (pH, complexing agents) is then necessary. The composition of the electrolyte is modulated so as to maximize the probability of desired reactions and to minimize the unwanted reactions.

#### II.1.2.4 Overpotential

An external potential difference has to be provided to move away from equilibrium. Overpotential  $\varphi$  is the difference in the electrode potential of an electrode between its equilibrium potential ( $E_{eq}$ ) and its operating potential when a current is flowing ( $E(I)$ ). The overpotential increases with increasing current density. If  $E(I) < E_{eq}$ , the electron consumption at the cathode is favored, i.e.  $\text{Ox}^{z+} + z\text{e}^- \longrightarrow \text{Red}$ . On the contrary, if  $E(I) > E_{eq}$ , the reaction that release of electrons

where  $q$  is the coordination number, then the Nernst equation is modified:

$$E_{eq} = E^\circ - \frac{RT}{zF} \ln K_f + \ln \frac{[\text{MX}_q^{n-pq}]}{[\text{X}^{p-}]^q} \quad (\text{II.7})$$

with  $K_f$  the stability constant of the complex ion. Since  $K_f$  is quite large for very stable complexes, the potential can shift substantially negatively.

Red  $\rightarrow$  Ox<sup>z+</sup> + ze<sup>-</sup> is favored. This deviation in potential, also called polarization, is not a simple phenomenon as the electrochemical reactions occur in several phases. The overpotential is a combination of several factors, among them activation, concentration and resistance overpotentials:

- The activation overpotential results from the limited rate of a charge-transfer step, and can be seen as threshold to be overcome before the reaction starts.
- The concentration overpotential results from a finite mass-transfer rate from bulk electrolyte to electrode or vice versa. The current density is therefore limited by the concentration of reacting species, their diffusion rate, temperature, or flow rate increase. Agitation and a high electrode surface area help to improve the mass-transfer.
- The resistance overpotential, result of ohmic resistances, does not directly influence the electrochemical reaction but decreases the charge transfer between anode and cathode. The resistance overpotential  $\varphi_{\Omega}$  obeys Ohm's law:

$$\varphi_{\Omega} = I.R_{\Omega} \quad (\text{II.12})$$

where I is the current (A) and  $R_{\Omega}$  the resistance of the solution ( $\Omega$ ).

Finally, the reaction rate is measured as current density and depends on many parameters such as the electrode potential, the electrode area and the rate of mass transport of the electroactive species to the electrode surface.

### II.1.3 Operating parameters during electroplating

#### II.1.3.1 Current distribution

Current density and its distribution play a centrally important role in determining the quality of the final deposit. The thickness distribution of electrodeposits depends on the current distribution over the cathode, which determines the local current density at the surface. Electrodeposition cell geometry, electrolyte and electrodes conductivity, reaction kinetics (activation overpotential) and convection are factors having an effect on the homogeneity of the electrodeposition [219]. According to the relative importance of each factor, three distributions types can be distinguished:

1. The primary current distribution depends only on the current and resistance of the electrolyte on the path from anode to cathode. The activation and concentration overpotentials are neglected. In this case the distribution is totally dependent on the electrochemical cell geometry, especially on the size of the electrodes and the distance between them. The resulting current lines are denser on the edges of the cathode.
2. The secondary current distribution depends on both the resistance of the electrolyte path and the reaction overpotential, but the concentration overpotential is still neglected. In the case of small scale electrodeposition, when the mass transfer is slow and the electrolyte resistance is small, the edge effect of the primary distribution tends to be smoothed and the resulting electrodeposited layer is more homogeneous. In the case of electrodeposition on large surfaces of resistive material, the current is higher near the electrical contacts.
3. In the tertiary current distribution, all the effects are negligible compared with the limiting effect of mass transport. The local current density is entirely determined by the local diffusion layer thickness (hydrodynamics). Control and generation of homogeneous hydrodynamic conditions is therefore crucial for the synthesis of homogeneous electrodeposited layers.

All the three are involved in different degrees in the overall cathode deposition process.

#### II.1.3.2 Electrolyte

Generally, in the electroplating process, bath concentration plays an important role to the plating performance. Increase of metal ion concentration causes higher deposition rates and enhanced

current distribution uniformity. The electrolyte contains many components that all have specific functions, as shown in Table II.1. Anions, such as  $X^-$  in Figure II.1, do not participate in the electrochemical reaction but their drift from the cathode to the anode supports the current flow through the solution.

**Table II.1:** Electrolyte components of interest

Component	Role	Example
Metal ion	Source of metal	Copper sulfate
Anion	Maximize solution Provide anode reaction Conductivity pH control	Sulfate, chloride
Auxiliary salt	Ionic strength and conductivity Buffering and pH control	Sulfuric acid
Complexing agents	Kinetic stability Deposit morphology control	Cyanide, citrates, tartrates
Impurities	Detrimental to efficiency or purity	
Inorganic additives	Assist anode life Impurity removal	
Organic additives	Cathode leveling Impurity control and improved efficiency Grain refiner Mist suppressor	Polyethers, amines
Water	Solvent	
Suspended solids	Incorporation into cathode or remove as cell sludge	Flocculating agent

### II.1.3.3 Agitation

Agitation systems ensures general solution uniformity and prevent excessive ion depletion or gas accumulation at the anode and cathode surfaces. It permits to use high current densities plating processes [221]. Stirring systems include rotating disk electrode, fountain plating, random jet arrays, comb-like and paddle cell [219, 222]. As the mass transfer created by stirring systems, called advection or forced convection, influences homogeneity and deposition current, the choice of an optimal stirring system is important for controlling the electrodeposition process.

### II.1.3.4 Uniformity

There are two levels of uniformity that need to be controlled:

- Microscopic uniformity, i.e. the morphology of the electrodeposited material. Smooth films are required so as to completely cover the underlying layer.
- Macroscopic uniformity, i.e. the thickness of the electrodeposited film must be constant over the largest area possible.

These two parameters are affected by electrolyte composition and deposition conditions (voltage, current) and configuration of the electrodeposition cell and mass transport (convection, repartition of current lines). The deposited films need to be uniform at both microscopic and macroscopic scale in order to have a constant composition at all points.

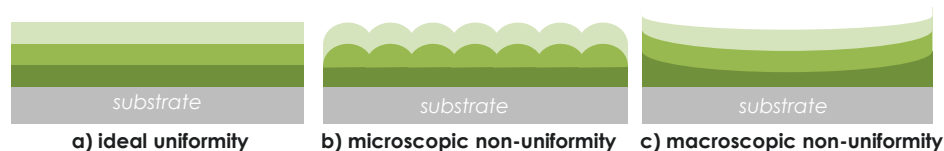


**Figure II.3:** Schematic illustration (cross-section) of stacked precursor uniformity, adapted from [223]. b) shows microscopic non-uniformity of the second layer and c) shows macroscopic non-uniformity in the first layer.

### II.1.3.5 Electrodeposition method

To perform an electrodeposition, two methods can be used. In the potentiostatic method, the potential is applied between the anode and the cathode. The potentiostatic method is used when the process is sensitive to small variations of the working electrode potential. For the galvanostatic method, the current is applied between the anode and the cathode. It is used for robust processes which need high deposition rates. The current between working and counter electrodes is controlled, and the potential between working and reference electrodes is automatically adjusted to the value required to maintain the current. The galvanostatic method is more suitable for industrial processes.

## II.2 Experimental approaches for the fabrication of kesterite by electrodeposition

### II.2.1 Electrodeposition: a high potential process for industrial fabrication of thin films absorber layers

Electrodeposition is a well-established process for depositing metals and metallic alloys at industrial level. ED is also emerging as a deposition method for semiconductors, as it is interesting for large area, low cost processing of materials [224]. In the case of semiconductors electrodeposition for thin films solar cells, proof of manufacturability on large areas was given with electrodeposited cadmium telluride modules which reached over 10% efficiency in 2001 [225]. CdTe semiconductors can directly be electrodeposited as the free energy of formation of the compound plays a major role in allowing self-regulation of the composition, close to stoichiometry. One-step deposition of a quaternary system like  $\text{CuIn}_x\text{Ga}_{1-x}(\text{S,Se})_2$  (CIGS),  $\text{Cu}_2\text{ZnSnS}_4$  (CZTS) or  $\text{Cu}_2\text{ZnSnSe}_4$  (CZTSe) is much more challenging as for binaries like CdTe. A simpler approach is to deposit layers of the metal precursor as a stack in the desired atomic ratio, and convert the metal stack to a semiconductor by reactive annealing in a sulfur or selenium atmosphere. Alternatively, the three metals can be deposited simultaneously before sulfurization or selenization. Feasibility of electrodeposition-annealing to form absorber layers has already been demonstrated for CIGS cells [226–228]. For instance, NEXCIS developed an industrial CIGS fabrication process that relies on electroplating of copper, indium and gallium on large surface substrates ( $60 \times 120 \text{ cm}^2$ ). NEXCIS reached 17.3 % (cell) and 14.0 % (module) record power conversion efficiencies at the pilot line manufacturing facilities through a full industrial process [229,230]. The extension of ED processes to the fabrication of kesterite thin films by electroplating of copper, tin and zinc has been demonstrated in the last years at research scale.

### II.2.2 Kesterite fabrication routes

There are three main strategies for kesterite electrodeposition: co-deposition of the metals components, simultaneous deposition of the CZTS or CZTSe quaternary, or stacked elemental layers (SEL) route, represented in Figure II.4, all followed by an annealing step.

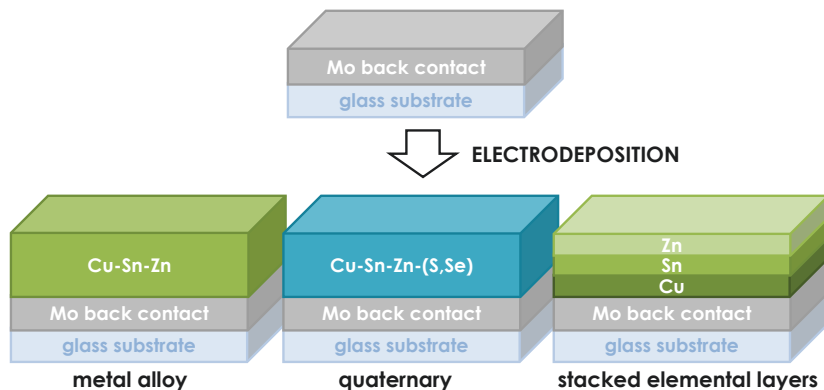


**Figure II.4:** Schematic representations of the three main kesterite precursor electrodeposition approaches employed in literature.

Pioneering Scragg’s PhD work (2007-2010) [223,231–233] on the fabrication of CZTS based solar cells by electrochemical stacked metal layers approach followed by rapid thermal processing (RTP) sulfurization led to 0.8% (2008, [231]) and 3.2% (2010, [233]) efficient kesterite devices. Araki et al. reported devices by ED followed by sulfurization, a 0.98% (2009, [234]) device by SEL

approach, and 3.16% (2009, [235]) with co-electrodeposited Cu-Zn-Sn precursor. Ennaoui et al. also employed electrodeposition of a Cu-Zn-Sn mixed layer followed by sulfurization of the metallic precursor in H<sub>2</sub>S at 550 °C for the formation of CZTS film, with a device power conversion efficiency reaching 3.4% (2009, [236]). It is only in 2012 that reported efficiencies for electrodeposited kesterite increased above 7%, with IBM group 7.0% [31] CZTSe and 7.3% CZTS [29] devices fabricated by electrodeposition of a stacked metallic precursor at pre-industrial scale (15 × 15 cm<sup>2</sup>). Since then, many groups reported efficiencies in the 1 – 6% power conversion efficiency range, following different strategies for kesterite electrodeposition. In 2014, 8% efficiencies were reported for CZTS by a stacked metal layer approach [30], and for CZTSe by metal alloy codeposition route [32]. A couple of reviews about electrodeposition processes for kesterite fabrication can be found in literature [18, 19].

### II.2.2.1 Cu-Sn-Zn metal alloy deposition route

Co-electrodeposition of the three metals is a simple method as it requires a single bath, a single step, which is convenient for the fabrication process. However, fine tuning of the electrodeposition conditions (electrolyte composition, potential, etc) is necessary to control the composition and morphology of the precursor. Due to the difference in standard redox potentials between Cu, Sn and Zn (Fig. II.2), complexing agents need to be added to the electrolyte in order to narrow the potential gap between the three elements.

**Table II.2:** Kesterite electrodeposited by Cu-Sn-Zn metal alloy route.

Potential is given <sup>a</sup> vs SCE; <sup>b</sup> vs Ag/AgCl; <sup>c</sup> vs MSE reference electrode.

Material	$\eta$ %	Chemistry	pH	$E$ or $J$	$T$ °C	$t$ min	$A$ cm <sup>2</sup>	$e$ nm	Phases
CZTSe	8.0 [32]	CuSO <sub>4</sub> , ZnSO <sub>4</sub> , SnCl <sub>2</sub> ; C <sub>6</sub> H <sub>5</sub> Na <sub>3</sub> O <sub>7</sub>	-	-1.18V <sup>b</sup>	-	20	3×4	-	Sn Cu-Sn, Cu-Zn
CZTS	5.0 [237]	CuSO <sub>4</sub> , ZnSO <sub>4</sub> , SnCl <sub>2</sub> ; C <sub>6</sub> H <sub>5</sub> Na <sub>3</sub> O <sub>7</sub>	-	0.13 ASD	-	33	-	-	-
CZTS	- [238]	CuSO <sub>4</sub> , ZnSO <sub>4</sub> , SnCl <sub>2</sub> ; C <sub>6</sub> H <sub>5</sub> Na <sub>3</sub> O <sub>7</sub>	-	-1.21V <sup>b</sup>	-	30	-	1500	Cu <sub>6</sub> Sn <sub>5</sub> , CuZn
CZTSe	5.8 [239]	CuSO <sub>4</sub> , SnSO <sub>4</sub> , ZnSO <sub>4</sub> ; C <sub>4</sub> H <sub>6</sub> O <sub>6</sub> , C <sub>6</sub> H <sub>5</sub> Na <sub>3</sub> O <sub>7</sub> ; K <sub>2</sub> SO <sub>4</sub>	4.75	-1.9V <sup>c</sup>	25	-	2	1000- 5000	Sn Cu <sub>6,26</sub> Sn <sub>5</sub> or Cu <sub>6</sub> Sn <sub>5</sub> CuZn or Cu <sub>5</sub> Zn <sub>8</sub>
CZTSe	4.5 [240]	CuSO <sub>4</sub> , SnSO <sub>4</sub> , ZnSO <sub>4</sub> ; C <sub>6</sub> H <sub>8</sub> O <sub>7</sub> , C <sub>6</sub> H <sub>5</sub> Na <sub>3</sub> O <sub>7</sub>	6.6	-1.3V <sup>b</sup>	65	60	2×2	-	Cu, Sn CuZn, CuSn, Cu <sub>5</sub> Sn <sub>8</sub>
CZTS	3.6 [236]	Na <sub>4</sub> P <sub>2</sub> O <sub>7</sub>	-	-	-	20	10×10	600	-
CZTS	3.6 [241]	CuSO <sub>4</sub> , SnSO <sub>4</sub> , ZnSO <sub>4</sub> ; K <sub>2</sub> C <sub>4</sub> H <sub>4</sub> O <sub>6</sub> , C <sub>6</sub> H <sub>5</sub> Na <sub>3</sub> O <sub>7</sub>	6	-1.2V <sup>a</sup>	25	-	-	600	Sn Cu <sub>6</sub> Sn <sub>5</sub> , Cu <sub>5</sub> Zn <sub>8</sub>
CZTS	3.2 [235]	CuSO <sub>4</sub> , ZnSO <sub>4</sub> ; SnCl <sub>2</sub> ; C <sub>6</sub> H <sub>5</sub> Na <sub>3</sub> O <sub>7</sub>	-	-1.1~1.2V <sup>b</sup>	RT	20	2×2	1000	Cu, Sn, CuZn, Cu <sub>5</sub> Zn <sub>8</sub>
CZTS	2.9 [242]	CuSO <sub>4</sub> , SnSO <sub>4</sub> , ZnSO <sub>4</sub> ; C <sub>4</sub> H <sub>6</sub> O <sub>6</sub> /C <sub>6</sub> H <sub>5</sub> Na <sub>3</sub> O <sub>7</sub> /EDTA; HCl, lactic acid	4.75	-	RT	-	0.7	-	-
CZTS	2.7 [243]	CuCl <sub>2</sub> , SnCl <sub>4</sub> , ZnCl <sub>2</sub> ; C <sub>6</sub> H <sub>5</sub> Na <sub>3</sub> O <sub>7</sub> ; C <sub>4</sub> H <sub>6</sub> O <sub>6</sub>	4.5-5.5	-1.15V <sup>b</sup>	RT	45	2×2	-	-
CZTS	2.0 [244]	CuCl <sub>2</sub> , SnCl <sub>4</sub> , ZnCl <sub>2</sub> ; thiourea; lactic acid, NaOH	6	-0.3 to -1.2V <sup>b</sup>	RT	60	1.5	-	-
CZTSe	2.7 [245, 246]	CuSO <sub>4</sub> , SnSO <sub>4</sub> , ZnSO <sub>4</sub> ; C <sub>6</sub> H <sub>5</sub> Na <sub>3</sub> O <sub>7</sub> hydroquinone, H <sub>2</sub> SO <sub>4</sub>	5.5-6.0	-1.3V <sup>b</sup>	20	-	1×2.5	630	Sn, $\eta$ -Cu <sub>6,25</sub> Sn <sub>5</sub> , $\epsilon$ -CuZn <sub>5</sub>
CZTS	2.2 [247]	CuSO <sub>4</sub> , SnSO <sub>4</sub> , ZnSO <sub>4</sub> ; C <sub>6</sub> H <sub>5</sub> Na <sub>3</sub> O <sub>7</sub>	6.2	-1.25 <sup>b</sup>	26	10	2.2×2.2	830	Sn, Cu <sub>6</sub> Sn <sub>5</sub> , Cu <sub>5</sub> Zn <sub>8</sub>
CZTSe	1.7 [248]	CuSO <sub>4</sub> , SnSO <sub>4</sub> , ZnSO <sub>4</sub> ; C <sub>6</sub> H <sub>5</sub> Na <sub>3</sub> O <sub>7</sub>	-	-1.2~1.25V <sup>a</sup>	-	120	1	500	Zn, Sn, Cu <sub>6</sub> Sn <sub>5</sub> , CuZn <sub>2</sub>

Best results were obtained using metals sulfates and chlorides as metal source with complexing/buffering agents such as citrates (tri-sodium citrate C<sub>6</sub>H<sub>5</sub>Na<sub>3</sub>O<sub>7</sub>, citric acid C<sub>6</sub>H<sub>8</sub>O<sub>7</sub>) and tartrates (tartaric acid C<sub>4</sub>H<sub>6</sub>O<sub>6</sub>, potassium tartrate K<sub>2</sub>C<sub>4</sub>H<sub>4</sub>O<sub>6</sub>), as shown in Table II.2. Above



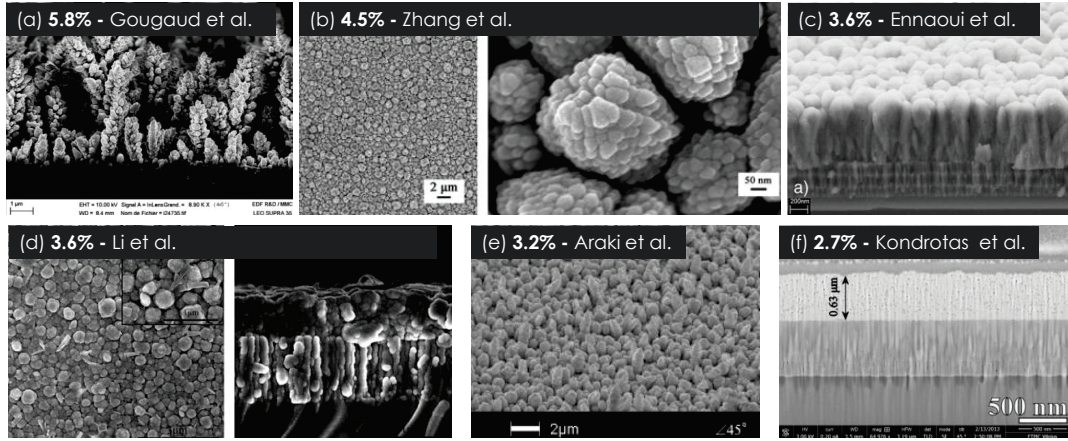


**Figure II.5:** SEM surface and cross-sectional images of Cu-Sn-Zn precursors produced by co-electrodeposition. (a) [239], (b) [240], (c) [236], (d) [241], (e) [235], (f) [245].

3% efficiencies were obtained in pioneering works [235,236]. In 2013 and 2014, remarkable efficiencies have been obtained by different groups: 4.5% [240], 5.8% [239], 8% [32] for CZTSe devices. Co-electrodeposition or electroless plating of Cu-Sn-Zn have also been reported by [249–254]. The depositions listed in Table II.2 are performed by potentiostatic method from diluted electrolytes at room temperature on small-scale substrates. Typical depositions rates are 5 – 50 nm/min, which is slow when compared with industrial standards. Moreover, many of the deposited alloys exhibited columnar structure and rough surface, as shown in Figure II.5, with the presence of dendrites in some cases.

### II.2.2.2 Cu-Zn-Sn-S or Cu-Zn-Sn-Se quaternary deposition route

The main advantage of this route is the inclusion of chalcogen in the precursor layer. Introduction of selenium or sulfur may alleviate the volume extension in the resultant film after chalcogenation. Nonetheless, even if the four elements which compose kesterite are present in the precursor layer, a further thermal treatment is always required in order to improve the crystal quality. Sodium thiosulfate or sodium sulfate is here used to release sulfur into the precursors [114,255–265]. 3.6% [264], 5.5% [260] and 7.1% [37] efficient CZTS devices were obtained but the solution is difficult to stabilize due to disproportionation reaction. Other sulfur sources such as thiourea [266] may be employed for CZTS quaternary deposition [267,268]. Concerning Cu-Zn-Sn-Se, Septina et al. used sodium selenite as selenium source [42,269–271] and reported a 1.1% device for the Cu-Sn-Zn-Se/Cu-Sn-Se stack [42].

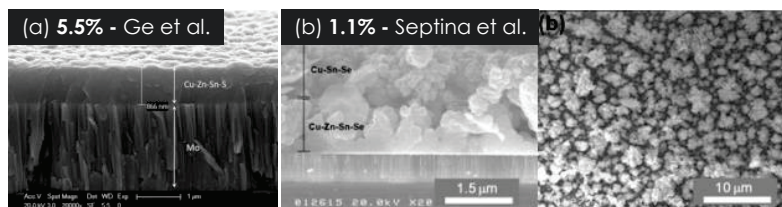


**Figure II.6:** SEM surface and cross-sectional images of Cu-Sn-Zn-S and Cu-Sn-Zn-Se precursors produced by quaternary electrodeposition. (a) [260], (b) [42].

The quaternary deposition method presents the same advantages (a single step process) and drawbacks (a fine tuning of the electrodeposition conditions is required) as the co-electrodeposition route, but with the additional issue of S or Se source stability in the electrolyte. Using potentiostatic conditions, the quaternary precursors are deposited at 20 – 45 nm/min. Usually morpholo-

**Table II.3:** Kesterite by Cu-Sn-Zn-S or Cu-Sn-Zn-Se quaternary electrodeposition. Potential is given <sup>a</sup> vs SCE; <sup>b</sup> vs Ag/AgCl; <sup>c</sup> vs MSE reference.

Material	$\eta$ %	Chemistry	pH	$E$	$T$ °C	$t$ min	$A$ cm <sup>2</sup>	$e$ nm	Phases
CZTS	7.1 [37]	CuSO <sub>4</sub> , ZnSO <sub>4</sub> , SnSO <sub>4</sub> ; C <sub>4</sub> H <sub>6</sub> O <sub>6</sub> , C <sub>6</sub> H <sub>5</sub> Na <sub>3</sub> O <sub>7</sub> Na <sub>2</sub> S <sub>2</sub> O <sub>3</sub>	-	-1.15V <sup>b</sup>	RT	30	3×2.5	-	-
CZTS	5.5 [260]	CuSO <sub>4</sub> , ZnSO <sub>4</sub> , SnSO <sub>4</sub> ; C <sub>6</sub> H <sub>5</sub> Na <sub>3</sub> O <sub>7</sub> Na <sub>2</sub> S <sub>2</sub> O <sub>3</sub>	5.9	-1.15V <sup>b</sup>	RT	30	4×5	870	-
CZTS	3.6 [264]	CuSO <sub>4</sub> , ZnSO <sub>4</sub> , SnSO <sub>4</sub> ; C <sub>6</sub> H <sub>5</sub> Na <sub>3</sub> O <sub>7</sub> , C <sub>4</sub> H <sub>4</sub> O <sub>6</sub> K <sub>2</sub> Na <sub>2</sub> S <sub>2</sub> O <sub>3</sub>	-	-1.1 and -1.15V <sup>b</sup>	-	20	2.5×2.5	-	-
CZTS	3.1 [272]	CuSO <sub>4</sub> , ZnSO <sub>4</sub> , SnSO <sub>4</sub> ; C <sub>6</sub> H <sub>5</sub> Na <sub>3</sub> O <sub>7</sub> , K <sub>2</sub> C <sub>4</sub> H <sub>4</sub> O <sub>6</sub> Na <sub>2</sub> S <sub>2</sub> O <sub>3</sub>	-	-1.15V <sup>b</sup>	-	30	-	675	CuZn <sub>5</sub> , Cu <sub>3</sub> Sn
CZTSe	1.1 [42]	CuSO <sub>4</sub> , ZnSO <sub>4</sub> , SnCl <sub>4</sub> ; lactic acid, NH <sub>3</sub> Na <sub>2</sub> Se <sub>2</sub> O <sub>3</sub>	2.5-2.6	-0.6V <sup>b</sup>	24	30	-	1300	-

gies are porous and dendritic, as shown in Figure II.6. Ge et al. managed the deposition of dense Cu-Sn-Zn-S layer, but its composition is Sn-rich, which is not the desired composition for optimal kesterite device performance (Cu-poor, Zn-rich, see *Introduction*).

### II.2.2.3 SEL route

The stacked elemental layers (SEL) approach has some advantages over co-deposition, including an easier precursor composition tuning by changing independently the charge flow in each electrodeposition step. Furthermore, SEL is highly compatible with industry because of electrolyte stability and the possibility to operate at much higher current densities since there is no need to balance the deposition rates of several metals at once.

**Table II.4:** Kesterite by stacked elemental layer approach

Material	$\eta$ %	Stack	$T$ °C	$t$ min	$A$ cm <sup>2</sup>	$e$ nm	Phases
CZTS	8.1 [159]	Cu/Sn/Zn	-	-	-	-	Cu, Sn, Zn
	8.0 [30]		-	-	-	1000	Cu, Sn, Zn
	5.6 [273]		25	-	-	-	Cu, Sn, Zn
CZTS	7.3 [29]	Cu/Sn/Zn; Cu/Zn/Sn	-	-	15×15	700	-
CZTSe	7.0 [31]		-	<1	15×15	125/180/125	-
CZTSe	5.9 [274]	Cu/Sn/Zn; Cu/Sn/Cu/Zn	RT	-	2.5×2.5	600	-
	5.5 [206]	Cu/Sn/Zn	-	-	2.5×2.5	-	-
	4.5 [275]	Cu/Sn/Zn; Cu/Sn/Cu/Zn	-	-	-	600	-
CZTSe	4.8 [48]	Cu/Sn/Zn	RT	<2	4×4	-	Cu, Sn, Zn
CZTS	3.4 [276]	Cu/Sn/Zn; Cu/Sn/Cu/Zn	-	-	2.5×2.5	-	-
	3.2 [223, 233]	Cu/Sn/Cu/Zn	-	-	2.5×2.5	600	Cu, Cu-Sn, Cu-Zn
	0.8 [231]	Cu/Sn/Zn	RT	-	2.5×1	1000	-
CZTSSe	3.6 [277]	Cu/Sn/Zn	-	3; 30; 4	-	-	-
CZTSS	1.7 [278]		-	3; 10; 8	-	-	-
CZTS	2.3 [279]	Cu/Sn/Cu/Zn	RT	-	2×2		
	2.2 [279]	Cu/Zn/Cu/Sn					
	2.1 [279]	Zn/Cu/Sn/Cu					
	2.0 [279]	Sn/Cu/Zn/Cu					
CZTS	1.0 [234]	Cu/Sn/Zn	-	-	-	-	-

There are some restrictions on the possible stacking orders when using electrodeposition methods to produce a layered precursor: the standard reduction potentials are very different (Fig. II.2 in page 34). For example, at the potential required to deposit Cu, a Zn deposit would be oxidized and stripped from the substrate. A logical deposition sequence for the stack would be from positive to increasingly negative standard redox potential, i.e. copper, then tin and then zinc. Altering this order could result in spontaneous dissolution of the underlying layer upon immersion in the deposition solution, which would make control of composition and uniformity difficult [223]. As expected, the best results were reported for Mo/Cu/Sn/Zn stacks, as shown in Table II.4. Mo/Cu/Sn/Cu/Zn stack were also reported by Scragg [233], Arasimowicz [275], where an intermediate Cu layer is added so as to improve Zn coverage. Recently, different stack orders were reported with intermediate Cu layers [279], but did not achieve more than 2.3% efficiency. Figure II.7 shows the morphology of some electrodeposited stacks. Generally, they exhibit more

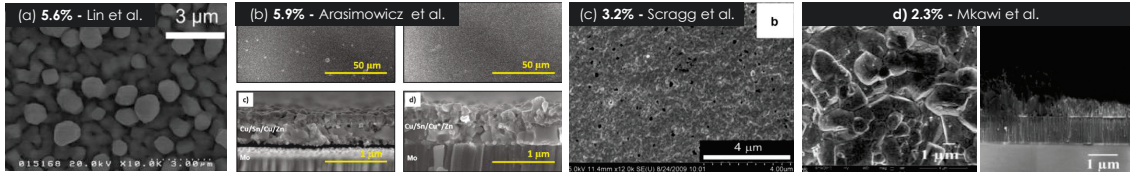


**Figure II.7:** SEM surface and cross-sectional images of electrodeposited Cu/Sn/Zn and Cu/Sn/Zn/Sn stacks. (a) [273], (b) [274], (c) [223], (d) [279].

compact structures than co-electrodeposited precursors. Other stack orders are also reported in literature such as Cu/Sn/Zn [252, 280–283]; Cu/Zn/Sn [283]; Sn/Cu/Zn [112]; Zn/Cu/Sn [284]; Cu/Sn/Zn/Cu, Cu/Zn/Cu/Sn [283] and Cu/Sn/Cu/Zn/Cu [285] without reported efficiency or for photoelectrode applications.

Mixed approaches involving stacked deposition of metals and alloys are also a possibility: Mo/Cu-Zn/Sn [286, 287], Mo/Cu-Zn/Cu-Sn [288, 289], Mo/Cu-Sn-Zn/Se [246]. Finally, ionic liquid solvents may be employed so as to avoid the water reduction issue [278, 290, 291]. A 3.6% device [277], also reported in Table II.4, was obtained with a stacked elemental approach including a hybrid electrodeposition process using both aqueous and ionic liquid solvents.

#### II.2.2.4 Comparison of kesterite electrodeposition routes

The advantages and drawbacks of the different ED precursor routes [18] are summarized in Table II.5. The advantage of the SEL approach over the metal and quaternary co-deposition approaches

**Table II.5:** Comparison of different ED routes vs specifications for thin films deposition.

Category	Cu-Sn-Zn alloy	Quaternary	SEL
<b>Chemistry</b>	- complex chemistry - stability issues	- very complex chemistry - no stable chalcogen source	+ independent, simpler electrolytes + stable electrolytes
<b>Process</b>	+ fast + single bath	- slow + single bath	++ faster - 3 steps
<b>Material</b>	- morphology issues - non-homogeneous on cm <sup>2</sup> - fine tuning of ED conditions necessary to control stoichiometry + Cu-Sn and Cu-Zn alloys	- morphology issues - non-homogeneous on cm <sup>2</sup> necessary to control stoichiometry + S or Se included	+ dense layers + uniform over large areas + easy control of stoichiometry + different stack orderings possible - 1 preferred stack order (Cu/Sn/Zn)

is that the deposition conditions and electrolyte can be tuned independently for each element. This allows uniform depositions on large areas, larger process windows, and higher process flexibility. Furthermore, the simpler chemistry of individual electrolytes allows for greater bath stability, easier maintenance, and hence better longevity. In this thesis, electrodeposition of kesterite precursors is performed by SEL route because of its high compatibility with industrial processes.

## II.2.3 Electrodeposition of Cu, Sn and Zn: an industrial approach

### II.2.3.1 Industry specifications

The industrial approach for the electrodeposition of a stacked Cu/Sn/Zn precursor presented in this thesis is based on the work of Fawaz et al. (NEXCIS internal report [292]). As electrodeposition is a widespread process with many applications, many different aqueous electrolyte chemistries are available commercially. The use of commercial solutions is preferred as they contain additive systems that allow to control very well the morphology, electrolyte stability and mechanical properties of the deposits. The role of the additives is described in Table II.1 page 36. Also commercial electrolyte pertain to a high range of concentration, limiting the mass-transport issues (reduced concentration overpotential). In this section different electrolytes 1) used in literature for kesterite electrodeposition or 2) available commercially will be presented. For industrial applications, the electrolytes should be compatible with the substrate, stable and with a long lifetime, allowing a room temperature process with high deposition rates. The electrolyte components should be cheap, abundant and non-toxic. The requirements for an industry-compatible electrodeposition process are listed in Table II.6.

**Table II.6:** Specifications for an industry-compatible electrodeposition process.

Category	Requirements
<i>Chemistry</i>	<ul style="list-style-type: none"> <li>• Compatibility with substrate (Mo on glass for CIGS or CZTS)</li> <li>• Abundant and cheap components (price &lt; 20 €/L)</li> <li>• Lifetime &gt; 1 year</li> <li>• Stable (+ 2000 m<sup>2</sup>/L)</li> <li>• Non toxic molecules</li> </ul>
<i>Process</i>	<ul style="list-style-type: none"> <li>• Ambient temperature 20 – 40 °C</li> <li>• Deposition rate &gt; 300 nm/min</li> <li>• Easy and fast constituents analysis (<math>t_{\text{analysis}} &lt; 1 \text{ h}</math>)</li> <li>• Easy bath replenishment (soluble anodes, pump dispenser)</li> </ul>
<i>Material</i>	<ul style="list-style-type: none"> <li>• Good adherence</li> <li>• No apparent defect (ex. nodules, stings)</li> <li>• Uniformity &lt; 5%</li> <li>• Low impurity content (&lt;10 ppm) for C, O, Fe, Mn, Cr, Ni, Al.</li> </ul>
<i>Environnement</i>	<ul style="list-style-type: none"> <li>• Rinse water waste management</li> </ul>

**Chemistry: safety considerations first** One of the most important criteria in an industrial environment concerns the safety. Their safety classifications, i.e. risk phrases which can be found in the material safety data sheet (MSDS) help to discriminate the toxic/dangerous components, A description of all the risk phrases is given in *Annex C*. Carcinogenic, mutagenic substances and compounds that are toxic for reproduction (CMR) substances should not be used. Electrolytes including carcinogenic, mutagenic and toxic for reproduction (CMR) compounds are directly eliminated. CMR compounds typically have risk phrases such as R45, R49 or R40 (carcinogenic), R46 or R68 (mutagenic) or R60, R61, R62 and R63 (reprotoxic)<sup>2</sup>. Cyanide electrolytes or other toxic components are also discarded.

<sup>2</sup>In 2015, the risk and safety statements will be replaced by hazard statements and precautionary statements in the course of harmonising classification, labelling and packaging of chemicals by introduction of the UN Globally Harmonized System of Classification and Labelling of Chemicals (GHS). The new hazard statements in use will be H340, H341 (mutagenic) H350, H351 (carcinogenic) and H360, H361, H362 (toxic for reproduction).

**Process** The electrodeposition process should be performed at room temperature with high deposition rates. Electrolytes that require to operate at high temperature will be discarded. Also, in order to deposit the metals at high speed, electrodeposition will be performed by the galvanostatic method (page 37) with appropriate current densities. The choice of electrolytes depends on their suitability for high-speed ED processes.

### II.2.3.2 Copper electrodeposition

The electrolytes used for Cu fall into two main categories: acid electrolytes, where  $\text{Cu}^{\text{II}}$  is thermodynamically stable, and alkaline electrolytes, which use strong complexing agents to stabilize  $\text{Cu}^{\text{II}}$  and avoid the precipitation of the copper hydroxide  $\text{Cu}(\text{OH})_2(\text{s})$  [293]. Cu electrolytes used for depositing a precursor of kesterite are detailed in Table II.7.

**Table II.7:** Copper deposition parameters for kesterite fabrication by the SEL approach.

Potential  $E$  is given <sup>a</sup> vs SCE; <sup>b</sup> vs Ag/AgCl; <sup>c</sup> vs MSE reference.

Current density  $J$  is given in  $\text{A}/\text{dm}^2(\text{ASD})$ .

Material	Efficiency and Ref. %	Components	pH	$E$ or $J$	$T$ °C	$t$ min	$A$ $\text{cm}^2$
CZTS	8.1 [159]; 8.0 [30]; 5.6 [273]	$\text{CuSO}_4$ $\text{C}_6\text{H}_5\text{Na}_3\text{O}_7$ , $\text{C}_6\text{H}_8\text{O}_7$	-	-0.4V <sup>b</sup>	25	-	-
CZTS ; CZTSe	7.3 [29]; 7.0 [31]	$\text{CuSO}_4$ $\text{H}_2\text{SO}_4$ , additives, HCl	-	1 ASD	-	<1	$15 \times 15$
CZTSe; CZTS	5.9 [274]; 5.5 [206]; 3.2 [233]	$\text{CuSO}_4$ NaOH, sorbitol, Empigen BB	-	-1.07 [206], -1.08V <sup>a</sup> [274]; -1.2V <sup>b</sup> [233]	RT	-	$2.5 \times 2.5$
CZTSe	4.8 [48]	$\text{CuSO}_4$	-	5 ASD	RT	<2	$4 \times 4$
CZTSSe	3.6 [290, 294]	$\text{CuSO}_4$	-	0.82 ASD	RT	<3	64
CZTSS	1.7 [278]	-	-	0.42 ASD	-	3	-
CZTS	2.3 [279]	$\text{CuCl}_2$ NaOH, sorbitol	-	-0.9, 1.2V <sup>b</sup>	RT	12-28	$2 \times 2$
CZTS	1.0 [234]	$\text{CuSO}_4$ $\text{H}_2\text{SO}_4$	-	1.5 ASD	-	-	$2.5 \times 2.5$
CZTS	0.8 [231]	$\text{CuCl}_2$ NaOH, sorbitol	-	-1.14V <sup>b</sup>	RT	-	$2.5 \times 1$

The most common electrolytes for copper electrodeposition are acidic copper sulfate solutions. In these acid solutions, the addition of sulfuric acid improves the conductivity of the solution and prevents the precipitation of basic salts. However, in acidic aqueous electrodeposition conditions, the Mo working electrode substrate initially dissolves as  $\text{Mo}^{3+}$  before being passivated by a layer of  $\text{MoO}_2$  or  $\text{MoO}_3$  in presence of oxygen, preventing effective nucleation of the metals [282]. The choice of Mo-coated soda-lime glass is explained by its use as ohmic back contact in CIGS, where the formation of a thin layer of  $\text{Mo}(\text{S,Se})_2$  enhances the device performance. Different approaches have been considered in order to avoid the formation of the Mo oxides passivation layer during the electrodeposition process.

- Chemistry: the use of additives such as citrate and tartrate (mild acid conditions) allow to remove the surface oxides by complexing  $\text{Mo}^{3+}$  and prevent further oxidation [30, 273, 281]. In alkaline electrolytes, soluble molybdate ions  $\text{MoO}_4^{2-}$  and  $\text{HMoO}_4^-$  are formed [223, 282], which do not passivate Mo.
- Substrate: a coating with a very thin Pd interlayer using a solution containing  $\text{PdCl}_2$  [280, 295] can protect the substrate and allow an efficient deposition. However, the effects of Pd on the resulting absorber layer properties are still unknown, and palladium is expensive (more than 26000 dollars per kilogram [8]). The Mo layer can also be protected by using an intermediate metal seed layer (typically less than  $0.1 \mu\text{m}$  thick) between the substrate and the deposit, which can be deposited by electrodeposition or physical vapor deposition (PVD) methods.

Many groups used alkaline electrolytes [206, 233, 274, 279]. A first route is based on cyanide as complexing agent [284], which is very effective and produces high-quality deposits but it is obvious that the cyanide toxicity is a considerable disadvantage. Safer cyanide-free routes require the addition of strong complexing agents in the electrolyte to stabilize  $\text{Cu}^{\text{II}}$  ions [293]. For instance, Scragg et al. used sorbitol as a complexant [231–233], based on a bath developed by Barbosa et al [296] with a quaternary ammonium surfactant to reduce the roughness of the layers [233].

In this thesis, in order to avoid the Mo oxidation issue, a thin copper seed layer is deposited over the molybdenum substrate by sputtering, as represented in Figure II.8.

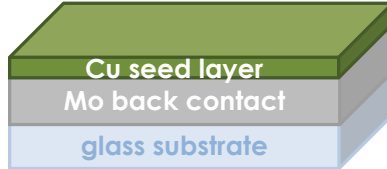


**Figure II.8:** Schema of Cu seed layer, previously deposited by PVD, allowing to avoid Mo substrate compatibility issues [297].

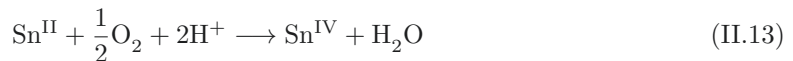
Therefore, with the seed layer, a stable acid copper sulfate chemistry can be used for copper electrodeposition. One should note that copper depositions performed by the galvanostatic method (applying direct current) are realized very quickly (less than a few minutes, at deposition rates of 100 – 450 nm/min [29, 31, 278, 290, 294]) on quite large substrates, showing a great compatibility with industrial processes. In this work, the electrodeposition is also performed applying direct current. The Microfab SC acid copper plating (Enthone Inc.), especially designed for semiconductor applications, and its components are summarized in Figure II.8. No CMR or toxic component is present in this electrolyte. It allows the electrodeposition of copper layers at room temperature with current densities enabling a high-speed process. This Microfab SC acid copper electrolyte is also used for the electrodeposition of copper layers in CIGS’s precursors at NEXCIS, demonstrating a high compatibility with an industrial process at  $60 \times 120 \text{ cm}^2$  scale.

**Table II.8:** ENTHONE’s copper commercial chemistry used in this thesis.

Type and name	Component name (Products)	Safety classification	Operation
<b>Acid copper sulfate</b> <i>Microfab SC</i>	Make-up (Copper sulfate; Sulfuric acid)	R35, R51/53	21 – 27 °C
	Sulfuric acid	R35	1.0 – 2.5 ASD
	Hydrochloric acid	R34, R37	
	Additive MD	R35	
	Additive LO	None	

### II.2.3.3 Tin electrodeposition

The electrodeposition of Sn can be realized both with acidic and alkaline electrolytes. Table II.9 describes the Sn electrolytes used for kesterite precursor deposition in literature. As Sn standard potential is negative (Figure II.2 page 34), tin electroplating is accompanied by hydrogen gas evolution and, in acid electrolytes, by stannous reduction [298]. Indeed, the standard reduction potential  $E^\circ(\text{Sn}^{4+}/\text{Sn}^{2+})$  is higher than  $E^\circ(\text{Sn}^{2+}/\text{Sn})$ , favoring the oxidation of  $\text{Sn}^{\text{II}}$  in tin acidic baths to stannic  $\text{Sn}^{\text{IV}}$  [299]. This reaction is spontaneous, and will occur if there is any dissolved oxygen present in the bath, which is the case if the bath surface is exposed to air.



Oxidation of  $\text{Sn}^{\text{II}}$  may also occur by the contamination of  $\text{Cu}^{\text{II}}$  ions [300, 301] due to the difference between their standard reduction potentials. Therefore, in tin acid electrolytes (fluoroboric acid,

sulfates, chlorides, methanesulfonic acid), additives must be employed in order to inhibit  $\text{Sn}^{\text{IV}}$  formation, to suppress hydrogen gas evolution, and to obtain significantly smoother and denser tin coatings [298, 302–304]. In alkaline baths, where Sn ions are complexed under stannate form  $[\text{Sn}(\text{OH})_6]^{2-}$ , no additives are needed to inhibit  $\text{Sn}^{\text{IV}}$  formation because the deposition is done at very negative potentials, and the parallel hydrogen evolution is sufficient to prevent  $\text{Sn}^{\text{II}}$  oxidation. However, the hydrogen may diffuse inside the deposited tin layer, making it brittle. Sorbitol can be added to alkaline Sn in order to improve layer stability and adhesion [231, 279], but methanesulfonic acid ( $\text{CH}_3\text{SO}_3\text{H}$ ) has shown to allow a better coverage of the deposit [232].

**Table II.9:** Tin electrodeposition parameters for kesterite fabrication by the SEL approach.

Potential  $E$  is given <sup>a</sup> vs SCE; <sup>b</sup> vs Ag/AgCl; <sup>c</sup> vs MSE reference.

Current density  $J$  is given in  $\text{A}/\text{dm}^2$ (ASD).

Material	Efficiency and Ref. %	Components	pH	$E$ or $J$	$T$ °C	$t$ min	$A$ $\text{cm}^2$
CZTS	8.1 [159]; 8.0 [30]; 5.6 [273]	$\text{Sn}(\text{SO}_3\text{CH}_3)_2$ $\text{CH}_3\text{SO}_3\text{H}$ ; Empigen BB	-	-0.54,-0.55V <sup>b</sup>	25	-	-
CZTS	7.3 [29]	Technistan 89 RTU (Technic Inc.)	-	2 ASD	-	<1	15×15
CZTSe	7.0 [31]	Microfab 300 MU (Enthone Inc.)	-	1 ASD	-	<1	15×15
CZTSe; CZTS	5.9 [274]; 5.5 [206]; 3.2 [233]	$\text{Sn}(\text{SO}_3\text{CH}_3)_2$ $\text{CH}_3\text{SO}_3\text{H}$ ; Empigen BB	-	-0.75V <sup>b</sup> [206]; -0.64V <sup>b</sup> [274]; -0.72V <sup>b</sup> [233]	RT	-	2.5×2.5
CZTSe	4.8 [48]	$\text{Sn}(\text{SO}_3\text{CH}_3)_2$ $\text{CH}_3\text{SO}_3\text{H}$ ; RX-851 (Rongxing Electronics)	-	0.3 ASD	RT	<2	4×4
CZTSSe	3.6 [290]	ionic liquid	-	0.045 ASD	-	30	-
CZTSS	1.7 [278]	ionic liquid	-	0.2 ASD	-	10	-
CZTS	2.3 [279]	$\text{SnCl}_2$ NaOH, sorbitol	-	-0.7V <sup>b</sup>	RT	17-26	2×2
CZTS	1.0 [234]	$\text{SnSO}_4$ $\text{H}_2\text{SO}_4$ , additive	-	1.5 ASD	-	-	2.5×2.5
CZTS	0.8 [231]	$\text{SnCl}_2$ NaOH, sorbitol	-	-1.21V <sup>b</sup>	RT	-	2.5×1

In literature (Table II.9), methanesulfonic acid-based electrolytes are commonly used and are able to stabilize  $\text{Sn}^{\text{II}}$  over a wide pH range [30, 206, 233, 273, 274]. However methanesulfonic acid is toxic (risk sentences: R21/22, R34, and classified “Accute Toxicity” in the new UNGHS system) so safer electrolytes are preferable for an industrial process. In various electrolytes used in literature (Table II.9), surfactants such as Empigen BB are also added to improve the surface morphology of the deposits [233]. Finally Sn has been deposited at a high plating rate (600 nm/min [31]) with commercial electrolytes using direct current, while potentiostatic Sn depositions have been performed at slower rates. Table II.10 summarizes different commercially available tin electrolyte chemistries and their components.

**Table II.10:** Comparison of different ENTHONE’s commercial Sn chemistries (from Fawaz et al.’s work [292]).

Type and name	Component name (Products)	Safety classification	$T$ (°C), $J$ (ASD), rate
<b>Acid tin sulfate</b> <i>Stannostar GSB</i>	Tin sulfate	R48/22, R36/37/38, R43, R50	15 – 28 °C
	Sulfuric acid	R35	0.5 – 2.0 ASD
	GSB Make-up (Methacrylic acid; QACs)	R34	1 $\mu\text{m}/\text{min}$ (at 2 ASD)
	GSB Brightener (Methacrylic acid; 1,4-dihydroxybenzene)	R36/37/38, R40, R68	
	Additive N (Unknown)	-	
<b>Acid tin sulfate</b> <i>Stannostar GSB 3</i>	Tin sulfate	R48/22, R36/37/38, R43, R50	18 – 25 °C
	Sulfuric acid	R35	0.5 – 2.0 ASD
	GSB-3 Carrier (Methacrylic acid)	R36/37/38	1 $\mu\text{m}/\text{min}$ (at 2 ASD)
	GSB-3 Brightener (Propane-2-ol; 4-Phenyl-3-buten-2-one)	R1/R36/R43/R67	
	A9 (Glutaral)	R20/22, R41, R37/38, R42/43	
<b>Acid tin sulfate</b> <i>Stannostar GSM</i>	Tin sulfate	R48/22, R36/37/38, R43, R50	15 – 30 °C
	Sulfuric acid	R35	0.5 – 2.0 ASD
	GSM Smoothing agent (Unknown)	-	1 $\mu\text{m}/\text{min}$ (at 2 ASD)

Most of the acid chemistries are eliminated because they include a toxic component: 1,4-dihydroxybenzene (highlighted in red) is a **CMR** compound, and glutaral (in orange) is toxic. The only remaining electrolyte is Stannostar GSM, a commercial acid tin sulfate chemistry, which contains tin sulfate, sulfuric acid and an additive. Sn deposition with Stannostar GSM can be performed at room temperature and appropriate current densities (0.5 – 2.0 ampere per square decimeter (**ASD**)), enabling a high deposition rate of the tin layer.

### II.2.3.4 Zinc electrodeposition

Zinc has a standard reversible potential of -0.76 V versus normal hydrogen electrode (**NHE**), as shown in Figure II.2. Whatever the pH, the zinc electrode potential is always more negative than hydrogen. Consequently hydrogen evolution occurs at the cathode as a competitor to zinc deposition, resulting in a decrease of current efficiency and eventually in some atomic hydrogen diffusion into the substrate [305]. In the 1970s most commercial zinc plating was done in conventional cyanide baths, but the strong international effort to lower pollution emissions has led to the development of other processes. Today alkaline noncyanide and acid chloride baths comprise most of the production. Zincate baths, with good hydrodynamic control and appropriate additives (carriers and brighteners, for instance quaternary ammonium compounds [306]) are now a highly successful process [305, 307]. In kesterite literature, the most used electrolytes are acid sulfate, chloride and methanesulfonic, as described in Table II.11. In order to avoid changes of pH at the electrode surface (due to consumption of  $H^+$  by the hydrogen evolution reaction), a pH buffer is often used [30, 233, 273]. Additives are always used to control the morphology and help reduce hydrogen evolution. Nucleation of Zn on Sn is critical; therefore, the uniformity of the Zn film is highly dependent on the uniformity of the underlying Sn.

**Table II.11:** Zinc deposition parameters for kesterite fabrication by the SEL approach.

Potential  $E$  is given <sup>a</sup> vs **SCE**; <sup>b</sup> vs **Ag/AgCl**; <sup>c</sup> vs **MSE** reference.

Current density  $J$  is given in  $A/dm^2$ (**ASD**).

Material	Efficiency and Ref. %	Components	pH	$E$ or $J$	$T$ °C	$t$ min	$A$ $cm^2$
CZTS	8.1 [159]; 8.0 [30]; 5.6 [273]	ZnSO <sub>4</sub> K <sub>2</sub> SO <sub>4</sub> ; Hydron buffer	3	-1.2V <sup>b</sup>	25	-	-
CZTS	7.3 [29]	ZnSO <sub>4</sub> , CH <sub>3</sub> SO <sub>3</sub> H	2.0	1 ASD	-	<1	15×15
CZTSe	7.0 [31]	ZnSO <sub>4</sub> , CH <sub>3</sub> SO <sub>3</sub> H	2.0-2.3	2 ASD	-	<1	15×15
CZTSe	5.9 [274]; 5.5 [206];	ZnCl <sub>2</sub> KCl, Hydron buffer, additive	3	-1.15V <sup>b</sup> [206]; -1.23V <sup>b</sup> [274];	RT	-	2.5×2.5
CZTS	3.2 [233]	ZnSO <sub>4</sub> K <sub>2</sub> SO <sub>4</sub> , hydron buffer	3	-1.2V <sup>b</sup>	-	-	-
CZTSe	4.8 [48]	ZnSO <sub>4</sub> CH <sub>3</sub> SO <sub>3</sub> H, NaOH	2	2 ASD	RT	<2	4×4
CZTSSe	3.6 [290]	-	-	0.18 ASD	-	4	-
CZTSS	1.7 [278]	ionic liquid	-	0.17 ASD	-	8	-
CZTS	2.3 [279]	ZnCl <sub>2</sub> KCl, Hydron buffer	3	-0.9V <sup>b</sup>	RT	14-32	2×2
CZTS	1.0 [234]	ZnSO <sub>4</sub>	-	1.5 ASD	-	-	2.5×2.5
CZTS	0.8 [231]	ZnCl <sub>2</sub> hydron buffer	3	-1.20V <sup>b</sup>	RT	-	2.5×1

For the electrodeposition of Zn in this work, similarly to Cu and Sn electrolytes, a commercial electrolyte is used. Table II.12 summarizes different commercially available zinc electrolytes chemistries and their components.

Electrolytes containing toxic elements such as boric acid are discarded. There are only few remaining electrolytes: an acid zinc chloride (Enthobrite CLZ-973) and two alkaline zinc (Enthobrite NCZ-Dimension K and 5001). Fawaz et al. [292] tried different electrolytes and selected the one which showed experimentally more compatibility with the underlying layers. Therefore, they se-



**Table II.12:** Comparison of different ENTHONE’s commercial Zn chemistries (from Fawaz et al. [292]’s work).

Type and name	Component name (Products)	Safety classification	Operation
<b>Acid zinc chloride</b> <i>Enthobrite CLZ 950</i>	Zinc chloride	R22, R34, R50/53	20 – 45 °C
	<b>Boric acid</b>	<b>R60, R61</b>	0.5-4 ASD
	A (Ethoxylated alkyl alcohol)	R22, R41	
	B (1-methoxy-2-propanol, 4-Phenyl-3-buten-2-one)	R43, R67	
	Potassium chloride	-	
<b>Acid zinc chloride</b> <i>Enthobrite CLZ-973</i>	Ammonium chloride	R22, R36	
	A (Thiodiglycol ethoxylate, Poly(oxy-1,2-ethanediyl))	-	
	B (2-chlorobenzaldehyde, Sodium salt)	R34	
<b>Alkaline zinc</b> <i>Enthobrite NCZ-Dimension K</i>	Zincate solution (Sodium hydroxide, Zinc oxide)	R35, R50/53	25 – 45 °C
	A (Unknown)	-	1.0 – 5 ASD
	B (Sodium metabisulfite)	R36, R43, R31	
	C (Unknown)	-	
	Conditioner (Silicic acid, sodium salt)	R41, R36/37/38	
<b>Alkaline zinc</b> <i>Enthobrite NCZ 5001</i>	A (Unknown)	-	20 – 42 °C
	B (Unknown)	R31	2.0 – 4.0 ASD
	C ( <b>Thiourea</b> )-optional component	<b>R40, R63</b>	
	Conditioner (Silicic acid, sodium salt)	R41, R36/37/38	

lected the Enthobrite NCZ 5001, one of the alkaline zinc chemistry, as the additive C is not necessary.

### II.2.3.5 Summary: choice of electrolytes

The chemistries that have been chosen for the electrodeposition of kesterite precursors have a limited toxicity, are able to be operated at room temperature, and available commercially. Electrodeposition with these chemistries can be performed at high speed rate with direct current. These criteria fulfill the main industry’s safety and process requirements. Another criteria of great importance — for the future deployment of this technology — is the price. The selected electrolytes, their composition, and the components respective prices are summarized in Table II.13.

**Table II.13:** Summary: selected electrolytes, composition and price.

The cost by electrodeposited m<sup>2</sup> is estimated by taking into account metal and of additives consumption. Metal consumption is assumed to correspond to the deposition of 170 nm of Cu, 210 nm of Sn and 150 nm of Zn. Additives consumption is assumed in L by A.h according to the replenishment procedure described in Experimentals section.

Electrolyte	Composition and required concentration	Component price	Electrolyte price per L	Cost by deposited m <sup>2</sup>
<b>Acid Copper Sulfate</b> <i>Microfab SC</i>	Make-up (CuSO <sub>4</sub> , Cu: 27 – 30 g/L; H <sub>2</sub> SO <sub>4</sub> : 150 – 170 g/L)	34 €/L	34.8 €	2.17 €
	Additives (MD: 6 – 9 mL/L; LO: 1 – 4 mL/L)	120 €/L		
<b>Acid Tin Sulfate</b> <i>Stannostar GSM</i>	SnSO <sub>4</sub> , Sn: 20 – 25 g/L	32.6 €/kg	1.6 €	0.12 €
	H <sub>2</sub> SO <sub>4</sub> : 155 – 175 g/L			
	Additive GSM smoothing agent: 30 mL/L	28.4 €/L		
<b>Alkaline Zinc</b> <i>Enthobrite NCZ 5001</i>	Zincate solution (Zn(OH) <sub>4</sub> <sup>2-</sup> , Zn: 12 – 20 g/L)	3.4 €/L	1.3 €	0.23 €
	NaOH			
	Additive A: 8 – 15 mL/L	9.0 €/L		
	Additive B: 0.25 – 2 mL/L	4.3 €/L		

Copper, tin and zinc metals prices, as already discussed in the *Introduction*, are low compared to indium and gallium prices used in CIGS, so the copper-, tin- and zinc- based electrolytes prices are expected to be quite low. Between the three electrolytes, the copper chemistry used at Nexcis is the most expensive one, because of the high purity of its components which is necessary for semiconductor applications. Tin and zinc electrolytes are cheaper, with prices around 1 – 2 €/L, respectively. Electrolyte consumption (metal, additives) cost has been estimated in Table II.13. For each electrodeposited square meter, approximately 2 € is consumed in Cu deposition while

less than 0.4 € is used for Sn and Zn deposition. A low price is of great importance for low-cost fabrication of kesterite precursors. The electrolytes, which seem to respond to most of the chemistry and process requirements, also need to be adequate for the desired electrodeposited material properties.

### II.2.4 Desired precursor properties for high-efficient kesterite devices

What characterizes a “good” precursor layer may be the subject of discussions. However, there is a common accord concerning several criteria: the deposited layers should present a good adherence to the underlying layers, no apparent defects in the layer, uniform morphologies and compositions over the substrate area, and provide an accurately controllable thickness and composition. More requirements are discussed in detail in the following.

**Uniformity** The deposited films need to be uniform at both microscopic and macroscopic scale in order to have a constant composition at all points. If microscopic non-uniformities are present in the precursor layer, there will be local composition variations in the resulting CZT(S,Se) absorber film, and macroscopic non-uniformities will lead to a compositional gradient across the film area (See page 37).

**Composition** It is well known that the best kesterite device efficiencies are obtained for copper-poor, zinc-rich metal composition (see *Introduction* [6, 10, 177, 179]). The metal composition is determined by the precursor composition — and to a lesser extend, by the undesired metal losses during the annealing step — so the typical precursor composition is copper-poor, zinc-rich compared to kesterite stoichiometry. This composition range is often exprimed in terms of ratios between the metallic elements i.e.  $Cu/(Zn+Sn)<1$  and  $Zn/Sn>1$ . With the stacked layers approach, the composition of the precursor layer is adjusted by varying the thickness of each individual metal layer. As seen on page 33, equation II.3, the thickness of an electrodeposited layer depends on the duration of the deposition step. By adjusting this duration, the desired stoichiometry is obtained. The metal ratios are calculated by the following equations (assuming 100% current efficiency):

$$\frac{Cu}{Sn + Zn} = \frac{\rho_{Cu}e_{Cu}}{M_{Cu}} \times \frac{M_{Sn}M_{Zn}}{\rho_{Sn}e_{Sn}M_{Zn} + \rho_{Zn}e_{Zn}M_{Sn}} \quad (\text{II.14})$$

and

$$\frac{Zn}{Sn} = \frac{\rho_{Zn}e_{Zn}}{M_{Zn}} \times \frac{M_{Sn}}{\rho_{Sn}e_{Sn}} \quad (\text{II.15})$$

where  $\rho_{Cu}$ ,  $\rho_{Sn}$ ,  $\rho_{Zn}$  are the densities ( $\text{g}/\text{m}^3$ ) of copper, tin and zinc materials, respectively,  $M_{Cu}$ ,  $M_{Sn}$ ,  $M_{Zn}$  the molar masses in  $\text{g}/\text{mol}$ , and  $e_{Cu}$ ,  $e_{Sn}$ ,  $e_{Zn}$  the respective thicknesses of copper, tin and zinc layer. Reversely, the desired thicknesses can be calculated from the metal ratios and precursor total thickness.

**Thickness** During the chalcogenation step, the precursor undergoes a volume expansion which is related to the insertion of S and/or Se in the lattice.



**Figure II.9:** Schematic illustration (cross-section) of volume expansion.

In the case of sulfurization, the volume of the absorber layer is reported to be about 2 [308], 2.7 [223], 3 [29], up to 4 [191] times the original thickness of the stacked metallic precursor film

because the densities of the films may vary. A similar or higher expansion volume is expected for selenization, as the Se atom is bigger than the S atom. In order to have a 2 – 3  $\mu\text{m}$  thick absorber layer, the typical thickness for the higher efficient kesterite devices, the precursor’s total thickness should be below one  $\mu\text{m}$ . Thicknesses of several precursors are reported in Tables II.2 and II.4, and are generally below one micron. As a result of the large volume expansion that occurs during chalcogenation, surfaces of the absorber layer obtained from an electrodeposited precursor are reported to be rough [31].

**Phases and structure** A low-temperature annealing — also called soft-annealing — can be performed with electrodeposited precursors in order to:

- Improve the intermixing of the elements by alloying [29] or artificially accelerate the naturally occurring elemental alloying [18];
- Improve the morphology: compactness, homogeneity and adhesion of the resulting kesterite film to the Mo layer [273], smoothness of the kesterite surface [30], or promoted recrystallization of the grains [251];
- Reduce the oxides to their metallic forms when performed  $\text{H}_2$  atmosphere [245].

The low-temperature annealing may also “dry” the electrodeposited precursor from remaining water or organic components, similarly to other solution-deposited precursors [17], and therefore avoid the apparition of cracks during the high-temperature annealing. High efficient devices produced by electrodeposition methods often include a low-temperature annealing, as shown in table II.14. Soft-annealing treatment is also reported for alloying of sputtered precursors (at 350°C [309]).

**Table II.14:** Low temperature thermal treatments in literature

Material	Efficiency %	Precursor type	$T$ °C	$t$ min	Conditions	Phases
CZTS	8.1 [159]	Cu/Sn/Zn	310	20-200	Evacuated	$\text{Cu}_6\text{Sn}_5$ , $\text{Cu}_5\text{Zn}_8$ , Sn, Zn
CZTS	8.0 [30]		310	40-150	ampoule	$\text{Cu}_6\text{Sn}_5$ , CuZn, $\text{Cu}_5\text{Sn}_8$
CZTS	5.6 [273]		350	20-60		$\text{Cu}_6\text{Sn}_5$ , $\text{Cu}_5\text{Zn}_8$ , $\text{Cu}_3\text{Sn}$
CZTS	7.3 [29]	Cu/Sn/Zn, Cu/Zn/Sn	210-350	30	$\text{N}_2$	Cu-Sn, Cu-Zn
CZTSe	7.0 [31]		360	30		Cu-Zn, Cu-Sn
CZTSe	5.9 [274]	Cu/Sn/Zn; Cu/Sn/Cu/Zn	350	30	$\text{N}_2$ in RTP	$\text{Cu}_6\text{Sn}_5$ , $\text{Cu}_5\text{Zn}_8$ , Cu, Sn
CZTSe	4.5 [275, 310]					$\text{Cu}_6\text{Sn}_5$ , $\text{Cu}_5\text{Zn}_8$
CZTSe	4.8 [48]	Cu/Sn/Zn	250	25	inert, 1 bar	$\text{Cu}_6\text{Sn}_5$ , $\text{Cu}_5\text{Zn}_8$
CZTSe	2.7 [245]	Cu-Sn-Zn	200; 350	60	Ar; $\text{H}_2$ ; Ar + $\text{H}_2$	$\text{Cu}_{6.25}\text{Sn}_5$ , $\text{Cu}_5\text{Zn}_8$
CZTS	- [251]	Cu-Sn-Zn	250-350	60	Ar	$\text{Cu}_6\text{Sn}_5$ , $\text{Cu}_5\text{Zn}_8$

Typically, the as-electrodeposited precursors include Sn elemental phase along with Cu-Sn and Cu-Zn alloys, but also Cu and Zn elemental phases, as reported in Tables II.2 and II.4. Cu-Sn alloys include  $\eta$ - $\text{Cu}_6\text{Sn}_5$ ,  $\eta'$ - $\text{Cu}_{6.25}\text{Sn}_5$ ,  $\varepsilon$ -(Cu-Sn) phases, which are the stable alloys reported to form at room-temperature according to the Cu-Sn phase diagram [311]. Cu-Zn alloys include  $\gamma$ - $\text{Cu}_5\text{Zn}_8$ ,  $\beta'$ -(Cu-Zn),  $\text{CuZn}_2$ ,  $\varepsilon$ - $\text{CuZn}_5$  which is in accordance with the Cu-Zn phase diagram. No alloy between Sn and Zn is reported, as predicted by the Cu-Sn-Zn ternary diagram [312, 313]. The phases and structure depend on the precursor composition and thickness. A short thermal treatment at 200 – 350 °C is sufficient to alloy the stacked precursor. After thermal treatment,  $\eta$ - $\text{Cu}_6\text{Sn}_5$ ,  $\eta'$ - $\text{Cu}_{6.25}\text{Sn}_5$ ,  $\gamma$ - $\text{Cu}_5\text{Zn}_8$  alloys are the most frequently reported alloys, along with elemental Sn. Zn elemental phase totally disappears. Alloying presents the possibility of mixing Zn and Sn intimately while both elements are segregated from one another if no alloying step is introduced [310]. The different precursor microstructures observed after a 300 °C soft annealing step are shown in Figure II.10 [274, 275].

In comparison, alloyed precursors in reference [29] show a columnar microstructure, while alloyed precursors in reference [31] exhibit a matrix microstructure. Alloying of Cu/Sn/Zn precursors is

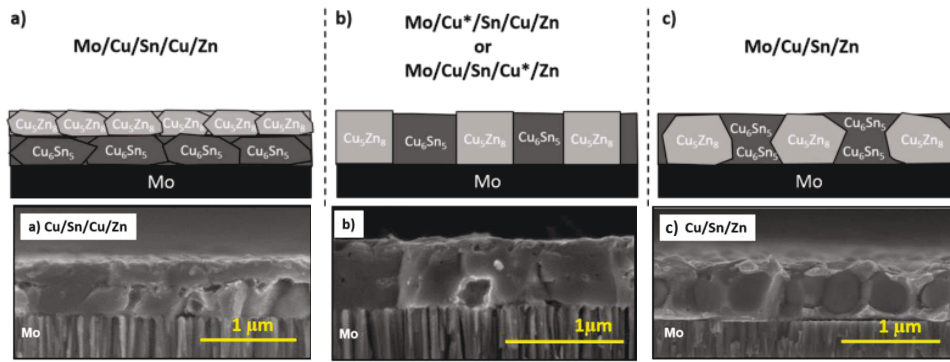


**Figure II.10:** Three types of microstructure developed after low-temperature annealing of electrodeposited Cu-Sn-Zn stacks: (a) bi-layered, (b) columnar and (c) matrix, courtesy of Arasimowicz's PhD thesis [274].

the preferred route for obtaining high-efficient kesterite devices.

## II.3 Experimentals

The methodology described in this section is extracted from Fawaz et al.'s work and results [292]. An overview of the electrodeposition process flow is presented in Figure II.11.

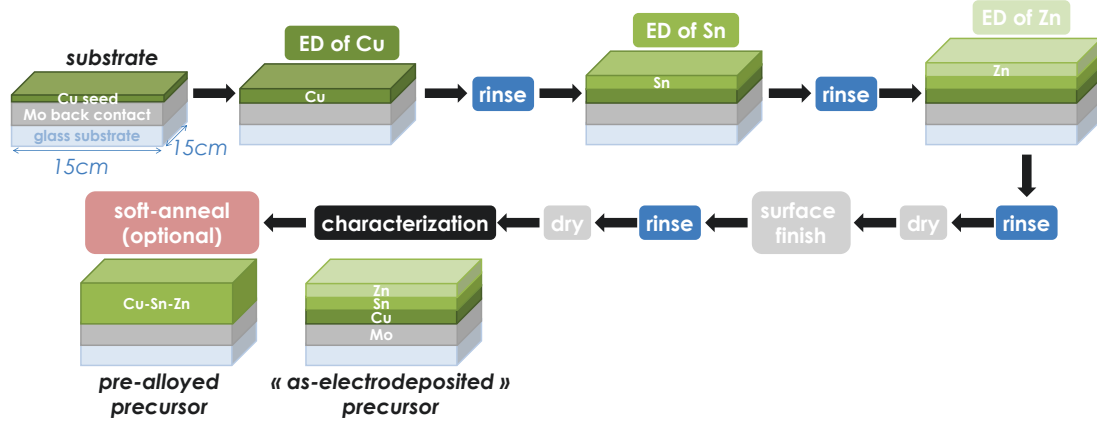


Figure II.11: Overview of the electrodeposition sequence.

### II.3.1 Substrates

The substrates used in this investigation are standard molybdenum-coated soda lime glasses (SLG/Mo) of dimension  $30 \times 60 \text{ cm}^2$  or  $60 \times 120 \text{ cm}^2$ . The Mo-coated 3 mm thick glass substrates, prepared by NEXCIS, are also used in NEXCIS CIGS modules production line. 600 nm thick Mo layers are deposited by sputtering. The substrates also contain a Cu seed layer of 80 nm thickness [297]. After sputtering, the substrates are stored in inert atmosphere in order to minimize the formation of oxides at the surface. The substrates are cut to  $15 \times 15 \text{ cm}^2$  or smaller size for electrodeposition.

### II.3.2 Chemistry

#### II.3.2.1 Electrolyte composition

The metal stacks of Cu, Sn and Zn are electroplated from selected commercial electrolytes. Their composition is detailed in Table II.15.

Table II.15: Initial electrolyte composition

Metal	pH	Metal salt	Electrolyte	Additives
Copper	acid (0.5)	$\text{CuSO}_4$ , Cu: 27 – 30 g/L	$\text{H}_2\text{SO}_4$ 150 – 170 g/L	HCl 40 – 70 mg/L (ppm) MD 6 – 9 mL/L LO 1 – 4 mL/L
Tin	acid (1)	$\text{SnSO}_4$ , Sn: 20 – 25 g/L	$\text{H}_2\text{SO}_4$ 155 – 175 g/L	GSM smoothing agent 30 mL/L
Zinc	alkaline (13)	$\text{Zn}(\text{OH})_4^{2-}$ , Zn: 12 – 20 g/L	NaOH 130 – 160 g/L	A 8 – 15 mL/L B 0,25 – 2 mL/L

Electrolytes associated safety considerations and prices are presented in the previous section. The copper layer is deposited from an acid copper sulfate bath. Tin is electrodeposited from an acid tin sulphate chemical bath and zinc is electrodeposited from a basic zinc electrolyte.

### II.3.2.2 Electrolyte concentration control and replenishment

In all the electrolytes, metal and acid content should be maintained by frequent analytic control of the electrolyte. The composition of the electrolyte may change because of 1) metal and additives consumption for the electrodeposition process, 2) drag-out of the solution during the electrodeposition process, 3) evolution of the electrolyte with ageing. The electrolytes' composition is regularly quantified by inductively coupled plasma/optical emission spectroscopy (ICP-OES) (iCAP 6000 SERIES, Thermo Scientific) and titration (785 DMP Titrimo, 728 Stirrer, 776 Dosimat, Methrom), as described in Table II.16.

**Table II.16:** Bath characterization methods, more information can be found in *Annex B*.

Parameter	Characterization method	Chemicals
Cu, Sn, Zn concentration	ICP	
H <sub>2</sub> SO <sub>4</sub> concentration	Titration	NaOH 1 mol/L
Cl <sup>-</sup> concentration		AgNO <sub>3</sub> 0.1 mol/L + HNO <sub>3</sub>
NaOH concentration		HCl 1 mol/L
Sn <sup>IV</sup> concentration		I <sub>2</sub> 0,1 N
A, B additives	Hull cell	

Tin and zinc replenish automatically thanks to the presence of a tin or zinc anode but in case of variations, their content may be readjusted. The Cu, Sn and Zn metal contents are replenished by adding copper sulfate, tin sulfate and zincate solution, respectively. In the case of the tin electrolyte, tin (II) content should be kept constant. The pH control is performed by replenishment in sulfuric acid for Cu and Sn electrolytes, and sodium hydroxide for Zn electrolyte. The pH should be controlled carefully so as to avoid Zn(OH)<sub>2</sub> precipitation. In addition, in Cu electrolyte, hydrochloric acid is added when necessary to provide chloride ions. The additives are replenished according to their consumption, which depend on amperes hours applied to the electrolyte. For instance, in Zn electrolyte, for 10<sup>4</sup> A.h, 1.5 L of additive A and 1.5 L of additive B should be replenished to the solution. Additives A and B, which control the deposition rate and the brightness of the deposit, can also be replenished on Hull cell tests basis (the Hull cell procedure is given in *Annex B*, page 147).

**Table II.17:** Additive consumption rate

Electrolyte	Additive	Consumption rate (mL/Ah)
Cu	MD, LO	1.0 – 3.0
Sn	Smoothing agent	0.2 – 0.4
Zn	A, B	0.15

Finally, in all the electrolytes, evaporative losses are replaced with deionized water.

### II.3.3 Process conditions

The deposition set-up at 15 × 15 cm<sup>2</sup> is shown in Figure II.12.

The electrodeposition set-up includes:

- The reactor, a 50 L tank containing the electrolyte;

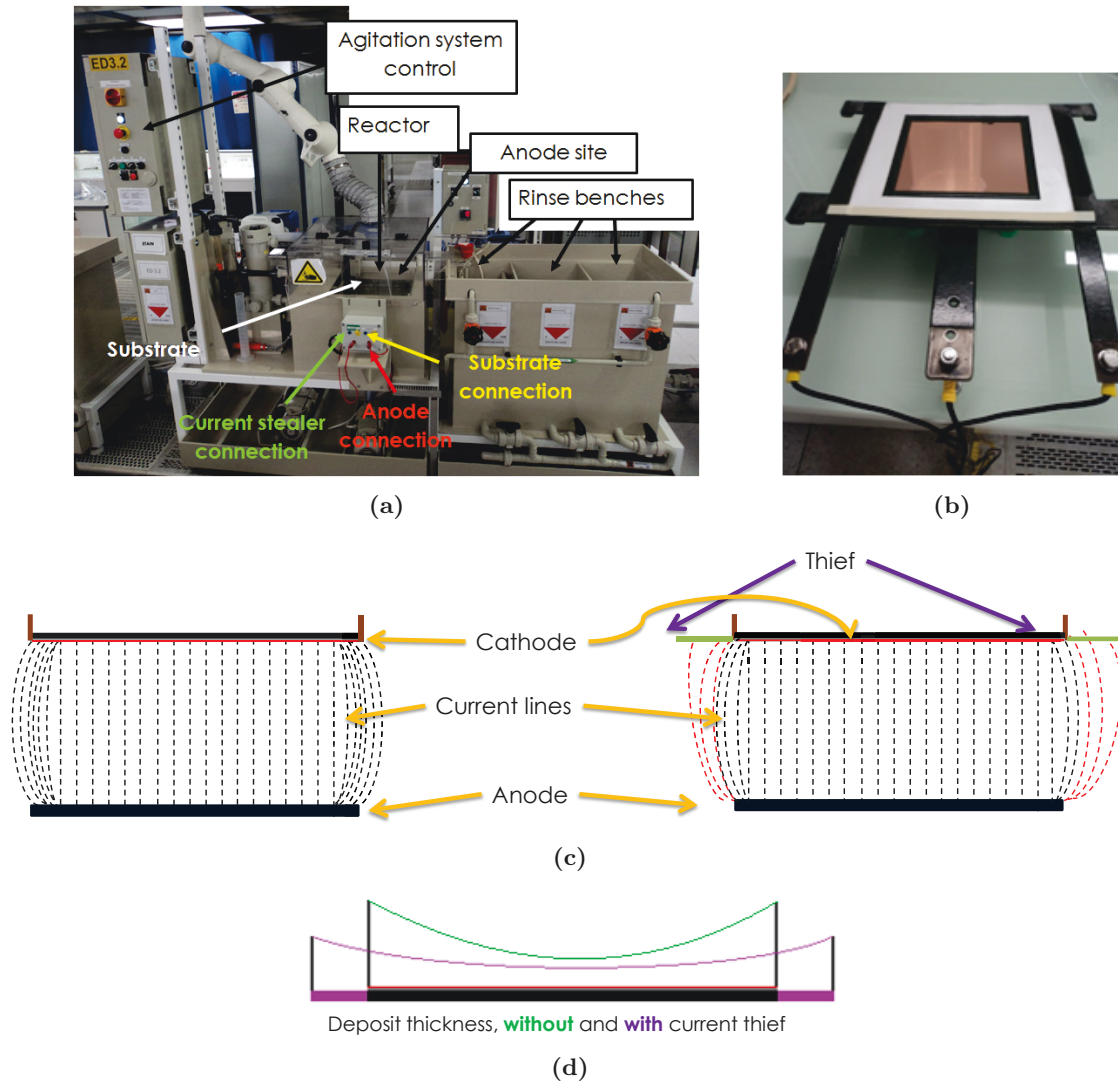


**Figure II.12:**  $15 \times 15 \text{ cm}^2$  electrodeposition set-up (a) reactor and (b) sample holder equipped with a current thief. (c) Influence of the current thief over the current lines distribution and (d) resulting deposit thickness.

- An agitation system (comb or paddle), necessary to ensure a good macroscopic uniformity of the deposits. The agitation system improves the mass transfer and removes hydrogen bubbles at the surface of the cathode;
- A filtration system;
- A substrate holder equipped with current thieves. Metallic thieves (also called robbers) are metal screens placed around the edge of the substrates, where there is a high current density, so as to attract the excess electrical flow. They allow to vary the current lines inside the solution, thus reducing edge effects, as shown in Figure II.12. The current applied to the thief is controlled by an external power supply (Micronics MX 10V-50A).
- An anode, which is insoluble (DSA, stable anode) for copper, or soluble and composed of the electroplated metal (tin or zinc);
- An external controllable current source (AUTOLAB Galvanostat and BSTR10A Current booster) in order to plate the metals using direct current, which is more compatible with an industrial process;

- Rinse benches: the first rinse bench is supplied with heating (40°C) and a pump, and the second and third rinse benches are in cascade overflow.

There is no need for heating resistances and temperature control because the depositions are realized at room temperature.

Each metal has its own set-up, allowing to deposit successively the three layers in a very short amount of time and limiting the cross-contamination. Copper, tin, and zinc layers are electrodeposited using direct current and current densities of 5, 10, and 20 ASD, respectively. Typical deposition times are very short, 30 – 110 s, and are adjusted in order to obtain the desired thickness. The samples are thoroughly rinsed with deionized water between each deposition. After zinc deposition they are dried with N<sub>2</sub>. The “surface finish” consists of a 10 seconds dip into 0.1% M nitric acid (HNO<sub>3</sub>) solution. This dip aims to remove the oxide layer at the surface of the precursor. After the dip, the sample is thoroughly rinsed with water and dried.

### II.3.4 Low-temperature annealing of metallic stacks

The pre-alloying of metallic stacks is carried out in a drying oven, also called air oven (Memmert GmbH, Germany). The oven is pre-heated to 200 °C before the pre-alloying. When the oven is at 200 °C, the sample is introduced. After 30 min in the oven, the sample is removed and cooled down naturally in ambient atmosphere. No vacuum nor inert atmosphere is needed for this step.

### II.3.5 Material and bath characterization

“As-electrodeposited” precursor composition is systematically measured by X-ray fluorescence (XRF) with a Fischerscope X-Ray XDV-50 equipment (Helmut Fisher AG). The XRF is previously calibrated with precursors of known composition (i.e., measured by inductively coupled plasma (ICP)). The precursor composition is measured on 16 points over the sample area, allowing to calculate the relative standard deviation (RSD), which gives an indication of macroscopic uniformity. Precursor composition profiles are obtained with a GDOES GD Profiler 2 (Horiba Jobin Yvon) or Tof-SIMS analysis (Biophy Research). Surface and cross-sectional SEM images are recorded using a XL40 FEG microscope (Philips) at a voltage of 10 kV or a Zeiss Series Auriga field emission scanning electron microscope (Zeiss) at a voltage of 5 kV. X-ray diffraction (XRD) spectra are recorded with a INEL Equinox 3000 diffractometer using Cu K $\alpha$  radiation. More information and details about the characterization techniques can be found in *Annex B*.



## II.4 Results and discussion

In this section, the suitability of ED as industrial deposition method for Cu-Sn-Zn metal precursors is examined. In a first place, lifetime and stability of the selected chemistries are examined. Secondly, the process robustness of such technique is studied. Finally, the properties of the electrodeposited and alloyed precursors are presented.

### II.4.1 Chemistry: Lifetime and stability

Ideally, the electrolytes should be during more than one year in time, enabling to deposit the metal over more than 2000 square meters of substrate for one liter of solution. Electrodeposition of kesterite precursors is still a “R&D” activity, which is performed at  $15 \times 15 \text{ cm}^2$ . Evaluation of the stability is only possible for hundreds of deposition “runs”, i.e.  $2 - 7 \text{ m}^2$  of substrate for 50 liters of solution. However, during the 3 years period of the PhD work, it is possible to evaluate the lifetime of the electrolytes, and this will be discussed in this section.

#### II.4.1.1 Copper

Figure II.13 shows that the concentration of Cu electrolyte components is stable for one year. The Cu electrolyte is used for more than 2 years without change of the bath, showing high lifetime and great stability. Concerning the impurities, Al, Ti, Fe, Ni and Cr contents remain very low (below 10 ppm). However high In, Sn and Zn impurities contents are found in the Cu electrolyte, probably due to cross-contamination with CIG and CZT precursors. Indeed, the copper electrolyte is also used at NEXCIS for electrodeposition of Cu-In-Ga (CIG) precursors.

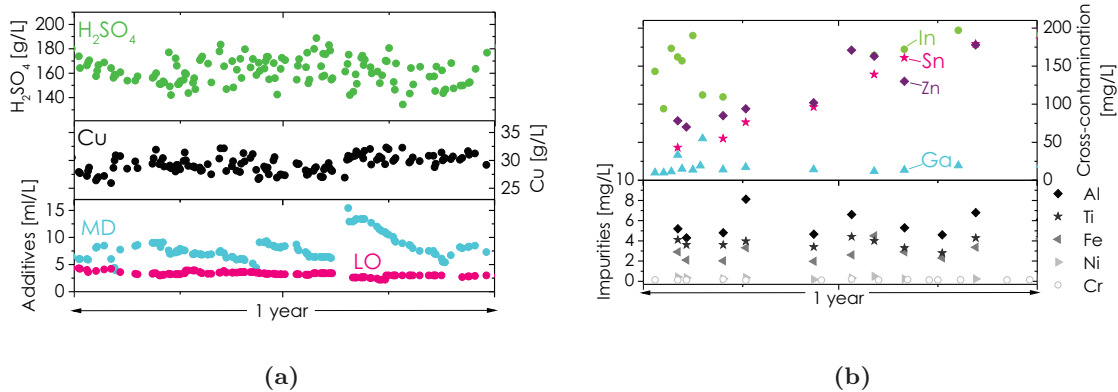


**Figure II.13:** Concentration of (a) Cu,  $\text{H}_2\text{SO}_4$  and MD and LO additives and (b) Cu electrolyte impurities traced for one year.

#### II.4.1.2 Tin

Figure II.14a represents the evolution of the Sn electrolyte over a whole year. The total Sn content was decreasing and had to be replenished regularly by the addition of  $\text{SnSO}_4$ .

However, the measure of the total concentration of Sn alone is not sufficient to understand the main issue of the Sn electrolyte evaluation. After one year, the electrolyte’s appearance changed from translucent to a yellow turbid color as shown in Figure II.15.

As already mentioned when reviewing the different tin electrolytes on page 45, in acid electrolytes, stannate  $\text{Sn}^{\text{II}}$  tends to oxidate to stannic  $\text{Sn}^{\text{IV}}$  in presence of oxygen, which leads to a decrease

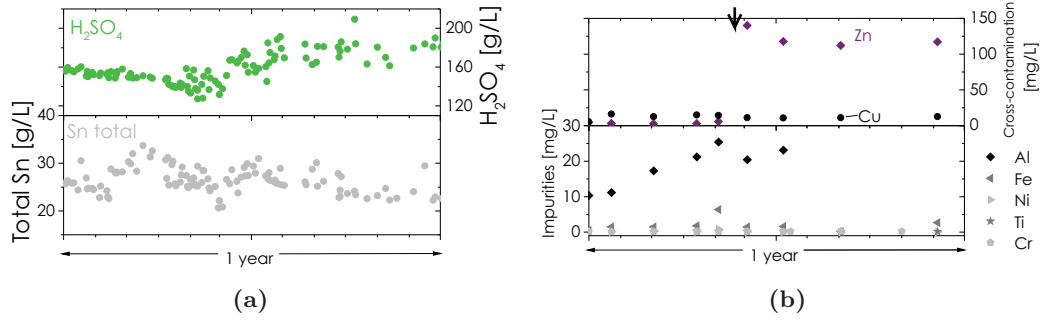


**Figure II.14:** Concentration of (a) Sn,  $\text{H}_2\text{SO}_4$  and (b) Sn electrolyte impurities followed for one year. The arrow indicates a probable external Zn contamination.

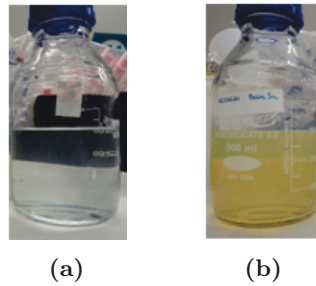


**Figure II.15:** Tin bath stability issue illustrated by images of (a) new and (b) 1 year aged baths.

of  $\text{Sn}^{\text{II}}$  concentration in the bath. Hydrated tin(IV) oxide exists in two distinct modifications:  $\alpha$ -stannic acid (also called “ortho-stannic acid”), which forms as a glassy granulated gel material, and  $\beta$ -stannic acid (also called “meta-stannic acid”), which exists as a fine white powder with a particle size typically in the  $\mu\text{m}$  region. The chemical composition of the hydrated tin(IV) oxides is imprecise, both being usually represented by the formula,  $\text{SnO}_2 \cdot x\text{H}_2\text{O}$ , where  $x$  is between 1 and 2 (also written as  $\text{H}_2\text{SnO}_3$ ). The two species can exist in a colloidal form with very high specific surface area. They can adsorb the organic additives used in the solution and therefore cause problems because their effective concentration in solution is decreased. During prolonged usage and idling periods, oxidation of the stannous ion into stannic ion, in a colloidal form, conducts to the precipitation of yellow  $\text{Sn}^{\text{II}} - \text{Sn}^{\text{IV}}$  aggregates, and a turbid appearance, as shown in Figure II.15. In addition, the presence of copper(II) in the tin bath favors tin(II) oxidation. The copper impurity concentration in the tin electrolyte is around 10 – 20 ppm, as shown in Figure II.14b, probably due to cross-contamination.

One of the consequences of the tin oxidation is the presence of aggregates at the surface of the electrodeposited Sn layers, as shown in Figure II.16a.

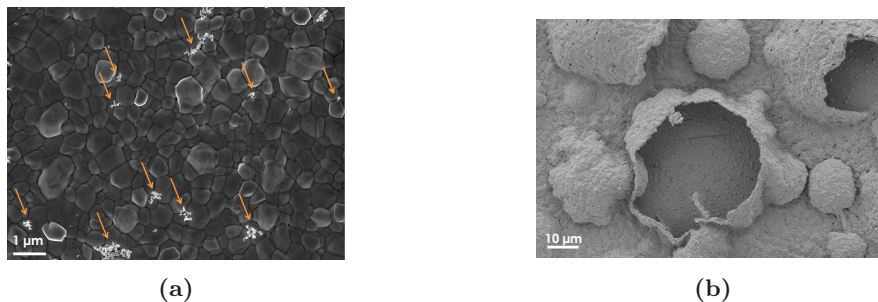


**Figure II.16:** Surface SEM images of (a) Cu/Sn sample (particles or “aggregates” are pointed out by the arrows) and (b) CZTSe absorber with holes. For both samples the Sn layer was deposited using an aged Sn electrolyte.

The effect of these aggregates on the subsequent kesterite absorber quality is not clear, but is expected to be detrimental. Although no evidence is found, it is assumed that these aggregates may have an influence on the presence of holes in the absorber layer, shown in Figure II.16b. In order to become aware of the oxidation reaction by other means than the color of the solution,  $\text{Sn}^{\text{II}}$  has to be differentiated from the  $\text{Sn}^{\text{IV}}$  concentration in the solution. A quantitative analysis of the  $\text{Sn}^{\text{IV}}$  amount by iode titration allows to discriminate the  $\text{Sn}^{\text{II}}$  amount from the total Sn amount. Monitoring of the  $\text{Sn}^{\text{II}}$  concentration allows to calculate the oxidation rate, as shown in Figure II.17. The oxidation is found to be time-dependant, with a  $\text{Sn}^{\text{II}}$  loss rate of  $0.023 \text{ g} \cdot \text{L}^{-1} \cdot \text{day}^{-1}$ .

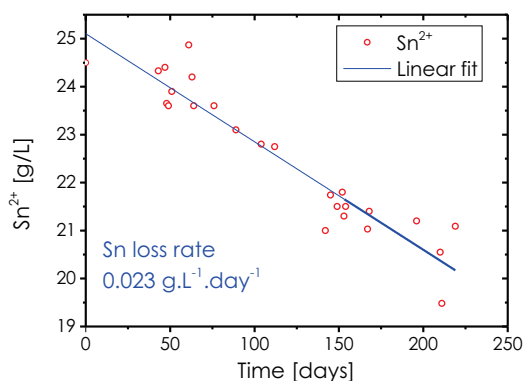


**Figure II.17:** Estimation of  $\text{Sn}^{\text{II}}$  loss rate by  $\text{Sn}^{\text{IV}}$  colloid formation, from KESTCELLS's project [314].

In order to limit the oxidation and its effects (the “Sn aggregates”), different options are envisaged:

- Minimization of the oxygen source. 1) Limiting air contact with the electrolyte is very difficult to implement at industrial scale. 2) The addition of **anti-oxidants agents** in the plating bath keeps the oxidized tin to a minimum. These antioxidants scavenge any free oxygen in the bath by outcompeting against stannous ions, thereby depleting the bath of oxygen so that the stannous ion conversion reaction is suppressed due to lack in oxygen reactants.
- Removing/avoiding  $\text{Sn}^{\text{IV}}$  colloids. 1) In an **alkaline electrolyte** the  $\text{Sn}^{\text{IV}}$  hydroxide precipitate is solubilized as  $\text{Sn}(\text{OH})_6^{2-}$  ion (as previously mentioned in paragraph II.2.3.3 page 45), but in this work electrodeposition is performed with an acid electrolyte; 2) **Filtration** can remove some of this material. However, the filtration process does not remove all solids from the bath; 3) Stannic  $\text{Sn}^{\text{IV}}$  can be removed by the addition of a liquid **flocculating agent** such as ortho-phosphoric acid ( $\text{H}_3\text{PO}_4$ ) that helps to coagulate colloidal tin(IV). Addition of a flocculating agent at a concentration of 1 – 2 mL/L enables a quick and complete sedimentation of the precipitate without affecting the operation of the electrolyte. The remaining supernatant liquid has a decreased tin content. After analysis, concentration of  $\text{Sn}^{\text{II}}$  and free acid are adjusted and the bath is replenished with fresh solution.

Figure II.18 shows the evolution of the main Sn components concentration over one year, including the regular analysis of  $\text{Sn}^{\text{II}}$ ,  $\text{Sn}^{\text{IV}}$  removal with flocculating agent and bath regeneration.

At first sight, the Sn electrolyte is kept clear from cloudy appearance. The “Sn particles” presence at the surface of the Sn electrodeposited layer is reduced. The sulfuric acid content was kept between 160 and 200 g/L.  $\text{SnSO}_4$  is regularly added and  $\text{Sn}^{\text{IV}}$  removed (by the flocculating agent method) so as to keep the  $\text{Sn}^{\text{II}}$  content above 20 g/L. In this work, the Sn electrolyte chemistry lifetime does not exceed a year, because the electrolyte has to be regularly cleared from  $\text{Sn}^{\text{IV}}$ . However,  $\text{Sn}^{\text{II}}$  oxidation is time-dependant. This causes problems when only a few substrates are processed, but in the case of an industrial line (high throughput) the impact of  $\text{Sn}^{\text{II}}$  oxidation would be minimized.

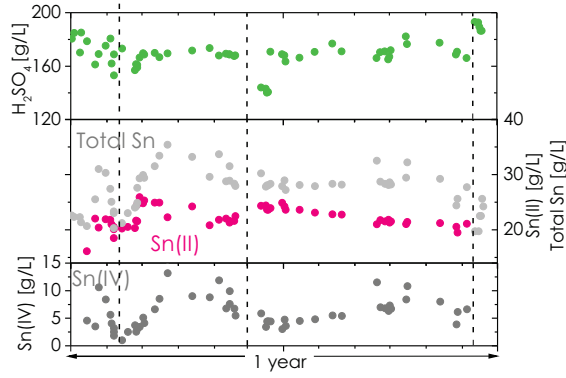


**Figure II.18:** Main Sn components concentration measured over one year. The dashed lines indicate  $\text{Sn}^{\text{IV}}$  removal by flocculating agent, followed by fresh Sn electrolyte replenishment, or a total regeneration of Sn electrolyte. The  $\text{Sn}^{\text{II}}$  amount is calculated by subtracting the  $\text{Sn}^{\text{IV}}$  amount from the total tin content.

### II.4.1.3 Zinc

The zinc bath composition traced over one and two years is shown in Figure II.19.

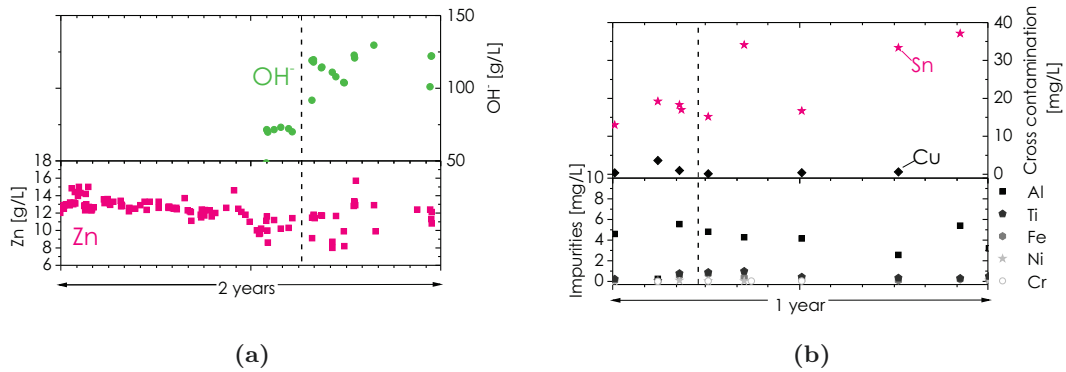


**Figure II.19:** Concentration of (a) Zn,  $\text{OH}^-$ , measured over two years and (b) Zn electrolyte impurities, measured over one year. The dashed lines indicate when the electrolyte is regenerated.

Zn content is very stable over time (no replenishment needed), because its content adjusts automatically with the presence of the Zn electrode. Due to measurement issues, it is not possible to assess the stability of the  $\text{OH}^-$  content. Additives A and B are not quantified, but they are replenished on the basis of a Hull cell analysis. Figure II.19b shows the impurities concentration in the Zn electrolyte. Most of the measured impurities had concentrations below 10 ppm, except for the Sn content which increased over time, probably due to cross-contamination.

### II.4.1.4 Conclusions on electrolytes' lifetime and stability

In summary, copper and zinc electrolytes proved to last for more than one year, meaning that their lifetime is adequate for industrial applications. The tin electrolyte had stability issues due to its tendency for  $\text{Sn}^{\text{II}}$  oxidation. Further studies to enhance the additive analysis methods (smoothing agent for Sn electrolyte, A and B for Zn electrolyte) may help to improve the bath lifetimes. Changing from the current Sn electrolyte to a more stable chemistry should also be considered. However, the new chemistry has to fulfill all requirements such as safety, room temperature operation conditions, etc.

## II.4.2 Process and material optimization

In this section, the deposition parameters (deposition rate, total duration, etc.) are examined. Resulting current efficiency and uniformity of the deposited layers are studied.

### II.4.2.1 Initial deposition parameters: preliminary work

The SEL route has the great advantage that precursor composition can be easily adjusted by varying the thickness of each layer. Deposition times can be tuned to adjust each layer thickness. The composition target is Cu-rich ( $\text{Cu}/(\text{Zn}+\text{Sn}) < 1$ ) and Zn-poor ( $\text{Zn}/\text{Sn} > 1$ ), because the best kesterite devices are reported for this composition range [6, 179]. The initial composition target is  $\text{Cu}/(\text{Zn}+\text{Sn})=0.78$ ,  $\text{Zn}/\text{Sn}=1.35$  and a total thickness of 675 nm, similarly to the ED precursor prepared by Ahmed et al. [29]. This corresponds to a 210 nm copper layer, a 265 nm tin layer and a 200 nm zinc layer. Initial deposition parameters have been determined by Fawaz et al. [292]. Optimum applied currents to the substrate and to the current stealer, agitation rate, deposition duration, and bath temperature are summarized in Table II.18. These parameters were optimized so as to allow high speed deposition, in order to be compatible with industry low-cost high-throughput requirements.

**Table II.18:** Initial optimum parameters for Cu/Sn/Zn electrodeposition at  $15 \times 15 \text{ cm}^2$  size, determined by Fawaz et al. [292].  $t$  is the duration of deposition,  $e$  the thickness of the deposited layer and  $\eta$  the current efficiency.

Metal	Agitation speed r/min	$J_{\text{substrate}}$ ASD	$J_{\text{stealer}}$ ASD	$t$ s	$e$ nm	RSD %	$\eta$ %
Cu	30	0.5	1	92	210	5.3	74
Sn	700	1	1	48	265	6.2	65
Zn	700	2	2	53	199	2.5	40

The resulting deposits thicknesses and uniformity (relative standard deviation (RSD)), measured by XRF, are also reported in Table II.18. The relative standard deviation is a measure of the thickness uniformity over the sample area (here,  $15 \times 15 \text{ cm}^2$ ). An example of uniformity for an electrodeposited Cu/Sn/Zn precursor is given in Figure II.20.

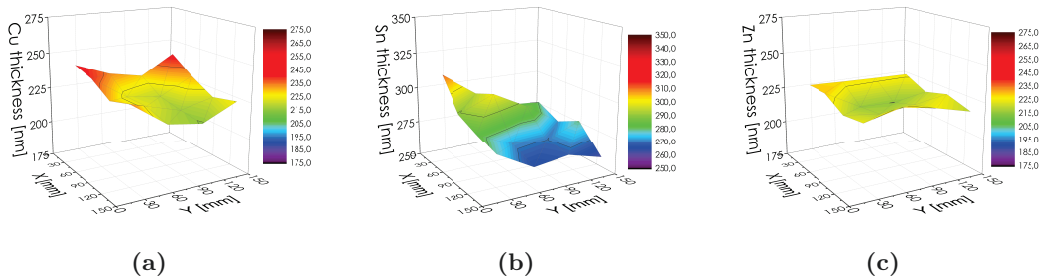


**Figure II.20:** (a) Cu layer, RSD of 3.9%, (b) Sn layer, RSD of 4.7% and (c) Zn layer, RSD of 2.2% thicknesses (nm) measured by XRF on a  $15 \times 15 \text{ cm}^2$  electrodeposited Cu/Sn/Zn precursor.

The current efficiency  $\eta$  is calculated according to the thickness predicted by Faraday's law, and is also given in Table II.18. Current efficiency for copper was around 75%. Tin and zinc were deposited with lower current efficiencies, probably because of competition with the hydrogen evolution reaction. Indeed, as shown in Figure II.2 on page 34, standard redox potentials for  $\text{Sn}^{2+}/\text{Sn}$  and  $\text{Zn}^{2+}/\text{Zn}$  are lower than for the  $\text{H}^+/\text{H}_2$  redox couple. Other parameters — additive concentration, ageing of the electrolyte, quality of electric contacts (cable, surface of the stealer, contact

between the substrate and the holder) — can influence the quality of the deposits. Starting from these initial parameters, the deposition duration is continuously adjusted so as to obtain the desired layer thickness.

#### II.4.2.2 Evolution of deposition parameters over time

Deposition time is the main adjustable variable to obtain the desired thickness. Deposition rate, deduced from thickness and deposition time, depends on electrolyte and substrate. Indeed, an electrolyte ages and the components concentration may vary; a daily adjustment is needed. In addition, for thicker substrates (thicker underlying layer, or thicker deposited layer), the resistivity increases and reduces the deposition rate.

**Copper deposition parameters** For copper, the deposition step duration is around 105 s, slightly longer as the initially proposed by Fawaz et al 92 s. The copper thickness is maintained at around 220 nm (as measured by XRF). Relative standard deviation of thickness generally stays below 10%. Deviations around 4 – 6% show the good uniformity of the electrodeposited Cu layer. The deposition rate is of 120 nm/min.

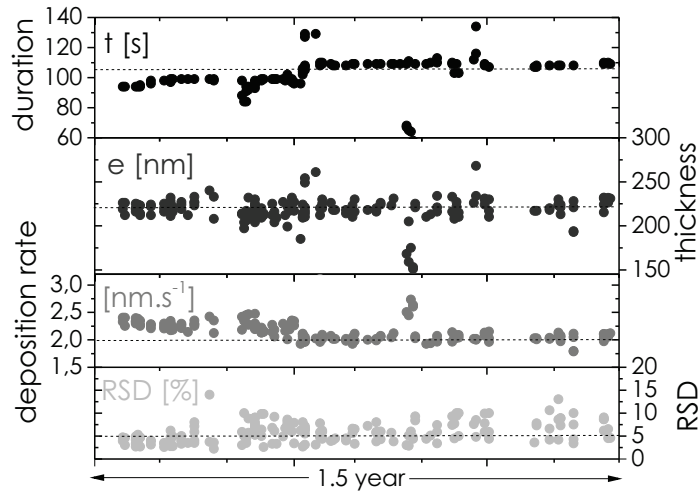
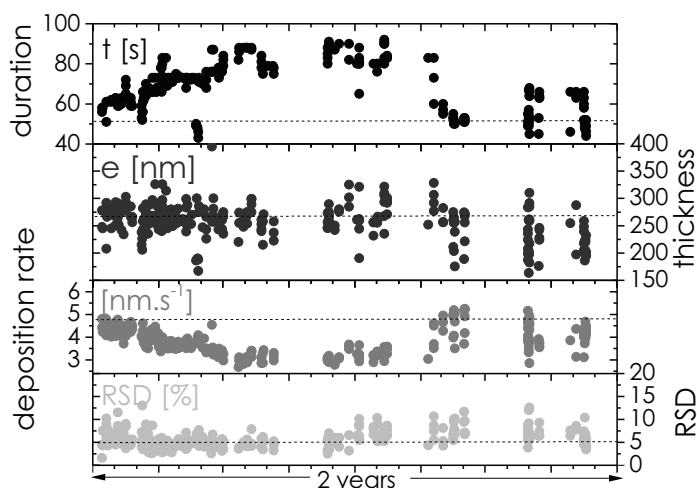


Figure II.21: Cu deposition parameters

**Tin deposition parameters** Tin deposition times were adjusted several times, for two main reasons: first, to vary the overall metal composition of the precursor stack; second, because the Sn electrolyte is not very stable. As the chemistry evolves, a constant time adjustment is required in order to deposit the same thickness. Typical thicknesses are between 150 and 300 nm, as measured by XRF. Figure II.14a also shows the evolution of the deposition rate. This rate has the tendency to decrease when the electrolyte degrades with oxidation, and to increase again when the electrolyte is regenerated. The decrease in deposition rate means that competitive reactions, such as reduction of  $\text{Sn}_{(aq)}^{\text{IV}}$  or hydrogen evolution are favored by electrolyte ageing. The deposition rate is quite high, between 180 – 350 nm/min. The variation in Sn layer thickness is more important as for copper, and the RSD is generally between 3 to 10%, mostly around 4 – 7%.

**Zinc deposition parameters** As for the Sn electrolyte, zinc deposition times were adjusted several times. A large decrease in deposition time, accompanied by an increase in deposition rate and in thickness deviation, is the consequence of a lack of additives replenishment (no A nor B added for a 6 months period). In the Zn bath, the additives actually compete with the main



**Figure II.22:** Sn deposition parameters

reduction reaction of  $\text{Zn}_{(aq)}^{\text{II}}$  into Zn, resulting in enhanced uniformity. In order to keep the Zn layer uniform over the  $15 \times 15 \text{ cm}^2$  area, A and B were regularly added, allowing a controlled deposition rate of around 240 nm/min. When optimizing the parameters, the deviation in zinc layer thickness varied around 2 – 3%, showing a very good uniformity over the sample area.

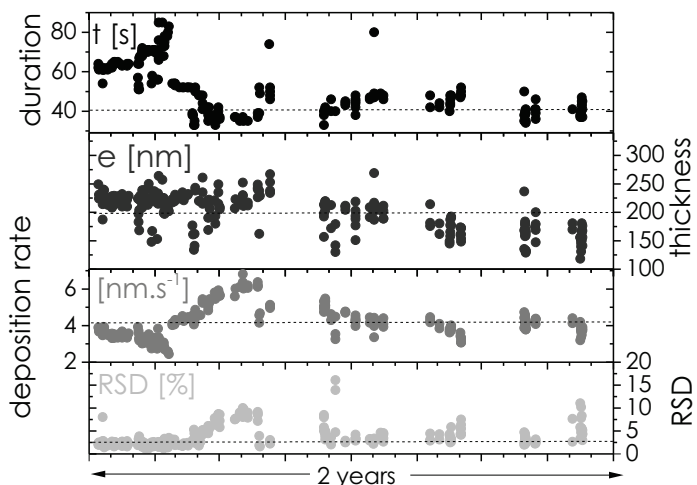


**Figure II.23:** Zn deposition parameters

The working range for different deposition parameters is summarized in Table II.19. Since many different thicknesses and compositions were desired, this range does not only represent an intended reproducibility, but the limits of the range. Sn and Zn were deposited with a current efficiency of around 30 to 70%, depending on the electrolyte ageing. Depositions are very fast (below 2 min), showing a great compatibility with the industrial process. The thickness of the complete precursor metallic stacks varies between 0.5 and 0.8  $\mu\text{m}$ , as measured by XRF.

#### II.4.2.3 Uniformity of the Cu/Sn/Zn precursor

It is of great importance to produce layers of uniform thickness in order to control the composition over the entire substrate area. Working at pre-industrial scale, this is a particularly relevant point. The relative standard deviation (RSD) gives an indication of the macroscopic uniformity of the

**Table II.19:** Deposition durations and resulting film thicknesses, as determined by XRF.

	Cu	Sn	Zn
Deposition duration $t$ (s)	80 – 120	45 – 90	30 – 70
Thickness $e$ (nm)	200 – 250	175 – 325	125 – 250
Deposition rate (nm/min)	120	180 – 350	240
Current efficiency $\eta$ (%)	74 – 80	31 – 61	26 – 72

layer. We aim to keep the RSD for each individual metallic layer below 6% over  $15 \times 15 \text{ cm}^2$  substrates in order to obtain good precursor composition uniformity. However, many samples exhibit higher RSD, as shown in Figures II.21, II.22, II.23. Many factors can cause non-uniformity and an increase in RSD:

- Bad electric contacts (cable, surface of the current stealer, contact between the substrate and the holder). Cables can be exchanged, the surface of the stealer cleaned with nitric acid, the contacts tightened.
- Electrolyte ageing, additives concentration variation. When the electrolyte is aged and oxidized, the Sn layer is less uniform. The Zn layer macroscopic uniformity is ensured by the additives.

An example of uniformity for an electrodeposited Cu/Sn/Zn precursor is given in Figure II.20. In order to improve the uniformity of the precursors, not only the thin Cu seed layer but the whole 160 – 190 nm Cu layer is deposited by PVD. Afterwards, electrodeposition of tin followed by zinc is performed on a soda-lime glass (SLG)/Mo/Cu substrate. The resulting uniformity is shown in Figure II.24.

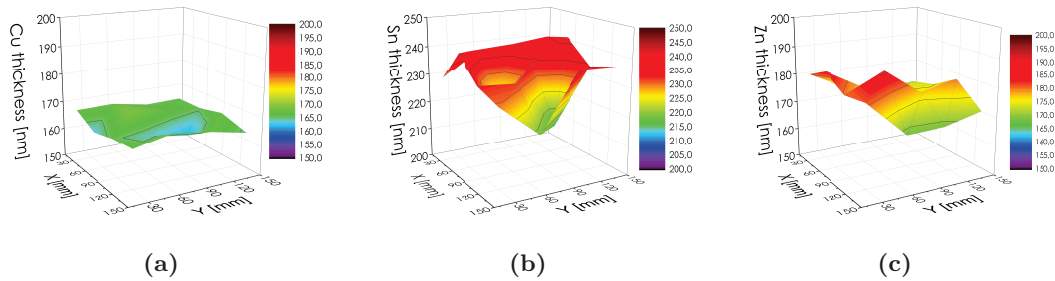


**Figure II.24:** (a) Cu layer, RSD of 1.2%, (b) Sn layer, RSD of 2.9% and (c) Zn layer, RSD of 3.4% thicknesses (nm) measured by XRF on a  $15 \times 15 \text{ cm}^2$  Cu/Sn/Zn precursor with a copper layer deposited by PVD and electrodeposited Sn and Zn layers.

Finally, copper and zinc layers are often deposited with good lateral uniformities over  $15 \times 15 \text{ cm}^2$  (RSD < 3 – 4%), which is desirable in order to avoid deviations in composition. However, larger thickness variations of the electrodeposited tin layer are still observed (RSD 5 – 6%, as shown in Figure II.22). Tin layer deposition is reported to be challenging also when using physical vapor deposition, and results in the formation of films with a rough morphology [49].

#### II.4.2.4 Morphology of Cu, Sn and Zn deposits: adherence and defaults

Scanning electron microscopy (SEM) images of the precursor metal stack surface as shown in Figure II.25 reveal good layer morphologies of the surfaces. The films completely cover the underlying layers. No pits are detected. The Sn film shows a large grain size. Zinc deposits show needle-like morphologies; the crystals seem to grow vertically, which can be attributed to the strong lateral blocking effect of the additives.



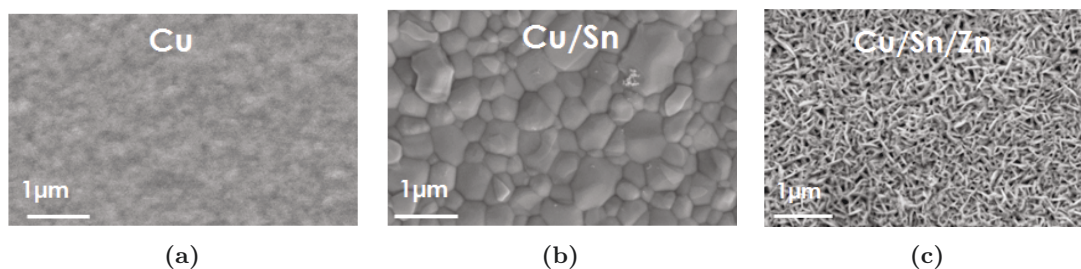


**Figure II.25:** Electrodeposited (a) Cu, (b) Sn and (c) Zn SEM surface images.

#### II.4.2.5 Composition profile and phases

Figure II.26a shows a cross-sectional SEM image of the electrodeposited precursor. The composition profile, or gradient over the layer thickness, is given by the GDOES profile in Figure II.26b. Cu is concentrated at the back of the precursor, near the molybdenum layer. Cu is followed by Sn and finally Zn is located at the top of the precursor. This composition profile is in agreement with the order of deposition of the different layers: Cu/Sn/Zn.

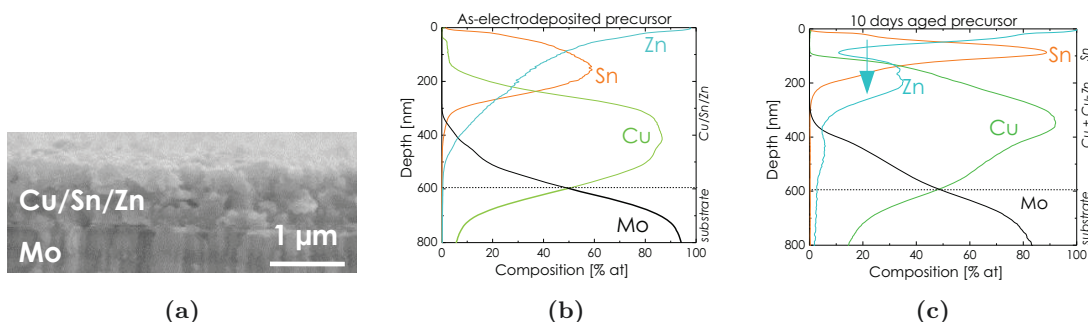


**Figure II.26:** (a) Morphology (cross sectionnal SEM image), (b) initial and (b) a few days aged GDOES depth composition profiles (in atomic percentage versus film depth) of the electrodeposited precursor. Comparison of (b) and (c) profiles shows that zinc element (in blue) migrates towards the copper layer (in green). The migration is represented by the blue arrow. It should be noted that the GDOES depth profiles are broad due to surface roughness effects.

As expected, the XRD pattern of an “as-electrodeposited” Cu/Sn/Zn precursor, shown in Figure II.27, is observed to be a mixture of elemental Cu, Sn and Zn, similarly to some electrodeposited Cu/Sn/Zn stacks reported in literature [273].

However, a few hours after electrodeposition, at room temperature and atmospheric pressure, a part of the zinc layer migrates towards the copper layer, as shown in Figure II.26c, and forms the  $\epsilon$ -CuZn<sub>5</sub> alloy. After a few days, the zinc layer is no longer detected by XRD and the only zinc alloy observed is the  $\epsilon$ -CuZn<sub>5</sub> phase. Over time (months) it is replaced by the  $\gamma$ -Cu<sub>5</sub>Zn<sub>8</sub> phase. The fast formation of  $\epsilon$ -CuZn<sub>5</sub>, followed by the more stable  $\gamma$ -Cu<sub>5</sub>Zn<sub>8</sub> has already been reported for electroplated Zn on a Cu substrate [315]. In addition, reaction between Cu and Zn is favored over reaction between Cu and Sn [283]. With natural ageing, no Cu-Sn or Zn-Sn alloy is detected.

#### II.4.2.6 Low-temperature annealing

In this thesis, the metal stack is low-temperature annealed in air for 30 – 120 min. Air annealing is convenient for industrial processes. The treatment is carried out at 200 °C in order to promote Cu-Sn and Cu-Zn alloys formation while keeping a flat morphology. Higher temperature treatments (>230 °C) resulted in the formation of bumps on the precursor layer (Figure II.28), probably due to the low melting point of elemental tin (230 °C).

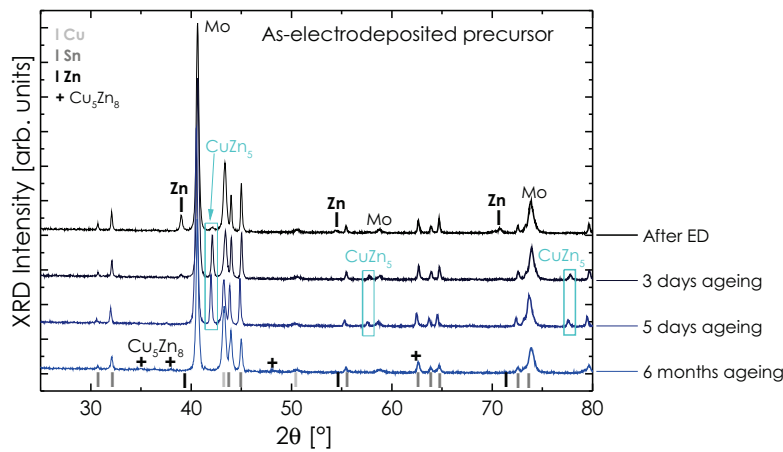


**Figure II.27:** XRD pattern of electrodeposited precursor

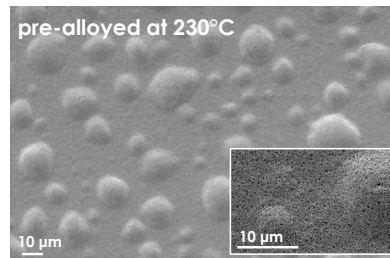


**Figure II.28:** Surface SEM image of a precursor alloyed at 230°C

The morphology and composition profile of the precursors pre-alloyed at 200°C is given in Figure II.29. Compared to the as-electrodeposited precursor (Figure II.26a), more crystalline features appear in the alloyed precursor (Figure II.29a). Moreover, a bi-layer structure is formed after the low temperature annealing. GDOES in Figure II.29b reveals the migration of zinc — initially at the surface of the precursor — towards the copper layer. The change in morphology is accompanied by the formation of alloys.

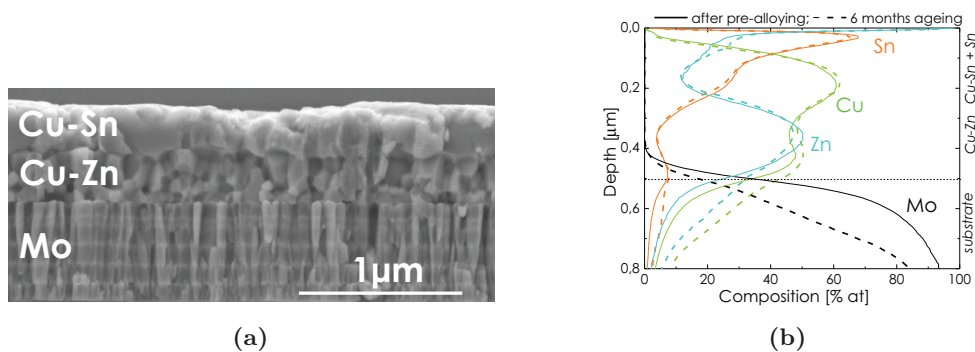


**Figure II.29:** (a) Morphology (SEM) and (b) composition (GDOES) depth profile of the 200°C pre-alloyed precursor after pre-alloying (full lines) and after 6 months ageing (dashed lines).

According to Sn-Zn-Cu system phase equilibrium studies at 180 – 250 °C [312], no ternary compound is expected. After the 200 °C annealing, alloy formation in the metallic precursor is observed. Directly after electrodeposition, only elemental Cu, Sn and Zn are detected by XRD analysis, while the alloys  $\text{Cu}_6\text{Sn}_5$  and  $\text{Cu}_5\text{Zn}_8$  and remaining elemental Sn reflections are detected after the pre-alloying, as shown in Figure II.30.

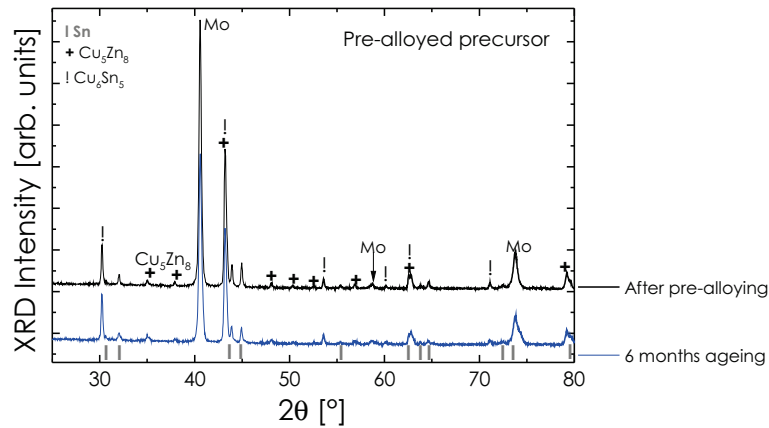


**Figure II.30:** XRD pattern of alloyed precursor

Combination of GDOES and XRD data indicates the formation of a Cu-Zn alloy at the back of the precursor layer while the surface area of the precursor consists of a mixture of Cu-Sn alloy and Sn. As expected from the limited mutual solubility of Sn and Zn, no Sn-Zn alloy was observed. With the pre-alloying, the color of the precursor film changes from white-grey to grey-gold, due to the formation of brass (Cu-Zn) and bronze (Cu-Sn) alloys. Independently of the applied pre-alloying time (up to 120 min), the GDOES composition profile of the alloyed precursor, as presented in Figure II.29b, does not change. Higher temperature thermal treatments (350 °C) are reported to form the same alloys, and additionally the  $\text{Cu}_3\text{Sn}$  phase [273], as described in Table II.14. As the pre-alloying thermal treatment is performed in air atmosphere, the precursor may be oxidized. No oxide formation was detected by XRD or GDOES analysis, but ToF-SIMS analysis shows the presence of an oxide layer close to the surface of the precursor layer (Figure II.31).

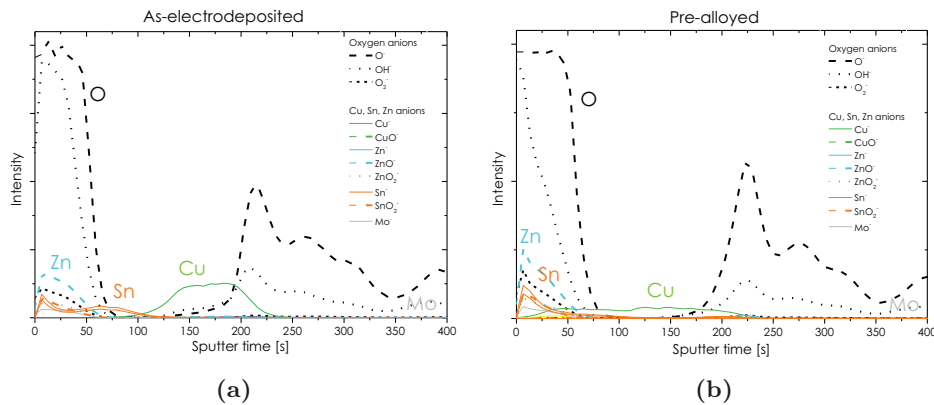


**Figure II.31:** ToF-SIMS profile of (a) electrodeposited and (b) pre-alloyed precursor.

Oxygen anions are detected in the surface area of the precursor, for both the one-month aged electrodeposited precursor with no pre-alloying and the pre-alloyed precursor. Evidently, the pre-alloying in air does not significantly increase oxygen diffusion through the precursor layer. The oxide layer may have formed by natural oxidation of the surface when exposed to air atmosphere at room temperature.

In summary, the low temperature annealing transforms the initial Mo/Cu/Sn/Zn precursor into a Mo/Cu-Zn/Cu-Sn stack, referred to as Mo/Cu-Sn-Zn. In contrast to some fully intermixed pre-alloyed precursors reported in literature [29, 31], the precursors observed here exhibit a bi-layer structure, which may be due to the stacking order and a pre-alloying temperature below the tin melting point. Bi-layer micro-structures have also already been reported for alloyed precursors

[274], as shown in Figure II.10 page 51. The phases are summarized in Figure II.32 for the as-electrodeposited precursor and low temperature annealed precursor.

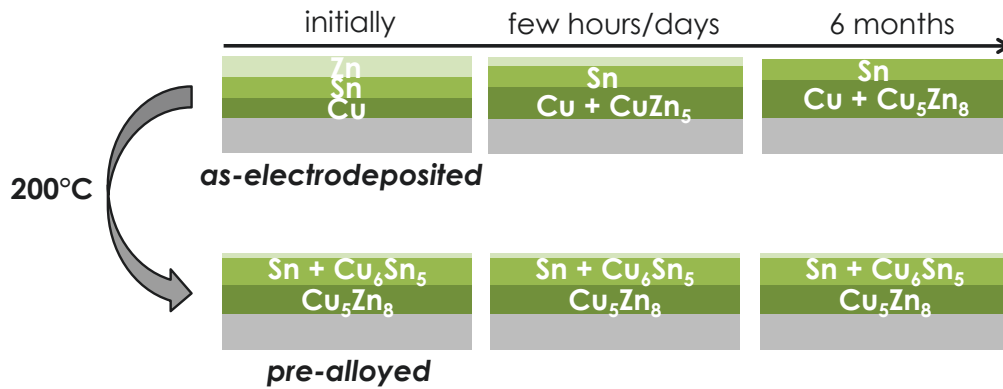


**Figure II.32:** Schematic of precursor structure, as-electrodeposited and pre-alloyed, and its evolution with natural ageing.

One considerable advantage of the 200 °C annealing step is the stabilization of the precursor. Indeed, after pre-alloying, the precursor composition profile measured by GDOES remained stable for several months, whereas without pre-alloying Zn tends to migrate fastly (hours to days) towards the copper layer to form CuZn<sub>5</sub> alloy, and more slowly (months) to form the more stable Cu<sub>5</sub>Zn<sub>8</sub>.

## II.5 Discussion and Conclusions

The aim of this chapter is the development of an electrodeposition procedure for the preparation of Cu-Sn-Zn films on  $15 \times 15 \text{ cm}^2$  substrates. These precursors are then annealed in the presence of chalcogens (S, Se) in order to form kesterite thin films. The requirements for the electrodeposition procedure are: (1) compatibility with an industrial process, i.e. high deposition speed, large area substrates, non-toxic chemicals, (2) good control of the Cu-Sn-Zn film composition (3) uniformity of the precursor at microscopic and macroscopic scale. The SEL (stacked elemental layer) route is found to best match these requirements. In this work, the precursor is deposited in a stacking order that is in agreement with the order of reduction potentials: Mo/Cu/Sn/Zn. The electrolytes for Cu, Sn and Zn are commercially available solutions: an acid Cu sulfate, an acid Sn sulfate and an alkaline non-cyanide Zn electrolyte. This work together with the preliminary work done by Fawaz et al. allow the choice of optimum deposition conditions. The metals are deposited from commercially available solutions at high speed rates, 120 to 350 nm/min, showing great compatibility with industry high-throughput requirements. A summary of the criteria for an industry-compatible electrodeposition process is shown in Table II.20.

**Table II.20:** Specifications for an industry-compatible electrodeposition process

Specification	Achievement
<b>Chemistry</b>	
<ul style="list-style-type: none"> <li>• Compatible with Mo substrate</li> <li>• Abundant and cheap components</li> <li>• Lifetime</li> <li>• Stable (+2000 m<sup>2</sup>/L)</li> <li>• Non toxic molecules</li> </ul>	Cu seed layer Cu $\approx 35 \text{ €/L}$ , Sn and Zn $< 5 \text{ €/L}$ Cu, Zn $> 1 \text{ year}$ but Sn $\approx \text{a few months}$ Evaluated only until 0.25 (Cu), 0.15 (Sn) and 0.09 (Zn) m <sup>2</sup> /L OK
<b>Process</b>	
<ul style="list-style-type: none"> <li>• Ambient temperature 20 - 40°C</li> <li>• Deposition rate</li> <li>• Easy and fast constituents analysis</li> <li>• Easy bath replenishment</li> </ul>	OK 120-350 nm/min OK for main components, need further investigations for additives OK for main components, need further investigations for additives
<b>Material</b>	
<ul style="list-style-type: none"> <li>• Good adherence</li> <li>• No apparent default (ex. nodules, stings)</li> <li>• Uniformity <math>&lt; 5\%</math></li> <li>• Low impurity content (<math>&lt; 10 \text{ ppm}</math>) for C,O,Fe,Mn,Cr,Ni,Al</li> </ul>	OK OK OK for Cu and Zn layers, 5-6% for Sn no impurities in electrolytes, not evaluated yet in precursors
<b>Environnement</b>	
<ul style="list-style-type: none"> <li>• Rinse water waste management</li> </ul>	work in progress by Kestcells project [314]

Until now, the main problem is considered to be the Sn oxidation issue. Sn oxidation limits the Sn electrolyte lifetime, is the probable cause for the presence of aggregates at the surface of Sn layer and worsens its uniformity. However, as Sn oxidation is time dependent, if Sn electroplating is continuously performed, more Sn is lost by drag out than through Sn oxidation, thus the problem becomes less significant. Future investigations on the analytical methods for the additives, an automated replenishment, and rinse water waste management are required to further improve the process in view of industrial optimization. Concerning the latest point, it was demonstrated that Cu, Sn and Zn are easily precipitated by acid-alkaline reactions [314].

Finally, the copper, tin, and zinc layers were electrodeposited using direct current and current densities of 5, 10, and 20 mA/cm<sup>2</sup>, respectively. Typical deposition times are very short, 30 – 120 s, and are adjusted in order to obtain the desired thickness. By varying the thickness, various metal stoichiometries were obtained within the Cu-poor and Zn-rich composition range, for which the best device efficiencies have been reported until now. Stable alloys are formed when the precursors are annealed at low temperature (200 °C) for 30 – 120 min in an air annealing oven.

# Chapter III

## Absorber formation

### Contents

---

III.1	Background . . . . .	71
III.1.1	The annealing process . . . . .	71
III.1.2	Kesterite annealing strategies in literature . . . . .	72
III.1.2.1	Chalcogen insertion method . . . . .	72
III.1.2.2	Annealing systems . . . . .	72
III.1.2.3	Annealing parameters . . . . .	76
III.1.3	Challenges in kesterite absorber manufacturing . . . . .	77
III.1.3.1	Volatility issues . . . . .	77
III.1.3.2	Secondary phases control . . . . .	78
III.1.3.3	Compatibility with back contact . . . . .	78
III.1.3.4	Chalcogen partial pressure . . . . .	80
III.2	Experimentals . . . . .	81
III.2.1	Substrates . . . . .	81
III.2.2	Precursors . . . . .	81
III.2.3	Optional Se capping layer . . . . .	81
III.2.4	Annealing systems . . . . .	82
III.2.5	Characterization of the absorber material . . . . .	85
III.2.5.1	Composition . . . . .	85
III.2.5.2	Morphology . . . . .	85
III.2.5.3	Phases . . . . .	85
III.2.6	Device fabrication and characterization . . . . .	86
III.2.6.1	Device fabrication . . . . .	86
III.2.6.2	Device characterization . . . . .	87
III.3	Results . . . . .	88
III.3.1	Sulfurization in NEXCIS system . . . . .	88
III.3.1.1	Experimentals . . . . .	88
III.3.1.2	Uniformity and composition control . . . . .	88
III.3.1.3	Morphology and secondary phases, impact on device performance . . . . .	91
III.3.1.4	Summary . . . . .	93
III.3.2	Selenization in NEXCIS system . . . . .	93
III.3.2.1	Experimentals . . . . .	93
III.3.2.2	Uniformity and composition control . . . . .	94
III.3.2.3	Morphology and secondary phases, impact on device performance . . . . .	95
III.3.2.4	Summary . . . . .	96

III.3.3 Selenization in IRDEP systems . . . . .	96
III.3.3.1 Uniformity and composition control . . . . .	96
III.3.3.2 Morphology and secondary phases, influence on device performance . . . . .	98
III.3.3.3 Summary . . . . .	100
III.3.4 Selenization in IREC system . . . . .	101
III.3.4.1 Composition control and uniformity . . . . .	101
III.3.4.2 Morphology and secondary phases, influence on device performance . . . . .	102
III.3.4.3 Summary . . . . .	107
III.4 Conclusions . . . . .	<b>108</b>

---

In this thesis, kesterite semiconductor thin-films are prepared in a two-step process by depositing a precursor layer with suitable elemental composition that is subsequently heat-treated in a chalcogen-containing environment. This chapter explores different methods to perform the thermal treatments, the associated issues and solutions, and examines the suitability of the different methods for the industrial fabrication of high-performance kesterite absorbers.

## III.1 Background

### III.1.1 The annealing process

Annealing involves the heating of a material into a controlled atmosphere, maintaining it at a defined temperature, and cooling. The atoms within a solid material diffuse, so that the material progresses towards its equilibrium state. The heat increases the rate of diffusion by providing the energy needed to break bonds. Here, the annealing step allows the formation and crystallization of the kesterite semiconductor material CZTS(e) (CZTS or CZTSe) from Cu-Sn-Zn or Cu-Sn-Zn-S(e) precursors, and ensure the adequate electronic properties, as represented in Figure III.1.

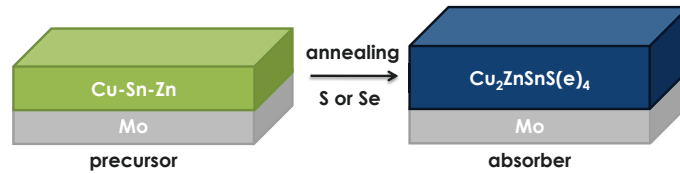


**Figure III.1:** Conversion of a Cu-Sn-Zn metallic precursor into a absorber layer by annealing.

The annealing process for kesterite is in theory very similar to CIGS annealing process: heat treatment in presence of chalcogen vapors (S and/or Se) converts a metallic precursor into a quaternary semiconductor. For CIGS, the chalcogen is inserted on a Cu-In-Ga or Cu-In-Ga-S(e) precursor, substituted by Cu-Sn-Zn or Cu-Sn-Zn-S(e)<sup>1</sup> precursors for the formation of CZTS(e). At high temperatures, the Se or S is incorporated into the film by absorption and subsequent diffusion. Inert atmospheres such as argon or nitrogen are required in order to avoid the oxidation of the metal's surface at such high temperatures.

Reaction pathways for the formation of kesterite with binary and/or ternary compounds as intermediates are often proposed:

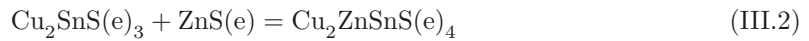
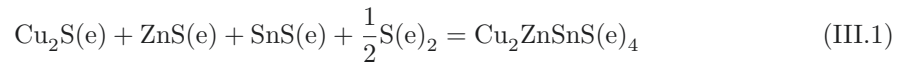
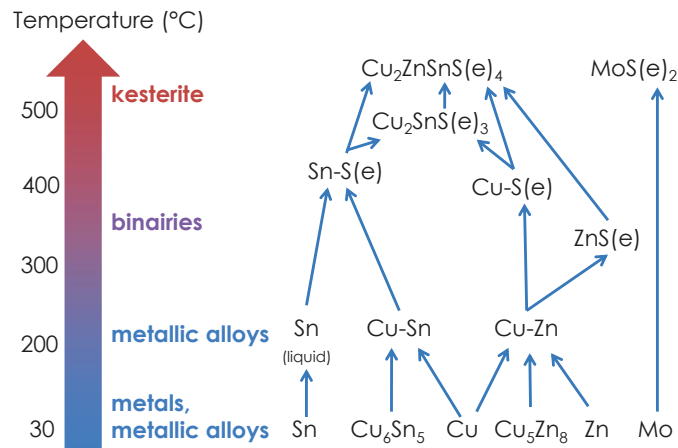


Figure III.2 shows a possible reaction sequence for the formation of kesterite from Cu-Sn-Zn precursors. However the reaction sequences depend on the metals which are in first contact with the chalcogen (precursor stack order), the tendency of each element to react with one another [316] and to diffuse, the metal ratios in the precursor [317] and the annealing conditions (pressure, temperature, amount of chalcogen). For instance, in some conditions, the binary Cu-S(e) phase is not detected, suggesting that all the Cu is bound to intermetallic phases before its conversion into a ternary or quaternary phase [200]. In the case of CZTSe, Se melts at 220°C and selenide phases generally form above 200 – 400°C from reactions of metallic alloys with liquid Se [199, 318]. Kesterite phase CZTSe may form at temperatures as low as 300°C but higher temperatures should be applied in order to maximize the conversion of binary and ternary phases into the main CZTSe phase [199]. In the case of CZTS, similarly the ZnS, Cu-S and SnS binaries form above 300 – 500°C [319]. A high temperature is desirable for a sufficient CZTS crystallization and full conversion of the undesirable secondary phases [319].

<sup>1</sup>In this chapter the notation S(e) will be used when the situation both applies to S and Se compounds.





**Figure III.2:** An arrow diagram for the possible phase formation during annealing.

### III.1.2 Kesterite annealing strategies in literature

#### III.1.2.1 Chalcogen insertion method

A wide range of thermal treatment systems have been used to form kesterite layers. The chalcogen S and/or Se can be:

- Inserted directly via the annealing atmosphere (reactive annealing);
- Already included in a Cu-Zn-Sn-S(e) precursor before the reactive annealing, which is not the case for the precursor layers produced within this work; or
- Deposited on a Cu-Sn-Zn precursor before the reactive annealing via different methods such as thermal evaporation [320, 321], electrodeposition [246] or CBD [322].

The formation of mixed sulfur/selenium compounds CZTSSe (not studied in this Chapter) can be realized by insertion of sulfur or selenium in the precursor and subsequent thermal treatment with the other chalcogen, or by a thermal treatment in an atmosphere containing both chalcogens. In all cases, a high temperature thermal treatment is required in order to ensure the adequate crystallinity and electronic properties. In this section, annealing processes leading to high-efficient kesterite devices are classified by chalcogen insertion method during the annealing step.

#### III.1.2.2 Annealing systems

**Confined chalcogen (CC)** One first chalcogen insertion method is the insertion of Se or S powder or pellets in a closed — or confined — environment, which creates a chalcogen partial pressure reacting with the precursor (generally with an argon or nitrogen inert atmosphere), as described in Figure III.3.

The graphite box has the advantage of a “confined” chalcogen atmosphere which decreases the loss of volatile elements. The volume of the chamber is kept low in order to maximize the Se or S partial pressure. During the annealing, S(e) vapor is confined in the graphite box, the S(e) pressure reaches the equilibrium S(e) vapor pressure. Thus, the equilibrium selenium vapor pressure  $P_{S(e)}$  is given by the temperature of the annealing. However confined systems are usually provided with safety relief valves in order to avoid overpressure. Thereby, graphite box is not a totally closed system and some vapors may escape the reaction chamber. In this case, the annealing is actually performed under non-equilibrium conditions. Non-equilibrium conditions range in severity from a leaky graphite box to a cold wall inside a vacuum chamber [36]. The graphite box is the most widely used system for sulfurization and selenization of kesterite precursors, as shown in Table III.1.

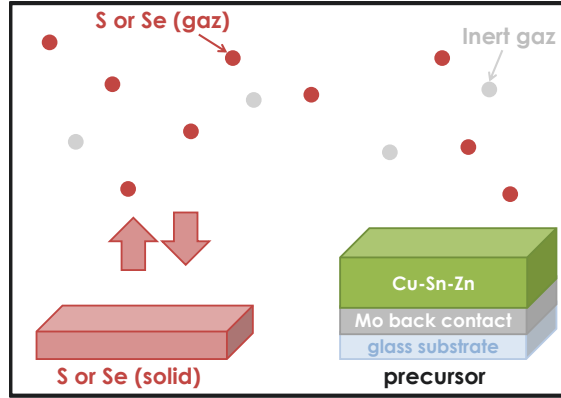


**Figure III.3:** Confined chalcogen (CC) system, schema adapted from [38].

**Table III.1:** Graphite box, a confined chalcogen (CC) system.

<sup>a</sup> Absorber thickness.

<sup>b</sup> The precursor is introduced into the already hot reaction chamber.

Precursor deposition methods (when different from electrodeposition (ED)): \* H<sub>2</sub>S reactive sputtering; # Sputtering;

<sup>†</sup> Spin-coating: solution.

Precursor	$\eta$ %	Chalcogen (mg)	Atmosphere (mL/min)	Pressure mbar	$T$ °C	Ramp °C/min	$t$ min	$A$ cm <sup>2</sup>	$e^a$ μm
<b>Formation of CZTS</b>									
Cu-Zn-Sn-S*	7.9 [33]	S (20)	Ar	300-350	560-570	fast <sup>b</sup>	10	2.5×2.5	-
Sn/Cu/Zn <sup>#</sup>	5.5 [319]	S (50); Sn (5)	Ar	1000	550	20	30	2×2	2-3
Zn/Sn/Cu <sup>#</sup>	5.0 [308]	S (50)	-	7.10 <sup>-3</sup>	580	RTP	5	2.5×2.5	-
Cu/ZnSn/Cu <sup>#</sup>	4.6 [323]	S (500)	-	-	560	100	30	2.5×5	5-6
ED-Cu/Sn/Cu/Zn	3.2 [233]	S (100)	10% H <sub>2</sub> , N <sub>2</sub>	500	575	-	120	2.5×2.5	2
ED-Cu/Sn/Zn	0.8 [231]	S	Ar	1000	550	40	120	2.5×1	1
<b>Formation of CZTSe</b>									
Sn/Cu/Zn <sup>#</sup>	8.2 [34]	Se, Sn	Ar	1.5 + 1000	450 + 550	-	30 + 15	5×5	-
Cu-Zn-Sn-Se <sup>†</sup>	8.0 [35]	Se (300)	-	-	540	530	15	2.5×2.5	1.8
Cu-Zn-Sn <sup>#</sup>	7.1 [38]	Se	N <sub>2</sub>	1013	500	40	20	-	1.5
Sn/Cu/Zn <sup>#</sup>	6.0 [324]	Se (50); Sn (4-5)	Ar	1000	525	20	45	2.5×2.5	-
ED-Cu/Sn/Zn	5.9 [274]	Se (100); SnSe (20)	10% H <sub>2</sub> , N <sub>2</sub>	500	550	RTP	4	-	-
ED-Cu/Sn/Zn	5.8 [274]	Se (100); SnSe (20)	10% H <sub>2</sub> , N <sub>2</sub>	10	550	20	30	-	-
ED-Cu-Zn-Sn	5.8 [239]	Se	-	-	530	40	15	-	-
Sn/Cu/Zn <sup>#</sup>	4.8 [49]	Se (50); Sn (5)	Ar	1-2	450	20	45	2×2	4
ED-Cu-Zn-Sn	4.5 [240]	Se	Ar	40	500	RTP	60	-	> 2
ED-Cu-Zn-Sn	2.7 [245]	Se	Ar	-	550	20	-	-	2 - 4.5

The graphite box is used to anneal Cu-Sn-Zn precursors and Cu-Zn-Sn-S(e) precursors. The total duration of this annealing ranges from a few minutes — thanks to the use of RTP heating systems — to a few hours. Power conversion efficiencies around 8% have been obtained with a graphite box system, for CZTS and CZTSe-based devices [33–35].

The sealed ampoule or quartz tube (Table III.2) works on the same principle as the graphite box. Instead of a confined system, this is a totally closed system, no vapor can escape from the chamber. Equilibrium conditions are easily obtained in a sealed quartz tube. Thermal treatments performed in sealed ampoule or quartz tube ensure a high chalcogen partial pressure, which is favorable for the introduction of chalcogen into the precursor layer. However, the use of high pressures results in the risk of overpressure and explosion of the sealed ampoule. In an industrial context, these systems have to be carefully designed and controlled.

Similarly as for the graphite box, both Cu-Sn-Zn and Cu-Sn-Zn-S(e) precursors are annealed with the sealed ampoule system, and lead to >7% power conversion efficiency kesterite devices [29–31, 37].

**Table III.2:** Sealed ampoule or quartz tube, a confined chalcogen (CC) system.<sup>a</sup> Absorber thickness.Precursor deposition methods: # Sputtering; <sup>s</sup> Evaporation.

Precursor	$\eta$ %	Chalcogen (mg)	$P_{S(e)}$	Atm	$T$ °C	Ramp °C/min	$t$ min	$A$ cm <sup>2</sup>	$e^a$ μm
<b>Formation of CZTS</b>									
ED-Cu/Sn/Zn	5.6-8.0 [30,273]	S (5 – 10)	1000	-	580-590	-	10	-	2.5
ED-Cu/Sn/Zn	7.3 [29]	S (2 – 5)	-	N <sub>2</sub>	585	20	12	-	-
ED-Cu-Sn-Zn-S	7.1 [37]	S (500)	-	-	570	300	15	3×2.5	0.9 – 2
Cu-Zn-Sn-S <sup>#</sup>	3.2 [191]	S (2 – 4)	-	-	520	4.2 – 8.4	120	0.5×1.5	1.2
<b>Formation of CZTSe</b>									
ED-Cu/Sn/Zn	7.0 [31]	Se (40 – 45)	-	N <sub>2</sub>	585	20	7	-	-
Cu-Zn-Sn-Se <sup>s</sup>	3.0 [325]	SnSe	0.13	-	470	-	30	-	1

**Independent chalcogen source (IC)** The three or two-zone furnace (schematized in Figure III.4) provides a sulfur/selenium source independent from the annealing zone allowing thereby a better control of the reaction path.

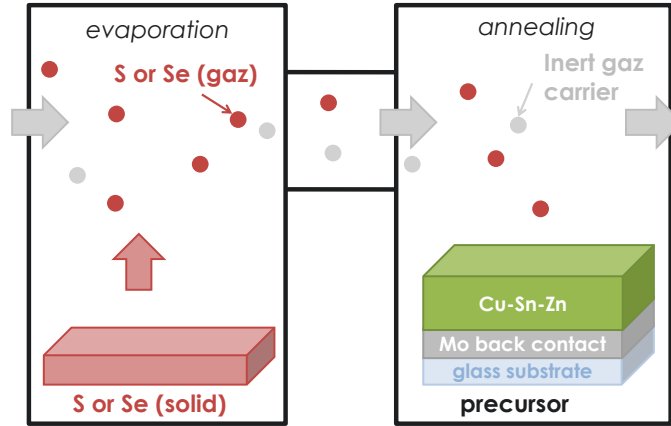


**Figure III.4:** Schematic representation of a three or two-zone furnace, an independent chalcogen source (IC) system, adapted from Bodeux et al. [38]. The intermediate zone, which is located between evaporation and annealing chambers and can act as an independent cracking chamber, is optional.

The chalcogen is sublimed in the evaporation chamber and carried by an inert gas carrier to the annealing chamber. The chamber temperatures can be independently controlled. If the evaporation chamber temperature is higher, more chalcogen will evaporate and be carried to the reaction chamber. A third zone between the evaporation chamber and the annealing chamber can be heated separately and act as a cracking chamber. Its purpose is to reduce the poly-atomic  $S(e)$  species ( $\sum S(e)_i (i = 1 - 8)$ ) to smaller molecular species, predominantly  $S(e)_2$ . Cracked  $S(e)$  should be more reactive than non-cracked  $S(e)$ . Kesterite devices prepared using a three or two-zone furnace are listed in Table III.3.

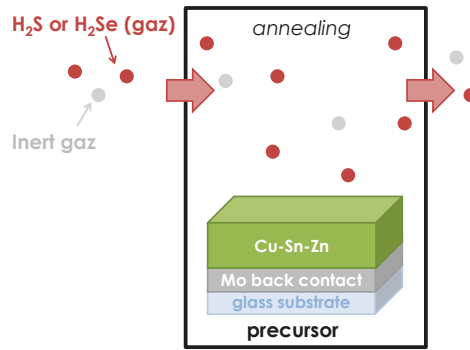
Three or two-zone systems are used for the chalcogenation of metal precursors and quaternary precursors in few minutes to few hours. The chalcogen chamber temperature may start from 200°C, a lower temperature as for the reaction chamber, because S or Se is already evaporated at these temperatures. A best power conversion efficiency of 8% has been obtained with a two-zone annealing system [32].

In the hydrogen sulfide/selenide method, the  $H_2Se$  or  $H_2S$  compound is carried via a gas mixture flux and reacts with the substrate, as schematized in Figure III.5.

**Table III.3:** Three or two-zone tube furnace, an independent chalcogen (IC) system.<sup>a</sup> Absorber thickness.

Precursor deposition methods: # Sputtering.

Precursor	$\eta$ %	Chalcogen (mg)	Gas carrier (mL/min)	Pressure mbar	$T_{chalcogen}$ °C	$T_{cracking}$ °C	$T$ °C	Ramp °C/min	$t$ min	$A$ cm <sup>2</sup>	$e^a$ μm
<b>Formation of CZTS</b>											
ZnS/SnS/Cu#	7.5 [135]	S	-	1013	300	n/a	570	-	30	-	0.5
ED-Cu-Zn-Sn	3.6 [241]	S	Ar	500	200	n/a	580	10	60	-	2
ED-Cu-Zn-Sn	2.9 [242]	S (500)	5% H <sub>2</sub> , N <sub>2</sub>	-	250	-	580	10	120	0.7	1.5
ED-Cu-Zn-Sn	2.7 [241]	S	Ar	100000	200	n/a	580	10	60	-	2
ED-Cu/Sn/Cu/Zn	2.3 [279]	S (30000)	N <sub>2</sub> (40)	-	240	-	580	12-30	120	2×2	2
<b>Formation of CZTSe</b>											
ED-Cu-Zn-Sn	8.0 [32]	Se	Ar	-	-	n/a	300 + 400-600	10	5 + 15	3×4	4.5
Cu-Zn-Sn#	4.1 [38]	Se	N <sub>2</sub>	1013	260	900	600	300	3	-	3.5
ED-Cu-Zn-Sn	1.7 [248]	Se	-	-	380	n/a	550	-	30	1	1.5
ED-Cu-Zn-Sn-Se	1.1 [42]	Se (1000)	N <sub>2</sub> (200)	-	350	n/a	575	-	5	-	1

**Figure III.5:** H<sub>2</sub>Se or H<sub>2</sub>S furnace, an independent chalcogen source (IC) system.

H<sub>2</sub>Se and H<sub>2</sub>S offer the fastest Se or S incorporation into the absorber layer as they are very reactive, but they present the disadvantage of being highly toxic<sup>2</sup> so strict safety measures must be enforced regarding their handling and use. Therefore, their use in an industrial context is not desirable for safety reasons. Nevertheless, a H<sub>2</sub>Se selenization approach has been developed for large-scale CIGS manufacturing. This typically takes place in batch processes, which deliver good uniformity and quality but at the cost of long processing times (requiring many oven systems in parallel) and safety issues [326]. Kesterite devices prepared with H<sub>2</sub>S or H<sub>2</sub>Se are shown in Table III.4.

**Table III.4:** H<sub>2</sub>S / H<sub>2</sub>Se.<sup>a</sup> Absorber thickness.

Precursor deposition methods: # Sputtering. + Colloid ink spray.

Precursor	$\eta$ %	Chalcogen	Flow	Pressure mbar	$T$ °C	Ramp °C/min	$t$ min	$A$ cm <sup>2</sup>	$e^a$ μm
<b>Formation of CZTS</b>									
Cu-Zn-Sn-S#	8.6 [131]	5% H <sub>2</sub> S in N <sub>2</sub>	-	400	280 + 510-530	5	15	10×10	<1
Cu-Zn-Sn-S#	6.8 [327]	5% H <sub>2</sub> S in N <sub>2</sub>	-	1013	350 + 550	-	30 + 60	-	1
Cu-Zn-Sn-S <sup>+</sup>	5.0 [39]	3% H <sub>2</sub> S in Ar	3 – 4 L/h	1013	200 + 525	10-20	10 + 60	5×5	-
Cu-Zn-Sn-S#	4.2 [328]	10% H <sub>2</sub> S in Ar	-	500	510	-	15	-	-
ED-Cu-Zn-Sn	3.6 [236]	5% H <sub>2</sub> S in Ar	-	-	550	2	120	10×10	1
<b>Formation of CZTSe</b>									
Cu/Zn/CuSn#	9.7 [61], 10.4 [15]	10% H <sub>2</sub> Se in N <sub>2</sub>	-	5	460	-	15	5×5	1

The hydrogen sulfide/selenide is diluted into an inert gas. CZTSe device power conversion efficien-

<sup>2</sup>The risk sentences for H<sub>2</sub>S and H<sub>2</sub>Se are R12, 26, 50 and R12, 26 respectively, see *Annex C* for the risk sentences listing.

cies over 10% have been reached thanks to a hydrogen selenide process at relatively low temperature (460°C) [15].

**Chalcogen in precursor (CP) - Hot plate heating** Hot plate high temperature ( $> 500^\circ\text{C}$ ) thermal treatments (Table III.5) are used when a Cu-Zn-Sn-S(e) precursor is deposited by solution, ink or nano-particles approach in order to evaporate the solvents and to form CZTS(e).

**Table III.5:** Hot plate annealing.

<sup>a</sup> Absorber thickness.

Precursor deposition methods: <sup>§</sup> Evaporation; <sup>‡</sup> Hydrazine; <sup>+</sup> Colloid ink spray.

Precursor	$\eta$ %	Chalcogen	Atm. Pressure mbar	$T$ $^\circ\text{C}$	Ramp $^\circ\text{C}/\text{min}$	$t$ min	$A$ $\text{cm}^2$	$e^a$ $\mu\text{m}$
<b>Formation of CZTS</b>								
Cu-Zn-Sn-S <sup>§</sup>	6.8-8.4 [132,329,330]	S or none	1013	540-570	-	5	-	-
Cu-Zn-Sn-S <sup>+</sup>	2.0 [39]	none	N <sub>2</sub>	200 + 525	0-20	10 + 15	5×5	≈ 2
<b>Formation of CZTSSe</b>								
Cu-Zn-Sn-S-Se <sup>‡</sup>	9.6-12.6 [21,23-25]	S or none	-	$> 500$ -540	-	-	-	1.5-2.5
Cu-Zn-Sn-Se <sup>§</sup>	11.6 [13]	Se	N <sub>2</sub>	≈ 590 [13]	-	-	-	2.2

Highest efficient kesterite devices are produced by IBM group, using hydrazine precursor deposition followed by hot plate annealing [21, 23–25]. Larramona et al. [39] also reported a 2.0% efficient CZTS device by hot plate annealing of a Cu-Sn-Zn-S precursor by molecular solution. However, this hot plate step is generally followed by a subsequent sulfurization in H<sub>2</sub>S (5.0% [39]) or selenization in a conventional graphite box (8.6% by Larramona et al. [150], 9.5% by Hillhouse group [45, 143, 331]).

In summary, the most common annealing techniques used for the synthesis of kesterite are the graphite box, a confined chalcogen system (CC) (Table III.1) and the three or two-zone tube furnace, an independent chalcogen system (IC) (Table III.3). In all cases, some of the chalcogen vaporizes during the reactive annealing, a loss which should be limited by atmosphere control (chalcogen partial pressure) or by providing an excess of chalcogen. All the annealing systems presented in this section allow to fabricate high-efficient kesterite devices ( $> 8\%$ ). In this section, the annealing systems have been classified by location of the chalcogen source during annealing (CC, IC or CP). The annealing systems can also be classified according to operating conditions such as heating rate or operating pressure.

### III.1.2.3 Annealing parameters

**Temperature** For all the systems described in the previous section, the annealing temperature is typically between 450 and 600 °C, with a majority of thermal treatments around 550°C. Indeed, a high temperature is needed to reach the full conversion of binary and ternary phases into kesterite [199, 319]. The temperature also influences the kesterite grain size, and the thickness of the interfacial MoS(e)<sub>2</sub> layer. High temperatures will create a thick MoS(e)<sub>2</sub>, which may decrease the device performance [63, 332].

**Heating rate** The processes may be classified in two categories, independently of the chalcogen insertion method, according to their heating rate (ramp) :

- Conventional “slow” thermal processes, with a temperature ramping up from below 10 °C/min, (more than one hour to reach the desired temperature) to 40 °C/min (15 minutes of heating before temperature is reached);
- Rapid thermal processes, also known as RTP, with a heating rate of 200 – 500 °C/min (2 – 10 °C/s). This is achieved by heating with halogen lamps, rather than via the use of resistive heating elements. Rapid thermal processing is a more industrially viable method

of forming thin film absorber layers than time intensive conventional thermal processing. The annealing step consists in a very fast temperature ramping up and a short time during which temperature is hold at a constant level. Another advantage of a fast annealing is the limitation of chalcogen losses: processing times are much shorter than conventional thermal processes, thus allowing kinetically driven grain growth processes to proceed more quickly than thermodynamically driven decomposition reactions [44].

**Annealing duration** The “dwell” time or the duration of the higher temperature step ranges from a few minutes to 2 hours. In the early stages of kesterite development, long annealing times (a few hours) were used, but it has been shown that kesterite forms quickly and long annealing durations are not necessary. Now, most of the thermal treatments last less than 40 minutes, which is enough for the growth of large kesterite grains.

**Pressure** The thermal treatment can be performed at low pressure (under vacuum) or in atmospheric conditions, with a background inert pressure from a few mbar to 1013 mbar.

### III.1.3 Challenges in kesterite absorber manufacturing

#### III.1.3.1 Volatility issues

**Volatile compounds** The chalcogens S and Se are not the only volatile elements in the Cu-Sn-Zn-S or Cu-Sn-Zn-Se systems. SnS, SnSe and Zn compounds are highly volatile, as shown in Figure III.6. Therefore, at low pressure and high temperature, the control of Sn and Zn contents is expected to be challenging.

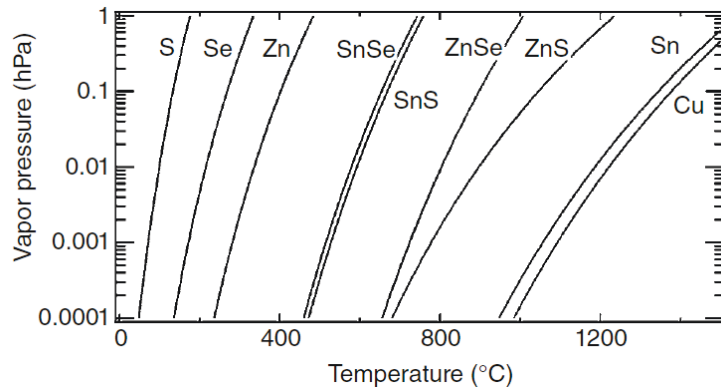
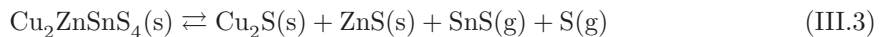


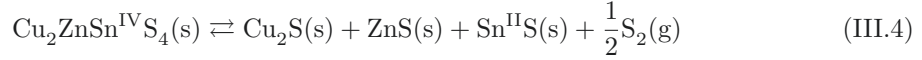
**Figure III.6:** Saturating vapor pressure for Cu, Zn, Sn, S, Se and compounds, from [40] and Weber’s PhD thesis [333].

Sn loss is frequently observed during the annealing process [27, 41–45]. Zn loss is also reported to occur during the annealing step [44, 46, 47]. Under high temperature and low pressure, the Sn-S(e) compounds are highly volatile and will be evaporated when binaries are formed on the kesterite formation reaction path, but also by decomposition of Sn-S(e) phases rich in sulfur or selenium. S(e) and Sn-S(e) evaporate directly. SnS(e)<sub>2</sub>, Sn<sub>2</sub>S<sub>3</sub> and Cu-Sn-S(e) decompose into Cu-S(e) and gaseous SnS(e) and S(e) [223]. The losses can originate from the direct evaporation of volatile compounds or by decomposition of kesterite, as shown by the following mechanisms.

**Reversible CZTS decomposition** Weber et al. [207] reported significant Sn loss above 550 °C and proposed the following decomposition reaction of the CZTS phase into the binary metal sulfides and S:



Scragg et al. [208] studied more in detail this decomposition and proposed the following reversible mechanism to explain SnS desorption:



The mechanisms also apply to selenide kesterite CZTSe.

**Consequences and proposed solutions** Sn or Zn losses impede the thorough control of film composition and film homogeneity. To avoid substantial tin loss, two approaches may be taken or even combined [36].

- The thermodynamic approach is simply to supply or compensate for the loss of volatile species. The addition of SnS(e) powder in the reaction chamber [41, 136], Sn(s) [48, 49] or the evaporation of a SnSe<sub>2</sub> capping layer onto the absorber prior to the high-temperature treatment [50] have been proposed in order to prevent the decomposition reaction and introduce missing Sn into the film. Reciprocally, Berg et al. have shown that CZTS can form from a Cu-Zn precursor, elemental sulfur and SnS(s) [334].
- Kinetically, SnS(e) and S(e) loss may be limited by providing a diffusion-limiting step such as by annealing in a high background pressure of inert gas. The high background pressure slows the movement of the volatile species which reduces the rate of loss, and increases the partial pressure of volatile species above the thin film. Keeping the film deposition at low temperature or making the high-temperature thermal treatments at atmospheric pressure reduces the loss of Sn-related phases.

### III.1.3.2 Secondary phases control

The CZTS(e) kesterite absorber is a quaternary system<sup>3</sup>, which means that the composition ratios between the 4 elements need to be tuned in order to obtain the desired material and properties. Since S and/or Se is introduced through reaction with the precursor, the amount that is incorporated depends on the amount of the metal elements and their valency: Cu(I), Sn(IV) and Zn(II). This simplifies the quaternary system to a ternary one. In CZTS(e) literature, the ratios of atomic percentages Cu/(Zn+Sn) and Zn/Sn are often used to represent the composition of the metallic elements in the material. Both ratios are equal to one when the material is stoichiometric. A ternary phase diagram is the most useful way to summarize metal compositions in the Cu-Zn-Sn-S(e) system. An example of a ternary phase diagram is shown in Figure III.7.

In the *Introduction*, the Cu-Zn-Sn-S and Cu-Zn-Sn-Se systems have been described, showing that the single phase regions for CZTS or CZTSe are very narrow. Consequently, a small deviation in composition may lead to the appearance of secondary phase(s). Best device efficiencies have been obtained in the Cu-poor Zn-rich composition region (as shown in Figure III.7), where only ZnS(e) secondary phase is expected. However, local deviations in composition may lead to the presence of more detrimental Sn-S(e), Cu-S(e) and Cu<sub>2</sub>SnS(e)<sub>3</sub> secondary phases, making the control of the composition crucial. The effects of the secondary phases on device performance is also described in the *Introduction*.

### III.1.3.3 Compatibility with back contact

Molybdenum (Mo) is the most used back contact in kesterite based solar cells. Despite some issues (adherence, decomposition at back contact and thick MoS(e)<sub>2</sub> formation), Mo has been shown to be the best back contact in terms of power conversion efficiency [335].

<sup>3</sup>CZTSSe is a pentenary system, not studied in this chapter but the same challenges apply.

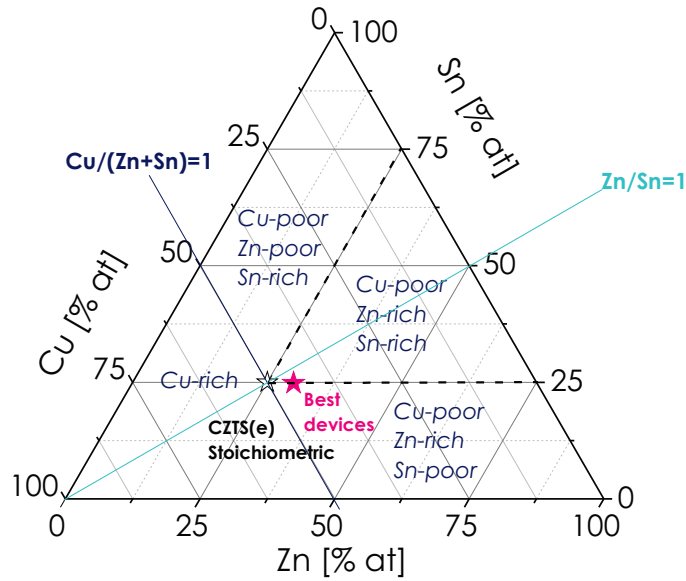
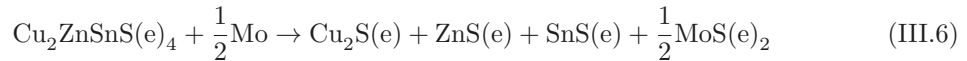


**Figure III.7:** Metal composition ternary phase diagram of a Cu-Sn-Zn-S(e) system.

**Adherence** Many factors can cause a poor adherence between the absorber layer and the back contact: differences in expansion between Mo and the semi-conductor, stress in the absorber layer due to the volume expansion caused by chalcogen incorporation, and porous morphology (presence of holes at the interface) [336]. Poor adherence can lead to a detachment of the absorber layer from the Mo substrate during or after annealing.

**CZTS(e) decomposition at back contact** A detrimental decomposition at the back contact is also observed [201], and leads to an increased Sn loss by desorption of SnS(e), according to the following mechanism:



**Formation of MoS(e)<sub>2</sub>** Interfacial MoS(e)<sub>2</sub> with proper thickness will be helpful to form ohmic contact and improve adhesion between CZTS(e) film and Mo back contact, similarly as in CIGS solar cells. However, the formation of a thick interfacial MoS(e)<sub>2</sub> layer is a serious problem for CZTS(e) solar cells, an overall reverse correlation between the device performance and interfacial MoS(e)<sub>2</sub> thickness has been observed by Shin et al. [63]. The overthick MoS<sub>2</sub>/MoSe<sub>2</sub> layer will reduce the thickness of Mo layer dramatically and deteriorate the electrical contact of CZTS(e) to Mo substrate, both of which will increase the series resistance of the device significantly. High temperatures and high chalcogen partial pressure create an overthick MoS(e)<sub>2</sub> [63, 332]. Ways to achieve a thinner MoS(e)<sub>2</sub> are to reduce the temperature and/or the duration of the annealing and/or the chalcogen pressure but they may have an impact on kesterite crystallization and MoS(e)<sub>2</sub> orientation.

The introduction of a Se diffusion thin barrier layer at the back contact interface such as TiN [33, 63, 337], ZnO [324, 338], TiB<sub>2</sub> [339], Ag [340, 341], Bi [342] or C [137] can help to limit the formation of MoS(e)<sub>2</sub>. The thin barrier layer will also prevent the decomposition reaction of kesterite with Mo [33, 324]. A soft prealloying process, acting as a temporary Se diffusion barrier during high temperature selenization, also proved to reduce the thickness of interfacial MoS(e)<sub>2</sub> [130].



#### III.1.3.4 Chalcogen partial pressure

At fixed annealing temperature, the S(e) partial pressure ( $P_{S(e)}$ ) plays a role on the MoS(e)<sub>2</sub> thickness [63]. A low S(e) partial pressure is effective to suppress the formation of overthick MoS(e)<sub>2</sub>. However an elevated chalcogen partial pressure is beneficial to reduce SnS(e) losses as S(e) is involved in the SnS(e) volatility reactions (formation of binaries, kesterite reversible decomposition reaction) [208]. In addition, the kesterite electronic structure is very sensitive to low  $P_{S(e)}$ , with formation of defects due to S(e) deficiency [63]. In summary, though the low Se partial pressure is effective to suppress the formation of MoS(e)<sub>2</sub>, it can be detrimental for composition control and a lot of defects caused by S(e) deficiency may form in the CZTS(e) absorber.

## III.2 Experimentals

An overview of the experimental procedure is given in Figure III.8. The electrodeposited precursors, optionally Se-capped and cut, are annealed in different systems under sulfur or selenium vapors. The resulting kesterite absorber material CZTS(e) is characterized. Devices are also fabricated in order to study the effects of absorber properties variations on the kesterite-based devices performance.

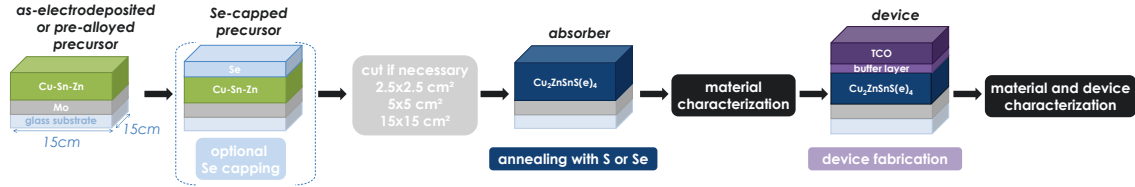


Figure III.8: Experimentals overview

### III.2.1 Substrates

Molybden-coated soda-lime-glass substrates including a thin barrier layer are used in order to avoid back contact kesterite decomposition and thick MoS(e)<sub>2</sub> issues. The thin barrier layer is described in a patent [343] and allows to control MoS(e)<sub>2</sub> thickness.

### III.2.2 Precursors

The thermal treatments in this work are performed on smaller parts of the 15 × 15 cm<sup>2</sup> electrodeposited Cu/Sn/Zn precursors, with or without pre-alloying low temperature thermal treatment. For more informations on the precursors the reader is referred to *Chapter 2: Electrodeposition*.

### III.2.3 Optional Se capping layer

The selenium capping layer is deposited at NEXCIS by evaporation (Balzers BAK760 evap coating system) or vapor transport deposition (VTD) on 15 × 15 cm<sup>2</sup> precursors. When using a Se capping layer with a default of selenium versus the target stoichiometric CZTSe, further selenium presence is needed during the annealing step. On the contrary, a Se capping layer presenting an excess of selenium may be a sufficient selenium source for CZTSe formation. When deposited by evaporation, the Se capping layer is thick, homogeneous, uniform and dense, as shown in Figure III.9a. The VTD deposited Se capping layer is porous, as shown in Figure III.9b.

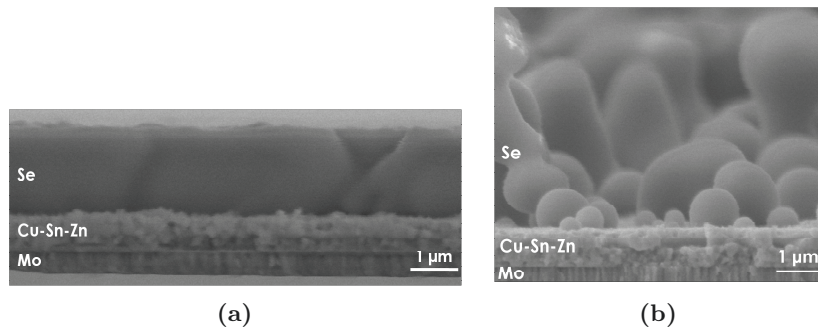


Figure III.9: Cross-sectional SEM images of (a) evaporated and (b) VTD deposited Se capping layers on Cu-Sn-Zn precursors.

### III.2.4 Annealing systems

Thermal treatments are performed in confined systems and independent chalcogen source systems. The different annealing systems used in collaboration with different institutes, and their main characteristics are described in Table III.6.

**Table III.6:** Thermal treatment systems, including confined chalcogen systems (CC) and independent chalcogen (IC) systems, as described in Background section.

Name (Institution)	Chalcogen mg	Atm	Pressure mbar	$T$ °C	Ramp °C/min	$t$ min	$A$ cm <sup>2</sup>
CC-NEXCIS	S (100)	Ar	7 – 500	500 – 600	RTP: 120 – 600	0 – 10	15×15
IC-IRDEP	Se (500-5500)	N <sub>2</sub>	985	500 – 610	RTP: 180 – 400	3	2.5×2.5
CC-IRDEP	Se (20-70)	Ar	1013	550	40	15	2.5×2.5
CC-IREC	Se (50); Sn (5)	Ar	1.5 + 1000	300 – 400 + 550	20	15 + 30	5×5

For convenience, the systems are labeled as CC (for confined chalcogen) and IC (for independent chalcogen source) followed by the institution name. CC-NEXCIS and IC-IRDEP are RTP systems, allowing very fast heating rates, while CC-IRDEP and CC-IREC are tubular furnaces. Thermal treatments in CC-NEXCIS and CC-IREC systems are performed under vacuum while CC- and IC-IRDEP annealing systems are atmospheric systems. The use of different annealing systems allows to explore different strategies for kesterite fabrication.

**CC-NEXCIS** NEXCIS RTP confined chalcogen system, described in Broussillou’s PhD thesis [336], allows very fast annealing times ( $< 10$  min). The annealing of  $15 \times 15$  cm<sup>2</sup> precursors is performed in sulfur or selenium atmosphere. The sulfur can be introduced as a powder in the reaction chamber and disposed around the precursor (typically 100 mg, as shown in Figure III.10c). The selenium is inserted before the reactive annealing by depositing a Se capping layer on the precursor.

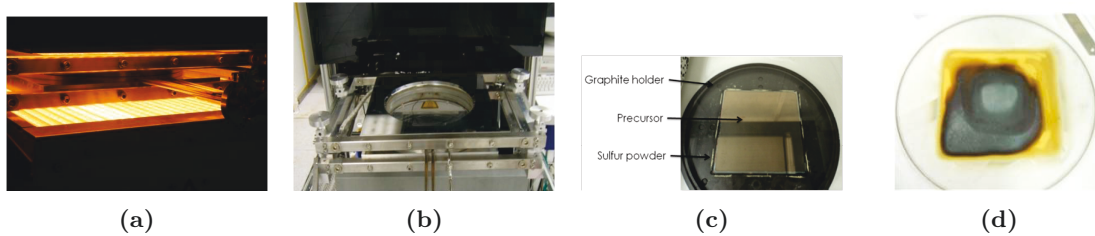


**Figure III.10:** System CC-NEXCIS, a  $15 \times 15$  cm<sup>2</sup> RTP system, composed of (a) IR heating lamps, (b) a reaction chamber, (c) a graphite holder and (d) a quartz cover. The precursor and eventually sulfur powder are disposed in the graphite holder as shown in (c), covered by the quartz cover, and placed inside the reaction chamber. Vapors may condensate on the cover (cold walls) as shown in (d).

The standard thermal treatment is performed according to the following steps:

1. Pump and Purge. The chamber is pumped and purged with argon. A low Ar background pressure ranging from 7 to 500 mbar is maintained.
2. Heating of the reaction chamber with heating ramps as fast as  $2 - 10$  °C/s with IR heating lamps (shown in Figure III.10).
3. Thermal treatment. For the duration of the thermal treatment, all temperatures are kept constant. When the high temperature step is finished, the heating lamps are shut down and allow the cooling down of the system.

After each treatment, the graphite holder and reaction chamber are cleaned with a cloth while the quartz lcover (Figure III.10d) is cleaned by dipping into a sulfuric acid solution.

**IC-IRDEP** System IC-IRDEP is an atmospheric-pressure rapid thermal processing furnace in which selenium and substrate temperatures are independently controlled and for which elemental selenium vapors are transported by nitrogen carrier gas flow. In this IRDEP three-zone tube furnace, described in [38], selenium is evaporated from a crucible held near 260 – 430 °C in the first zone, whose temperature is independent of the annealing temperature. The crucible is fulfilled with approximately 10 g of Se pellets, and weighted after the annealing process so as to calculate the amount of evaporated Se. The second zone is a cracking zone held at 900°C, whose purpose is to reduce the poly-atomic Se species ( $\sum Se_i (i = 1-8)$ ) to smaller molecular species, predominantly  $Se_2$ . Cracked selenium is expected to be more reactive than non-cracked selenium. Selenium vapor is transported by  $N_2$  flux along the furnace to the annealing zone where the sample is located, as shown in Figures III.4 and III.11a. The  $15 \times 15 \text{ cm}^2$  precursors are cut into smaller pieces (up to  $2.5 \times 2.5 \text{ cm}^2$ ) in order to fit into the holder.

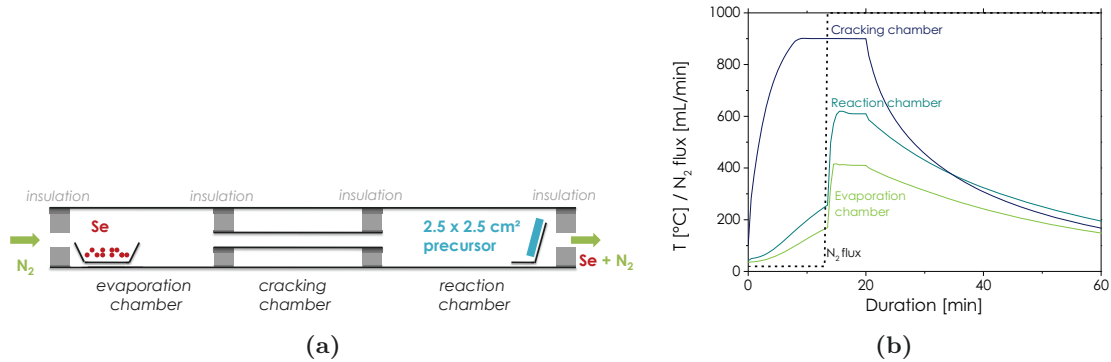


**Figure III.11:** (a) Schematic representation and (b) standard temperature profile of system IC-IRDEP, a three-zone RTP.

The standard thermal treatment is performed according to the following steps (also represented in Figure III.11b):

1. Pump and Purge. The chambers are pumped and purged with nitrogen. After that, a 20 L/min flow of nitrogen circulates through the chambers.
2. Heating of the cracking chamber. In between  $t=0$  min and  $t=2$  min, the cracking chamber is heated from room temperature to 900 °C, and then the temperature is kept constant.
3. Heating of the evaporation and reaction chamber, and start of  $N_2$  flux. At  $t=13.5$  min, the nitrogen flux is increased to 1000 L/min . From  $t=13.5$  min to  $t=16.5$  min, the evaporation chamber is heated to 410°C and the reaction chamber to 610°C.
4. Thermal treatment. From  $t= 16.5$  min to  $t=20$  min, all the temperatures are kept constant. Afterwards, the system is cooled down.

After each treatment, the system is cleaned by applying a 15 min 900°C thermal treatment under 20 L/min  $N_2$  flow at 1 mbar, simultaneously to the three chambers, in order to evaporate the remaining selenium.

**System CC-IRDEP** System CC-IRDEP, described by Bodeux et. al [38], is an atmospheric tubular furnace in which the sample and selenium pellets ( $\approx 70$  mg) are disposed into the same graphite box under argon, as shown in Figure III.12b. The presence of valves allows to keep the atmosphere confined. The graphite box principle is also described in reference [336] (page 98). The annealing is generally performed in the configuration of one or two  $2.5 \times 2.5 \text{ cm}^2$  samples. The

precursors are annealed under an overall atmosphere of  $10^5$  Pa consisting of partial pressures of Ar and Se vapor resulting from the evaporation of the Se pellets.

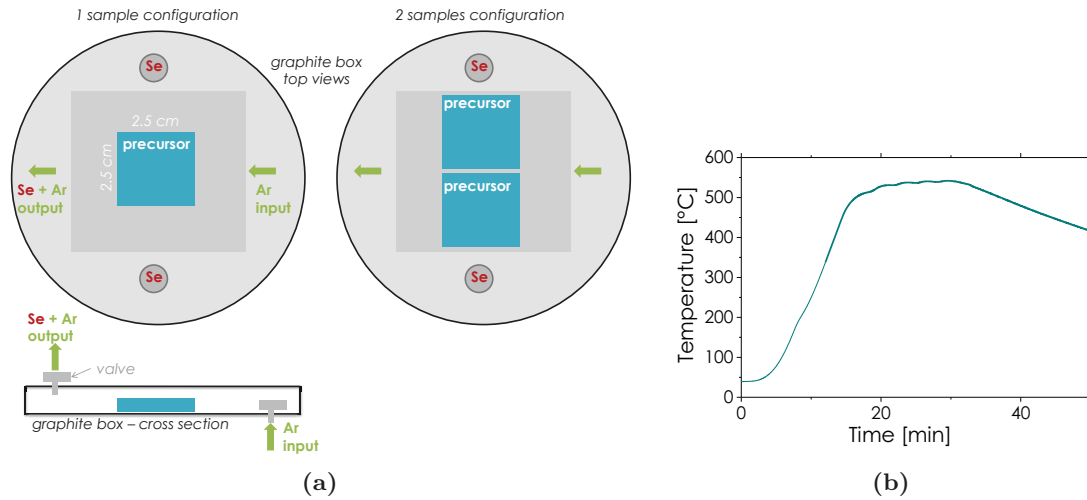


**Figure III.12:** (a) Schematic representation and (b) standard temperature profile of system CC-IRDEP graphite box in tubular furnace.

The standard thermal treatment is performed according to the following steps (Figure III.12b):

1. Pump and Purge. The chamber is pumped and purged with argon. An argon flow at atmospheric pressure is established.
2. Heating of the reaction chamber up to  $600\text{ }^{\circ}\text{C}$  at a rate of  $40\text{ }^{\circ}\text{C}/\text{min}$ .
3. Thermal treatment. For the duration of the thermal treatment (15 minutes), the temperature is kept constant. When the high temperature step is finished, the heating resistance is shut down and allows the system to cool down.

After each treatment, the graphite holders are cleaned with a cloth.

**System CC-IREC** Similarly to system CC-IRDEP, system CC-IREC is a graphite box inside a tubular furnace. System CC-IREC is capable of working in vacuum ( $10^{-4}$  mbar) or in an inert gas Ar atmosphere. The  $15 \times 15\text{ cm}^2$  precursors are cut into smaller pieces (of size below  $5 \times 5\text{ cm}^2$ ) in order to fit into the graphite box used for the annealing. Se powder (50 mg, Alfa Aesar 99.999% purity) and Sn powder (5 mg, Alfa Aesar 99.999%) are placed into the crucibles, as shown in Figure III.13a. The thermal treatment applied is a two-step process already described for the selenization of sputtered metal precursors [113].

While a selenium source is necessary to form the quaternary kesterite phase, elemental Sn is also introduced in order to limit Sn losses observed with the other thermal treatments. The standard thermal treatment is performed according to the following steps, as described in Figure III.13b:

1. Pump and Purge. The chamber is pumped and purged with argon. A 1.5 mbar argon flow is established.
2. Heating of the reaction chamber at a rate of  $20\text{ }^{\circ}\text{C}/\text{min}$ .
3. Thermal treatment: 1<sup>st</sup> step. The temperature is maintained at  $350\text{ }^{\circ}\text{C}$  for 30 minutes. Sn and Se vapors are evaporated into the annealing atmosphere under low Ar pressure, forming quickly the volatile Sn-Se compounds [49]. At the end of the 1<sup>st</sup> step, the argon pressure is adjusted to approximately 800 mbar and all the valves are closed (so as to reach a total pressure of 1 bar at  $550\text{ }^{\circ}\text{C}$ ).
4. Heating of the reaction chamber at a rate of  $20\text{ }^{\circ}\text{C}/\text{min}$ .

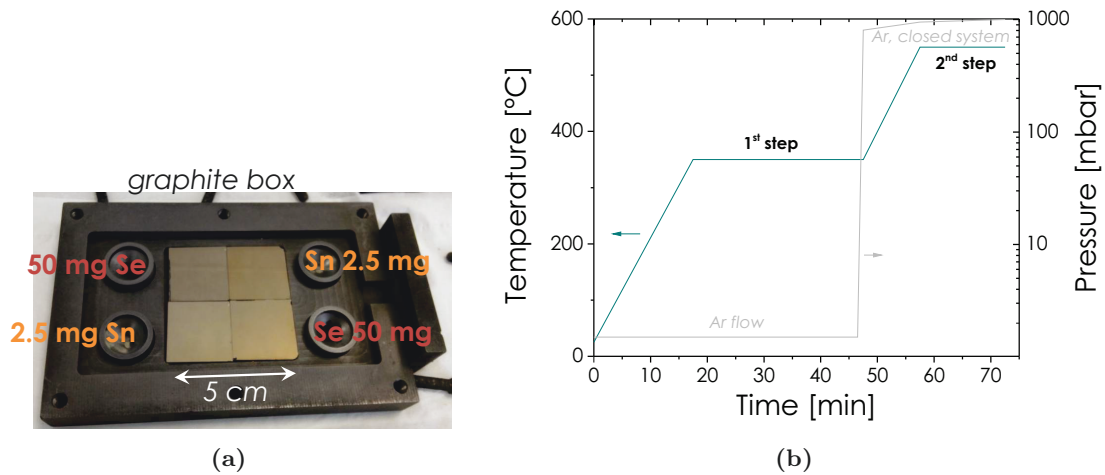


**Figure III.13:** Precursors are placed into (a) the graphite box together with Se and Sn powders, and annealed with (b) standard temperature profile of system CC-IREC.

5. Thermal treatment: 2<sup>nd</sup> step. The temperature is kept constant at 550 °C for 15 minutes. After the annealing, the furnace cools down naturally (during approximately 2 – 3 h).

After each treatment, the graphite boxes are cleaned with a cloth.

## III.2.5 Characterization of the absorber material

### III.2.5.1 Composition

Absorber composition is systematically measured by XRF with a Fischerscope X-Ray XDV-50 equipment (Helmut Fisher AG). The XRF is previously calibrated with absorbers of known composition (i.e., measured by ICP, iCAP 6000 SERIES, Thermo Scientific). The precursor composition is measured on 9 to 49 points over the sample area, allowing to calculate the relative standard deviation (RSD), which gives an indication of macroscopic uniformity (see *Annex B*). Absorber composition profiles are obtained with a GDOES GD Profiler 2 (Horiba Jobin Yvon), or SIMS analysis (Biophy Research). Atomic compositions are also examined by energy-dispersive X-ray (EDX) analysis with 10-20-kV acceleration voltage using an Oxford Instruments X-Max detector.

### III.2.5.2 Morphology

Surface and cross-sectional scanning electron microscopy (SEM) images are recorded using a XL40 FEG microscope (Philips) at a voltage of 10 kV or a Zeiss Series Auriga field emission scanning electron microscope (Zeiss) at a voltage of 5 kV. SEM top-view and cross section images are useful to have an insight on absorber morphology. Informations on the presence of holes at the interfaces, or defects (pinholes), grain size, grain boundaries and thickness of the absorber material are obtained.

### III.2.5.3 Phases

XRD and Raman spectroscopy are common methods to study crystalline thin films and are described in *Annex B*. X-ray diffraction (XRD) spectra are recorded with a INEL Equinox 3000 diffractometer using Cu K $\alpha$  radiation. The suitability of XRD and Raman spectroscopy methods for the detection of kesterite secondary phases has already been discussed in the *Introduction*. XRD and Raman spectroscopy allow to identify Cu-S(e) and Sn-S(e) secondary phases. However, the

quantitative discrimination of the most likely secondary phases ZnS and  $\text{Cu}_2\text{SnS}_3$  from  $\text{Cu}_2\text{ZnSnS}_4$  or ZnSe and  $\text{Cu}_2\text{SnSe}_3$  from  $\text{Cu}_2\text{ZnSnSe}_4$  is known to be very challenging. Smaller XRD peaks can be attributed exclusively to kesterite (experimental and calculated spectra [31, 344]) thereby confirming the presence of CZTS(e), but ZnS(e) and  $\text{Cu}_2\text{SnS}(e)_3$  cannot be ruled out. Berg et al. [203] have shown that even using more complex and time-consuming Rietveld refinement analysis techniques to analyse X-ray diffractograms, only more than 10% ZnS and 50%  $\text{Cu}_2\text{SnS}_3$  can be discriminated from  $\text{Cu}_2\text{ZnSnS}_4$ . In comparison, Raman measurements performed with green-wavelength excitation can discern more than 30%  $\text{Cu}_2\text{SnS}_3$  from  $\text{Cu}_2\text{ZnSnS}_4$  while ZnS is indiscernible. These results show that XRD and Raman data interpretation is limited concerning secondary phases.

As a way out, multiple-wavelength Raman analysis, using UV in addition to green light excitation proved to be a powerful method in order to discern ZnS from CZTS, as previously suggested by Fontané et al. [345] and discussed in the *Introduction*. Therefore multiple-wavelength Raman scattering measurements are performed in back scattering configuration with a LabRam HR800-UV and T64000 spectrometers (Horiba Jobin Yvon). For the HR800-UV system, diode pumped solid-state laser with a wavelength of 785.0 nm was used for excitation. In this system, excitation and light collection are made through an Olympus metallographic microscope, with a laser spot size of the order of 1 – 2  $\mu\text{m}$  (depending on the excitation wavelength). To avoid effects in the spectra related to potential microscopic inhomogeneities, the spot is rastered over an area of  $30 \times 30 \mu\text{m}^2$ . Furthermore, the T64000 system works coupled with an ion- $\text{Ar}^+$  laser, and measurements are made with a 457.9 nm excitation line, projecting a 100  $\mu\text{m}$  spot size on the sample. In all cases and to avoid the presence of thermal effects in the spectra, the power excitation density is around  $50 \text{ W}/\text{cm}^2$ . The first-order Raman spectrum of monocrystalline Si is measured as a reference before and after acquisition of each Raman spectrum, and the spectra are corrected with respect to the Si line at  $520 \text{ cm}^{-1}$ .

## III.2.6 Device fabrication and characterization

### III.2.6.1 Device fabrication

Devices are prepared with different absorbers in order to compare the device performance. In this chapter, devices are fabricated with the processes described in Table III.7, in the same institute where the annealing is undertaken.

**Table III.7:** Device finishing standard procedure, by institute.

<sup>a</sup> At IREC, the devices are not etched by KCN, but they are post-annealed at 200 °C as described in reference [346].

Institute	NEXCIS	IRDEP	IREC
Etching	KCN	KCN	- <sup>a</sup>
Buffer layer	CdS	CdS	CdS
Thickness (nm)	50	50	70
TCO	i-ZnO + ZnO:Al	i-ZnO + ZnO:Al	i-ZnO + $\text{In}_2\text{O}_3$ :Sn
Thickness (nm)	80 + 450	50 + 350	50 + 350
Cell size (mm $\times$ mm)	$5 \times 10$	$5 \times 5$	$3 \times 3$
Contacts?	Ni/Al	no	no
Area (active area) ( $\text{cm}^2$ )	0.5 (0.435)	0.1	0.089

KCN etching is the standard etching applied for CIGS fabrication, because it removes Cu-S(e) binary secondary phases from the surface. It is also widely used for kesterite device fabrication. The influence of etching is discussed in detail in *Chapter 4: Device optimization*. Similarly, cadmium sulfide CdS is the most common buffer layer for thin films photovoltaics (CIGS, CZTS but also CdTe) because of its wide bandgap. CdS is generally deposited by CBD. The influence of the

buffer layer is also discussed in detail in *Chapter 4: Device optimization*. The window layer (TCO) is usually deposited by sputtering.

### III.2.6.2 Device characterization

The electrical properties of the cells are characterized by current voltage measurements in the dark and under illumination at 25°C (AM1.5 global spectrum). At NEXCIS, J-V curves are measured using a Sol3A Class AAA solar simulator from Newport (Irvine, CA, USA) and a Keithley 2651A source meter (Keithley instruments, Inc., Cleveland, OH, USA) and the temperature is controlled by a water-cooled system. EQE curves are measured using an in-house set-up build with Newport equipment. At IREC, the measurement of the optoelectronic properties is carried out using a Sun 3000 Class AAA solar simulator from Abet Technologies (uniform illumination area of  $15 \times 15 \text{ cm}^2$ ) (Milford, CT, USA) providing a AM1.5G spectrum, and a Keithley source meter unit. The spectral response measurements are performed using a pre-calibrated Bentham PVE300 system, allowing to obtain the external quantum efficiency (EQE) of the cells.



### III.3 Results

The formation of a Cu-Sn-Zn-S(e) film of desired composition is a challenging task. In addition, uniformity issues add further challenges. In this section, an overview of the composition control and uniformity is given for different annealing strategies. Despite their numerous similarities, the annealing systems can not be compared directly as too many parameters may influence the results. Therefore the annealing results are presented for each annealing system, classified by institution. The resulting absorbers' morphology and the presence of secondary phases is discussed, together with their influence on device performance.

#### III.3.1 Sulfurization in NEXCIS system

##### III.3.1.1 Experimentals

NEXCIS system is a large scale RTP confined chalcogen system. Different heating ramps can be used, from 10 to 2 °C/s and the total annealing duration is between 3 and 10 min. In particular, the very fast annealing (A, 10 °C/s, 3 min) and fast annealing (B, 2 °C/s, 9 min) are studied, as shown in Figure III.14. A 350 – 450 °C reactive thermal treatment (C) in presence of sulfur is also introduced, as an intermediate step before the higher temperature (550 °C) fast annealing (B).

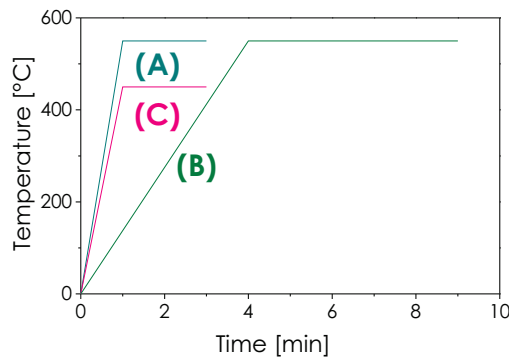


**Figure III.14:** Temperature profiles for RTP annealing in CC-NEXCIS system. (A): Very fast annealing; (B): Fast annealing; (C): Intermediate reactive thermal treatment. Background argon pressure during the annealing is 7 mbar.

##### III.3.1.2 Uniformity and composition control

After sulfurization in system CC-NEXCIS, a 15 × 15 cm<sup>2</sup> RTP system, the measured absorber metallic composition is very different from the initial Cu-Sn-Zn precursor metallic composition, indicating metal losses. Significant losses of Sn and/or Zn are observed, as illustrated in Figure III.15, strongly related to the temperature profile used during the annealing (Fig. III.14 page 88).

For very fast annealings (A), the main loss is of Zn, whereas for fast annealings (B) it is of Sn. The associated absorber uniformity is shown in Table III.8 and typical images of the resulting Cu-Zn-Sn-S samples are shown in Figures III.16 and III.17.

The absorber annealed with temperature profile (B) exhibits a large standard deviation of Sn (more than 18%), indicating a non-homogeneous distribution of the tin content in the absorber film over the sample area. Sn non-homogeneity is also observed in the XRF mapping of the Sn content in Figure III.17b, where regions with very low Sn content are identified. Furthermore the sample surface exhibited different colors in these regions, from darker to lighter grey (Figure III.17a). These observations are consistent with the change of composition towards lower Sn content, due to

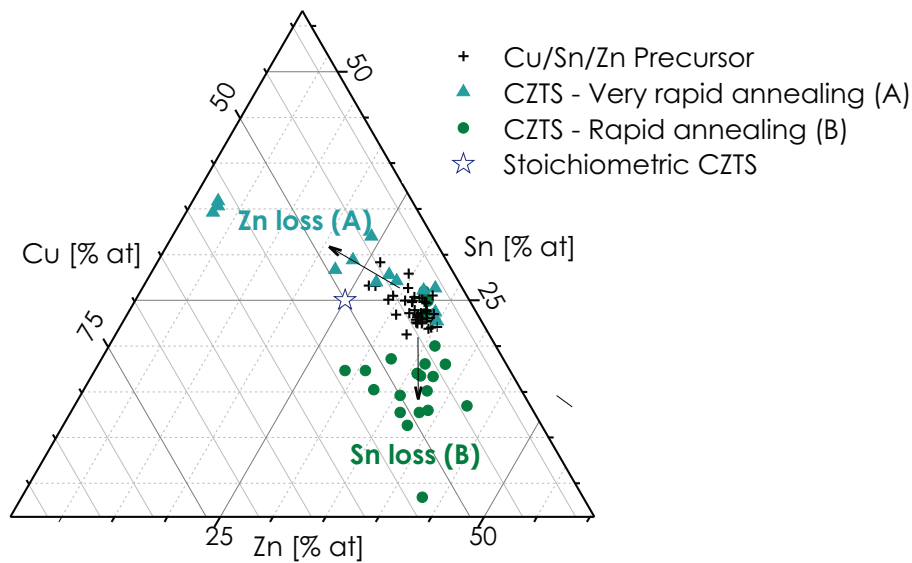


**Figure III.15:** Precursor composition (crosses) and CZTS absorber film composition (triangles and circles) with very fast annealing (A, 10 °C/s, 3 min) and fast annealing (B, 2 °C/s, 9 min) performed under 7 mbar background pressure

**Table III.8:** Relative standard deviation (RSD) of the absorber composition, extracted from XRF mappings (49 points for a 15 × 15 cm<sup>2</sup> sample, edge exclusion of 1 cm).

RSD (%)	Cu	Sn	Zn	S
System CC-NEXCIS - Fast annealing (B)	3.7	18.8	8.0	6.2

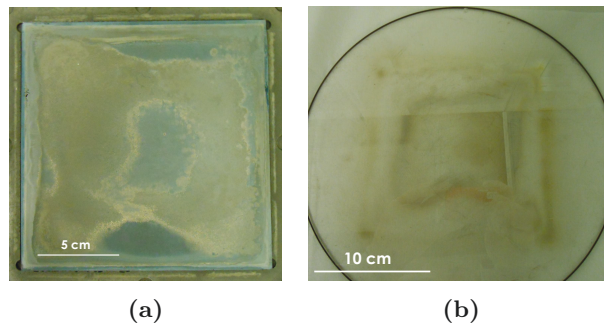


**Figure III.16:** (a) Cu-Zn-Sn-S sample and (b) glass cover after annealing (A).

Sn loss. Evaporated S and SnS compounds condensate on the glass lid cover, as shown in Figure III.17c.

For longer annealing duration than (A) but with the same heating ramp, Sn loss is also observed, indicating that Zn is lost during the first stage of the reaction, while Sn loss occurs later during the annealing. Applying a slower heating ramp than (A) but maintaining the same annealing duration, Zn loss is observed, but in a lower proportion, indicating that Zn loss increases with the ramp heating rate. In RTP systems, the reaction path is driven by kinetics; Zn loss is observed for very fast annealings, because Zn has not enough time to react with S to form the less volatile and more stable phase ZnS. Zn loss is not surprising as Zn is located at the top of the metal stack. Zn loss is also reported in literature for Cu/Sn/Cu/Zn [223] and Sn/Cu/Zn [44] stacks. However, the Cu/Sn/Zn stack order is preferable during the electroplating with respect to the respective

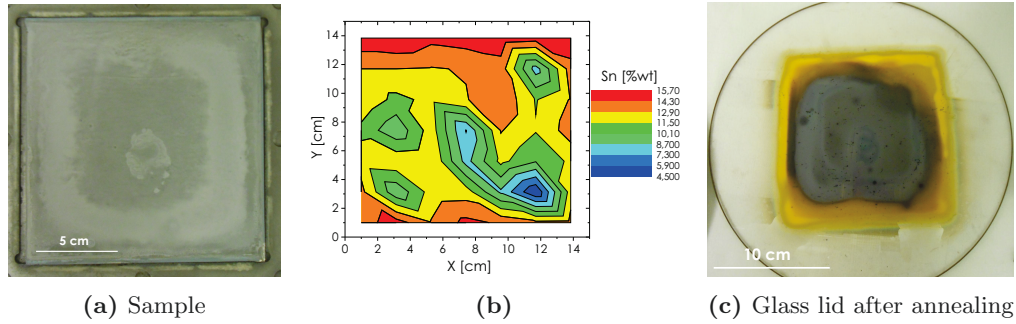


**Figure III.17:** (a) Cu-Zn-Sn-S sample, (b) XRF mapping of Sn element in the Cu-Zn-Sn-S layer and (c) glass cover after temperature profile (B) annealing process.

standard reduction potentials (as described in *Chapter 2*), and Zn loss is also reported when Zn is not in the top layer (Zn/Sn-Cu [347], and n layers of Zn/Sn/Cu [348], Zn/Cu/Sn, Zn/Sn/Cu, Sn/Zn/Cu [44]), so changing the precursor stack order is not considered in this study. When increasing the annealing duration (and applying a lower ramp up rate), the main loss is of Sn, as expected by the volatility of SnS. With longer duration, the sulfur partial pressure decreases, displacing equilibrium to the SnS evaporation side. Furthermore, SnS loss increases with annealing time, for at least two potential causes: SnS loss can originate from its desorption from the surface (Equation III.3 page 77) and from the kesterite decomposition at the back contact (Equation III.6).

**Influence of the background inert pressure in RTP** As the volatile elements evaporation is favored by a low background pressure, the influence of the background pressure in the RTP system is studied. The background pressure in system A is adjusted using argon before the annealing starts. In the previous section, the thermal treatments are performed under 7 mbar of Ar. When varying the background pressure from 7 to 500 mbar, the sulfur is not incorporated uniformly over a  $15 \times 15 \text{ cm}^2$  area, as shown in Figure III.18. The sulfur only gets incorporated into the lateral parts of the samples, closer to the sulfur source. At the center of the sample, the color of the surface changes, and the sulfur content decreases drastically from close to 50% to about 10%.

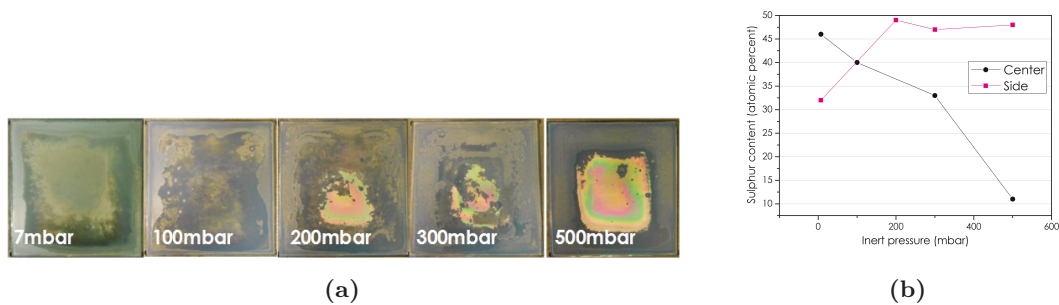


**Figure III.18:** (a)  $15 \times 15 \text{ cm}^2$  samples surface images and (b) incorporated sulfur content in atomic percentage in dependency on the background pressure, with temperature profile (A).

To incorporate sulfur in a uniform way is not trivial as the inert pressure in the chamber should be low enough to ensure a good distribution of the sulfur vapors. With the increase in background pressure, the sulfur needs higher temperatures to vaporize, and the formed vapors do not have enough time to spread in the entire chamber. 50% of sulfur is needed in the Cu-Sn-Zn-S layer to form the stoichiometric kesterite ( $\text{Cu}_2\text{ZnSnS}_4$ ). The best sulfur incorporation over the largest area (at the center of the sample) is obtained at 7 mbar background pressure.

### III.3.1.3 Morphology and secondary phases, impact on device performance

After very fast annealings (A), the absorbers show small grains and the electrical performance is dramatically bad (no efficiency). Meanwhile, when increasing to annealing time (B), the grains become larger, up to some  $\mu\text{m}$  and working devices up to 1.8% are obtained, showing that a longer annealing time is desirable for grain growth and kesterite formation (Fig. III.19).

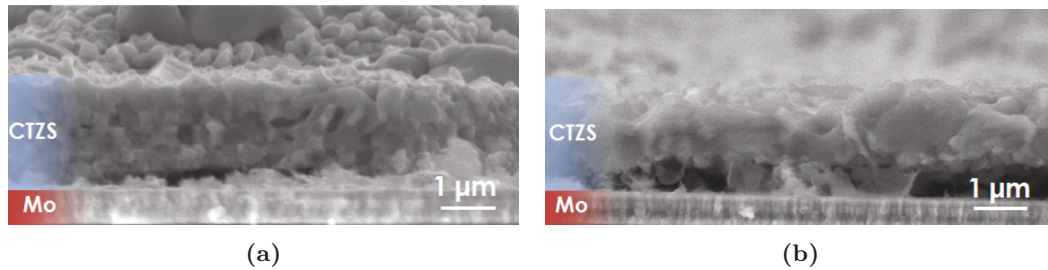


**Figure III.19:** CZTS absorbers SEM cross-section images after (a) temperature profile (A) and (b) temperature profile (B).

However, as previously discussed, temperature profile (B) is associated with a higher Sn loss, which is undesirable for composition control and device performance. When composition is deviated from stoichiometric CZTS, formation of undesirable secondary phases and non-compact morphology become more likely. SEM image (Figure III.20) shows that Zn or SnS evaporation cause morphology defects like holes.

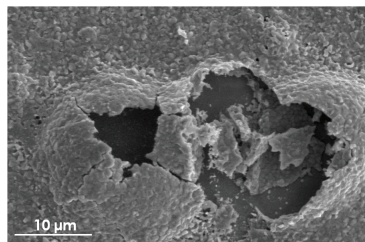


**Figure III.20:** Surface SEM image of an absorber obtained with annealing (B).

**Enhanced absorber morphology by reactive pre-alloying** An additional intermediate annealing step (C) is performed in RTP system CC-NEXCIS in presence of sulfur. This step aims to homogenize the incorporation of sulfur into the  $15 \times 15 \text{ cm}^2$  sample, and to convert Zn into ZnS. The  $350 - 450 \text{ }^\circ\text{C}$  thermal treatment, described in Figure III.14, in presence of sulfur (100 mg) leads to the formation of ZnS at the top surface, as demonstrated by XRD and GDOES in Figure III.21.

This reactive pre-alloying, leading to the formation of a ZnS “capping layer”, helps to stabilize the precursor and to obtain more compact absorbers. After this pre-alloying, the layer is annealed with thermal treatment (B) in presence of sulfur. A compact kesterite layer is then obtained, as shown in Figure III.22, with large grains up to some micrometers.

The improvement in absorber morphology is accompanied by an improvement in device efficiency, as shown in Figure III.23a. The best cell shows 2.4% ( $0.435 \text{ cm}^2$  active area) power conversion efficiency, corresponding to an increase of 33% compared to 1.8% efficiency obtained with annealing (B) based devices. In devices with intermediate step (C), current and FF are higher, and the series resistance is lower than in devices with only annealing (B) ( $8.3 \text{ mA/cm}^2$ , 56%,  $9.5 \Omega \cdot \text{cm}^2$  vs.  $6.9 \text{ mA/cm}^2$ , 46%,  $15.3 \Omega \cdot \text{cm}^2$ , for the respective best cells). This confirms that the current flow across the device is facilitated when less morphological defects are present.

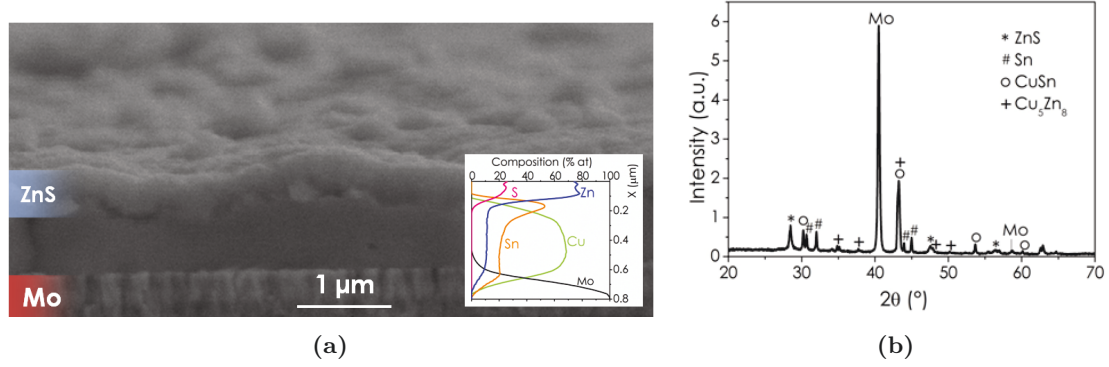


**Figure III.21:** (a) SEM image with GDOES composition profile and (b) XRD pattern of Cu-Sn-Zn-S film after reactive pre-alloying (C).

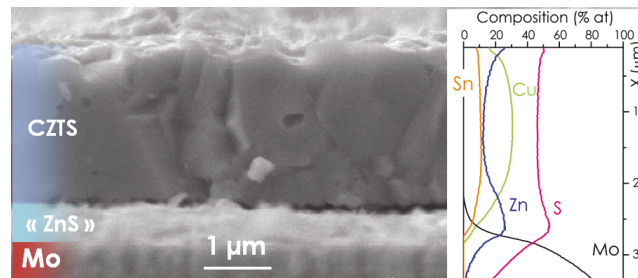


**Figure III.22:** Cross-sectional SEM image and GDOES composition profile of an absorber obtained with reactive pre-alloying (C) + annealing (B).

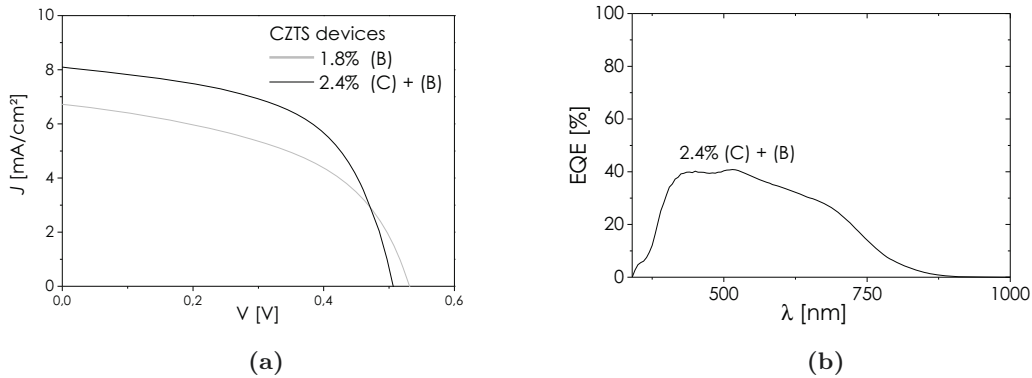


**Figure III.23:** (a) J-V and (b) EQE curves of best CZTS devices prepared with absorbers annealed in system CC-NEXCIS.

Still, efficiencies are highly limited by low  $J_{SC}$  ( $<10$  mA/cm<sup>2</sup>), compared to the  $J_{SC}$  for highest efficiencies (7 – 9%) CZTS solar cells, with 20 mA/cm<sup>2</sup> [29, 132, 349]. The quantum efficiency, shown in Figure III.23b, also indicates a low current (maximum EQE of 40%). The absorber's bandgap, estimated by taking the inflection point of the EQE curve, is of 1.68 eV, which is higher than pure-sulfur CZTS devices typical bandgap — ranging from 1.45 [132, 319] to 1.6 eV [29]. However, in this work, the bandgap may have been overestimated by the bandgap determination method (see Annex B). The average power conversion efficiency measured over a  $5 \times 5$  cm<sup>2</sup> area is only 1%, showing that the uniformity of the layers can be improved. The main reason for low device performances is the non-adherence between the different layers and morphological problems due to elemental losses. Another factor limiting the efficiency is the presence of Zn-rich regions (probably due to the presence of ZnS), which may be responsible for high series resistance, lowering  $J_{SC}$  and FF. The GDOES profile in Figure III.22 shows that excess Zn is present at the top and

the back of the absorber. Segregation of excess Zn at the back of the absorber is believed to be harmless or beneficial [124] but it may increase the series resistance through the presence of voids, and the top Zn excess probably reduces the efficiency of the device by blocking the current at the surface [195]. Therefore, the control of the location of Zn excess segregation is of importance. Improvement of the thermal treatment and Zn rich phase removal by etching the surface of the absorber with HCl [350] could further limit the negative effects of Zn excess.

#### III.3.1.4 Summary

Elemental losses during the annealing process make the control of the final composition difficult, leading to a deviation from the targeted stoichiometry and the appearance of damaging morphology defects. In order to achieve an uniform distribution of the sulfur vapors over a large area, a low background pressure is necessary. As a result, at lower pressure, Zn, SnS, and S volatility is enhanced. The introduction of a reactive pre-alloying step helps limiting the losses, with a clear improvement in morphology and an increase in device performance. The best device shows 2.4% power conversion efficiency, which is still low compared to literature.

### III.3.2 Selenization in NEXCIS system

Considering material availability, pure-sulfur kesterite is more desirable than selenium-containing compounds (see *Introduction*). However, deeper defects, and/or higher defect densities are expected in CZTS than in CZTSe. CZTSe devices in literature show better performances and reduced  $V_{OC}$  deficits compared to CZTS, and are worth to investigate. In this section, the selenization of precursors in the CC-NEXCIS annealing system is investigated.

#### III.3.2.1 Experimentals

The selenization is undertaken under the same conditions as the sulfurization, however the selenium is not incorporated as a powder in the reaction chamber<sup>4</sup>, but deposited as a capping layer onto the Cu-Sn-Zn precursor prior to the annealing. The temperature profiles used for selenization are described in Figure III.24. (A) and (B) are similar as the temperatures profiles used for sulfurization in the previous section. Temperature profile (D) includes an additional low temperature step.

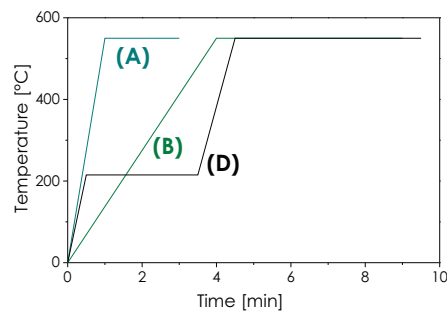


**Figure III.24:** Temperature profiles for selenization in the CC-NEXCIS annealing system. (A): Very fast annealing; (B): Fast annealing; (D): Very fast annealing with a 215 °C intermediate step. Background argon pressure during the annealing is 7 mbar.

<sup>4</sup>Selenium is toxic (risk phrases R23/25, 33, 53 or H301, H331, H373, H413 in the GHS system, see *Annex C*), therefore in an industrial context it is preferable to avoid inhalation risks.

## III.3.2.2 Uniformity and composition control

After annealing (A) or (B), the metallic composition varies, showing a loss of Zn, as demonstrated in Figure III.25. Loss of Sn is not observed, probably because the Se capping layer prevents Sn loss. Selenium tends to be easily evaporated during the thermal annealing process because the melting temperature of selenium (221 °C) is low. The introduction of a 3 minute step at 215°C in a very fast annealing (temperature profile (D), Figure III.24) shows to help reducing the Zn losses, probably because selenium has more time to start melting and reacting with the zinc of the precursor. Indeed, a low temperature step helps to retard selenium evaporation and to transform Se into a relatively non-volatile species [321]. The formation of binary ZnSe is predicted to reduce the Zn loss as ZnSe is less volatile than Zn.

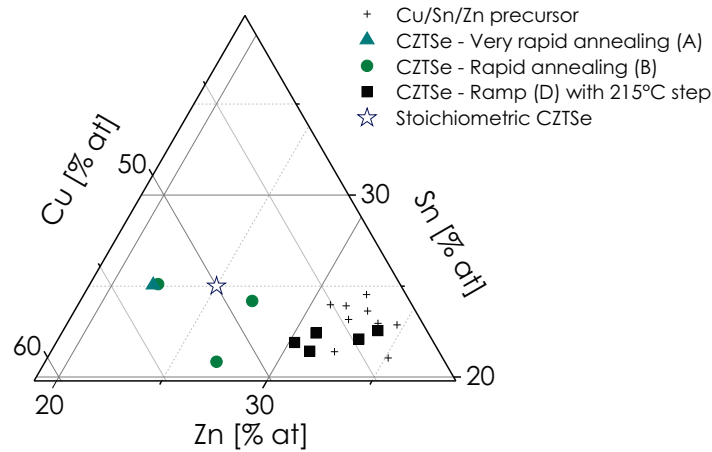


**Figure III.25:** Precursor composition (crosses) and CZTSe absorber film composition with very fast annealing (A, 10 °C/s, 3 min): triangles, fast annealing (B, 2 °C/s, 9 min): rounds and very fast annealing including a 215°C step (D, 10 °C/s, 9 min): squares, all performed under 7 mbar background pressure.

The standard deviation of the resulting Cu-Zn-Sn-Se film composition over the sample area is shown in Table III.9. The values are below 5%, which is a good uniformity for a sample of 15 × 15 cm<sup>2</sup> area. Absorbers obtained with temperature profiles (B) and (D) exhibit similarly good uniformity over the sample area. Compared to Cu-Zn-Sn-S films prepared with the same annealing system A using the same temperature and pressure conditions (temperature profile (B)), the uniformity of Cu-Zn-Sn-Se films is greatly improved. Se capping layer provides a better Se incorporation than S powder disposed around the precursor, probably because the distribution of the chalcogen is more homogeneous.

**Table III.9:** Relative standard deviation (RSD) of the absorber composition, extracted from XRF mappings.

RSD (%)	Cu	Sn	Zn	Se
System CC-NEXCIS - Fast annealing (B)	2.1	3.2	4.1	2.1
System CC-NEXCIS - Very fast annealing with 215°C step (D)	2.9	5.2	4.3	1.3

An example of CZTSe layer appearance is given in Figure III.26, together with the image of condensated vapors on the glass cover (related to Zn loss) and the absorber layer Zn composition mapping. Despite the loss of Zn, the Zn composition is rather uniform across the sample area, indicating again that the Se-capping is beneficial for absorber composition uniformity.

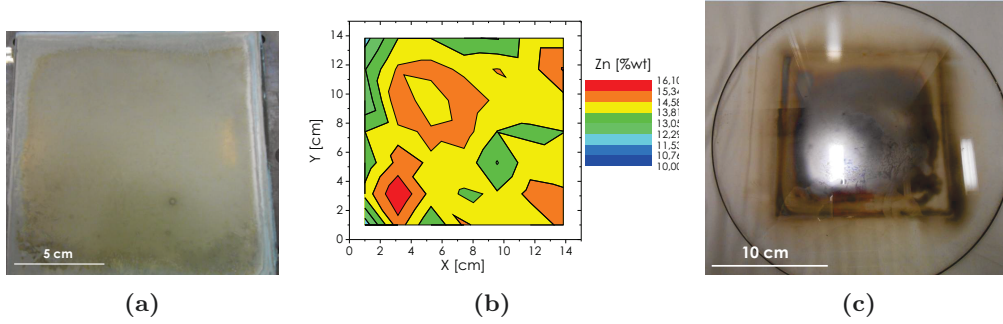


**Figure III.26:** (a) Cu-Zn-Sn-Se sample, (b) XRF mapping of Zn element over the Cu-Zn-Sn-Se film and (c) glass cover after annealing with temperature profile (D).

### III.3.2.3 Morphology and secondary phases, impact on device performance

A cross sectional image of the absorber film prepared with annealing (D) is shown in Figure III.27. The Cu-Zn-Sn-Se film is composed of a large grain layer (approximately a few microns) on top, and a smaller grain layer (sub-micron size) below. It is also observed that the large grain layer and small grain layer are not fully adherent. The GDOES shows that the small grain layer is richer in zinc. ZnSe secondary phase at the back and front interfaces is highly probable, although its presence could not be confirmed with the available characterization methods (XRD and green-wavelength Raman spectroscopy).

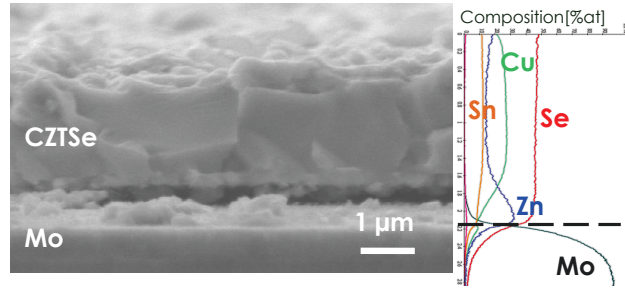


**Figure III.27:** Cross-section SEM image and GDOES composition profile of a Cu-Zn-Sn-Se absorber layer prepared with 215°C step annealing (D) in system CC-NEXCIS.

While devices produced with annealings (A) and (B) have 0% power conversion efficiency, the best device produced with annealing (D) exhibits an efficiency of 5.4% ( $0.435 \text{ cm}^2$ ), as shown in Figure III.28a. The open-circuit voltage of the best device is 367 mV, its short-circuit current  $30.9 \text{ mA/cm}^2$  and fill factor 47.7%. Series resistance of  $3.8 \Omega \cdot \text{cm}^2$  and shunt resistance of  $111 \Omega \cdot \text{cm}^2$  limit the fill factor and device efficiency, as can be observed by the shape of the J-V curve. Non-adherence of the absorber layer with the back contact may be a cause for resistive losses. In addition, Zn-rich regions at the front and back interfaces may also limit the current due to the presence of ZnSe secondary phase, similarly to ZnS for CZTS based devices. ZnSe has been reported to block the current when located at the absorber's surface [195, 196, 351]. CZTSe device performance is also severely limited by the difficulty in collecting photocarriers, as indicated by the large increase in EQE under reverse bias (-1V) for long wavelengths (Figure III.28b). The application of a reverse bias extends the depletion layer into the absorber layer. An increase in photocurrent is linked to a larger fraction of the minority photocarriers that are swept by the field, indicating that a larger depletion width improves the collection efficiency [352]. The poor collection efficiency in this cell is most likely caused by very low carrier lifetime, which can be due to a high defect density in the absorber layer or to high recombination loss at the back contact or at the front interface. The bandgap is approximated to  $1.0 - 1.1 \text{ eV}^5$ , which is in agreement with typical values reported for

<sup>5</sup>Here, the bandgap is determined by taking the intercept of  $[\text{ExEQE}]^2$  vs E near the band edge, which is a rough



CZTSe devices [13, 31]. An average efficiency higher than 4% is obtained over a  $5 \times 5 \text{ cm}^2$  area, as shown in Figure III.28c.

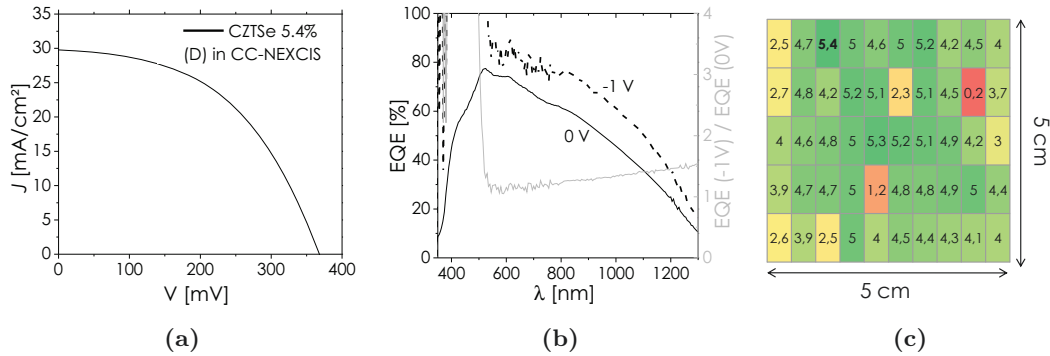


**Figure III.28:** (a) J-V curve, (b) EQE at 0 V, EQE under reverse bias (-1 V) and ratio EQE(-1 V)/EQE(0 V) of the best CZTSe device (5.4%). (c) Mapping of power conversion efficiency over a  $5 \times 5 \text{ cm}^2$  sample (i.e. 50 cells), including the 5.4% cell. Devices have been produced with absorbers annealed in system CC-NEXCIS with temperature profile (D).

### III.3.2.4 Summary

Introducing the chalcogen as a capping layer helps to improve the absorber uniformity and to reduce the evaporation of Zn. However, since some zinc is always lost after annealing, it is difficult to control the absorber composition accurately. Best device efficiency of 5.4% is obtained for a Zn-rich CZTSe device.

## III.3.3 Selenization in IRDEP systems

### III.3.3.1 Uniformity and composition control

Selenization of  $2.5 \times 2.5 \text{ cm}^2$  precursors in annealing systems IC-IRDEP and CC-IRDEP is undertaken under atmospheric conditions using the steps described in the section *Experimentals*. The ternary diagram in Figure III.29 shows the precursors and absorbers composition.

The absorbers are poorer in tin (around 20%) compared to the precursors (between 25 and 30%), for both CC- and IC-IRDEP systems. This change in composition indicates a loss of tin during the annealing, which can be related to SnSe volatility. The uniformity of different absorbers is given in Table III.10.

**Table III.10:** Relative standard deviation (RSD) of CZTSe absorbers composition, extracted from XRF mappings (36 points over  $2.5 \times 2.5 \text{ cm}^2$ ).

RSD (%)	Cu	Sn	Zn	Se
System IC-IRDEP (RTP)	2.0	4.3	3.7	1.4
System CC-IRDEP (Tubular)	2.4	5.8	4.2	1.9

In the IC-IRDEP RTP system, the compositional uniformity of selected samples is good over the sample area ( $2.5 \times 2.5 \text{ cm}^2$ ), as shown in Table III.10 and Figure III.30. Annealing conditions such as  $\text{N}_2$  flux or evaporation chamber temperature have proven to be of crucial importance for the fabrication of uniform absorber samples.

approximation (See Annex B).

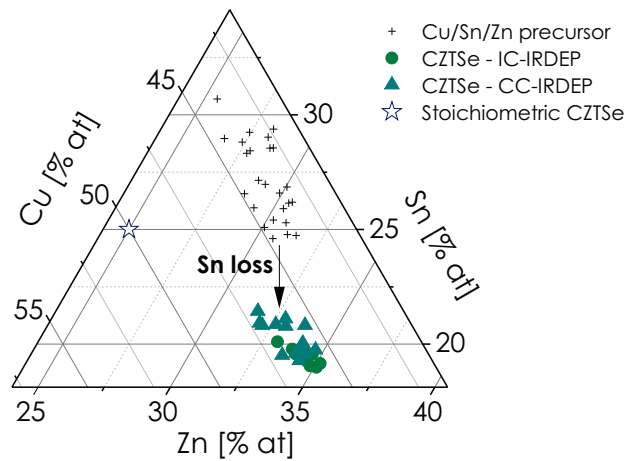


**Figure III.29:** Precursor composition (crosses) and CZTSe absorber film composition after annealing in system IC-IRDEP (circles) and system CC-IRDEP (triangles) under various conditions (standard annealing conditions and variations in temperature,  $N_2$  flux, Se amount).

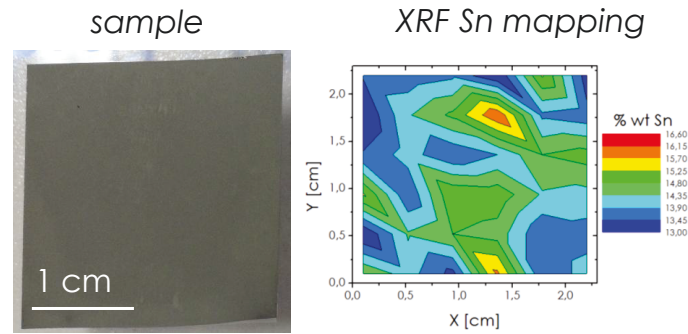


**Figure III.30:** Uniformity of an absorber annealed in IC-IRDEP system.

Samples annealed in the confined chalcogen (CC) system, exhibit good but lower uniformity compared to absorbers annealed in the IC system. Their surface has a non-uniform aspect, corresponding to a different distribution of tin content, as shown by the absorber image and corresponding tin content mapping (Figure III.31). In the CC system, the absorber aspect (at eye sight) and tin composition (measured by XRF) are strongly dependent on the annealing configuration (1 or 2 samples, as shown in Figure III.12a), thereby highlighting the non-uniform distribution of chalcogen vapors in the reaction chamber.

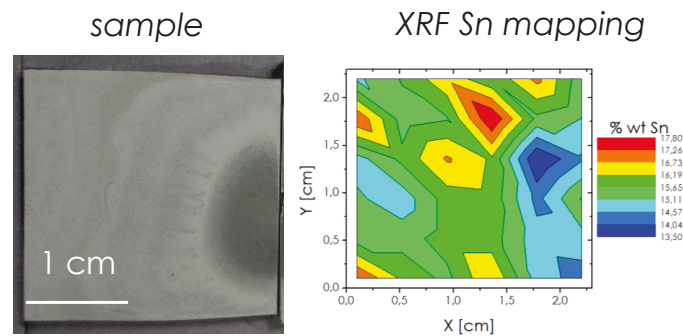


**Figure III.31:** Uniformity of an absorber annealed in CC-IRDEP system (2 samples configuration).

### III.3.3.2 Morphology and secondary phases, influence on device performance

**Selenization according to standard conditions** Absorbers annealed in the systems IC-IRDEP and CC-IRDEP (standard conditions described in the section *Experimentals*) present different morphologies and composition profiles, as shown in Figure III.32.

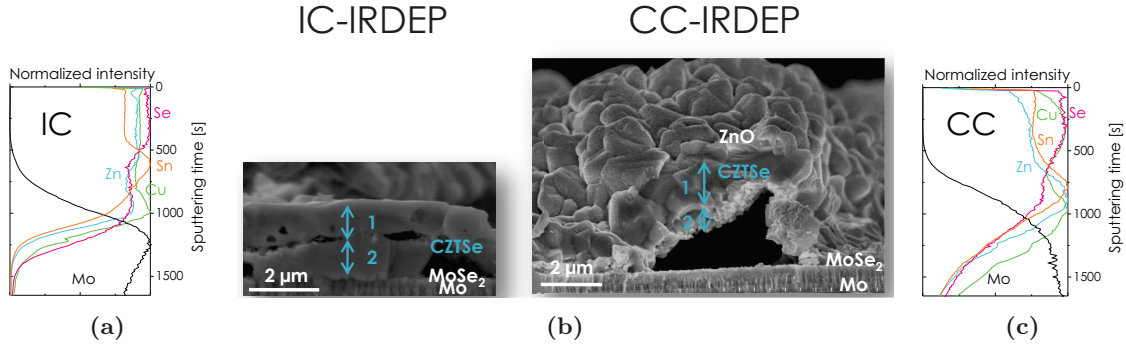


**Figure III.32:** (b) Cross-section SEM images and (a) (c) SIMS composition profiles of absorbers annealed in IC-IRDEP and CC-IRDEP systems.

Absorbers annealed in the three-zone furnace IC-IRDEP have larger kesterite grains ( $2 - 5 \mu\text{m}$ ) than CC-IRDEP absorbers ( $0.5 - 2 \mu\text{m}$ ) probably because of the higher selenization temperature ( $600$  vs.  $550^\circ\text{C}$ ). Both annealing procedures lead to a bi-layer absorber structure. In the case of IC-IRDEP annealing, the two layers are equal in thickness and are composed of large grains. The interface between the two large-grain layers is Sn-rich, as observed by SIMS, which may provide a leakage pathway (shunt resistance). In the case of CC-IRDEP annealing, the bottom layer is much smaller than the top layer and has very small grain size, similarly to the structure observed after selenization in CC-NEXCIS annealing system (Figure III.27). The small grain layer is richer in Zn and Sn than the large grain layer, probably because of the presence of secondary phases. Finally, the absorber annealed in the confined chalcogen system also presents a chaotic morphology, with voids and lifting of the absorber layer, which may be caused by SnSe evaporation during the annealing.

The XRD patterns of absorbers produced in annealing systems IC- and CC-IRDEP are represented in Figure III.33. Main XRD peaks can be attributed to kesterite  $\text{Cu}_2\text{ZnSnSe}_4$ . Binary ZnSe, and the ternary phase  $\text{Cu}_2\text{SnSe}_3$  are difficult to discriminate from CZTSe as their lattice parameters are very similar (See *Introduction*). The secondary phase SnSe is detected by XRD in the absorber annealed in the CC-IRDEP system.

The best device efficiency is of 4.2% with an absorber annealed in the IC-IRDEP system (vs. 3.5% with an absorber annealed in CC-IRDEP system). Average high series resistances of 4 and  $11 \Omega \cdot \text{cm}^2$  and low shunt resistances of 33 and  $40 \Omega \cdot \text{cm}^2$  for devices produced with IC- and CC-annealed absorbers, respectively, show that the device performance is severely limited by resistive effects. The Sn-rich interface between the two layers of the IC-annealed absorber may be the reason for a low shunt resistance. The presence of SnSe secondary phase and non-adherence of the absorber to the back contact seem to be the main causes for resistive losses in the CC device. Other parameters extracted from the J-V curves can be found in Table III.11 on page 100.

**Enhanced morphology by Se-capping** Before the annealing, the precursors can be covered by a Se capping layer, as described in the section *Experimentals*. The Se layer is deposited with sub-stoichiometry and the remaining selenium is incorporated during the annealing. The resulting absorbers' morphologies are shown in Figure III.34. In comparison with the absorbers obtained from uncovered precursors (Figure III.32), the absorbers from Se-capped precursors have a more compact morphology. Noticeably, the voids and non-adherence between the absorber and back contact observed for the absorbers annealed in the CC-system are dramatically reduced. The size

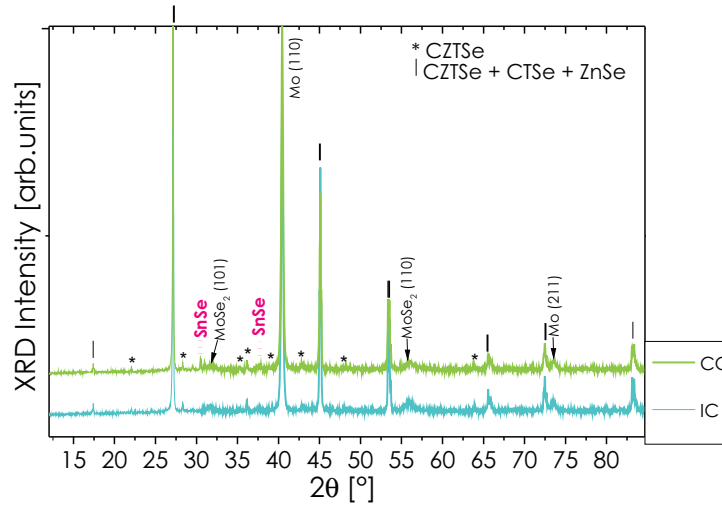


**Figure III.33:** XRD pattern of absorbers annealed in atmospheric systems IC- and CC-IRDEP.

of the grains and composition profiles are relatively similar to the absorbers prepared without Se capping layer.

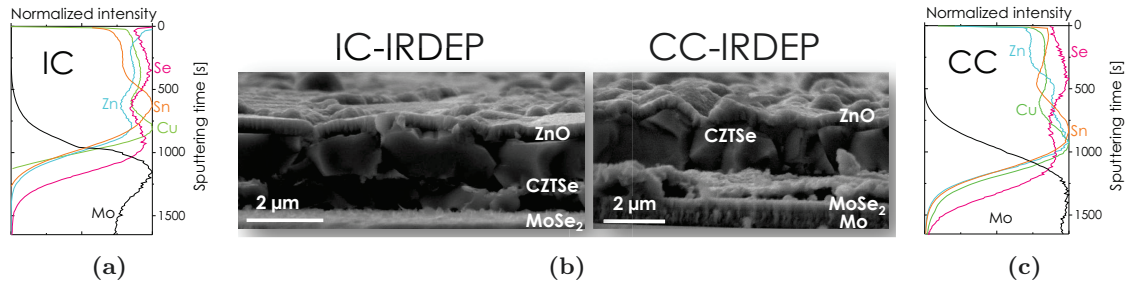


**Figure III.34:** (b) Cross-section SEM images and (a) (c) SIMS composition profiles of absorbers annealed in IC-IRDEP and CC-IRDEP systems from Se-capped precursors.

SnSe secondary phase is not detected in the XRD patterns (not shown here) of the absorbers prepared with Se-capped precursors, neither after annealing in the IC-system nor after annealing in the CC-system. This demonstrates that Se-capping is beneficial to avoid the presence of secondary phases. Power conversion efficiencies as high as 5.5% are obtained with the IC-IRDEP system and 5.3% with the CC-IRDEP system. All the opto-electronic parameters extracted from the J-V curves are detailed in Table III.11.

Devices prepared with Se capped metal precursors exhibit better performances and better uniformity (lower *RSD*) than devices from uncovered precursors. The addition of the Se-capping layer is helpful to improve the absorbers' morphology, uniformity and to limit the presence of secondary phases. Best device (5.5%) characteristics are the following: open circuit voltage 345 mV, short circuit current 30.3 mA/cm<sup>2</sup>, and fill factor 52.7%. EQEs of some of the best devices are represented in Figure III.35.

The best devices' bandgap is approximated to 0.95 – 1.0 eV<sup>6</sup>, which is in accordance with typical bandgap values reported for CZTSe devices [13, 31, 353]. In the intermediate and long wavelength region ( $\lambda > 600$  nm), EQE of CZTSe devices increases under -1V reverse bias, indicating that a larger depletion width improves the collection efficiency, testifying an insufficient carrier collection due to interface recombination and/or deficient minority charge carrier diffusion length. However,

<sup>6</sup>Here, the bandgap is determined by taking the intercept of  $[\text{ExEQE}]^2$  vs  $E$  near the band edge, which is a rough approximation (See Annex B).

**Table III.11:** CZTSe devices optoelectronic parameters, produced with absorbers annealed in IC- and CC-IRDEP systems from bare and Se-capped precursors. Main optoelectronic parameters (power conversion efficiency  $\eta$ , open circuit voltage  $V_{OC}$ , short-circuit current  $J_{SC}$ ) are reported in the following way: best value at cell size (area:  $0.1 \text{ cm}^2$ ), average value for the full sample ( $36 \text{ cells}$ , i.e.  $2.5 \times 2.5 \text{ cm}^2$ ) and its RSD. The reported values for the fill factor (FF), series resistance and shunt resistance are averaged values of the complete sample.

Precursor type	Annealing system	$\eta$ (%)			$V_{OC}$ (mV)			$J_{SC}$ (mA/cm <sup>2</sup> )			FF (%)	$R_S$ ( $\Omega \cdot \text{cm}^2$ )	$R_{SH}$ ( $\Omega \cdot \text{cm}^2$ )
		Max	Ave	RSD (%)	Max	Ave	RSD (%)	Max	Ave	RSD (%)	Ave	Ave	Ave
Cu-Sn-Zn	IC-IRDEP	4.2	2.0	71	343	253	36	28.1	22.1	27	32	4	33
Cu-Sn-Zn/Se	IC-IRDEP	5.5	2.0	53	345	247	23	30.3	23.0	21	33	3	17
Cu-Sn-Zn	CC-IRDEP	3.5	2.0	32	353	286	22	27.8	21.1	23	34	11	40
Cu-Sn-Zn/Se	CC-IRDEP	5.3	3.9	13	350	323	4	30.7	28.3	4	43	7	73

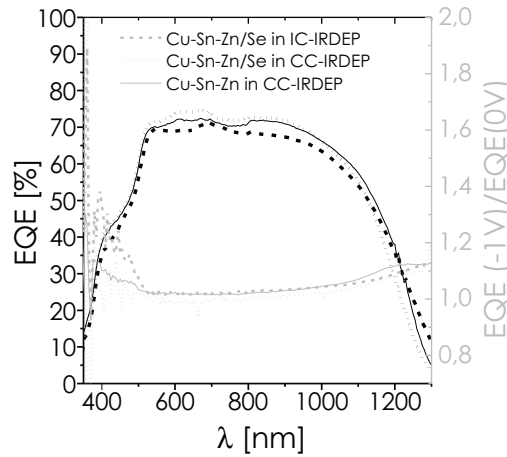


**Figure III.35:** EQE of CZTSe devices prepared with absorbers annealed in systems IC-IRDEP and CC-IRDEP with uncovered and Se-capped precursors.

here the increase of EQE at -1V is of smaller magnitude than the one observed for CZTSe devices produced with CC-NEXCIS system and NEXCIS device finishing (Figure III.28b), suggesting that the interface and/or charge carrier diffusion length are improved in IRDEP CZTSe devices.

### III.3.3.3 Summary

Both confined chalcogen (CC) and independent chalcogen (IC) IRDEP annealing systems are suitable for kesterite fabrication. In all cases a Sn loss is observed, which is detrimental for composition control. Even if better uniformity is achieved for absorbers annealed in IC-IRDEP system, the small sample size ( $2.5 \times 2.5 \text{ cm}^2$ ) does not allow to conclude on large-scale uniformity. A selenium-capping layer improves the absorbers morphology and uniformity, which is in agreement with the results of the previous section (Selenization of Se-capped precursors in large scale RTP system). However, high series resistance (non-adherence of the absorber to the back contact and small grains in CC-annealed absorbers) and low shunt resistance (current pathways via Sn-rich interface in IC-annealed absorbers, presence of SnSe secondary phase in CC-annealed absorbers) lower the devices' performance.

### III.3.4 Selenization in IREC system

#### III.3.4.1 Composition control and uniformity

The absorber composition after annealing in CC-IREC system, illustrated in Figure III.36, does not show major variation from the precursor composition. Elemental Sn and Se in the initial annealing atmosphere fastly form volatile Sn-Se compounds and serve as a chalcogen source for CZTSe formation. High Se and SnSe partial pressures prevent the decomposition reaction of CZTSe at elevated temperatures and introduce Sn into a Sn-deficient film.

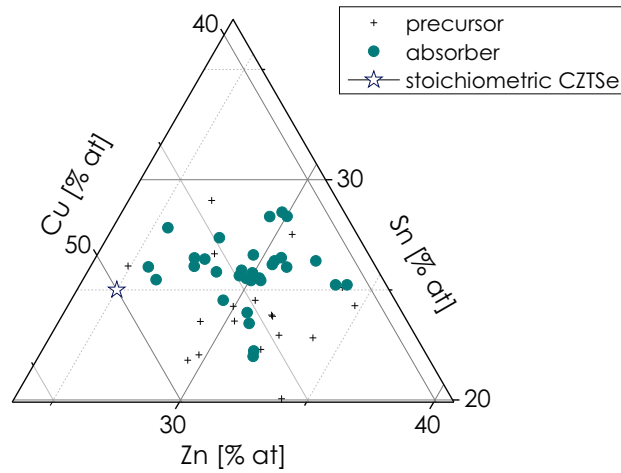


**Figure III.36:** Precursor composition (crosses) and CZTSe absorber film composition after annealing in CC-IREC system.

In addition, the absorbers composition is uniform over the sample area ( $5 \times 5 \text{ cm}^2$  for the largest samples), as shown in Table III.12 and Figure III.37.

**Table III.12:** Relative standard deviation (RSD) of the absorber composition, extracted from XRF mappings.

RSD (%)	Cu	Sn	Zn	Se
System CC-IREC	1.6	3.1	3.9	0.8

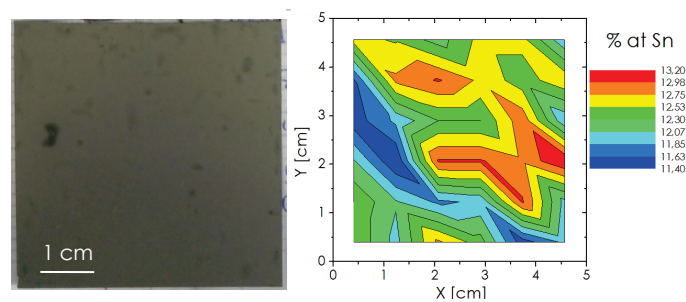


**Figure III.37:** Image of an absorber annealed in system CC-IREC.

### III.3.4.2 Morphology and secondary phases, influence on device performance

After the annealing, approximately 230 nm  $\text{MoSe}_2$  and 1.5 – 2  $\mu\text{m}$  CZTSe layers are obtained, as shown in Figure III.38. The absorber's GDOES depth profile indicates a lower Cu content at the back and front interface compared to the bulk suggesting that the composition is not uniform across the layer, and indicating the possible presence of secondary phases.

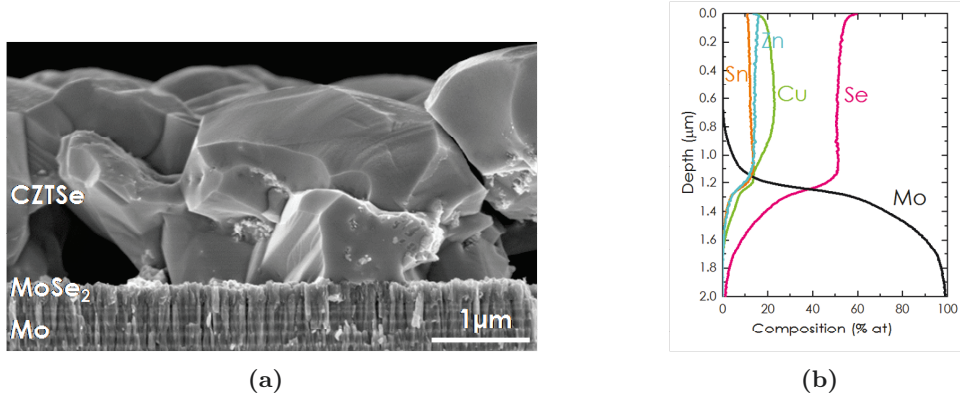


**Figure III.38:** (a) SEM cross-sectionnal image and (b) GDOES composition profile of a CZTSe absorber after annealing in system CC-IREC.

Limited losses allow an improved composition control, therefore the influence of the absorber composition on the eventual presence of secondary phases can be investigated in this section. The studied composition range is Cu-poor Zn-rich. After annealing, the absorbers have compositions of  $\text{Cu}/(\text{Zn}+\text{Sn})=0.67 - 0.82$  and  $\text{Zn}/\text{Sn}=0.86 - 1.32$ . Scanning electron microscopy combined with energy-dispersive X-ray (SEM + EDX) analysis reveals the presence of secondary phases on the absorbers surfaces.

**ZnSe secondary phase** As expected, ZnSe is detected on the surface of several absorbers. Characteristic small ZnSe grains cover almost completely the surface of Zn-richer absorbers. The coverage of ZnSe grains is not uniform at microscopic scale, as shown for a Zn-rich absorber in Figure III.39. Some regions are fully covered with small grains while on some regions, no secondary phase is observed.

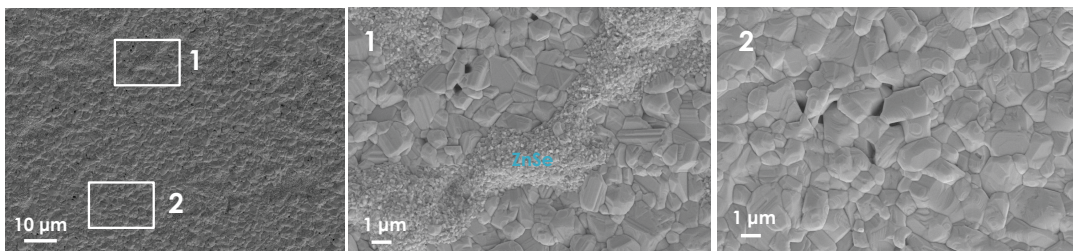


**Figure III.39:** SEM surface of a Zn-rich absorber ( $\text{Cu}/\text{Zn}+\text{Sn}=0.80$ ,  $\text{Zn}/\text{Sn}=1.25$ ), partly covered with small ZnSe grains.

Identification of ZnSe by XRD is very challenging due to the overlap with the CZTSe XRD pattern [198]. Therefore Raman spectroscopy using resonant conditions (457.9 nm excitation wavelength) is a very helpful tool in order to identify ZnSe phase at the surface of Zn-richer absorbers [202], as shown in Figure III.40.

In conclusion, ZnSe secondary phase can be detected by SEM surface analysis and identified by Raman spectra analysis. Figure III.41 summarizes the composition regions for which ZnSe is

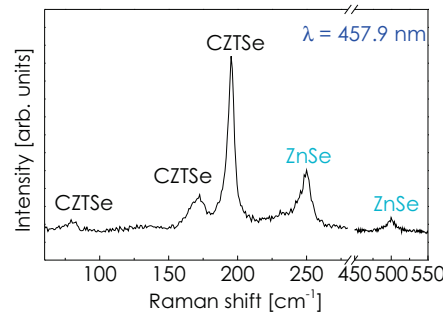


**Figure III.40:** Raman spectra of a Zn-rich absorber ( $\text{Cu}/\text{Zn}+\text{Sn}=0.69$ ,  $\text{Zn}/\text{Sn}=1.32$ ).

detected by SEM analysis. The ZnSe secondary phase is always detected when  $\text{Zn}/\text{Sn}>1$ , in the Cu-poor Zn-rich region of the ternary diagram, in agreement with literature observations [55,196,351].

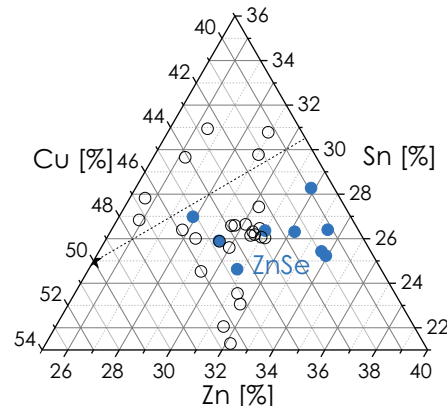


**Figure III.41:** Ternary diagram showing the detection zones for ZnSe secondary phase by SEM for different absorber composition. Note that not all samples were studied by SEM.

**Sn-Se ( $\text{SnSe}$ ,  $\text{SnSe}_2$ ) secondary phases** Characteristic Sn-Se grains are observed on many absorbers, as shown exemplarily in Figure III.42. These grains are also detected on the surface of some Zn-rich absorbers.

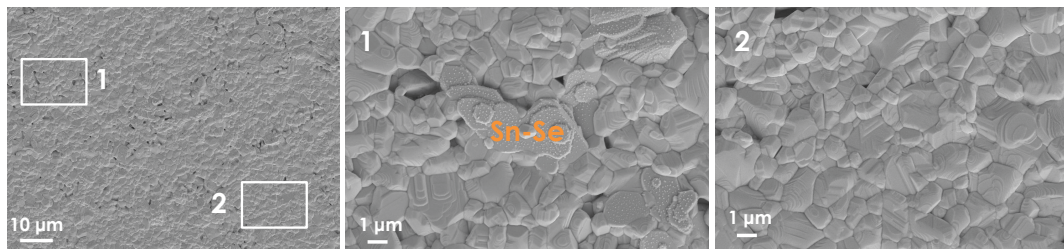


**Figure III.42:** SEM surface of a Sn-rich absorber ( $\text{Cu}/\text{Zn}+\text{Sn}=0.79$ ,  $\text{Zn}/\text{Sn}=0.89$ ), partly covered with small Sn-Se grains.

Figure III.43 shows  $\text{SnSe}$  and  $\text{SnSe}_2$  signatures in XRD patterns and Raman spectra (pre-resonant conditions: 785 nm excitation wavelength) in Sn-rich absorbers. The XRD peak at  $14.43^\circ$  corresponds to  $\text{SnSe}_2$  [194, 197, 200]. The peak around  $31^\circ$  is attributable to the most intense powder



diffraction peaks of SnSe and SnSe<sub>2</sub>, indicating the presence of SnSe, SnSe<sub>2</sub>, or co-existence of SnSe and SnSe<sub>2</sub> in the absorber [193,200]. SnSe peak at 37.78° could not be detected in our case.

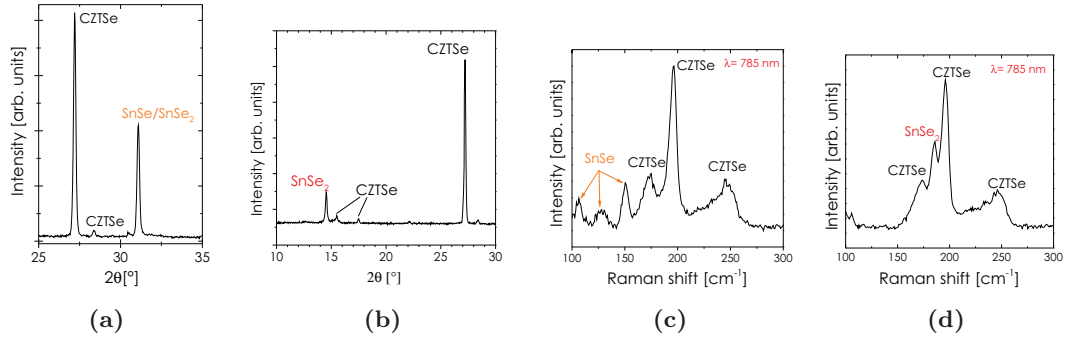


**Figure III.43:** (a), (b) XRD patterns and (c), (d) Raman spectra of Sn-rich absorbers. Absorber composition is (a) Cu/Zn+Sn=0.70, Zn/Sn=0.98, (b) Cu/Zn+Sn=0.79, Zn/Sn=0.89, (c) Cu/Zn+Sn=0.74, Zn/Sn=0.86 and (d) Cu/Zn+Sn=0.68, Zn/Sn=0.94.

In all the Sn-rich absorbers ( $Zn/Sn < 1$ ) and in some Zn-rich absorbers ( $Zn/Sn > 1$ ) which are very deficient in copper, Sn-Se secondary phases are detected by X-ray diffraction. SnSe and SnSe<sub>2</sub> secondary phases are also confirmed at the surface by Raman spectroscopy in Sn-rich absorbers ( $Zn/Sn < 1$ ) and in Zn-rich ( $Zn/Sn > 1$ ) absorbers. The presence of Sn-Se secondary phases in dependence of the absorber composition is represented in Figure III.44. Obviously, Sn-Se secondary phases are expected in Sn-rich Cu-poor conditions such as  $Zn/Sn < 1$ . In addition, Sn-Se secondary phases are detected for a Cu-poor composition region where  $Zn/Sn > 1$ , since this region is actually rich in Zn and in Sn, as represented in Figure III.7 and explained by Collord et al. [45]. In this composition region, Sn-Se secondary phases are detected quite easily by SEM analysis of the overall surface. However, their detection by XRD or Raman spectroscopy is more challenging as the secondary phases peaks are less intense, probably due to small concentrations and non uniform distribution at the surface.

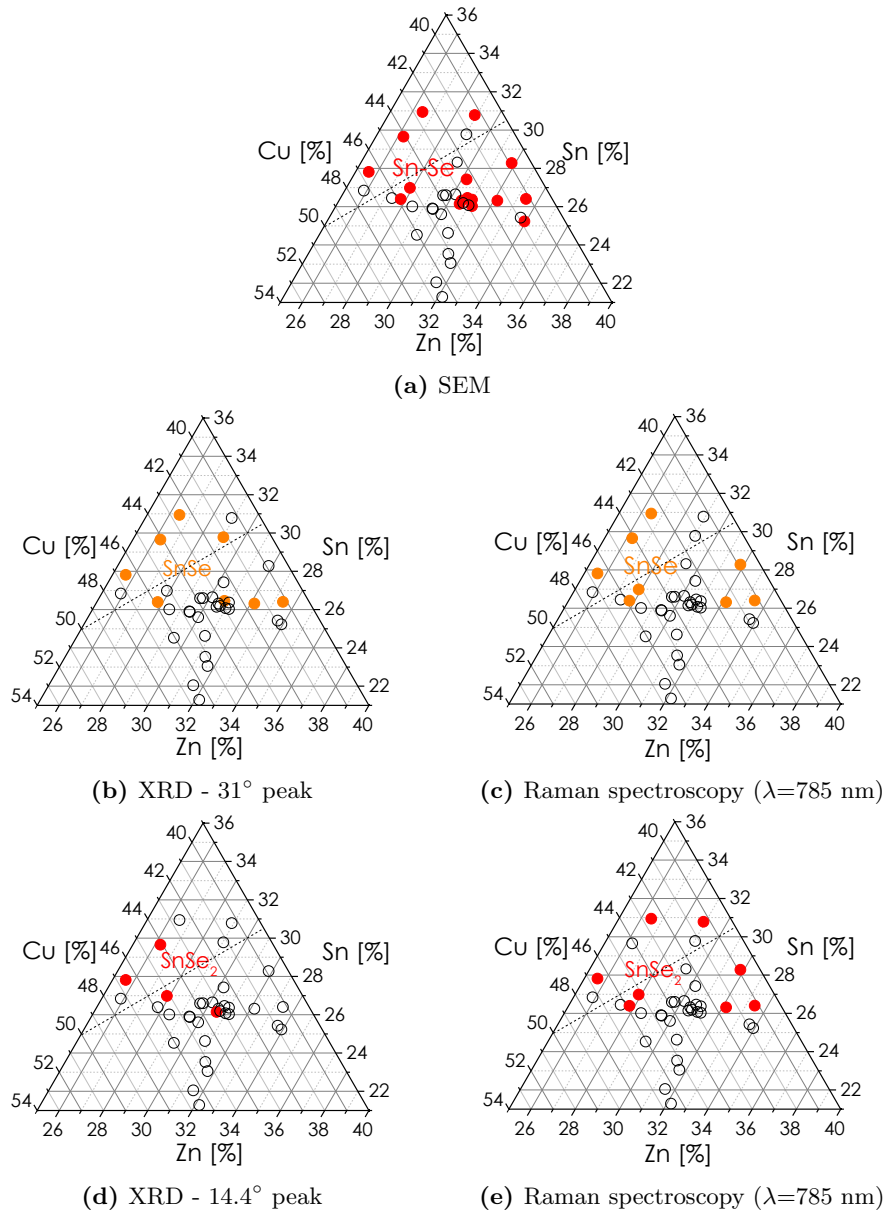


**Figure III.44:** Ternary diagram showing the Sn-Se ( $\text{SnSe}$ ,  $\text{SnSe}_2$ ) secondary phases presence composition regions, as detected by (a) SEM, (b), (d) XRD and (c), (e) Raman spectroscopy at 785 nm. The dashed line corresponds to  $\text{Zn}/\text{Sn}=1$ . Full circles indicate the detection of the concerned phase. Empty circles mean that the phase was not detected or that the sample was not characterized with the corresponding technique.

In a same absorber, different zones can be found, some of them showing Zn-rich, others Sn-rich phases or even no secondary phases. The amount of Zn-Se or Sn-Se secondary phases varies greatly with the Zn/Sn and Cu/(Zn+Sn) ratios and can be limited using precursors of optimum composition ( $\text{Cu}/(\text{Zn}+\text{Sn})=0.65 - 0.85$  and  $\text{Zn}/\text{Sn}=1.10 - 1.25$ ). SEM and Raman spectroscopy allow to characterize the surface while XRD is a bulk characterization method. The three characterization methods detected secondary phases in the same absorbers, indicating that when the secondary phases are present, a part of them is always located at the surface. The presence of these secondary phases on the surface is in agreement with the GDOES depth composition profile, where copper is shown to be depleted at the front interface. In this same GDOES composition profile, copper is also depleted at the front interface, therefore secondary phases may also be located at the back of the absorber. Sn-Se crystalline features are observed at the back of Sn-rich absorbers, as shown in Figure III.45a, and ZnSe is detected at the back of Zn-rich absorber (Figure III.45b).

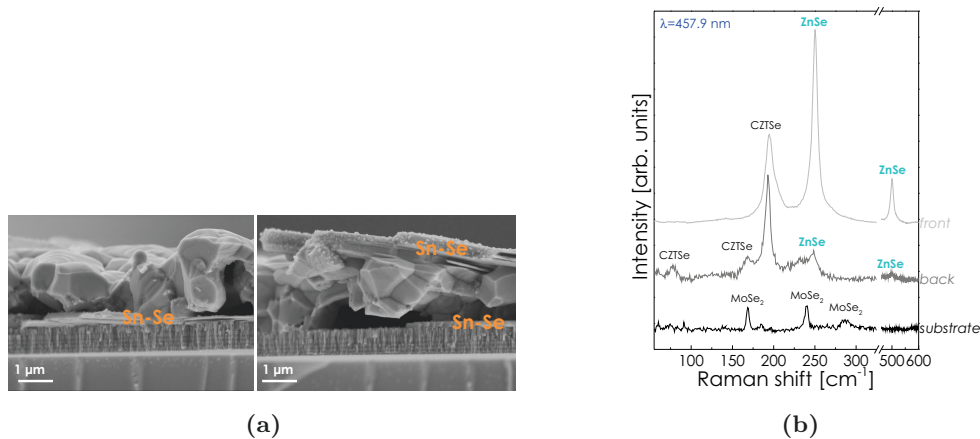


**Figure III.45:** Secondary phases detected at back contact by (a) SEM in a Sn-rich absorber ( $\text{Cu}/\text{Zn}+\text{Sn}=0.74$ ,  $\text{Zn}/\text{Sn}=0.86$ ) and by (b) Raman spectroscopy in a Zn-rich absorber ( $\text{Cu}/\text{Zn}+\text{Sn}=0.69$ ,  $\text{Zn}/\text{Sn}=1.32$ ).

**Effect of secondary phases on device efficiency** In conclusion, after reactive annealing, several secondary phases are identified at the surface of the absorbers. The secondary phases are detected both at the surface and at the back of the absorber, their presence within the bulk can not be ruled out. When present in large amounts, ZnSe is detected by pre-resonant Raman spectroscopy (457.9 nm) and Sn-Se by XRD and Raman spectroscopy (785 nm). As the secondary phases are present at the absorbers' surface, they are also detected by SEM surface analysis. Figure III.46a summarizes the different zones in the ternary diagram where secondary phases are present. Cu-Se secondary phase is not detected in this investigation probably because the studied compositions are Cu-poor.

The presence of secondary phases has an influence on device performance, as shown in Figure III.46b and Table III.13. The influence on device performance does not depend only on the presence of secondary phase or not but also on its location (in the bulk or at the interface) and concentration.

Sn-rich absorber-based devices exhibit the lowest efficiency, low open-circuit voltage and low shunt resistance, as expected from the presence of shunting Sn-Se secondary phases. Zn-richer absorbers-based devices are less efficient than Zn-rich ones, probably because of the presence of a large amount of ZnSe secondary phase, thereby limiting the short-circuit current. Intermediate composition (Zn/Sn of 1.03) absorbers-based devices are also less efficient than Zn-rich ones, as the presence of Sn-Se and ZnSe secondary phase is expected. A best device power conversion efficiency of 6.0% is achieved for a Zn-rich device of composition  $\text{Cu}/(\text{Zn}+\text{Sn})=0.73$ ,  $\text{Zn}/\text{Sn}=1.10$ , with an average of 5.3% for the sample. The best device has a short circuit current of 31.7 mA/cm<sup>2</sup>, an open-circuit voltage of 382 mV and a fill factor of 49.7%. The associated bandgaps, estimated by taking the

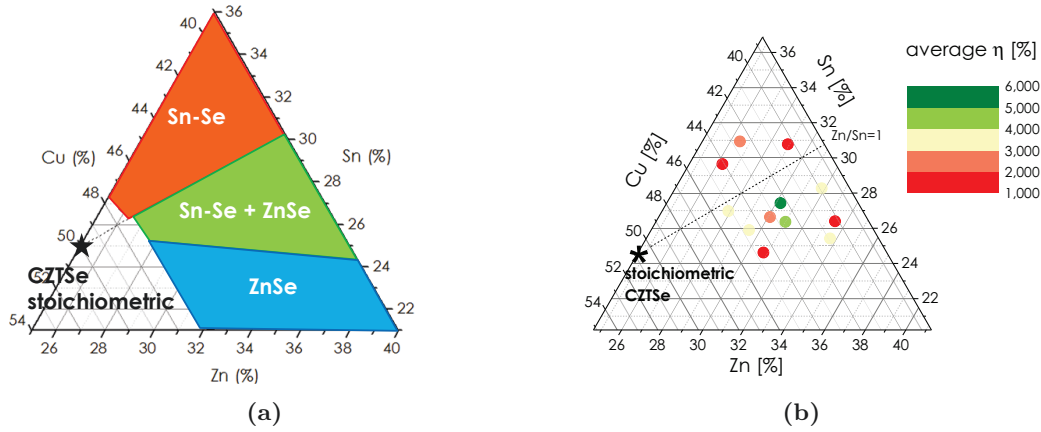


**Figure III.46:** Ternary diagrams showing the (a) zones of secondary phases presence and (b) average power conversion efficiency in dependence of absorber composition. Orange and blue zones present large amounts of  $\text{SnSe}/\text{SnSe}_2$  and  $\text{ZnSe}$  secondary phases, respectively. In the green area, the amount of secondary phases is limited when the composition is closer from stoichiometry but increases when the copper content decreases.

**Table III.13:** Kesterite devices optoelectronic parameters for different absorber composition, after annealing in system CC-IREC.  $\text{Cu}/(\text{Zn}+\text{Sn})$  and  $\text{Zn}/\text{Sn}$  ratios are measured by XRF on absorbers. Main optoelectronic parameters (power conversion efficiency  $\eta$ , open circuit voltage  $V_{OC}$ , short-circuit current  $J_{SC}$ ) are reported in the following way: best value at cell size (active area:  $0.087 \text{ cm}^2$ ), average value for the full sample ( $18$  to  $36$  cells, i.e.  $1.5 \times 2.5 \text{ cm}^2$  to  $2.5 \times 2.5 \text{ cm}^2$ ) and its RSD. The reported values for the fill factor (FF), series resistance and shunt resistance are averaged values of the complete sample.

Sample composition	Cu/(Zn+Sn)	Zn/Sn	$\eta$ (%)			$V_{OC}$ (mV)			$J_{SC}$ ( $\text{mA}/\text{cm}^2$ )			FF (%)	$R_S$ ( $\Omega.\text{cm}^2$ )	$R_{SH}$ ( $\Omega.\text{cm}^2$ )	$E_g$ (eV)
			Max	Ave	RSD (%)	Max	Ave	RSD (%)	Max	Ave	RSD (%)	Ave	Ave	Ave	Best cell
Sn-rich	0.68	0.94	1.7	1.3	23	261	241	7	19.9	17.0	15	31	5.5	21	1.04
Intermediate	0.82	1.03	4.2	3.2	28	335	297	15	31.1	27.8	10	38	3.3	31	1.02
Zn-rich	0.73	1.10	6.0	5.2	10	393	377	2	31.7	30.5	4	45	2.2	81	1.06
Zn-richer	0.69	1.32	3.6	3.2	9	356	347	2	27.0	25.6	4	36	5.2	36	1.05

inflection point of the EQE, are also given in Table III.13. The bandgaps range from 1.0 to 1.1 eV, which is typical for pure-Se CZTSe devices.

### III.3.4.3 Summary

The addition of elemental Sn into the reaction chamber of the CC-IREC annealing system (a graphite box), and of a first step carried out at  $350^\circ\text{C}$ , allowed a better control of absorber composition, without major Sn or Zn loss. Moreover, the absorber's composition shows a good uniformity over  $5 \times 5 \text{ cm}^2$  area. As a result, the CC-IREC annealing system makes it possible to study the effect of absorber composition on the presence of secondary phases and device performance. A best device efficiency of 6.0% is obtained for a Zn-rich CZTSe device.

### III.4 Conclusions

With the different annealing systems studied in this section, Cu-Zn-Sn-S and Cu-Zn-Sn-Se thin films are produced from Cu-Zn-Sn metal precursors. In the  $15 \times 15 \text{ cm}^2$  CC-NEXCIS system, a low background pressure is needed to achieve a good distribution of the chalcogen vapors. Under these conditions the compounds volatility is enhanced and it becomes very challenging to control accurately the composition. In the case of sulfurization, using different heating conditions leads to losses of Zn (very fast annealing) or SnS (fast annealing). In the case of selenization, the addition of a Se-capping layer improves the uniformity of the absorber layer and limits the losses. Thermal treatments performed at higher (atmospheric) pressures, in IC-IRDEP and CC-IRDEP ( $2.5 \times 2.5 \text{ cm}^2$ ) also show a loss of tin. One strategy to limit Sn loss is to saturate the SnS(e) content in the reaction chamber by addition of Sn or SnS(s), as reported by Redinger et al. [41]. This strategy has shown to pay off for the composition control of absorbers annealed in system CC-IREC. A summary of the results, including elemental losses during the annealing, can be found in Table III.14.

**Table III.14:** Main annealing results for different thermal treatment systems.

Name	Material	Losses?	Uniformity (RSD)	Best efficiency %	Absorber morphology	Zn excess location	Bandgap eV
CC-NEXCIS	CZTS	Zn, Sn	<20	2.4	fine grains/large grains	front and back	1.68
CC-NEXCIS	CZTSe	Zn	<6	5.4	fine grains/large grains	front and back	1.0 – 1.1
IC-IRDEP	CZTSe	Sn	<5	5.5	large grains/large grains	uniform	0.95 – 1.0
CC-IRDEP	CZTSe	Sn	<6	5.3	fine grains/large grains	back	0.95 – 1.0
CC-IREC	CZTSe	no	<4	6.0	large grains	front	1.0 – 1.1

With all the annealing systems that have been studied in this chapter, similar CZTSe device performances have been obtained (between 5.3% and 6.0%). When volatile compounds evaporate during the annealing, the absorber morphology is often damaged (holes, non-adherence at the back contact), which severely increases the series resistance and lower the device performances. If the composition is not accurately controlled, the presence of secondary phases is favored. Even in the best composition range for high device performance (Cu-poor Zn-rich), ZnSe and SnSe (SnSe, SnSe<sub>2</sub>) secondary phases are detected. These secondary phases have been reported to be detrimental to device efficiency and the quality of the CZTS(e) film surface. As absorber surface quality is crucial for the function of a photovoltaic cell — this surface forms one-half of the heterojunction that separates photogenerated carriers — the next chapter treats different routes for device optimization. The CC-IREC system, allowing a better composition control and uniformity, will be used for the investigation presented in the next chapter.

# Chapter IV

## Device optimization

### Contents

---

IV.1	Kesterite surface treatments	111
IV.1.1	Background	111
IV.1.1.1	Removal of Cu- and Sn-based secondary phases	112
IV.1.1.2	Removal of Zn-based secondary phases	113
IV.1.1.3	Passivation effect	113
IV.1.2	Experimentals	113
IV.1.2.1	Etchings	113
IV.1.2.2	Material Characterization	114
IV.1.2.3	Device completion	114
IV.1.2.4	Device Characterization	114
IV.1.3	Results	114
IV.1.3.1	Removal of secondary phases	115
IV.1.3.2	Influence of etching on the device performance	117
IV.1.3.3	Influence of the secondary phases on the device opto-electronic properties	118
IV.1.3.4	Conclusions	119
IV.2	Buffer optimization	120
IV.2.1	Background	120
IV.2.1.1	Cadmium sulfide	120
IV.2.1.2	Alternative buffers	120
IV.2.2	Experimentals	123
IV.2.2.1	Absorbers	123
IV.2.2.2	Buffer layer deposition parameters	123
IV.2.2.3	Device completion	123
IV.2.2.4	Material characterization	123
IV.2.2.5	Device Characterization	123
IV.2.3	Results	124
IV.2.3.1	CdS optimization	124
IV.2.3.2	Alternative buffer layers	126
IV.3	Front contact optimization	129
IV.3.1	Background	129
IV.3.1.1	TCO	129
IV.3.1.2	Metal contacts	129
IV.3.1.3	Anti-reflective coating	129
IV.3.2	Experimentals	130
IV.3.2.1	Device preparation	130

IV.3.2.2 Device characterization . . . . .	130
IV.3.3 Results: Implementation of metal contacts . . . . .	130
IV.4 Conclusions . . . . .	<b>131</b>
IV.4.1 Optimal parameters for high-efficient kesterite devices . . . . .	131
IV.4.2 Optimum processes . . . . .	133

---

Once the kesterite layer, a p-type semiconductor, is formed (*Chapter 3*), different steps are necessary for the completion of a device, including a wet chemical etching, deposition of a n-type buffer layer, and a conductive transparent window layer. In this chapter, the influence of these processing steps on the final device efficiency is studied, so as to 1) maximize the device efficiency, 2) explore the options compatible with an industrial process. This chapter focuses on the preparation of pure selenide CZTSe devices.

The junction of p-type and n-type semiconductors is the basis of a working solar cell. Its working principle has already been described in the *Introduction*. Two processes that proved themselves for the formation of a p-n junction in CIGS solar cells are KCN etching and CdS buffer layer deposition by CBD. These processes are commonly used for CZTSSe devices as well. KCN etching has proved to be efficient for the removal of detrimental  $\text{Cu}_x\text{S}(e)$  secondary phases, which may be present at the surface of chalcopyrite or kesterite absorbers. CBD is an established process for CdS deposition on CIGS and offers beneficial ancillary effects, such as etching of surface oxides from the absorber surface by  $\text{NH}_4\text{OH}$  present in the CBD solution [354]. However, these processes may not be optimal for the kesterite device performance. A defective buffer/absorber interface or an unoptimized band alignment can cause performance losses in kesterite devices. According to Mitzi et al. [179], recombination occurring at the kesterite/buffer interface would partially explain the  $V_{OC}$  deficit, one of the main reasons for the lower efficiencies of kesterite devices when compared to CIGS. Thus, optimization of the heterointerface is of crucial importance to obtain high-efficient kesterite devices.

## IV.1 Kesterite surface treatments

### IV.1.1 Background

The presence of local secondary phases in the kesterite absorber is detrimental to device performance and explains partly the losses in  $V_{OC}$ . The impact of the secondary phases depends on their nature (bandgap, concentration) but also on their location in the absorber. For instance the ZnSe secondary phase is reported to block the current when located at the surface, but to be harmless when located near the back contact [195]. Kanevce et al. [51] reported that secondary phases are a strong contributor to  $V_{OC}$  losses when located at the heterointerface, by increasing the impact of interface recombination. Therefore, removal of the secondary phases from the interface is of great interest in order to improve the device performance. The wet chemical etching principle is illustrated in Figure IV.1.

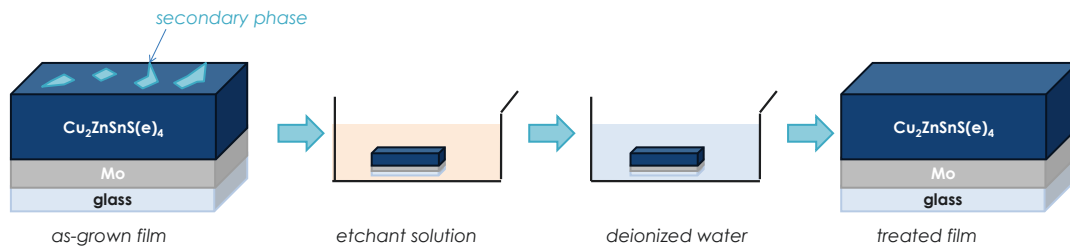


**Figure IV.1:** Schematic of etching principle. The sample is immersed in the etchant solution in order to treat the absorber’s surface.

Several etching procedures have been developed by different groups in order to remove the secondary phases from the kesterite surface, as shown in Table IV.1. The wet chemical etching procedures can provide many benefits: 1) Cleaning of the surface by removal of oxides, 2) Selective removal of detrimental secondary phases from the surface, 3) Surface passivation.



**Table IV.1:** Wet chemical etchings in literature.

Etchant solution (concentration)	$T$ °C	$t$ min	Secondary phases removed (etching rate) (nm/s)	Best cell $\eta$ (Unetch ref) %
KCN			Cu <sub>x</sub> S [238]	
KCN			CuS	4.1 [355]
KCN (10% wt)	RT	3	Cu <sub>2-x</sub> S [237,356,357]	
KCN (10% wt)	RT	30	Cu <sub>2</sub> Se [358]	
KCN (5% wt), KOH (0.5% wt)	20	2	Cu <sub>x</sub> Se, Se <sup>0</sup> , Cu <sub>x</sub> SnSe <sub>y</sub> , SnSe <sub>2</sub> , SnO <sub>2</sub> [359,360]	
KCN (5% wt)		1	Natives oxides, totally [354]	
KCN (1.5 M)		3	Cu-, Sn-based phases [52]	
KCN (10% wt)	RT		Cu-, Sn-, Se-phases	Improved [53]
(NH <sub>4</sub> ) <sub>2</sub> S (20% wt)	RT	15	Cu <sub>x</sub> Se [361]	-
(NH <sub>4</sub> ) <sub>2</sub> S (4-22% wt)	RT	1	SnS (1.1), SnS <sub>2</sub> (0.5), SnSe (1.2), SnSe <sub>2</sub> (0.2), CZTSSe (<0.13)	5.9 [54]
Br <sub>2</sub> -MeOH (0.02 M)		1	Cu-, Sn- related phase, probably CuSnSe <sub>3</sub>	5.8 (0.5) [192]
Br <sub>2</sub> -MeOH (1%)	RT		Cu-, Zn-, Sn-, Se-	Improved [362]
HCl (37% wt)		1	Zn-related, probably ZnSe	5.0 (4.4) [192]
Concentrated HCl	RT		Sn-, Se- but also Cu- and Zn-	Improved [362]
HCl (5% v/v)	75	5	ZnS	5.2 (2.7) [350]
HCl (8%)			probably oxides	5.0 (3.5) [39]
KMnO <sub>4</sub> (0.01M) / H <sub>2</sub> SO <sub>4</sub> (1M)	RT	0.5	ZnSe (1.4); CZTSe (1)	5.0 (3.6) [55]
+ Na <sub>2</sub> S (1M)	RT	+ 1		

#### IV.1.1.1 Removal of Cu- and Sn-based secondary phases

**KCN** KCN etchant solution is typically used to remove copper sulfides (Cu<sub>x</sub>S) and selenides (Cu<sub>x</sub>Se) from the surface of CIGS absorbers [363–365]. These secondary phases are known to increase the shunt conductance in chalcogenide-based photovoltaic cells. Based on the CIGS process, many groups include a KCN etching step in the fabrication of kesterite devices [61, 196, 233, 366]. Cyanide ions form complex compounds with Cu<sup>2+</sup> ions, but Sn-based phases and oxides are also removed [52, 53]. The impact of the KCN etch on the solar cell performances depends on the chemical composition of the CZTS(e) absorber. When Cu-S(e) phases are present, KCN etching removes the secondary phases [358] and solar cell performances improve. However, the impact of KCN etching in absence of Cu-based secondary phases — as Cu-poor growth conditions are typically used for the formation of kesterite — is unclear. On the one hand, KCN etching may be beneficial as oxides are removed from the absorber surface. In addition, KCN etching is reported to create a Zn-rich CZTS surface composition, resulting in a larger CZTS bandgap at the CZTS/CdS junction, which is expected to reduce interface recombination and the resulting open circuit voltage deficit [367]. On the other hand, Cu-rich CZTSe surface composition and lower device performance have been reported with long KCN/KOH etchings [360]. One of the main drawbacks of KCN is its high toxicity. An alternative, safer compound would be more suitable for industrial processing of photovoltaic cells. Alternative approaches based on a thermal treatment, chemical and electrochemical processes have been proposed for the removal of Cu<sub>x</sub>Se compounds from the CIGSe surface [361].

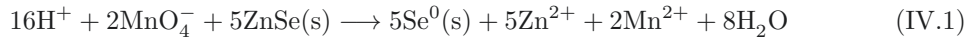
**(NH<sub>4</sub>)<sub>2</sub>S** Ammonium sulfide (NH<sub>4</sub>)<sub>2</sub>S has been proposed by Buffiere et al. [361] for the removal of Cu<sub>x</sub>Se phases in CIGSe compounds and by Xie et al. [54] for the removal of SnS(e)<sub>x</sub> secondary phases in CZTSSe absorbers. Compared with KCN, ammonium sulfide is a safer compound and already used for surface passivation in III–V technologies. Etching of Cu<sub>x</sub>Se phases is not reported by Xie et al., probably because no Cu<sub>x</sub>Se phases were present at the CZTSSe absorbers’ surface. The etching of Cu<sub>x</sub>Se or Sn-Se from the CIGSe or CZTSe surface can be explained by two simultaneously occurring effects: i) Dissolution of Se in aqueous ammonium sulfide and ii) Formation of complex compounds between remaining Cu<sup>2+</sup> or Sn<sup>2+</sup> and NH<sub>3</sub> ions. Furthermore, the ammonium sulfide treatment not only cleans the absorber surface by removing detrimental secondary phases and oxide/carbonate compounds but also leads to the formation of a sulfur-based compound on the extreme surface of the absorber layer by action of HS<sup>-</sup> ions. As a consequence, the absorber surface is passivated, leading to an increase in the minority carrier lifetime [54, 361].

**Bromine** Acidic bromine etching (HBr/Br<sub>2</sub>) is reported to etch CIGSe by oxidative action of Br<sub>2</sub>. In a first step Br<sub>2</sub> oxidates the metals Cu, In, Ga, leading to their preferential dissolution. In a second step, Se is oxidated and dissolved [368]. Bromine Br<sub>2</sub>-MeOH treatment is suggested to remove Cu-, Sn-related phases, such as Cu<sub>2</sub>SnSe<sub>3</sub> [192] from the CZTSe absorber's surface, improving thereby the device performance, especially the V<sub>OC</sub>. It is not clear if bromine etches selectively Cu-, Sn-based secondary phases from the CZTSe compound or if these phases are removed because they are located at the absorber surface.

#### IV.1.1.2 Removal of Zn-based secondary phases

**HCl** Hot hydrochloric acid solutions have been developed for the selective removal of Zn-rich secondary phases from the CZTS absorber surface, and show a significant impact on the optoelectronic properties of CZTS based solar cells [350]. Larramona et al. detected ZnS grains even after HCl etching, possibly because the etching was performed in different conditions (temperature, etching time). Still, they could observe a beneficial effect of HCl etching attributed to the removal of oxides [39]. For CZTSe, the Zn ratio at the CZTSe surface has been reported to decrease after concentrated HCl etching [192], which might indicate Zn-based secondary phases etching. However, it is not clear if concentrated HCl etches selectively the ZnSe secondary phase from CZTSe or if Zn-rich phases are removed because they are located at the absorber surface.

**Oxidative etching** Oxidative KMnO<sub>4</sub> /H<sub>2</sub>SO<sub>4</sub> + Na<sub>2</sub>S etching removes the ZnSe secondary phase, according to the following mechanism [55]. In a first step, ZnSe is oxidated to Se<sup>0</sup>.



Then Se<sup>0</sup> is dissolved with Na<sub>2</sub>S by the dismutation of Se<sup>0</sup> to Se<sup>-II</sup> and Se<sup>+IV</sup>.



López-Marino et al. have shown that Zn-rich CZTSe device performance significantly improves with oxidative KMnO<sub>4</sub> /H<sub>2</sub>SO<sub>4</sub> + Na<sub>2</sub>S etching [55].

#### IV.1.1.3 Passivation effect

Surface passivation might occur through HS<sup>-</sup> ions present in Na<sub>2</sub>S and (NH<sub>4</sub>)<sub>2</sub>S solutions. In a first step, the S ions (HS<sup>-</sup> due to the pH of the solution) react with the surface metallic oxides, breaking the bond between the chalcogen and the metals, forming soluble metal chalcogenide species and leaving H<sup>+</sup> in the solution. In a second step, the dangling bonds left at the semiconductor surface form H<sub>2</sub>(g) with the H<sup>+</sup> ions. The last step is the formation of chemical bonds between the free S<sup>2-</sup> of the solution and the chalcogen atoms of the semiconductor [54].

## IV.1.2 Experimentals

In this chapter, wet chemical etchings and buffer layer depositions are performed at IREC on absorbers produced through annealing in a graphite box (CC-IREC annealing system, see *Chapter 3*). The absorber size is 5 × 5 cm<sup>2</sup> at the most.

### IV.1.2.1 Etchings

In order to etch 5 × 5 cm<sup>2</sup> or smaller absorbers, 50 mL of each etching solution is prepared. Each etching is realized according to the following procedure: the sample is dipped into the etchant solution for the required time, rinsed thoroughly with deionized water and dried with N<sub>2</sub>. All etchings are performed at room temperature.

- (i) ZnSe secondary phases are etched by oxidative etching, as described by López-Marino et al. [55]. For the first step, a fresh  $\text{KMnO}_4$  (0.01 M) solution is mixed with  $\text{H}_2\text{SO}_4$  (1 M). For the second step a  $\text{Na}_2\text{S}$  (1 M) solution is prepared. The standard etching times are 30 s and 1 min, respectively. Between the two steps, the samples are rinsed with deionized water.
- (ii) Sn-Se secondary phases are etched by ammonium sulfide, as described by Xie et al. [54]. Etching of the absorbers is performed using a  $(\text{NH}_4)_2\text{S}$  [4 – 22% (w/w), Alfa-Aesar] for 1 to 2 minutes.
- (iii) Removal of both secondary phases is performed by applying etching (i) followed by etching (ii).

#### IV.1.2.2 Material Characterization

Absorber composition is systematically measured by XRF, as described in paragraph III.2.5.1 page 85 and in *Annex B*. Surface and cross-sectional SEM images are recorded using a Zeiss Series Auriga field emission scanning electron microscope (Zeiss) at a voltage of 5 kV. EDX analysis with 10 – 20 kV acceleration voltage is performed with an Oxford Instruments X-Max detector. The equipments used for XRD and Raman measurements are described in paragraph III.2.5.3 page 85.

#### IV.1.2.3 Device completion

The CdS buffer layer is deposited by CBD with  $\text{CdSO}_4$  and  $\text{Cd}(\text{NO}_3)_2$  cadmium precursors in 7 and 45 min respectively. Immediately after buffer deposition, the window layer of i-ZnO (50 nm) and indium tin oxide (ITO) (450 nm) is deposited with DC-pulsed sputtering of (CT100, Alliance Concepts). For optoelectronic characterization,  $3 \times 3 \text{ mm}^2$  cells were scribed using a microdiamond scribe MR200 OEG, thus avoiding the necessity of metallic grid deposition onto the ITO surface. Finally, all the completed devices are submitted to a 20 – 30 minutes 200 °C post-treatment on a hot plate, as described in reference [346].

#### IV.1.2.4 Device Characterization

The devices' opto-electronic properties are accessed by J-V and EQE measurements. Dark and illuminated J-V curves were measured using a Sun 3000 class AAA solar simulator (Abet Technologies Inc., uniform illumination area of  $15 \times 15 \text{ cm}^2$ ), starting from negative to positive voltages. Measurements were carried out at 25 °C, and before measuring the irradiance, the intensity of the solar simulator was calibrated to 1 sun AM1.5 by using a Si reference cell. Spectral response/external quantum efficiency (EQE) measurements were made using a Bentham PVE300 system (Bentham Instruments Ltd.) calibrated with a Si and Ge photodiode. Reversed voltage-biased EQE curves were collected by connecting a Keithley 2400 source meter (Keithley Instruments Inc.).

### IV.1.3 Results

As already described in *Chapter 3*, the presence of secondary phases at the absorber's surface depends on the composition. In the absorber composition range where high device efficiencies are obtained (Cu-poor composition), ZnSe and Sn-Se (SnSe,  $\text{SnSe}_2$ ) secondary phases are detected. Different etching solutions are applied to the absorbers:  $\text{KMnO}_4/\text{H}_2\text{SO}_4 + \text{Na}_2\text{S}$  [55] and  $(\text{NH}_4)_2\text{S}$  [54] solutions, which are reported to selectively etch ZnSe and Sn-Se secondary phases respectively. Depending on the absorber composition, (i) ZnSe, (ii) Sn-Se or (iii) ZnSe + Sn-Se etchings are applied on the absorbers surface.

## IV.1.3.1 Removal of secondary phases

(i) Acidic  $\text{KMnO}_4$  followed by  $\text{Na}_2\text{S}$  etching removed efficiently the small ZnSe grains from the surface of the absorbers. As expected when removing ZnSe from the surface, a decrease in Zn content and increase in Cu content was observed (Figure IV.5). ZnSe Raman peaks disappeared after etching as shown in Figure IV.2b. In Zn-rich absorbers ( $\text{Zn}/\text{Sn} > 1.3$ ), voids were detected after the etching procedure (Figure IV.2a). For Zn-rich films, small surface ZnSe aggregates are often reported, and can easily be removed by etching. By contrast, Zn-rich films exhibit larger aggregates of ZnSe that are associated with voids in the underlying film [196]. After etching these voids are exposed.

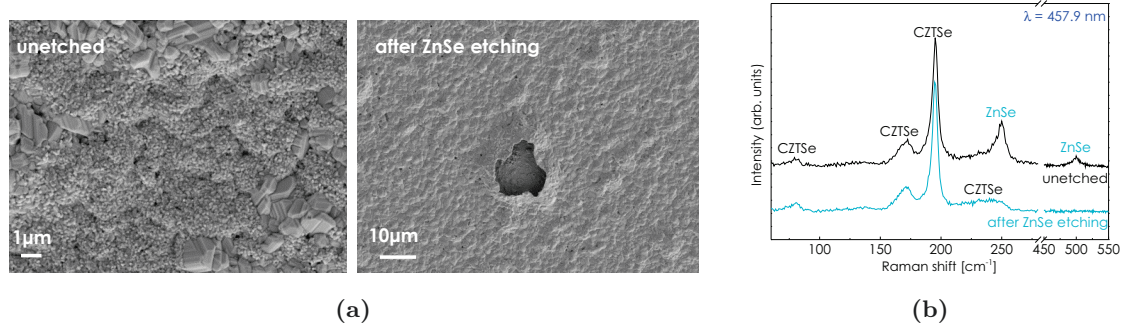


**Figure IV.2:** (a) Surface SEM images and (b) Raman spectra of Zn-rich absorbers ( $\text{Zn}/\text{Sn} > 1.3$ ) before and after removal of the ZnSe secondary phase from the surface by (i) acidic  $\text{KMnO}_4$  followed by  $\text{Na}_2\text{S}$  etching.

(ii)  $(\text{NH}_4)_2\text{S}$  etching removed Sn-Se secondary phases from the surface as demonstrated by Raman spectroscopy and X-ray diffraction on Sn-rich absorbers: after etching, the secondary phases are no longer detected (Figure IV.3b). As expected when removing Sn-Se rich phases by etching, a decrease in Sn content and an increase in Cu content are observed (Figure IV.5). At the absorber surface, the amount of Sn-Se rich crystalline features is reduced, the absorber surface becomes hollow (Figure IV.3a).

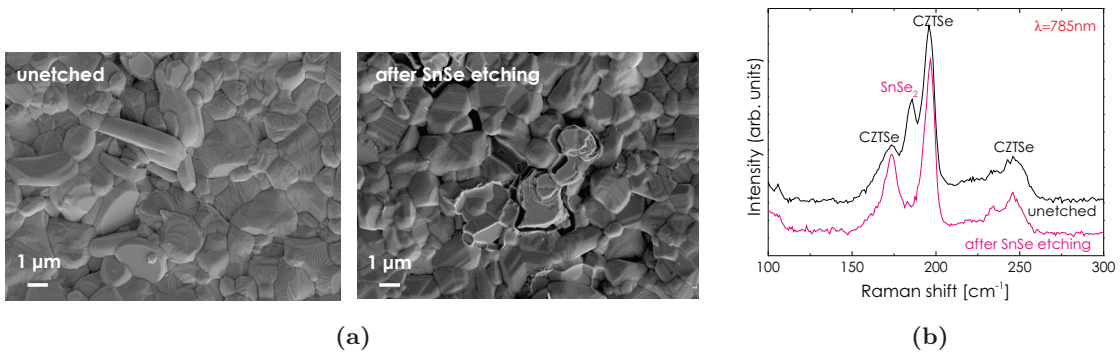


**Figure IV.3:** (a) Surface SEM images and (b) Raman spectra of Sn-rich absorbers before and after removal of Sn-Se ( $\text{SnSe}$ ,  $\text{SnSe}_2$ ) secondary phases from the surface by (ii)  $(\text{NH}_4)_2\text{S}$  etching. Detected Sn-Se modes vanish after etching procedure.

(iii) Combination of both etching procedures tends to reduce both Sn and Zn contents in the absorber, in agreement with the individual results for each etching procedure (Figure IV.5), and to reduce the presence of ZnSe and Sn-Se features at the surface, as shown in Figure IV.4.

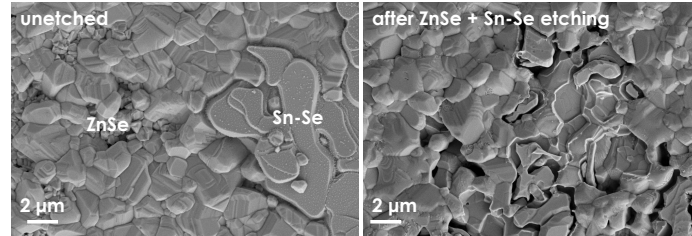


**Figure IV.4:** Surface SEM images showing the removal of ZnSe and Sn-Se (SnSe, SnSe<sub>2</sub>) secondary phases from the surface of a Sn-rich and Zn-rich absorber by (iii) acidic KMnO<sub>4</sub> followed by Na<sub>2</sub>S etching + (NH<sub>4</sub>)<sub>2</sub>S etching.

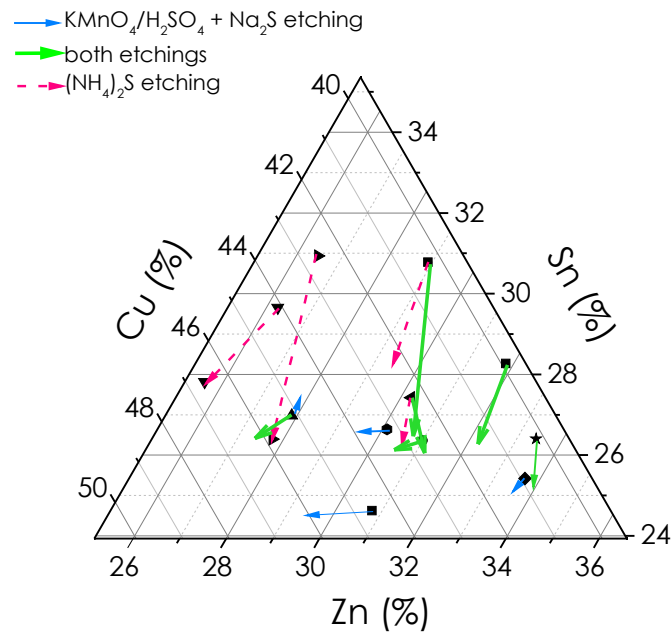


**Figure IV.5:** Ternary diagram illustrating the composition of unetched and etched absorbers. Changes in composition due to the applied etchings are indicated by arrows.

## IV.1.3.2 Influence of etching on the device performance

Table IV.2 shows optoelectronic properties of several devices obtained from CZTSe films with different compositions and etching conditions. The evolution of the solar cell parameters after etching is summarized in Table IV.3. For each composition, the absorber layer was cut into smaller parts in order to apply different etching procedures, and one part was kept unetched for reference.

**Table IV.2:** Kesterite devices optoelectronic parameters for different absorber composition and etching: (i) ZnSe, (ii) SnSe and (iii) ZnSe + SnSe etching. Cu/Zn+Sn and Zn/Sn ratios are measured by XRF on absorbers after etching. Main optoelectronic parameters (power conversion efficiency  $\eta$ , open circuit voltage  $V_{OC}$ , short-circuit current  $J_{SC}$ ) are reported in the following way: best value at cell size (active area:  $0.087 \text{ cm}^2$ ), average value for the full sample (18 to 36 cells, i.e.  $1.5 \times 2.5 \text{ cm}^2$  to  $2.5 \times 2.5 \text{ cm}^2$ ) and its RSD. The reported values for the fill factor (FF), series resistance and shunt resistance are averaged values of the complete sample.

Sample composition	Cu/Zn+Sn	Zn/Sn	Etching	$\eta$ (%)			$V_{OC}$ (mV)			$J_{SC}$ (mA.cm <sup>-2</sup> )			FF (%)	$R_S$ ( $\Omega$ .cm <sup>2</sup> )	$R_{SH}$ ( $\Omega$ .cm <sup>2</sup> )
				Max	Ave	RSD (%)	Max	Ave	RSD (%)	Max	Ave	RSD (%)	Ave	Ave	Ave
Sn-rich	0.68	0.94	unetch	1.7	1.3	23	261	241	7	19.9	17.0	15	31	5.5	21
Sn-rich	0.73	1.04	(ii)	4.9	3.8	21	390	360	8	28.7	26.4	6	38	2.4	39
Sn-rich	0.75	1.16	(iii)	5.0	3.1	39	390	346	9	28.8	23.1	19	37	4.7	39
Zn-rich 1	0.76	1.13	unetch	2.9	2.5	12	345	316	5	24.7	23.3	5	34	5.9	28
Zn-rich 1	0.78	1.11	(i)	5.1	4.3	12	376	355	5	30.7	29.0	4	41	1.9	50
Zn-richer	0.69	1.32	unetch	3.6	3.2	9	356	347	2	27.0	25.6	4	36	5.2	36
Zn-richer	0.70	1.33	(i)	1.4	1.2	17	275	243	8	19.0	16.7	9	31	6.2	21
Zn-rich 2	0.73	1.10	unetch	6.0	5.2	10	393	377	2	31.7	30.5	4	45	2.2	81
Zn-rich 2	0.76	1.16	(ii)	5.8	4.8	15	382	365	3	32.1	29.9	7	44	1.4	67
Zn-rich 2	0.75	1.20	(iii)	7.6	6.7	6	435	410	4	31.9	30.0	3	55	0.9	181
Intermediate	0.82	1.03	unetch	4.2	3.2	28	335	297	15	31.1	27.8	10	38	3.3	31
Intermediate	0.81	1.02	(i)	4.9	4.1	17	345	322	8	31.1	29.6	4	43	1.9	51
Intermediate	0.86	1.03	(iii)	5.7	4.3	15	368	327	7	31.0	29.4	3	45	1.3	51

Devices made from unetched Sn-rich absorbers (Sn-rich in Tables IV.2 and IV.3) exhibit low efficiencies (below 2%), showing the detrimental influence of Sn-Se secondary phases. All device parameters clearly improve with the application of (ii) Sn-Se etching or (iii) ZnSe + Sn-Se etchings. Also, devices with Sn-rich absorbers show a high relative standard deviation (RSD) of the optoelectronic parameters. These results are in agreement with the non-uniformity, low shunt resistance and low cell performance induced by the formation of SnSe<sub>2</sub> [138] and show that etching greatly reduces the negative impact of Sn-rich secondary phases at the surface [54].

Devices with unetched Zn-rich absorbers exhibit higher efficiencies than those with unetched Sn-rich absorbers (Table IV.2), thereby confirming that ZnSe is less detrimental to device performance than Sn-Se secondary phases. Table IV.3 shows that after (i) ZnSe etching  $\eta$ ,  $V_{OC}$ ,  $J_{SC}$ , FF,  $R_S$  and  $R_{SH}$  improved, demonstrating the beneficial effect of etching by reducing the ZnSe related current blocking at the surface. However, for Zn-richer films the etching provokes a drastic decrease of optoelectronic performances, since voids in the absorber are exposed when ZnSe was removed.

**Table IV.3:** Evolution of kesterite devices J-V parameters after (i) KMnO<sub>4</sub>/H<sub>2</sub>SO<sub>4</sub> + Na<sub>2</sub>S (ii) (NH<sub>4</sub>)<sub>2</sub>S or (iii) KMnO<sub>4</sub>/H<sub>2</sub>SO<sub>4</sub> + Na<sub>2</sub>S + (NH<sub>4</sub>)<sub>2</sub>S etching for different absorber compositions.

Sample	Initial $\eta$ (%)	Etching	Average parameter evolution after etching (%)					
			$\eta$	$V_{OC}$	$J_{SC}$	FF	$R_S$	$R_{SH}$
Sn-rich	<2	(ii) or (iii)	+160	+45	+45	+22	-35	+86
Zn-rich 1	2-6	(i)	+72	+12	+24	+21	-68	+79
Zn-richer	3-4	(i)	-62	-30	-35	-14	+19	-42
Zn-rich 2 & Intermediate	4-6	(iii)	+32	+10	0	+20	-60	+93

Best device efficiencies are obtained for absorbers of Zn-rich compositions and Zn/Sn ratio in the range of  $1.00 < \text{Zn/Sn} < 1.25$  (Zn-rich 2 and intermediate in Table IV.2), which are etched by a combination of both etching procedures (iii)  $\text{KMnO}_4/\text{H}_2\text{SO}_4 + \text{Na}_2\text{S} + (\text{NH}_4)_2\text{S}$ . Devices with unetched absorbers in this optimum composition range already exhibit efficiencies as high as 6.0%. After the combined etching (iii), Table IV.3 shows that  $\eta$ ,  $V_{OC}$ , FF,  $R_S$  and  $R_{SH}$  improve while  $J_{SC}$  remains high and unchanged, showing a better device improvement than with single etching (i) or (ii). A best device efficiency of 7.6% is reached.

In conclusion, selecting carefully the composition, thus limiting the amount of secondary phases, led to 6.0% best device efficiency. When the secondary phases are segregated at the surface, they can be removed by adapted etching procedures. In this study,  $\text{KMnO}_4/\text{H}_2\text{SO}_4 + \text{Na}_2\text{S} + (\text{NH}_4)_2\text{S}$  etching successfully improved the device performance. Best device efficiency increased from 6.0% to 7.6% by means of etching.

### IV.1.3.3 Influence of the secondary phases on the device opto-electronic properties

By comparing the opto-electronic properties of devices made with unetched absorbers (with secondary phases) and with etched absorbers (secondary phases — at least partly — removed from the surface), one can study the effect of the secondary phases on the device characteristics. Figure IV.6 shows that the current collection in the low wavelength region is improved after etching, especially in the absorption region of the ZnSe secondary phase, above 2.7 eV. Analyzing the spectral response, the ZnSe secondary phase current blocking behavior has first been observed by Colombara et al. [196]. Here the combination of both etching shows to be the best choice for reducing current losses in the low wavelength region of the external quantum efficiency (EQE) curve.

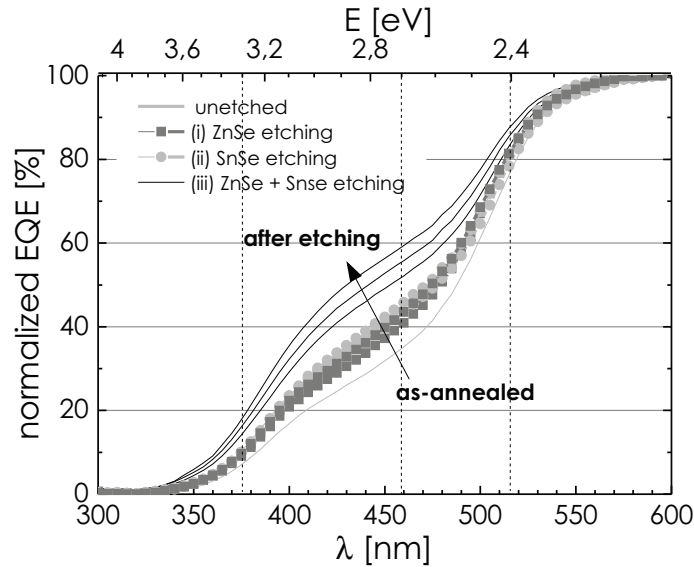


**Figure IV.6:** Normalized external quantum efficiency in the low wavelength region of CZTSe-based devices. Different surface treatments of the absorber influence the current collection in this region.

The short circuit current also greatly improves by removing Sn-Se secondary phases, as shown in Figure IV.7b by the increase of the area under the EQE curve. When submitted to a reverse voltage of -1V, the EQE of the unetched device increases in the low wavelength region, below 520 nm. An increase in EQE under reverse voltage can be related to an improved current collection. However, here, this increase is provoked by the photoconductance properties of the CdS layer, which absorbs light below 520 nm. The presence of shunting channels laterally distributed on the absorbers has been reported to favor this increase of EQE in the CdS absorption region under reverse voltage [195].

After removal of Sn-Se secondary phases from the surface, the peak in the EQE(-1V)/EQE(0V) curve disappears. Sn-Se secondary phases at the surface are probably at the origin of this EQE increase behavior. In addition, the increase of EQE in the CdS absorption region goes along with a global reduction of the EQE curve, which is traduced by a shift of the EQE(-1V)/EQE(0V) towards lower values.

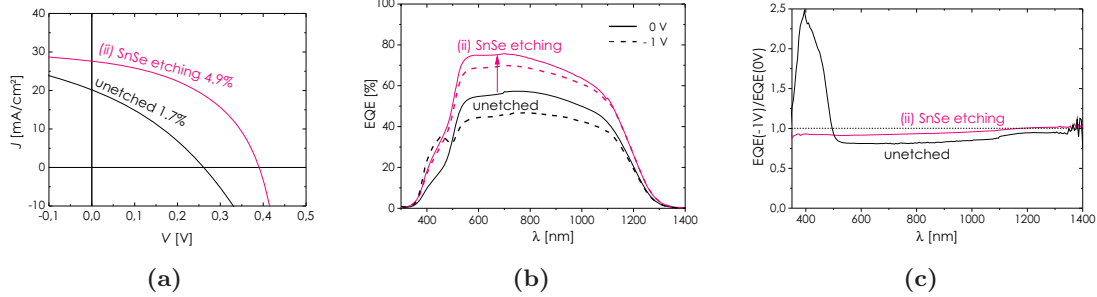


**Figure IV.7:** (a) J-V curve, (b) EQE curve at 0 V and under reverse voltage and (c) ratio of EQE under -1 V reverse voltage on EQE at 0 V of device made with Sn-rich absorbers unetched and (ii) etched with  $(\text{NH}_4)_2\text{S}$ .

Both effects (increase of EQE in the 300-450 nm region, and shift of the EQE towards lower values) show to be dependent on 1) the applied reverse voltage and 2) the amount of secondary phases (Sn-Se mainly) at the surface. When the value of the reverse voltage is more negative, these effects increase. When more secondary phases are present, the shunting of the device increases, and these effects increase, confirming that the shunting of the secondary phases is at the origin of these effects.

#### IV.1.3.4 Conclusions

In conclusion, secondary phases removal from the surface is highly beneficial, as it reduces the voltage deficit [51, 192], current losses [55], and improves shunt and series resistances. In addition, the possible surface passivation effect can help to improve the p-n junction and limit recombination [54, 55]. These results show the importance of a) the absorber composition, which determines the abundance and the nature of present secondary phases, b) secondary phases segregation control, by limiting their presence to the surface so that they may be removed via chemical etching, c) identification and characterization of the secondary phases and d) adjusted efficient chemical etching procedures, which may also provide passivation of the kesterite absorber surface. Best device performance is obtained when the absorber composition is of  $0.70 < \text{Cu}/(\text{Zn}+\text{Sn}) < 0.85$  and  $1.00 < \text{Zn}/\text{Sn} < 1.25$  and when combined etchings of Sn- and Zn-based secondary phases are applied. This part also highlights the importance of kesterite surface treatments, which play a crucial role in the p-n junction with the buffer layer. Interface optimization might be one of the keys for further improvement of kesterite solar cell performance.



## IV.2 Buffer optimization

### IV.2.1 Background

Once the kesterite surface is cleaned from detrimental secondary phases and oxides, the buffer layer is deposited. A n-type semiconductor forms a p-n junction with the p-type absorber.

#### IV.2.1.1 Cadmium sulfide

Cadmium sulfide, a n-type semiconductor with a bandgap ( $E_g$ ) of 2.3 – 2.6 eV [56, 57], is widely used for CIGS technology. Chemical bath deposition (CBD) is a useful method for obtaining a very thin conformal CdS film because it is inherently a low temperature process which does not damage the surface of the absorber during deposition and can be applied to rough surfaces. In this deposition process, CdS thin films are deposited using thiourea and ammonium [56]. The global reaction for the process is described by:



Deposition of CdS using CBD is based on the slow release of  $\text{Cd}^{2+}$  ions and  $\text{S}^{2-}$  ions in an aqueous alkaline bath and the subsequent precipitation of these ions on substrates suitably mounted in the bath. The slow release of  $\text{Cd}^{2+}$  ions is achieved by adding a complexing agent (ligand) to the Cd salt to form some cadmium complex species which, upon dissociation, results in the release of small concentrations of  $\text{Cd}^{2+}$  ions. The  $\text{S}^{2-}$  ions are supplied by the decomposition of thiourea or sodium thiosulfate. Cd may be provided by different Cd precursors such as  $\text{Cd}(\text{SO}_4)$  [57–59],  $\text{Cd}(\text{NO}_3)_2$ ,  $\text{CdCl}_2$ ,  $\text{CdI}_2$  or  $\text{Cd}(\text{CH}_3\text{COO})_2$  [57]. The CdS film properties such as thickness, structure, surface morphology and stoichiometry change with the cadmium source used for this process [57, 369]. Ammonium concentration may also influence device properties [370]. Cd is toxic so it may be desirable to replace it with a more environmentally favorable material. In addition to the environmental concerns, another disadvantage with the CdS buffer layer is that it absorbs light in the UV region of the solar spectrum, thereby reducing the carrier generation in this region.

#### IV.2.1.2 Alternative buffers

A number of alternative buffer layers have been tested for CIGS showing promising results [115]. Best results are obtained for  $\text{Zn}(\text{O},\text{OH},\text{S})$  and  $(\text{ZnMg})\text{O}$  layers, but also  $\text{ZnSnO}$  and  $\text{In}_2\text{S}_3$  buffer layers. The band gaps of alternative buffer layers are summarized in Table IV.4.

**Table IV.4:** Buffer layer bandgaps.  
<sup>a</sup> indirect bandgap.

Buffer layer	Bandgap (eV)
$\text{In}_2\text{S}_3$	2.1 <sup>a</sup> , 2.7 – 2.8 [115]
$\text{In}_2(\text{O},\text{S})_3$	2.0 – 3.6 [115]
CdS	2.3 – 2.6 [57]
(Cd,Zn)S	2.6 [371]
ZnO	3.3 [115]
$\text{Zn}(\text{O},\text{OH},\text{S})$ or $\text{Zn}(\text{O},\text{S})$	2.6 – 3.7 [115]
ZnS	3.6 – 3.8 [372]
(Zn,Mg)O	3.3 – 7.7 [115, 373–375]
ZnSnO	- [374]

Since  $\text{In}_2\text{S}_3$  (2.1 eV) exhibits an indirect band gap, its transparency is superior to that of CdS, which has a slightly larger (2.4 eV), but direct, optical gap [376]. Both ZnO and ZnS possess

large optical gaps of 3.3 and 3.6 eV, respectively. Buffer layers are usually deposited by CBD [123, 215, 215, 367, 376–378], but they can also be deposited by atomic layer deposition (ALD) [376], PVD methods (thermal evaporation [379], evaporation [380], sputtering [381, 382]), spray pyrolysis [115]. Note that for buffers deposited by CBD, (hydro)xides compounds can be expected. For instance, in Cd- (Zn-, In-) based buffer layers, the chemical states CdS (ZnS, In<sub>2</sub>S<sub>3</sub>), CdO (ZnO, In<sub>2</sub>O<sub>3</sub>), and Cd(OH)<sub>2</sub> (Zn(OH)<sub>2</sub>, In(OH)<sub>3</sub>), can coexist and have an effect on the bandgap value [124]. The quality of the p-n junction depends on the band alignment between p-type and the n-type semiconductors. In addition to low toxicity, a candidate buffer material has to provide an optimal alignment of its conduction band minimum with the one of the absorber. The conduction band offset (CBO) is the energy difference between conduction band minimum of the absorber and conduction band minimum of the buffer layer. If the two conduction band minima are aligned, there is no conduction band offset. Otherwise, the possible band alignments are illustrated in Figure IV.8.

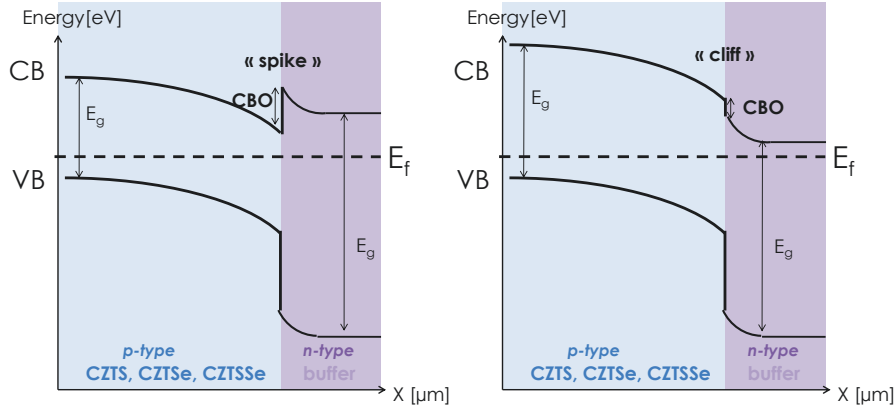


**Figure IV.8:** Band alignment at the kesterite/buffer layer heterointerface. A CBO can lead to the formation of a “spike” (type I interface) or a “cliff” (type II interface), depending on the sign of the offset.

A large positive CBO (spike) presents a barrier for minority carrier (electron) collection, reducing the short-circuit current. By contrast, negative offset (cliff) leads to an increased recombination at the buffer-absorber interface, thereby reducing open-circuit voltage. Ideally, the device should have a small 0 – 0.4 eV conduction-band offset spike [168]. A “cliff”-type band alignment, where the conduction band edge of the absorber layer is higher than that of the buffer layer, may be one of the reason for dominant interface recombination<sup>1</sup> [179, 180]. The conduction band offsets that have been calculated or experimentally determined for kesterite/buffer junctions are reported in Table IV.5.

**Table IV.5:** Conduction band offsets at kesterite / buffer layer interface.

Absorber	Conduction band offset type	Buffer [reference]
CZTS	Cliff	CdS [215, 367, 378, 380, 381, 383, 384]
CZTS	Spike (0 to 0.4 eV)	CdS [123, 125, 377, 385]; ZnO [382]
CZTS	Spike (> 0.4 eV)	In <sub>2</sub> S <sub>3</sub> [215, 379]; ZnO [384]; Zn(O,S) [215]; ZnS [385]
CZTSSe	Aligned bands or Spike (0 to 0.4 eV)	CdS [377, 380]; In <sub>2</sub> S <sub>3</sub> [376]; ZnO [376]
CZTSSe	Spike (> 0.4 eV)	ZnS [376]
CZTSe	Spike (0 to 0.4 eV)	CdS [123, 383]
CZTSe	Spike (> 0.4 eV)	CdS [123, 377, 383]; Zn(O,S) [386]

<sup>1</sup>Another reason for dominant interface recombination in a device is Fermi-level pinning at a position far from the conduction band edge.

The band alignment between pure-sulfide CZTS and different buffer layers has been widely studied. CdS may not be the best buffer layer for producing CZTS-based devices, as a cliff is most frequently reported than a small spike at CZTS/CdS interface. The presence of a cliff-like conduction band offset is in agreement with dominant interface recombination in CZTS/CdS devices. CZTS conduction band alignment with alternative buffer layers such as  $\text{In}_2\text{S}_3$ , ZnO, Zn(O,S), ZnS is not optimum neither, as it is often reported as a large spike. For the mixed sulfur/selenium CZTSSe absorber, different buffer layers (CdS, but also  $\text{In}_2\text{S}_3$  and ZnO) are reported to give an optimum band alignment. It is not clear whether the conduction band alignment between pure-selenide CZTSe absorber and CdS is a spike of optimum value or a non-optimum large spike. The alignment of alternative buffers with CZTSe has not been studied in literature, but a large spike can be expected.

Therefore, depending on the kesterite bandgap (S and/or Se), CdS, the most used buffer layer, may not be an ideal buffer material. Alternative buffer layers such as  $\text{In}_2\text{S}_3$  and ZnO — often presenting a large spike which may cause a barrier to the current flow — are not ideal neither. Non optimum CBOs can explain different behaviors observed in the devices. For instance, the current blocking effect has been observed experimentally for Zn(O,OH,S) buffer layers with CZTSSe [140]. The performance of solar devices prepared with different alternative buffer layers is shown in Table IV.6.

**Table IV.6:** Performance characteristics of Cd-free solar cells (versus CdS reference in parenthesis). <sup>a</sup> Multilayer.

Buffer layer	Buffer deposition method	Absorber	Absorber deposition method	$\eta$ %	$V_{OC}$ mV	$J_{SC}$ mA/cm <sup>2</sup>	FF %	Ref
$\text{In}_2\text{S}_3$	CBD	CZTS	sol-gel	0.4 (1.5)	590 (470)	2.8 (8.9)	22 (36)	[215]
$\text{In}_2\text{S}_3$	spray-pyrolysis	CZTSSe	spray-pyrolysis	2.4	360	16.9	-	[171]
$\text{In}_2\text{S}_3$	CBD	CZTS	sputtering	2.6 (5.5)	716 (641)	12.1 (15.9)	30 (54)	[387]
$\text{In}_2\text{S}_3$	spray-pyrolysis	CZTSSe	spray-pyrolysis	5.7	430	28.3	47	[388]
$\text{In}_2\text{S}_3$	CBD	CZTSSe	hydrazine solution	7.2 (7.8)	435 (465)	29.2 (27.1)	55 (62)	[376]
$\text{In}_2\text{S}_3$	CBD	CZTSSe	hydrazine solution	9.3	447	36.3	58	[142]
Zn(O,S)	CBD	CZTS	sol-gel	0 (1.5)	76 (470)	0 (8.9)	0 (36)	[215]
ZnS	ALD	CZTS	reactive sputtering	0 (7.3)	65 (652)	1.1 (17.5)	27 (64)	[134]
ZnS	CBD	CZTSSe	hydrazine solution	0 (7.8)	0.69 (465)	0.001 (27.1)	0 (62)	[376]
ZnO	ALD	CZTS	reactive sputtering	0.9 (7.3)	152 (652)	14.8 (17.5)	38 (64)	[134]
ZnS	electrodeposition	CZTS	electrodeposition	1.9	400	9.8	48	[372]
ZnS	RF-sputtering	CZTS	sputtering	2.1 (5.0)	311 (561)	12.2 (18.4)	56 (48)	[389]
ZnO	ALD	CZTSSe	hydrazine solution	2.5 (7.8)	348 (465)	21.0 (27.1)	34 (62)	[376]
ZnO	USP	CZTS	sputtering	4.3 (4.3)	650 (620)	13.8 (15.5)	48 (45)	[390]
ZnS	CBD	CZTSSe	monograin	4.5 (4.8)	596 (640)	15.4 (15.4)	49 (49)	[391]
Zn(O,S)	ALD	CZTS	reactive sputtering	4.6 (7.3)	482 (652)	17.2 (17.5)	56 (64)	[134]
Zn(O,S)	CBD with DMSO	CZTSe	co-evaporation	>5	336	-	-	[386]
Zn(O,S,OH)	CBD	CZTSSe	sputtering	5.8 (7.0)	389 (376)	29 (34)	52 (55)	[140]
Zn-based	CBD	CZTSSe	hydrazine solution	8.9	450	34.5	58	[142]
(Zn,Sn)O	ALD	CZTS	reactive sputtering	7.4 (7.2)	682	17.9	60	[392]
(Cd,Zn)S	CBD	CZTSSe	sputtering	9.0 (9.8)	415 (408)	34.7 (37.5)	63 (64)	[371]
(Zn,Mg)O	RF-sputtering	CZTSSe	sputtering	2.4 (7.2)	332 (361)	15.9 (34.2)	44 (59)	[375]
(Zn,Mg)O	RF-sputtering	CZTSSe	sputtering	2.8 (7.2)	323 (361)	18.8 (34.2)	44 (59)	[373]
CdS/ $\text{In}_2\text{S}_3$	CBD	CZTS	sputtering	4.2 (5.5)	651 (641)	13.7 (15.9)	47 (54)	[387]
$\text{In}_2\text{S}_3$ /CdS	CBD	CZTS	sputtering	6.6 (5.5)	714 (641)	17.6 (15.9)	53 (54)	[387]
CdS/(Zn,Mg)O	CBD/RF-sputtering	CZTSSe	sputtering	7.1 (7.2)	371 (361)	31.4 (34.2)	61 (59)	[373]
CdS/ $\text{In}_2\text{S}_3$	CBD	CZTS	PVD	8.0 (6.3)	686 (629)	20.8 (20.7)	56 (49)	[125]
CdS/(Zn,Mg)O <sup>a</sup>	CBD/RF-sputtering	CZTSSe	sputtering	10.9 (10.6)	470 (474)	36.2 (35.5)	64 (63)	[393]
CdS/ $\text{In}_2\text{S}_3$	-	CZTSSe	-	12.7 (12.6)	466	38.9	70	[26]

The best performances are obtained with the classical CdS buffer.  $\text{In}_2\text{S}_3$ -based devices also exhibited good efficiencies compared to their CdS counterparts. Hybrid buffer layers CdS/(Zn,Mg)O or CdS/ $\text{In}_2\text{S}_3$  gave very good efficiencies and reduced  $V_{OC}$  deficits [125, 394]. Indeed, the addition of (Zn,Mg)O or  $\text{In}_2\text{S}_3$  buffer layers is beneficial for band alignment tuning, therefore reducing the  $V_{OC}$  deficit, but when deposited directly on the absorber, these buffers often give lower efficiency. For instance the deposition of (Zn,Mg)O by sputtering directly on the absorber creates damages [373, 375]. The insertion of a CdS layer between (Zn,Mg)O and CZTSSe allow to suppress

the sputtering damages.

## IV.2.2 Experimentals

### IV.2.2.1 Absorbers

The absorbers are prepared by electrodeposition of Cu/Sn/Zn stacked precursors, as described in *Chapter 2*, followed by pre-alloying at 200°C. Pure-selenium kesterite CZTSe is formed by reactive annealing in a graphite box (System CC-IREC, described in *Chapter 3*). The absorbers' surface is treated by a combination of etchings (iii)  $\text{KMnO}_4 / \text{H}_2\text{SO}_4 + \text{Na}_2\text{S} + (\text{NH}_4)_2\text{S}$ , corresponding to the removal of ZnSe, SnSe and SnSe<sub>2</sub> secondary phases, as described in the previous section.

### IV.2.2.2 Buffer layer deposition parameters

Immediately after the etchings, a buffer layer is deposited by chemical bath deposition. Different cadmium precursor sources are used for the deposition of CdS, such as cadmium sulfate  $\text{CdSO}_4 \cdot \text{H}_2\text{O}$  and cadmium nitrate  $\text{Cd}(\text{NO}_3)_2$ . The depositions are performed as described in reference [34], at 65°C. Similarly,  $\text{In}_2\text{S}_3$  and ZnS are deposited from different precursors. The CBD deposition parameters are listed in Table IV.7.

**Table IV.7:** Buffer layers and their CBD deposition parameters.

Buffer name	Precursor	$t$ (min)
CdS 1	Confidential	10
CdS 2	Confidential	15
CdS 3	Confidential	10
CdS 4	$\text{Cd}(\text{NO}_3)_2$	45
CdS 5	$\text{CdSO}_4$	0.5; 7
$\text{In}_2\text{S}_3$ 6	$\text{In}(\text{NO}_3)_3$	20; 40
$\text{In}_2\text{S}_3$ 7	$\text{InCl}_3$	20; 40
ZnS 8	Confidential	30; 45

### IV.2.2.3 Device completion

The devices are completed in the same manner (TCO, scribing, post-treatment) as described in paragraph IV.1.2.3 page 114.

### IV.2.2.4 Material characterization

SEM and EDX analysis of full device structure is performed at HZB using a LEO (Zeiss) Gemini 1530 scanning electron microscope equipped with a field-emission gun and a Thermo Noran X-ray detector. Acquisition and evaluation of EDX elemental distribution maps are performed using the Thermo Fisher Scientific software Noran System Seven.

### IV.2.2.5 Device Characterization

J-V and EQE curves are measured with the equipment described in paragraph IV.1.2.4 page 114. To obtain red light J-V curves, a 550 nm long pass filter was used, which has over 90% transmittance for wavelengths above 550 nm and 0% for lower wavelengths, as described in [34]. 400 nm, 515 nm and 780 nm optical band pass filters are also used.

## IV.2.3 Results

### IV.2.3.1 CdS optimization

For comparison, different cadmium sulfide layers are deposited by chemical bath deposition. The CBD processes used to deposit the CdS layer are developed at IREC. The nature of the cadmium precursor is the main difference between the CBD solutions, allowing to vary thickness and properties of the CdS film. CdS depositions are carried out on kesterite absorbers of similar composition ( $\text{Cu}/\text{Zn}+\text{Sn}=0.75 - 0.78$  and  $\text{Zn}/\text{Sn}=1.12 - 1.18$ ) and etched with (iii)  $\text{KMnO}_4/\text{H}_2\text{SO}_4 + \text{Na}_2\text{S} + (\text{NH}_4)_2\text{S}$  in order to remove ZnSe and Sn-Se secondary phases from the surface. Opto-electronic parameters of the devices prepared with different CdS layers are shown in Figure IV.9.

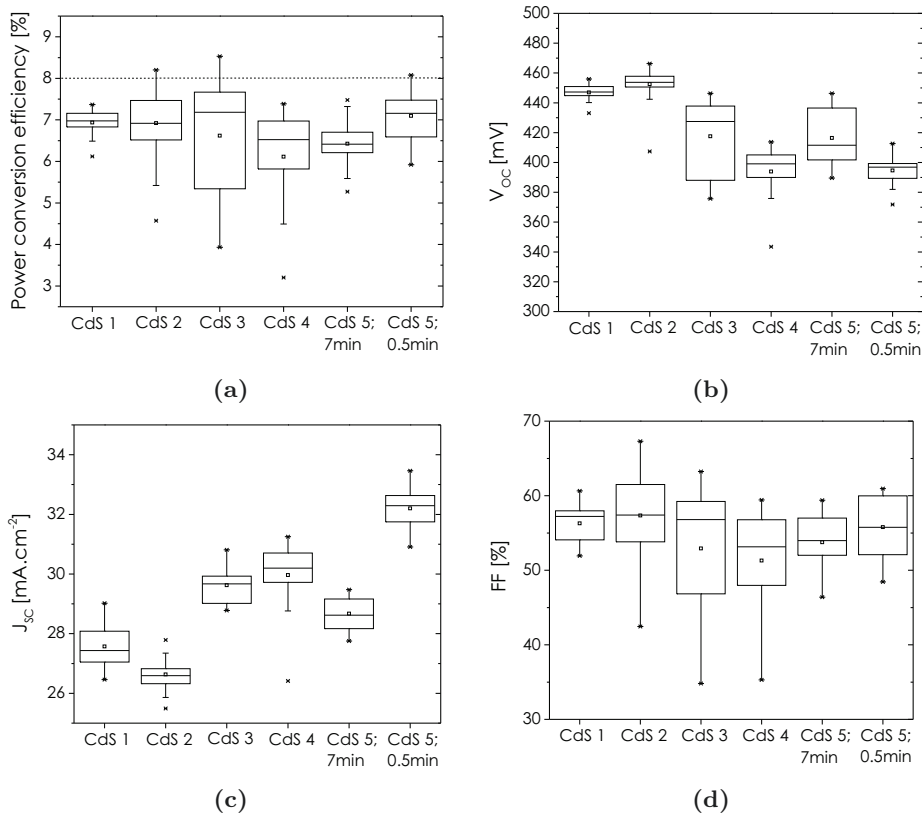


**Figure IV.9:** (a) Power conversion efficiencies  $\eta$ , (b) open-circuit voltages  $V_{OC}$ , (c) short-circuit currents  $J_{SC}$  and (d) fill factors FF of devices made with different CdS layers, measured after 5 min light soaking.

All devices reach efficiencies above 7%. Fill factors are relatively similar, typically between 50 and 60%. The devices exhibiting the best  $V_{OC}$  had the worst  $J_{SC}$ , and vice-versa. Devices prepared with CdS 1 or CdS 2 show very high  $V_{OC}$  compared to typical values reported for pure-selenide kesterite devices, but their  $J_{SC}$  is quite low. By contrast, the devices prepared with CdS 4 or CdS 5 (0.5 min) have lower open-circuit voltages and higher short-circuit currents. A record cell efficiency of 8.5% is reached with CdS 3, a compromise between high  $V_{OC}$  and high  $J_{SC}$ . Higher  $J_{SC}$  devices — produced with CdS 4 and CdS 5 (0.5 min) — show an increase in current for the 400 – 520 nm wavelength region in EQE, as shown in Figure IV.10.

The current improvement in this region of the spectral response can be attributed to a reduction of buffer related losses due to a thinner CdS layer. Here, CdS 4 and CdS 5 (0.5 min) are thin, as shown by the Cd mapping in the cross sectional images of the devices (Figure IV.11).

- CdS 4 (45 min) is deposited using a  $\text{Cd}(\text{NO}_3)_2$  precursor, which allows slower CdS chemical

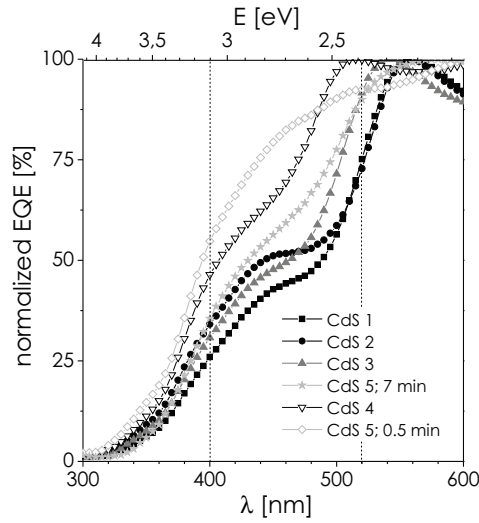


**Figure IV.10:** Normalized external quantum efficiency in the low wavelength region with different CdS layers.

bath deposition and a better control of CdS thickness, making it possible to deposit very thin layers of CdS [34].

- CdS 5 (0.5 min) is deposited with  $\text{CdSO}_4$  using very short times, allowing a very thin buffer layer to grow.

CdS 4 and CdS 5 (0.5 min) based devices exhibit higher  $J_{SC}$  when compared to the devices produced with other CdS in Figure IV.9c. Thin CdS buffer layers have already been reported to improve the performance of CIGS devices, by allowing more light to reach the junction [395]. By contrast, lower  $J_{SC}$  and higher  $V_{OC}$  devices (prepared with CdS 1 or CdS 2, in Figure IV.9b) show a current loss in the 400 – 520 nm wavelength region of the EQE spectra shown in Figure IV.10, probably because the CdS layer is thicker.

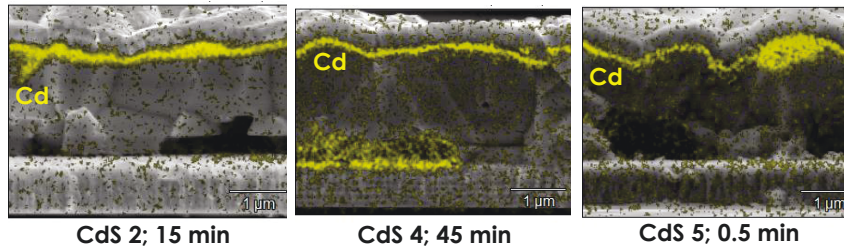


**Figure IV.11:** SEM cross-sectional images of devices made with different CdS layers. Cd (in yellow) is detected by EDX. The Cd-based layer is thicker for CdS 2 device. In CdS 4, Cd is detected at the back, probably because of holes in the absorber. CdS 4 is more homogeneous than CdS 5 (0.5 min) thanks to a slow deposition process.

The short-circuit current and the open-circuit voltage are also dependent on the conduction band alignment between the p-type absorber layer and the n-type buffer layer. In the case of a large “spike” (sometimes reported for CZTSe/CdS interface, cf. Table IV.5 page 121), the electron current flow in the device will be limited, leading to a distortion, or kink behavior, and light/dark curve crossover in the current-voltage curve. In addition, the potential barrier at the absorber/buffer interface depends not only on the CBO but also on internal material properties such as residual O-H bonds at the interface or doping density, which can increase the barrier height [396]. The barrier-induced distortion in the J-V curve is especially observed when using red or orange light (i.e. wavelength above 600 nm, low-energy photons) [397]. In this work, all the devices present the

red kink distortion in the J-V curves and/or a dark/light crossover, as shown in Figure IV.12.

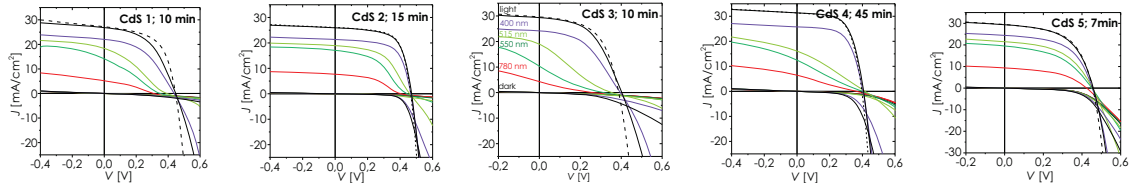


**Figure IV.12:** J-V curves of devices prepared with different CdS layers using four different optical band pass filters (400, 515, 550 and 780 nm).

Neuschitzer et al. observed that when a device is prepared with a “slow”-grown CdS layer (CdS 4, 45 min), the J-V curve distortion and dark/light cross-over are reduced or suppressed. In this work, using the same CdS 4 buffer layer, the devices exhibit J-V distortion and a strong cross-over. Therefore, the nature and amount of defects at the heterointerface is not only influenced by the CdS deposition process conditions but also by the absorber composition, the presence of secondary phases at the surface or their etching. Nonetheless, the distortion in the J-V curves disappears and the cross-over of all the devices is drastically reduced after 5 minutes of light-soaking, as shown in Figure IV.13. Under illumination, a “photo-doping” process takes place: the photons with a larger energy than buffer bandgap energy (blue light) generate electron-holes pairs in the buffer layer. The photogenerated holes compensate defects while the photogenerated electrons are not affected, thereby allowing a reduction of the spike potential barrier [34, 396].

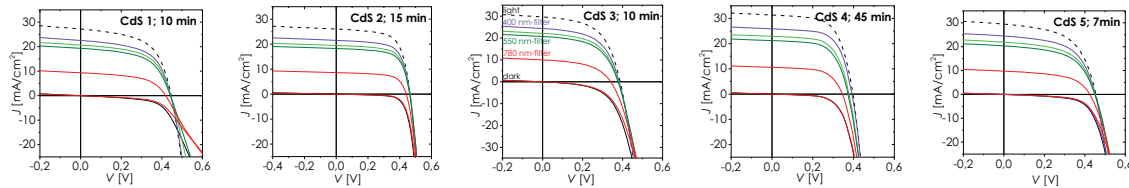


**Figure IV.13:** J-V curves of devices prepared with different CdS layers using four different optical band pass filters (400, 515, 550 and 780 nm), after 5 min of light-soaking.

In conclusion, the CdS buffer layer material properties have an influence on the opto-electronic properties of the kesterite devices. Reducing the thickness allows to improve the transparency in the UV range, thus improving the current generation and the  $J_{SC}$ . Nevertheless, the best  $V_{OC}$  are obtained with thicker buffer layers. Light-sensitive defects at the heterointerface limit the efficiency, but their effect is reduced after light-soaking. Non-uniformity of the layer, and defects due to roughness or holes in the absorber may also limit the efficiency. A deeper understanding of the heterointerface chemistry could help to further improve the efficiency. Finally, in this section, with an absorber composition of  $Cu/Zn+Sn=0.75 - 0.78$  and  $Zn/Sn=1.12 - 1.18$ , the best device is obtained with CdS 3, reaching 8.5% power conversion efficiency.

### IV.2.3.2 Alternative buffer layers

$In_2S_3$  and  $ZnS$  have been identified as potential cadmium-free candidates for the n-type buffer layer, as already shown in Table IV.6 page 122. Cadmium-free devices are prepared at IREC by CBD of  $In_2S_3$  and  $ZnS$ , according to Table IV.7. The depositions are carried out on the same absorber samples used in the previous section (CdS optimization), of composition  $Cu/Zn+Sn=0.75 - 0.78$  and  $Zn/Sn=1.12 - 1.18$ , in order to compare the device performance. Opto-electronic properties of the devices prepared with the Cd-free buffers are shown in Figure IV.14.

Power conversion efficiencies achieved with these cadmium-free devices are lower as for their CdS counterparts (Figure IV.9a). The best  $In_2S_3$ -based devices reach 4.5%, while  $ZnS$ -based devices efficiency remains at lower levels, with a maximum of 1%. Very few devices have been reported for

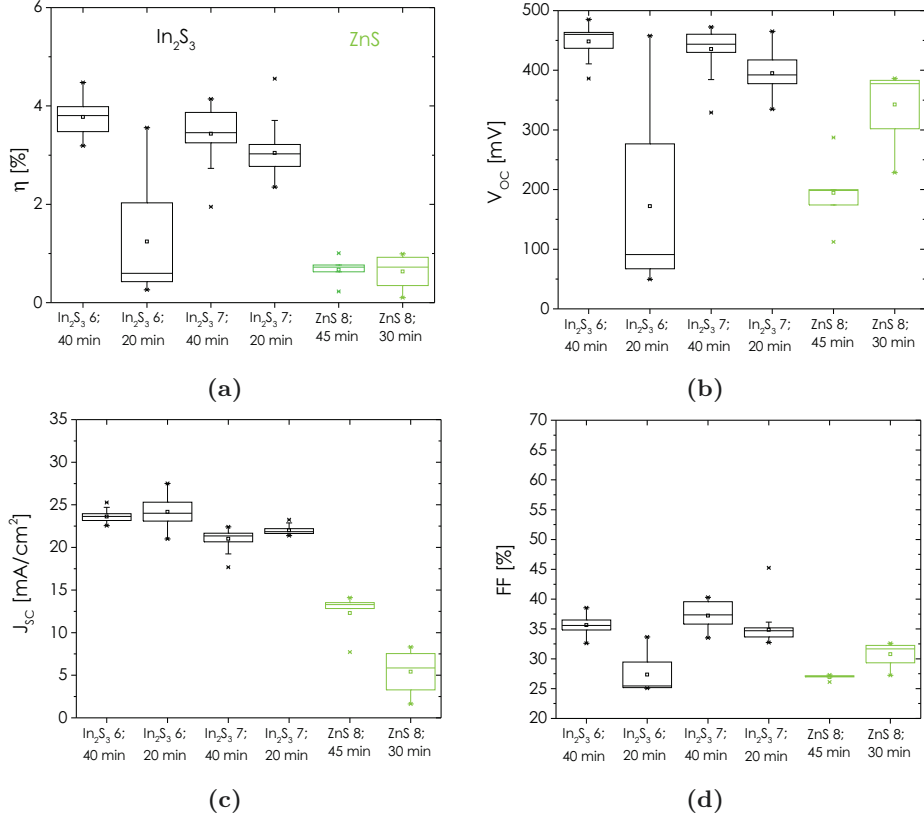


**Figure IV.14:** (a) Power conversion efficiencies  $\eta$ , (b) open-circuit voltages  $V_{OC}$ , (c) short-circuit currents  $J_{SC}$  and (d) fill factors FF of devices made with different  $\text{In}_2\text{S}_3$  and ZnS layers, measured after 2 hours of light soaking.

pure selenide CZTSe and alternative buffer layers, as shown in Table IV.6. One should notice that in this work the open-circuit voltages of  $\text{In}_2\text{S}_3$ -based devices are very high, up to 490 mV, which is the highest  $V_{OC}$  reported for a pure selenide kesterite device. However, low short circuit currents and very low fill factors impede to reach high device efficiency. When compared with CdS-based devices, the current generation in the low wavelength region increases, as shown in the EQE curve Figure IV.15a, which is predicted by the ZnS bandgap value of 3.6 eV and the indirect bandgap nature of  $\text{In}_2\text{S}_3$  (Table IV.4). However, for higher wavelengths, the current collection is poor, as shown by the increase of EQE under -1V bias (Figure IV.15c), resulting in a lower short-circuit current than for the CdS-based devices (Figure IV.15b).

In addition, the J-V parameters presented in Figure IV.14 are already measured after light soaking, with stabilized parameters. Initially, the performance of a  $\text{In}_2\text{S}_3$ -based device is even poorer, because of very low short-circuit current and FF (Figure IV.16). Under illumination  $J_{SC}$  increases quickly while  $V_{OC}$  remains stable. After a few minutes, the opto-electronic parameters stabilize. This light-soaking effect is well known for Zn(O,S)-based devices [140]. Here, even after light soaking, the device performance remains lower than CdS-based devices, mainly because of a still low FF and a distorted J-V curve.

Finally, high (ZnS) or indirect ( $\text{In}_2\text{S}_3$ ) bandgap buffers present — as expected — an improved current collection of the low wavelength photons, but their overall current collection is poor.  $J_{SC}$  and FF are increased by light-soaking, but not enough to reach CdS-based devices performance level. Different hypothesis can explain the poor current collection and fill factor, such as recombination of minority carriers at the interface, light-sensitive defects [34] or a too large conduction band offset. Conduction band offsets at CZTSe/ $\text{In}_2\text{S}_3$  and CZTSe/ZnS interfaces have not been reported yet, but a very high  $V_{OC}$  and reduced current collection could be due to a large conduction-band offset, as estimated for CZTS/ZnS, CZTSSe/ZnS and CZTS/ $\text{In}_2\text{S}_3$ -based devices in Table IV.5. Indeed,



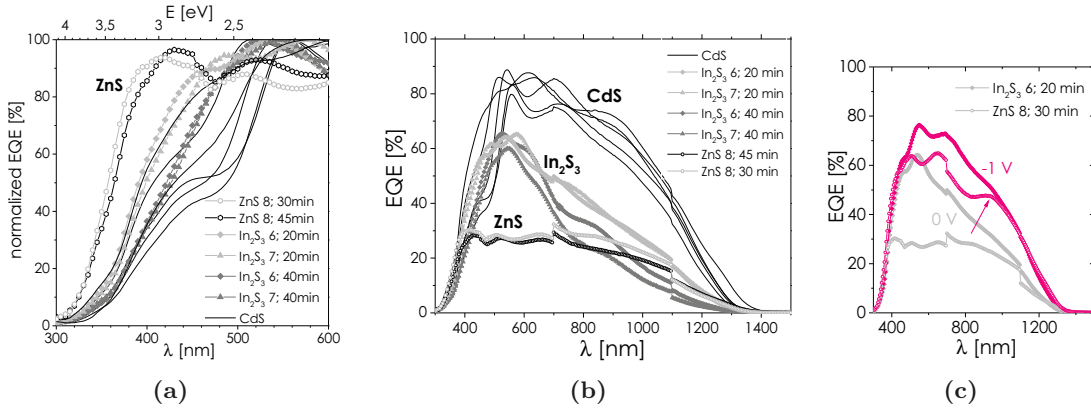


**Figure IV.15:** (a) Normalized EQE curves in the low-wavelength high-energy region, full EQE (b) at 0 V and (c) under reverse voltage of devices prepared with different buffer layers.

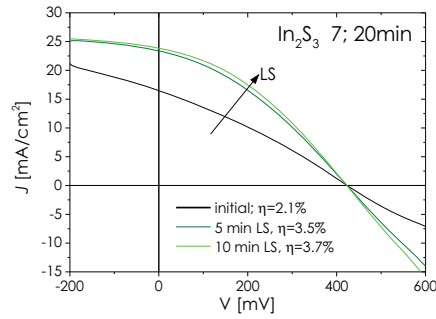


**Figure IV.16:** J-V curve of a CZTSe/In<sub>2</sub>S<sub>3</sub> based device measured after light-soaking (LS).

the achievement of larger  $V_{OC}$  could be considered as a benefit of utilizing wider band gap buffer that might induce the formation of a higher built-in potential [390]. The heterointerface chemistry is still not understood yet, and further optimizations need to be made in order to increase the performance of alternative buffer layers. At this stage, CdS is still the most suitable buffer for producing high efficient kesterite devices. However, using alternative buffer layers is interesting not only to avoid cadmium, but also to tackle the  $V_{OC}$  deficit issue. The use of an hybrid CdS/In<sub>2</sub>S<sub>3</sub> buffer layer in order to reduce the  $V_{OC}$  deficit by indium diffusion has been reported [26, 125, 394]. In this study, very high  $V_{OC}$  have been obtained with the In<sub>2</sub>S<sub>3</sub> buffer.

## IV.3 Front contact optimization

### IV.3.1 Background

#### IV.3.1.1 TCO

Complete solar modules often consist of interconnected cells without metal grid as front contact. The front contact should act as a window for light to pass through and as an ohmic contact for carrier transport out of the cell (large transmittance and high conductivity). The front contact in thin film solar cells is usually a transparent conductive oxide (TCO), which can be deposited at large scale and reasonable cost [110]. Indium tin oxide (ITO) and aluminium-doped zinc oxide (AZO) are widely used in thin film CIGS solar cells.

**ITO** ITO, a compound of indium oxide ( $\text{In}_2\text{O}_3$ ) and tin oxide ( $\text{SnO}_2$ ), is the predominant TCO used in optoelectronic devices. ITO exhibits both excellent electrical and optical properties. However, the concerns about In availability and price have spurred the development of alternatives TCOs [102].

**AZO** ZnO-based TCOs present numerous advantages such as low-cost, abundant material resources and non toxicity. ZnO heavily doped with Al (AZO) has been demonstrated to have low resistivity and high transparency in the visible spectral range. Its conductivity and the transparency are comparable to those of ITO. One disadvantage of ZnO-based TCOs is that they degrade much faster than ITO when exposed to damp and hot environment [102].

**Intrinsic ZnO** Since the buffer layer should be very thin (50 – 80 nm in thickness), pinholes in CdS may result in a direct contact between TCO and the absorber layer, creating short circuits (decrease in shunt resistance) and reducing dramatically the efficiency. Therefore, a thin intrinsic ZnO buffer layer (highly resistive transparent oxide) is inserted between TCO and CdS to prevent any short circuit. [102].

#### IV.3.1.2 Metal contacts

A combination of metal grids and TCO can give a much lower sheet resistance for limited losses in transmittance compared to TCO only, thereby improving solar panel efficiency [110]. The record efficiency cells are usually made with advanced evaporated front contacts, which are especially designed for a small surface area (typically  $1 \text{ cm}^2$ ).

#### IV.3.1.3 Anti-reflective coating

Additionally, an anti reflective coating (ARC) such as  $\text{MgF}_2$  may be deposited on CZTS(e) solar cells in order to reduce the reflectance and limit the optical losses, thereby improving the current generation and collection.

While each front contact layer has a distinct role (CdS/junction formation, TCO/current collection,  $\text{MgF}_2$  /anti-reflection), all three layers optically act in concert to determine what fraction of incident light is transmitted to the CZTSSe or is reflected from the device. Front contact CdS/TCO/ $\text{MgF}_2$  stack can be tuned (usually into thinner TCO and CdS layers) to maximize transmission to the kesterite absorber. An improvement in device efficiency from 11.1% to 12.0% has been reported by optical optimization of the front interface by Winkler et al. [398].

## IV.3.2 Experimentals

### IV.3.2.1 Device preparation

Mo/CZTSe/CdS/i-ZnO/ITO devices are prepared by electrodeposition of stacked precursors (*Chapter 2*), annealing of a  $5 \times 5 \text{ cm}^2$  precursor in presence of Se and Sn vapors in a graphite box (*Chapter 3*), etchings (iii)  $\text{KMnO}_4 / \text{H}_2\text{SO}_4 + \text{Na}_2\text{S} + (\text{NH}_4)_2\text{S}$ , corresponding to the removal of ZnSe, SnSe and  $\text{SnSe}_2$  secondary phases (section IV.1 Kesterite surface treatments page 111), deposition of a CdS buffer layer with  $\text{Cd}(\text{NO}_3)_2$  cadmium precursor (section IV.2 Buffer optimization page 120), and completion (TCO, post treatment, as described page 114). After the TCO deposition and post-treatment,  $0.5 \text{ cm}^2$  cells are mechanically scribed and a Ni/Al grid is evaporated on top of the TCO at IRDEP. The metallic grid is deposited by evaporation of Ni/Al with a finger-like pattern obtained by photolithography, thus leading to very thin fingers (3.5% shadowing) while keeping a high conductivity and low contact resistance. IRDEP metallic grid deposition process has also been used for champion CIGS cells [229].

### IV.3.2.2 Device characterization

The devices opto-electronic properties are characterized by J-V and EQE measurements at NEX-CIS. Dark and illuminated J-V curves are measured using a Sol3A class AAA solar simulator (Newport Corporation) following the E948-09 standard test method from ASTM [399]. Measurements were carried out at  $25 \text{ }^\circ\text{C}$  (water cooled system), and before measuring the irradiance, intensity of the solar simulator is calibrated to 1 sun AM1.5 by using a Si reference cell.

## IV.3.3 Results: Implementation of metal contacts

A best device efficiency of 9.1%, as shown in Figure IV.17 is obtained with the metal contacts, noticeably setting the new world record in power conversion efficiency for kesterite produced by electrodeposition. The open-circuit voltage of the device is 421 mV, its short-circuit current  $34.2 \text{ mA/cm}^2$  and fill factor 64.6. The short circuit current and fill factor are higher than for devices with no metal contacts, showing close to 10% improvement in  $J_{SC}$ .

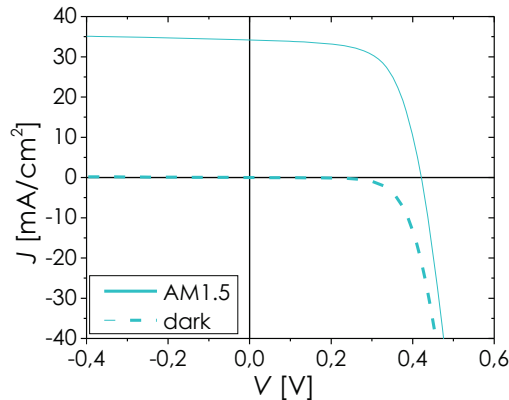


**Figure IV.17:** J-V curve of the CZTSe 9.1% record cell, measured after 30 min light soaking.

Further increase in device performance may be achieved by the addition of an anti-reflective coating and optical optimization.

## IV.4 Conclusions

### IV.4.1 Optimal parameters for high-efficient kesterite devices

The impact of the metallic composition within the Cu-poor range on the opto-electronic properties of the devices is summarized in Figure IV.18.

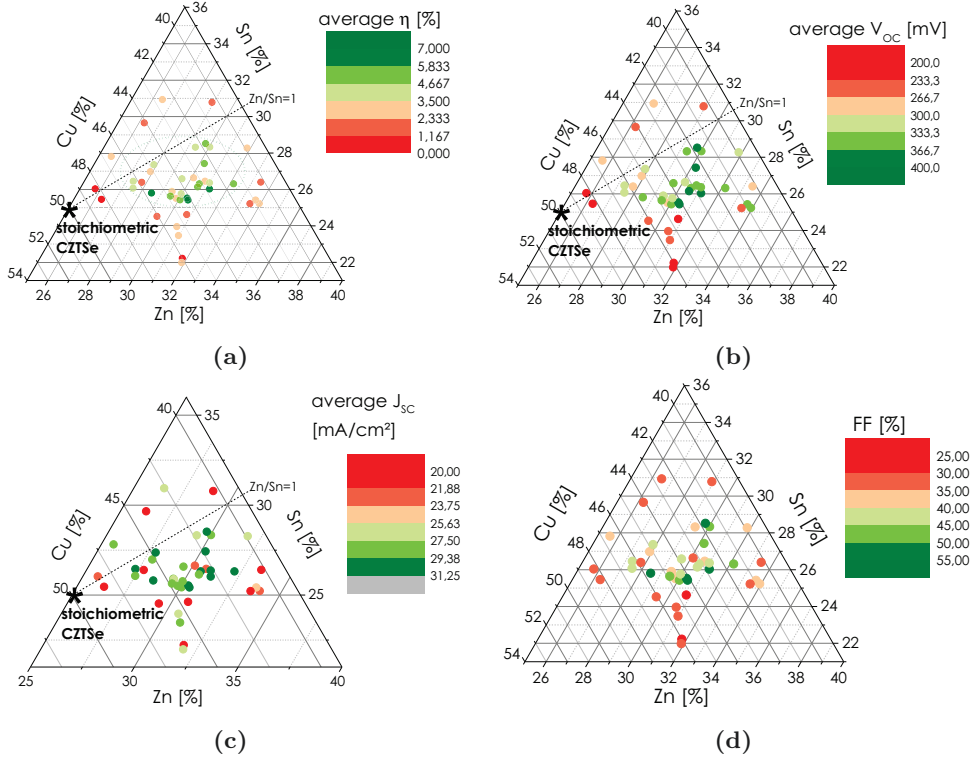


**Figure IV.18:** Ternary diagrams of (a) power conversion efficiencies  $\eta$ , (b) open-circuit voltages  $V_{OC}$ , (c) short-circuit currents  $J_{SC}$  and (d) fill factors FF in dependence of absorber composition. The composition is measured by XRF after etching, if applied. The devices are prepared by applying different etchings followed by deposition of CdS 4 or CdS 5 (7 min) buffer layer. Each point corresponds to one absorber composition, its color is associated to the average parameter of all the sample cells.

As expected, the best power conversion efficiencies are obtained for Cu-poor Zn-rich compositions, where  $Cu/(Sn+Zn) < 1$  and  $Zn/Sn > 1$ . More accurately, the highest efficiencies are obtained for compositions of  $0.70 < Cu/(Sn+Zn) < 0.85$  and  $1.00 < Zn/Sn < 1.25$ . Highest short-circuit currents are obtained for a relatively large region of the ternary diagram (but still in the Cu-poor Zn-rich region), while the highest  $V_{OC}$  seem to be limited to a small zone. Comparing the best pure-selenide CZTSe devices in this work and in literature, reported in Tables IV.8 and IV.9 respectively, the compositions are globally similar. The short-circuit currents are lower in this work than in literature, probably because of an unoptimized front interface (no metal contacts — the JV curve is measured directly on the TCO — and no anti-reflective coating). On the other hand, the open-circuit voltages are very high compared to reported pure-selenium kesterite devices.

The  $V_{OC}$  deficit — i.e. the difference between the  $V_{OC}$  of a device and its bandgap:  $E_g/q - V_{OC}$ , where  $E_g$  is the bandgap and  $q$  the electron charge — should be close to 0.5 volt in a good thin film solar cell.  $V_{OC}$  deficit is the one of main limiting factors for high-efficient kesterite devices. For high efficient pure-selenide CZTSe devices in literature, the  $V_{OC}$  deficit is comprised between

**Table IV.8:** Optoelectronic parameters of high-efficiency pure selenium  $\text{Cu}_2\text{ZnSnSe}_4$  (CZTSe) devices in this work.<sup>a</sup> (iii)  $\text{KMnO}_4 / \text{H}_2\text{SO}_4 + \text{Na}_2\text{S} + (\text{NH}_4)_2\text{S}$  etching.<sup>b</sup> Device with metal contacts.

Etch	Buffer	Cu/Zn+Sn	Zn/Sn	$\eta$ %	$V_{OC}$ mV	$E_g$ eV	$E_g/q-V_{OC}$ V	$J_{SC}$ mA/cm <sup>2</sup>	FF %
(iii) <sup>a</sup>	CdS 4 (45 min)	0.80	1.20	9.1 <sup>b</sup>	421	-	-	34.2	64.6
(iii)	CdS 3	0.75	1.18	8.5	446	1.06	0.61	30.8	62.1
(iii)	CdS 2	0.75	1.18	8.2	466	1.09	0.62	26.1	67.3
(iii)	CdS 4 (45 min)	0.74	1.25	8.2	425	1.05	0.62	30.9	62.7
(iii)	CdS 5 (0.5 min)	0.80	1.17	8.1	413	1.02	0.61	33.4	58.5
(iii)	CdS 5 (7 min)	0.78	1.15	7.5	442	1.04	0.60	29.1	58.1
(iii)	CdS 5 (7 min)	0.66	1.11	6.8	457	1.06	0.60	28.2	52.5
(iii)	$\text{In}_2\text{S}_3$ 6 (40 min)	0.78	1.12	4.5	483	-	-	24.0	38.6

**Table IV.9:** Optoelectronic parameters of high-efficiency pure selenium  $\text{Cu}_2\text{ZnSnSe}_4$  (CZTSe) devices in literature.<sup>a</sup> (i)  $\text{KMnO}_4 / \text{H}_2\text{SO}_4 + \text{Na}_2\text{S}$  etching.

Deposition method	Etch	ARC	Cu/(Zn+Sn)	Zn/Sn	$\eta$ %	$E_g$ eV	$V_{OC}$ mV	$E_g/q-V_{OC}$ V	$J_{SC}$ mA/cm <sup>2</sup>	FF %
co-evap	-	$\text{MgF}_2$	0.85	1.04	11.6 [13]	1	423	0.58	40.6	67.3
sputtering	KCN	$\text{MgF}_2$	0.83	1.2	10.4 [15]	1	394	0.61	39.7	66.4
co-evap	-	-	-	-	9.8 [60]	1	380	0.62	37.6	68.9
sputtering	KCN	$\text{MgF}_2$	0.7	1	9.7 [61]	1	408	0.59	38.9	61.4
co-evap	-	$\text{MgF}_2$	0.86	1.15	9.2 [62]	0.96	377	0.58	37.4	64.9
co-evap	-	$\text{MgF}_2$	-	1.3	8.9 [63]	1	385	0.62	42.6	54.3
sputtering	(i) <sup>a</sup>	-	0.77	1.21	8.2 [34]	1.02	392	0.63	32.4	64.4
ED	KCN	-	-	-	8.0 [32]	1.02	390	0.63	35.3	58
co-evap	KCN	-	-	-	7.5 [64]	-	356	-	35.4	60
sputtering	KCN	-	-	-	7.5 [65]	-	432	-	30.5	56.8
ED	NaCN	$\text{MgF}_2$	-	-	7.0 [31]	1.1	369	0.73	32.4	58.5

0.58 and 0.73 V, as observed in Table IV.9<sup>2</sup>. The calculation of  $V_{OC}$  deficit is dependent on the bandgap estimation method, and can vary, as explained in *Annex B* (section B.3 page 153).

- With the bandgap estimation method 1: inflection point, “whole peak” fitting (usually used in this thesis), the calculated  $V_{OC}$  deficit is in the same range as the best CZTSe devices reported in literature. Thus the high  $V_{OC}$  observed in this work may be related to an increased bandgap (Table IV.8).
- With the bandgap estimation method 2: inflection point, “band edge” fitting, the calculated  $V_{OC}$  deficit is included between 0.54 and 0.59 V (not shown here), showing an improvement compared to literature. Thus the high  $V_{OC}$  observed in this work might result from an improved interface by etching and buffer optimization.

Therefore it is still unclear if the high  $V_{OC}$  observed in this work are due to a higher bandgap, an improved interface, or both. For the  $\text{In}_2\text{S}_3$  devices, it is not possible to extract the bandgap from the EQE curve because the current collection of the high wavelength photons is very poor, but the bandgap of the kesterite material should be similar, indicating further improvement of the  $V_{OC}$  deficit compared to CdS-based devices.

Variations in the bandgap energies are observed to depend on the absorber composition. Figure IV.19 shows that the bandgap energies depend on the Cu content:  $E_g$  increases with a decreasing Cu/(Zn+Sn) ratio. Bandgap energies range from about 0.96 to 1.09 eV. Higher bandgaps are

<sup>2</sup>For mixed sulfur-selenium  $\text{Cu}_2\text{ZnSn}(\text{S},\text{Se})_4$  (CZTSSe) cells, the  $V_{OC}$  deficit has been reported to be larger than 0.6 V and to increase with a larger bandgap and sulfur content [179].

obtained for very Cu-poor films, which might contribute to higher open circuit voltages. An increase of copper concentration towards stoichiometry results in a decrease of the bandgap energy. Various assumptions may explain the bandgap variation with the composition change: formation of Cu-poor  $[\text{Zn}^{2+} + \text{V}_{\text{Cu}}]$  defects [10], exchange of Cu and Zn cations leading to order/disorder in kesterite [66], formation of lower bandgap Cu- rich secondary phases.

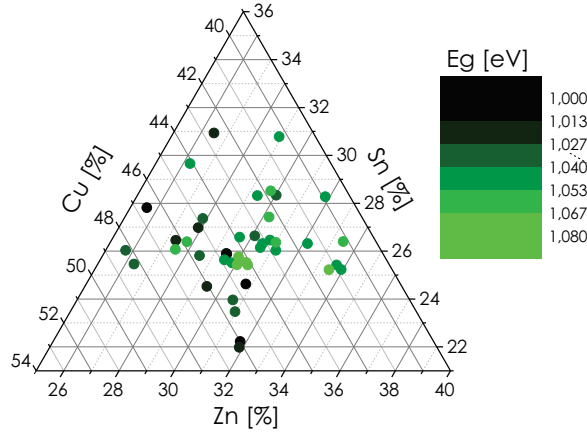


**Figure IV.19:** Bandgap (eV) extracted from the EQE curve versus absorber composition.

#### IV.4.2 Optimum processes

In conclusion, processes and conditions leading to higher device efficiencies have been identified: a) absorber composition (abundance and nature of present secondary phases); b) secondary phases segregation control (limiting their presence to the surface so that they may be removed via chemical etching); c) identification and characterization of the secondary phases; d) adjusted efficient chemical etching procedures, which may also provide passivation of the kesterite absorber surface; e) buffer layer optimization, a compromise between enhanced current with thin layers and enhanced potential and finally f) optimization of the front contact, which increases the current collection and generation by adding metal contacts and an anti-reflective coating. The improvements in CZTSe device efficiency that have been reached through this work by acting on these different levels are summarized in Figure IV.20.

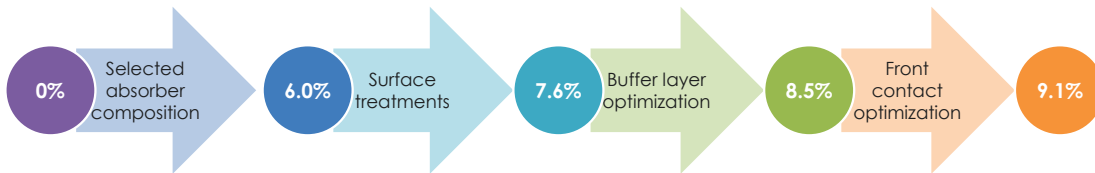


**Figure IV.20:** Summary of the device improvement evolution and the optimized steps.



# Chapter V

## Conclusions: Kesterite - an industrial approach

### Contents

---

V.1	PV technologies perspective . . . . .	<b>136</b>
V.2	Cost per energy unit - Example of CIGS . . . . .	<b>137</b>
V.2.1	Definition of the industrial line . . . . .	137
V.2.2	Production costs . . . . .	138
V.3	Kesterite — an industrial approach . . . . .	<b>139</b>
V.3.1	Low-cost processes . . . . .	139
V.3.1.1	First step: Electrodeposition . . . . .	140
V.3.1.2	Second step: Thermal treatments . . . . .	141
V.3.1.3	Buffer layer deposition . . . . .	142
V.3.2	High efficiency . . . . .	142
V.4	Perspective . . . . .	<b>143</b>

---



## V.1 PV technologies perspective

Today, the dominant photovoltaic (PV) technology is based on crystalline silicon. Since silicon-based PV technologies have been developed and commercialized for many years, c-Si is a mature technology (i.e., the ratio of commercial module efficiency over best laboratory cell efficiency is high). However, production of silicon wafers is expensive and requires a high energy input for purifying, crystallizing and sawing [83]. The ideal photovoltaic system would employ solar panels with high efficiency and very low production costs. The development of second and third generation PV technologies aim to reduce the module cost compared to c-Si. 2<sup>nd</sup> generation PV is based on thin film technologies, including the chalcopyrite  $\text{CuIn}_x\text{Ga}_{1-x}(\text{S,Se})_2$  (CIGS), currently on the market. The main advantage of thin film technologies is their high absorption coefficient for the solar spectrum. This enables the thickness of the light absorbing layers to be between 1 and 2  $\mu\text{m}$  as opposed to crystalline silicon, which needs to be 50 – 100 times thicker, allowing an economic use of active materials and a highly automated processing. However, in the last years, material concerns (indium and gallium are scarce and costly) have spurred on  $\text{Cu}_2\text{ZnSn}(\text{S,Se})_4$  (CZTSSe) kesterite development. Solar cell efficiency — at laboratory and commercial level — and module production cost of wafer-based Si, and thin-film CIGS and kesterite technologies are presented in Table V.1.

**Table V.1:** Comparison of wafer-based silicon, thin-film CIGS and kesterite PV Technologies in relation to their efficiency, cost, material considerations and reliability, thereby evaluating their long-term potential. <sup>a</sup> Efficiency data from [16,26,67–72] and <sup>b</sup> cost data from [73–78], all extracted from Tables I.1 and I.2, see *Introduction*.

Technology	Efficiency $\eta$ (%) <sup>a</sup> Best cell (Commercial module)	Module cost <sup>b</sup> €/Wp	Materials limitation	Reliability
c-Si	25.6 (16 – 21.5)	0.45 – 0.65	Ag electrode	ok
$\text{CuIn}_x\text{Ga}_{1-x}(\text{S,Se})_2$ (CIGS)	21.7 (12 – 15.5)	0.44 – 0.54	In	needs data
$\text{Cu}_2\text{ZnSn}(\text{S,Se})_4$ (CZTSSe)	12.7 (none)	n/a	ok	unknown

The long-term potential of a PV technology does not only rely on efficiency and cost but also on material and reliability considerations [73]. The fulfillment of all the criteria by wafer-based silicon and thin-film CIGS and kesterite PV technologies is discussed below.

- **High efficiency.** Currently, silicon based solar cells offer best power conversion efficiencies than their thin film counterparts. However the efficiency of main thin film technologies (CIGS, but also CdTe) have reached a high level in the last years, demonstrating their suitability for energy conversion at industrial scale. By 2019, average commercial modules efficiencies are expected to reach 17% and 15% for c-Si and thin films, respectively [79]. As customers appear to favor efficiency at the expense of cost — if the ratio cost/W is equal — any (new) thin-film technology (including kesterite) will have to show 10% conversion efficiency potential in the short, and a 15% potential in the medium term in order to succeed on the (pre)-market [16]. Today maximum power conversion efficiency for kesterite devices does not reach such efficiency requirements.
- **Low-cost.** Si-based PV production costs have been dramatically reduced between 2010 and 2013 thanks to reductions in module, inverter prices and manufacturing improvements [95,99] and have reach a stable level since 2014 [78]. Further cost reductions would involve a decrease in purification cost and a reduction in silicon amount by Wp. Currently Si and thin-film production costs are relatively close. However, compared to crystalline Si technology, the monolithic integration of thin-film solar cells can lead to significant manufacturing cost reduction. High-throughput, low-cost processes are one of the keys to thin film production costs reduction (the example of CIGS will be discussed in the next section).
- **Non-toxic, abundant and available materials.** For Si technologies, despite the abundant reserves of silicon (second most abundant element in the earth’s crust), the ultimate power

production potentials appear to be limited by silver (Ag) reserves, used as top (n-type) electric contact material [4]. If the use of silver as top electrode can be reduced in the future, there are no other significant limitations for c-Si solar cells. In the case of thin-film technologies, expected material shortages imposed by global indium (In) reserves — indium, a by-product of zinc production, is a scarce material with unstable and high prices — will affect the cost and development of CIGS modules. Kesterite, composed of earth-abundant elements such as copper, tin, zinc and sulfur, meets almost no restrictions (See *Introduction*, the use of selenium may be limiting).

- **Reliability and durability.** Wafer-based Si PV modules have demonstrated an impressive level of reliability in various forms of applications and installations. In the case of thin-film PV, much less data is available as Si-based modules. Metastable behavior has been observed in the case of CIGS, which even may improve device efficiency. Degradation has been reported in humid climates, and the modules appear to be unstable under exposure to moisture, therefore encapsulation seems to be one of the mayor challenges. In general there is no intrinsic reason why thin film cells/modules have to be less reliable/durable than their wafer-based c-Si counterparts [16]. The issue of whether kesterite devices will behave more like  $\text{Cu}_2\text{S}$  (fast degradation) or like CIGS in terms of device stability under operating conditions (e.g. light, heat, electrical load) must be resolved before a transition to commercialization can be envisioned.

## V.2 Cost per energy unit - Example of CIGS

### V.2.1 Definition of the industrial line

In order to analyze the cost, the production line is split in several production blocks which are themselves separated in segments. For each segment is associated a piece of equipment, the work-in-progress, the metrology (if any) and the incoming and outgoing stock (raw-products or processed pieces) [77]. For instance the front-end of a CIGS production line consists in 5 blocks: Back-contact/Precursor deposition/Absorber thermal treatment/Buffer chemical bath deposition/TCO window sputtering.

The data used to parameter the processing segments are:

- Takt time, the rate at which a finished product needs to be completed in order to meet customer demand, also described by the equation:

$$\text{Takt time} = \frac{\text{Available time for production}}{\text{Required units of production}} \quad (\text{V.1})$$

- Work-in-progress;
- Preventive maintenance time and occurrences so that parallel machines are never stopped simultaneously;
- Routing rules for the incoming and outgoing pieces.

The percentage of time during which all tools are operational is considered so that a total production time can be calculated for each segment and that incoming and outgoing stocks can be estimated in-between segments. The creation of out-going stocks and the need of incoming stock is estimated for different scenarios so that each segment is never out of supply. For instance, Broussillou et al. [77] envisaged scenarios with 2 or 3 electrodeposition machines, 2 or 3 thermal treatment units and 6 or 7 chemistry tools with the aim to saturate a single TCO sputtering tool (more than 100 MW/y). The back-contact processing time is similar to the TCO and the products after back-contact deposition can be quite easily stored as it is the first block in the production line, therefore it is not considered a variable parameter. After defining the number of machines necessary for the production unit, the placement of the machines in the fab needs to be optimized (CAPEX, automation, flexibility).

## V.2.2 Production costs

The production costs are function of the module efficiency, investment, material, personnel, energy, etc, as shown in Figure V.1. The final module cost (per watt peak) will depend on all these parameters.

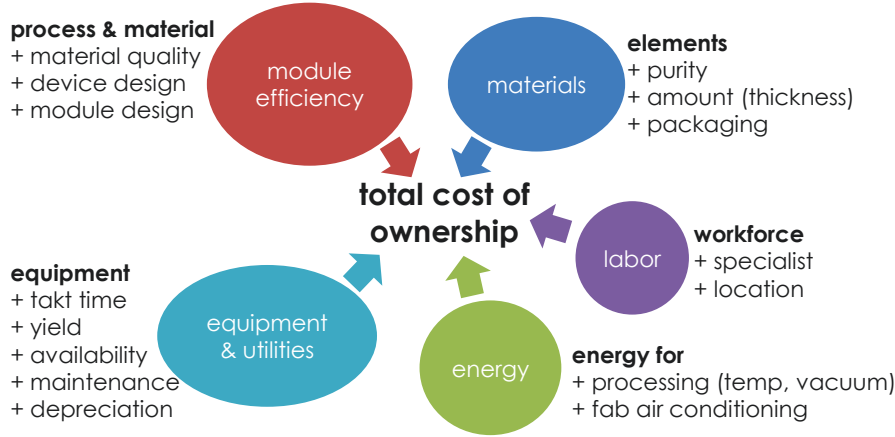


Figure V.1: Total cost of ownership.

For instance, module cost has been calculated by various actors for CIGS thin films as shown in Table I.2.

Table V.2: CIGS estimated module cost depending on hypotheses.

<sup>a</sup> Values in \$ have been converted using change rate of 1€= 1.12809\$ on 2015-09-02.

<sup>b</sup> SolarPower Europe predicts PV installation of 7000 to 17000 MW by year in Europe until 2019 [3].

Cost €/Wp <sup>a</sup>	Fab size <sup>b</sup> MW/year	Fab location	Module efficiency %	Process	Reference
0.34	1000	-	16.3	PVD + annealing	Bosch [400], 2014
0.36	1000	Europe	16	co-evaporation	Picon Solar [80]
0.40	500	Europe	14	ED + elemental S/Se	Scalenano [77], 2015
0.44	214	Asia	-	-	Manz [74], 2013
0.44	500	-	-	co-evaporation	Solibro [73], 2012
0.44	1000	Europe	13	co-evaporation	Picon Solar [75], 2014
0.45	500	Europe	14	PVD + H <sub>2</sub> S/H <sub>2</sub> Se	Scalenano [77], 2015
0.47	500	Europe	12.2	ED + elemental S/Se	Scalenano [77], 2015
0.49	500	Europe	12.8	PVD + H <sub>2</sub> S/H <sub>2</sub> Se	Scalenano [77], 2015
0.52	100	US	14	PVD + annealing	NREL [76], 2015
0.54	< 200	Europe	-	-	Manz [74], 2013

Large variations may be observed depend on the hypotheses that have been considered, allowing to identify the cost reduction potential.

**Manufacturing plant size and location.** Preliminary estimates indicate that scaling from 100 MW/year to 1 GW/year could reduce total module costs by 0.03 – 0.04\$/Wp, and manufacturing in a low-cost labor location could save an additional 0.05\$/Wp [76,80]. Therefore, large size plants are required to produce at low cost. As a consequence of the market growth, the entry ticket (i.e. factory size) for thin-film manufacturers to the market is becoming more and more expensive.

**Process** Currently, the best-performing CIGS devices and large modules are produced in two ways: by evaporation of the elements in vacuum; and by sputtering of the metals (PVD), followed by selenization with  $\text{H}_2\text{Se}$ . These two processes suffer from relatively slow throughput, poor material utilization, and relatively high vacuum. A lower-cost process should feature high deposition rates, high material utilization, and simpler equipment capable of processing very large substrates [401]. The cost analysis performed in the frame of Scalenano project shows that the non-vacuum process (e.g. ED) can lead to a 0.04€/W<sub>p</sub> decrease in the production cost of CIGS modules based on the assumption that large area 1 m<sup>2</sup> modules could be repeatedly produced at 14% [77].

**Module efficiency** The average value of PVD-based modules available today on the market is approximately 12.8%. Raising the module efficiency to 14%, one can expect 0.04€/W<sub>p</sub> decrease in the production cost [77]. From 13% to 16%, Luck [80] reports a decrease of 0.08€/W<sub>p</sub>. Indeed, an higher efficiency would allow to reduce the per-item cost (such as junction box) [80], thereby increase competitiveness with silicon solar cells.

For thin film solar cells such as CIGS, the gap between record cell efficiencies (21.7% [70]) and the values for full-size commercial modules (Solar Frontier 13.8% [71], Miasole 15.5% [72], average value of PVD-based modules 12.8% [77]) can be explained by:

- Fundamental differences (area, thickness of the window layer, contacts) allow for a difference in module to cell efficiency of 2 absolute % [97]. Indeed, the limited conductivity and transmittance of the front contact under the circumstances of a monolithically integrated solar panel may cause efficiency loss [110].
- Non-uniformity of material properties over large areas is the main reason to further limitations in module efficiency [97], and need to be improved.

Therefore, low-cost processes have to be investigated for the production of high-efficient thin film devices, with a special focus on efficiency and uniformity.

## V.3 Kesterite — an industrial approach

Earth-abundant kesterite, structurally related to CIGS in which indium is replaced with more plentiful and lower cost zinc and tin, has shown recent advances and reach a maximum device power conversion efficiency of 12.7% [26]. Kesterite can be considered a current favourite in terms of prospective earth-abundant metal systems to supplement the existing CIGS and CdTe technologies, in the quest for more ubiquitous solar energy deployment [163]. Kesterite thin films main advantages are: a lower cost than CIGS components; no element availability restriction (with the exception of selenium, cf. *Introduction*). They have high-potential for the future large-scale deployment of thin-film PV technologies. The two main pathways for kesterite solar cells to enter the market are 1) Introduction of kesterite manufacturing to an existing CIGS production plant or 2) Development of a revolutionary new manufacturing process with extreme low costs [402]. However, there is still a sizeable performance gap between the kesterite and the more mature CdTe and CIGS technologies. Kesterite devices must reach higher efficiencies (beyond 15% [16], 18% efficiency demonstration [175]) to compete with the current technologies while their manufacturing processes should be performed at high yield and low-cost.

### V.3.1 Low-cost processes

Typically, thin film for photovoltaic applications are deposited by evaporation or sputtering techniques that rely on vacuum environments. The integration of multiple evaporation or sputtering sources provides versatility that allows controlling the film composition and the corresponding phase profile, but also requires a large capital investment. Furthermore, a considerable amount of energy is required to deposit material from the target sources, and the relatively slow throughput

and low materials utilization are not beneficial for large-scale production. Kesterite absorber layers fabrication by non-vacuum or solution-based processes is usually split into a two-step process scheme, where the needed elements are first incorporated during an ambient/low temperature process followed by an annealing step. For assessing the up-scalability of a process, uniformity is the first condition that must be met, but others must be considered such as the compatibility with the rest of the manufacturing line, the reproducibility and robustness of the process as well as the cost-interest of the innovative process in comparison with existing ones [403].

### V.3.1.1 First step: Electrodeposition

Compared to evaporation or sputtering techniques that require vacuum conditions, non-vacuum deposition methods exhibit numerous advantages (see *Introduction*). Indeed, solution-based methods demand lower equipment costs, are suitable for large area and flexible substrates, and offer higher throughput, more efficient material usage and lower temperature processing [16]. For instance, the lower cost of electrodeposition and printing processes compared to PVD-based processes is confirmed by the cost analysis performed by Broussillou et al. for CIGS and CZTSSe materials [81] (Table V.2).

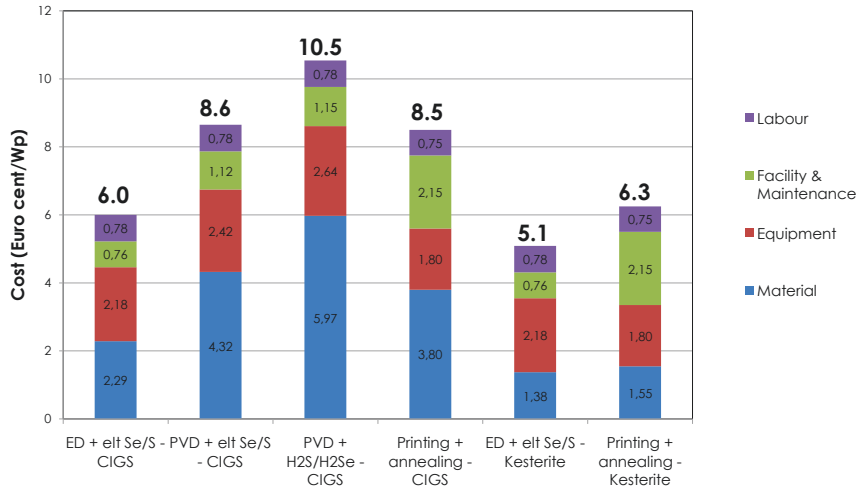


**Figure V.2:** Cost comparison of  $\text{CuIn}_x\text{Ga}_{1-x}(\text{S,Se})_2$  (CIGS) and  $\text{Cu}_2\text{ZnSn}(\text{S,Se})_4$  (CZTSSe) absorbers with ED, PVD or printing processes [81]. Estimation for 14% module efficiency. The printing process is less cost-competitive than electrodeposition due to the high cost for the ink and especially the nanoparticles included in the ink. For comparison, Horowitz et al. estimated a CIGS absorber cost between 8 and 11 c€/W<sub>p</sub> [76].

Not all non-vacuum processes reported in literature are compatible with large scale deposition. Indeed, a sol-gel solution deposited by spin-coating and annealed directly on a hot plate is a suitable process for lab scale samples but could never be used for large-scale industrial processes. Thus, even when promising results are obtained on small scale sample, upgrading the process to larger surfaces often implies to modify the process itself [81]. Solution-based approaches could be suitable for a real low-cost process since the reactive species are directly diluted as salts into readily printable liquid. The cost analysis for solution-based process developed for CZTSSe could not be assessed by Broussillou et al. [81] due to the novelty of the process still being developed, but the fact that the process does not use any nano-particles but a direct deposition of soluble salts could make it particularly interesting on a cost perspective if simple production methods such as doctor-blading can be used for deposition.

Electrodeposition-based processes are attractive industrial approaches for large-scale application and already well-established in the electronics industry. ED can be realized at room temperature using non-toxic and low-cost metallic salt solutions, which have long bath lifetimes and a high

metal using ratio ( $> 90\%$ ), thus avoiding waste of resources. In *Chapter 2* the development of an industrially-compatible electrodeposition route to fabricate Cu-Sn-Zn precursors has been studied. The ability to produce a film of controlled, uniform composition which can be varied rationally as required, satisfying to industry-compatibility requirements such as safety, high throughput and low cost has been successfully demonstrated.

### V.3.1.2 Second step: Thermal treatments

**Elemental chalcogen versus hydrogen sulfide/selenide** Currently, deposition of metals followed by selenization with  $\text{H}_2\text{Se}$  is a production method for the best-performing CIGS devices and large modules. However, when comparing elemental Se — nitrogen can be used as carrier gas for elemental selenium transport — and  $\text{H}_2\text{Se}$ , purchase of elemental selenium per unit mass is approximately a quarter of the price of hydrogen diselenide ( $\text{H}_2\text{Se}$ ). In addition to this inherent price difference,  $\text{H}_2\text{Se}$  has significant higher safety costs, related to transport and handling of this hazardous gas [326]. Even if an additional intermediate selenium deposition process by VTD is added prior to the annealing (so as to improve Se incorporation and uniformity), the cost of ownership is still lower than using  $\text{H}_2\text{Se}$  [326]. Therefore a process based on elemental chalcogen vapors is preferable for price and safety. The thermal treatment systems that have been studied through this work (*Chapter 3*) are described in Table V.3. They are all based on elemental S, Se and eventually Sn.

**Table V.3:** Thermal treatment systems

Name (Institution)	Chalcogen mg	Pressure mbar	Ramp $^{\circ}\text{C}/\text{min}$	$t$ min	$A$ $\text{cm}^2$	Best device %	RSD %	Composition control
<b>Confined chalcogen systems (CC)</b>								
A (NEXCIS)	S (100)	7	RTP: 120-600	0-10	15x15	5.4	5	Zn and Sn losses
C (IRDEP)	Se (20-70)	1013	40	15	2.5x2.5	5.3	6	Sn loss
D (IREC)	Se (50); Sn (5)	1.5 + 1000	20	15 + 30	5x5	6.0	4	ok
<b>Independant chalcogen system (IC)</b>								
B (IRDEP)	Se (500-5500)	985	RTP: 180-400	3	2.5x2.5	5.5	5	Sn loss

**Pressure** Main CIGS production technologies (sputtering + annealing or coevaporation) require the use of vacuum thermal treatment systems. In comparison, non-vacuum tools in which the process is performed at atmospheric pressure while the reactive gas mixture is safely contained offer significant cost reductions [326]. In that respect, atmospheric annealing systems IC-IRDEP and CC-IRDEP are preferable to vacuum annealing systems.

**Heating ramp** RTP systems are preferable to time intensive conventional annealing systems as they allow higher throughput (high speed process) and do not require an excessive amount of energy. Another advantage of a fast annealing is the limitation of chalcogen losses: processing times are much shorter than conventional thermal processes, thus allowing kinetically driven grain growth processes to proceed more quickly than thermodynamically driven decomposition reactions [44]. Therefore the RTP CC-NEXCIS and IC-IRDEP are more industrially viable annealing systems than conventional tube furnace CC-IRDEP or CC-IREC.

**Large-scale** Finally, the annealing systems also need to be able to operate at large-scale. CC-NEXCIS system is at pre-industrial scale while other annealing systems are at laboratory scale. Ideally, the thermal treatment system should also allow an easy maintenance (system stability), a low-risk process (overpressure, contamination), an easy measurement and control of the process parameters (temperature, pressure). The main advantage of CC-NEXCIS is the possibility to anneal large scale precursors, at a high speed, which is compatible with a pre-industrial process. However, due to uniformity, reproducibility and especially equipment availability issues, the

absorber formation studies have been completed with smaller scale annealing systems. IC- and CC-IRDEP systems present the benefit of being atmospheric systems, which is more favorable in terms of energetics, because no vacuum is required. Nonetheless, reproducibility issues impeded further process optimization. The CC-IREC system, although being a “slow” and “vacuum” system, allows to obtain a quite uniform absorbers with a good reproducibility, which is of great importance for process optimization.

In summary, different annealing systems have been used, with different degrees of compatibility with an industrial process. A RTP atmospheric process with elemental chalcogen seems to be the most suitable for a low cost of ownership, which suits the description of IC-IRDEP annealing system. However, lack of uniformity, reproducibility and robustness of the process impede the assessment of its industry-compatibility. The up-scalability of the annealing manufacturing processes studied in this work remains an open issue. The system CC-IREC, which is not the preferred system in terms of compatibility with industry requirements (vacuum, conventional furnace), allows the most accurate composition control, therefore it has been chosen for the efficiency optimization studies.

### V.3.1.3 Buffer layer deposition

Typically, tens of nanometers thick buffer layers are deposited after the formation of the absorber. The layers may be deposited by different methods [326]:

- Sputtering methods present high damage risks.
- ALD is a very slow process, and upscaling it to large substrates is costly.
- Wet chemical methods have logistic and cost (waste) aspects but they allow to deposit buffer layers at large scale. CBD, the preferred method, allow the removal of any oxide on the surface of the absorber layer, extreme conformity, and alteration of the absorber surface electrochemistry to yield a strongly n-type surface layer [16].

### V.3.2 High efficiency

**Kesterite formation issues** A major challenge in the making of CZTS as well as CZTSe material is to obtain single-phase kesterite. Compositional control in the CZTS(e) system is even more important than for CIGS owing to the relatively small range of chemical potentials for which the formation of CZTS(e) is thermodynamically stable. CZTS(e) is a material with a very complicated phase diagram, and as a consequence the resulting properties are very dependent on the processing route that is followed to achieve a certain composition. Loss of zinc or tin leads to loss of stoichiometry and precipitation of other secondary phases, such as Cu-S(e) (CuS(e),  $\text{Cu}_{2-x}\text{S(e)}$ ,  $\text{Cu}_2\text{S(e)}$ ), Sn-S(e) ( $\text{SnS(e)}$ ,  $\text{SnS(e)}_2$ ) and ZnS(e), which are detrimental to device performance. The best CZTS(e) cells have a slightly copper-poor and zinc-rich stoichiometry, where ZnS(e) — less detrimental than Cu- or Sn- based secondary phases — is expected. Addition of Sn(s) in the annealing reaction chamber (system CC-IREC) proved to help controlling the absorber composition, thereby limiting the presence of undesirable secondary phases and improving the device efficiency.

**Etching** KCN etching is often used in CIGS manufacturing in order to clean the surface and remove Cu-S(e) secondary phases. For pure-selenide kesterite, detrimental Sn-Se ( $\text{SnSe}$ ,  $\text{SnSe}_2$ ) and ZnSe secondary phases present at the Cu-poor CZTSe absorbers’ surface can be removed by the combination of etchants  $\text{KMnO}_4/\text{H}_2\text{SO}_4 + \text{Na}_2\text{S} + (\text{NH}_4)_2\text{S}$ , as demonstrated in *Chapter 4*. This etching combination, in comparison with KCN, includes more steps (three different dips) but is less toxic, thereby limiting the transport and handling of hazardous chemicals cost. Etching proved to greatly improve the device performance, therefore this step is crucial to efficient kesterite device fabrication. For pure-sulfur CZTS, the etching procedure has not been investigated in this

thesis, but  $\text{HCl} + (\text{NH}_4)_2\text{S}$  may be efficient for removal of ZnS and Sn-S ( $\text{SnS}$ ,  $\text{SnS}_2$ ) secondary phases.

**Buffer layer** The most common buffer layer is CdS but because of the toxicity of cadmium, cadmium-free alternatives such as Zn(O,S) and  $\text{In}_2\text{S}_3$  would be safer to deposit. Cadmium-free alternatives such as Zn(O,S) and  $\text{In}_2\text{S}_3$  offer in principle the possibility of improved cell efficiency because their optical transmission is higher than that of a CdS window layer, thereby enabling more light to reach the absorber. However, CdS is found to give the best device performances and its thickness can be tuned so as to have a compromise between high short-circuit current and high open-circuit voltage (*Chapter 4*).  $\text{In}_2\text{S}_3$  or other buffer have shown to be promising to reduce the  $V_{OC}$  deficit but still exhibit lower device performance. So far, record performances with alternative buffers are still lower than with CBD-CdS buffer layers, but certainly good enough to be considered as viable candidates for manufacturing.

## V.4 Perspective

In literature, 9 – 12% efficient kesterite devices have been obtained by different low-cost production methods, with a best device efficiency of 12.7% with a hydrazine-based process. Within this work, a 9.1% CZTSe device is produced using electrodeposition followed by annealing processes, setting up a new record of power conversion efficiency for kesterite prepared by electrodeposition. ED has the ability to produce a Cu/Sn/Zn film of controlled, uniform composition which can be varied rationally as required, satisfying to industry-compatibility requirements such as safety, high throughput and low cost. However, the devices power conversion efficiencies are still low compared to CIGS and CdTe ones, and the annealing process needs prove its up-scalability. Currently, CZTS(e) is still in a definite R&D stage.

- CZTS(e) processing is challenging as the mix of elements is volatile (e.g. Sn), and the CZTS(e) phase diagram has a very narrow compositional field of stability. The presence of secondary phases, especially at the absorber's surface, can cause a great harm to device performance. A precise composition control and improved uniformity allow to minimize the presence of undesirable secondary phases. The best devices are obtained for a Cu-poor Zn-rich composition (vs. stoichiometry), where the presence of conductive Cu-based secondary phases is unlikely. For this composition, the presence of ZnS(e) secondary phase is highly probable. When located at the back or in the bulk, ZnS(e) does not cause much harm, but when located at the absorber's surface, it hinders the current collection. Sn-based secondary phases may also be found and shunt the device. Removal of secondary phases from the surface by wet chemical etching has shown to be crucial to improve kesterite device efficiency. However, it is necessary not only to accommodate the processing challenges and presence of secondary phases but also to gain a better understanding of interfaces and defects in the CZTS(e) system in order to further increase device  $V_{OC}$  and fill factor and to narrow the performance gap with CIGS.
- Front interface optimization by surface treatments and buffer layer optimization is one of the keys to improve kesterite device  $V_{OC}$  and efficiency. Defects that form at the interface between the buffer layer and the copper-depleted kesterite surface influence the junction properties. Deeper investigations about the chemical and electrical properties of the kesterite surface and the junction it forms with buffer materials are needed.
- One other important factor limiting kesterite solar cells efficiency is the existence of tail states due to electrostatic potential fluctuations. The formation of charged defects, such as  $[\text{Cu}_{\text{Zn}}^- + \text{Zn}_{\text{Cu}}^+]$  (expected for all compositions), and the lower dielectric constant of CZTSSe (compared to CIGS) are suggested as the main factors determining the amplitude of the electrostatic potential fluctuations [213]. Cu-Zn disorder in kesterite may be reduced through low-temperature annealing for extended periods of time. In addition, kesterite properties may be adjusted by varying the metal composition or introducing extrinsic doping (Na, K, Li, O,



Ge, Si or other); avoiding the formation of deep and detrimental defect clusters; passivating the grain boundaries or increasing the bandgap at the surface (bandgap grading).

Tailoring material composition during processing, finding the ideal device structure, and closely monitor growth conditions and fabrication sequences will be the key to fabricate marketable, high-efficiency CZTS(e)-based solar cells at low cost. If a company manages to reach 15 – 18% marketable efficiency and production levels in comparison with c-Si based PV modules, commercial CZTS(e) may take a significant share in the market between 2020 and 2030 [16].

# Appendix A

## Photovoltaics perspectives

### A.1 PV in general

As described in the *Chapter 1: Introduction*, different energy generation scenarios are envisaged by the International Energy Agency (IEA) for 2050 [1]. Solar PV technologies are predicted to account for 1% to 16% — depending on the scenario — of the global electricity production in 2050, corresponding to 500 to 6400 TWh each year.

The output per watt (W) installed (also termed “watt-peak”, or Wp) required to produce such a quantity of energy depends on the capacity factor. The capacity factor of a power plant is the ratio of its actual output over a period of time, to its potential output when operating at full capacity continuously over the same period of time. For solar cells, the actual output depends on the solar resource, the orientation of the modules and the efficiency losses resulting from actual module temperature, module mismatch, varying irradiance conditions (daily rotation of the earth, seasonal changes, cloud cover), dirt, line resistance and conversion losses in the inverter. The capacity factor for PV may vary from 10% in low solar irradiance regions ( $1200 \text{ W/m}^2$ ) to 25% for well-designed plants in high insolation regions ( $2500 \text{ W/m}^2$ ) [1]. Table A.1 summarizes the worldwide installed peak capacity in 2050 depending on the PV deployment scenario and capacity factor considered. In the scenario of high PV deployment, based on a 25 percent capacity factor, the worldwide installed PV peak capacity in 2050 would be 2.9 TW.

**Table A.1:** Worldwide installed peak capacity (TW) in 2050.

PV deployment	Low 500 TWh	High 6400 TWh
Low capacity factor (10%)	0.6	7.3
High capacity factor (25%)	0.2	2.9

Nominal efficiency determines the required receptive area per watt. The nominal efficiency refers to the power generated under so-called “standard test conditions”: module temperature of  $25^\circ\text{C}$ , vertical irradiance of  $1000 \text{ W/m}^2$ , AM1.5 specific irradiance spectrum. For example, modules of  $1 \text{ m}^2$  would generate a maximum power of 100 W with 10% efficiency, and 200 W with 20% efficiency under the standard test conditions.

Assuming a peak power output of  $100 \text{ W/m}^2$  and a capacity factor of 25%, a total surface area of roughly  $29000 \text{ km}^2$  of photovoltaic panels would be required to produce high scenario 2.9 TW electricity. The low scenario (1% of the total electricity generation by PV) predicts roughly 0.2 TW installed PV capacity, requiring  $2000 \text{ km}^2$  of photovoltaic panels (Table A.2).

**Table A.2:** Surface covered by PV (km<sup>2</sup>) in 2050.

PV deployment Capacity factor	Low 500 TWh High 25%	High 6400 TWh Low 10%
10% efficiency: 100 W/m <sup>2</sup>	2 000	73 000
20% efficiency: 200 W/m <sup>2</sup>	1 000	36 500

## A.2 Part of thin film technologies

According to the IEA scenarios, the worldwide installed peak capacity in 2050 is predicted to be between 0.2 to 7.3 TW. Considering that thin films will represent 10% of the PV market, these technologies will account for 20 GW to 730 GW. If they represent 30% of the PV market, up to 2.19 TW can be installed by 2050, as shown in Table A.3.

**Table A.3:** Part of thin film technologies in 2050, depending on the PV deployment scenario and the part of thin films in the market share.

PV deployment Capacity factor Thin film market share	Low 500TWh High 25% 10%	High 6400TWh Low 10% 30%
Total thin films peak capacity (GW)	20	2190
Surface covered (km <sup>2</sup> ) with 10% efficiency	20	2190
Surface covered (km <sup>2</sup> ) with 15% efficiency	13.3	1460

In summary, taking into account the conservative hypotheses, one reaches to the conclusion of 20 GW of installed thin films installed in 2050, while the optimistic hypotheses predicts 2190 GW. Stamp et al. estimated an installed CIGS capacity ranging from 31 to 1401 GW in 2050, which is coherent with these estimations [103]. In 2015, the main thin-film solar cells manufacturers First Solar and Solar Frontier already claim for more than 10 GW of CdTe panels installed [404] and 2 GW of CIGS panels shipped [71], respectively. Therefore, it seems unlikely that thin film technologies will account for only 20 GW in more than 30 years from now. 880 GW is taken as an intermediate value between the low estimation of 20 GW and the high estimation of 2190 GW, and might be an overestimation as the thin-film market is likely to be shared between all thin-film technologies such as CdTe and amorphous silicon.

# Appendix B

## Characterization methods

### Contents

---

A.1 PV in general . . . . .	145
A.2 Part of thin film technologies . . . . .	146

---

### B.1 Bath analysis: Hull cell set-up

The Hull cell is useful for preliminary studies — Fawaz et al. worked at Hull cell size in order to choose the electrolyte formulation and to try out different precursor stack orders [292] — but also to qualitatively check the condition of an electroplating bath (ageing, additives replenishment). The Hull cell replicates the plating bath on a laboratory scale (267 mL of solution, as shown in Figure B.1) and allows the optimization of current density range, additive concentration, recognition of impurity effects and indication of macro-throwing power capability.

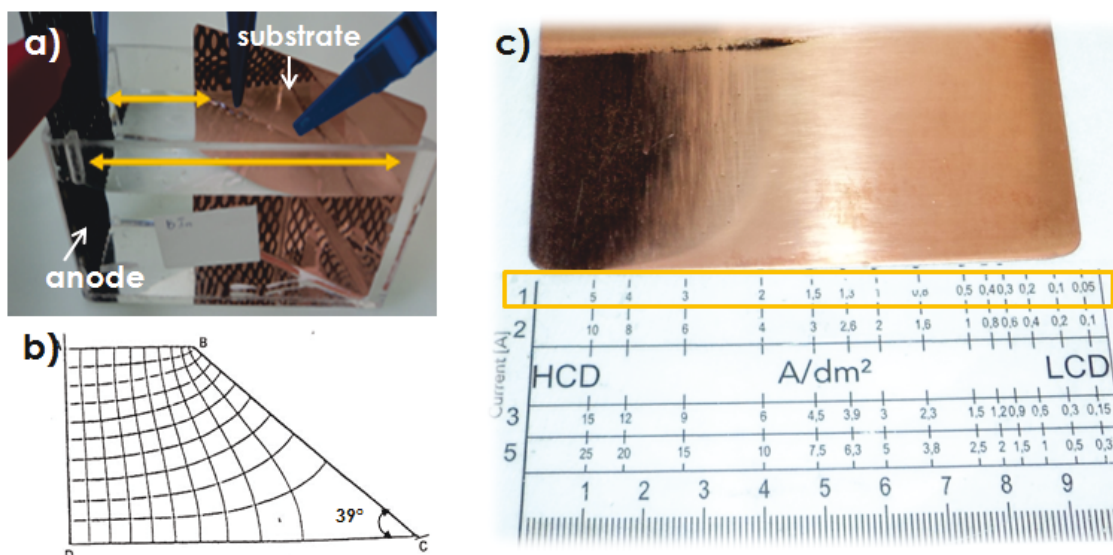


**Figure B.1:** Electrodeposition in Hull cell. (a) A  $3.7 \times 5 \text{ cm}^2$  substrate and an anode are placed into 267 mL of the electrolyte. (b) Schematic distribution of current lines. (c) Example of a Cu layer electrodeposited from acid copper electroplating bath onto a Cu bar after deposition at  $1 \text{ A/dm}^2$  for 1 min. The highlighted part on the rule represents the actual current density. At the left of the image, the copper layer deposited is thicker, because the current density is higher.

It is filled with a sample of the plating solution, an appropriate anode which is connected to a current source. The substrate is replaced with a Hull cell test panel (a smaller substrate, or for instance a copper bar). The Hull cell is a trapezoidal container, allowing one to place the test panel on an angle to the anode. As a result, the deposit is plated at different current densities which can be measured with a hull cell ruler. The following two pages show the Hull cell test procedure used for the alkaline zinc electrolyte.



Cookson Electronics

6008

## HULL CELL TEST

### ALKALINE ZINC PROCESSES

ENTHOBRITE® NCZ DIMENSION, ENTHOBRITE® NCZ DIMENSION K, ENTHOBRITE® NCZ 5001

### GENERAL REMARKS

The electrolyte cannot only be checked for correct operation by an analysis, but also by a Hull cell test. This test can also help to find out whether further additions of replenisher are necessary. In many cases problems can be avoided by using unobjectionable and tested chemicals only.

### HULL CELL TEST

#### CONTAINER

Hull cell

#### HEATING

Magnetic stirrer with adjustable heating, water bath

#### ANODE

Steel panel 80 x 60 mm  
(The anode should rest evenly against the Hull cell wall)

#### CATHODE

Standard Hull cell panel (steel, already zinc plated)

#### MOVEMENT/AGITATION

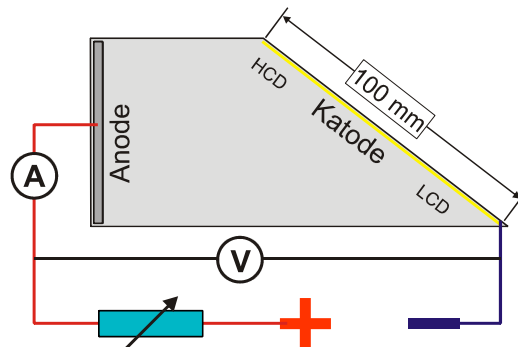
None

#### ELECTROLYTE MAKE-UP

According to the applicable current Technical Data Sheet, or use customer's electrolyte to be analysed. Apportioning of additives as per TDS.

#### ELECTROLYTE VOLUME

250 mL



enthone



Cookson Electronics

**PLATING PARAMETERS**

Rectifier with a residual ripple of less than 5 %.

Amperage 2.0 A

Temperature 25°C

Time of exposure 10 min (bear the current load in Ah/L in mind!)

**SEQUENCE OF OPERATIONS**

**PRE-TREATMENT**

- Stripping of the zinc coat (hydrochloric acid 1:1)
  - Alternatively, for panels not already zinc plated:
  - Anodic cleaning
  - Rinsing
  - Acid dip in hydrochloric acid 1:1
- Rinsing
- Rubbing off the stripping/acid dip residues with a paper tissue
- Rinsing

**ELECTROPLATING**

- Put the panel into the Hull cell
- Time of exposure 10 min

**POST-TREATMENT**

- Rinsing
- Brightening (5.0 mL/L of nitric acid 54-55 %), 15 sec
- Rinsing
- Drying

**CRITERIA FOR ASSESSMENT**

- Brightness
- No clouds, no haze
- No burns
- No stains or dark deposits
- Please also refer to the troubleshooting list in the TDS

Make sure the applicable safety regulations are conformed to!

enthone

## B.2 Composition analysis

### B.2.1 ICP

Inductively coupled plasma/optical emission spectrometry (ICP/OES) is a powerful tool for the determination of metals in a variety of different sample matrices [405]. With this technique, liquid samples are injected into a radiofrequency (RF)-induced argon plasma using one of a variety of nebulizers or sample introduction techniques. The sample mist reaching the plasma is quickly dried, vaporized, and energized through collisional excitation at high temperature. The atomic emission emanating from the plasma is viewed in either a radial or axial configuration, collected with a lens or mirror, and imaged onto the entrance slit of a wavelength selection device. Single element measurements can be performed cost effectively with a simple monochromator/photomultiplier tube (PMT) combination, and simultaneous multi-element determinations are performed for up to 70 elements with the combination of a polychromator and an array detector. The analytical performance of such systems is competitive with most other inorganic analysis techniques, especially with regards to sample throughput and sensitivity. ICP is used both for measuring the concentration of elements in the electrolytes and in the thin films.

### B.2.2 XRF and RSD

#### B.2.2.1 Principles of X-ray fluorescence (XRF)

In an atom, electrons are fixed at specific energies, and this determines their orbits. Additionally, the spacing between the orbits is unique to the atoms of each element. The principle of XRF is schematized in Figure B.2 [406–408].

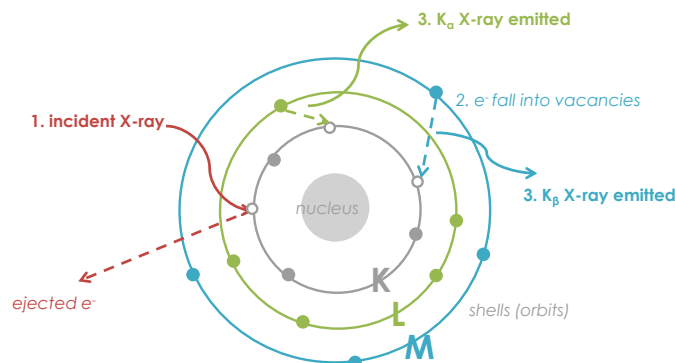


**Figure B.2:** X-ray fluorescence principle, adapted from [407, 408].

1. When a material is subjected to X-ray bombardment, the interaction of X-ray photons with atoms cause the displacement of an inner orbit electron (the electron leaves the atom). This displacement happens when the X-ray beam energy is higher than the binding energy of the electrons with which it interacts. When electrons are knocked out of their orbit, they leave behind vacancies, making the atom unstable.
2. The atom must immediately correct the instability by filling the vacancies that the displaced electrons left behind. Those vacancies can be filled by electrons from higher energy orbits that move down to a lower energy orbit where a vacancy exists. Electrons have higher binding energies the further they are from the nucleus of the atom.
3. Therefore, an electron loses some energy when it drops from a higher electron shell to an electron shell closer to the nucleus. Excess energy, released as this electron falls towards the nucleus, is emitted as a secondary "fluorescence" X-ray photon having a discrete energy



corresponding to the difference in energy between the two orbital levels involved in the transition. The distance between the two orbital shells is unique to each element, as mentioned above.

The energy lost can be used to identify the element from which it emanates, because the amount of energy lost in the fluorescence process is unique to each element. The individual fluorescent energies detected are specific to the elements that are present in the sample. In analytical determinations, the intensity of this characteristic fluorescence radiation is measured, as this signal is, after correction for X-ray absorption/ enhancement effects, proportional to the atomic concentration of the respective element. The quantity of energy released will be dependent upon the thickness of the material being measured. The most sensitive response is normally obtained by fluorescence of K-lines, which result from transitions following ionisation of a K-shell electron. Two principal K-lines ( $K_\alpha$  and  $K_\beta$ ) are emitted, corresponding to X-ray photons emitted during the transition of electrons from L to K and M to K orbital shells respectively, as shown in Figure B.2. Basically, the X-ray fluorescence unit consists of an X-ray tube and a proportional counter. Emitted photons ionize the gas in the counter tube proportional to their energy, permitting spectrum analysis for determination of the material and thickness. For more information, the reader may refer to [406, 409, 410].

### B.2.2.2 Relative standard deviation (RSD)

The composition is determined by measuring  $N$  points by XRF over a given area, as shown in Figure B.3.

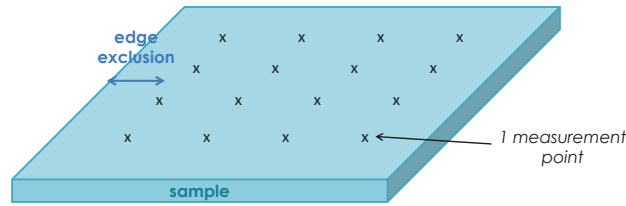


**Figure B.3:** Schema of the points measured by XRF on a sample of a given area.

The mean  $\mu$ , the sum of the determined values divided by  $N$ , is taken as composition of the sample.

$$\mu = \frac{1}{N} \sum_{k=1}^N x_k \quad (\text{B.1})$$

The standard deviation  $\sigma$  is a measure that is used to quantify the amount of variation or dispersion of a set of data values.

$$\sigma = \sqrt{\frac{1}{N} \sum_{i=1}^N (x_i - \mu)^2} \quad (\text{B.2})$$

The coefficient of variation (CV) is a standardized measure of dispersion of a probability distribution or frequency distribution. It is defined as the ratio of the standard deviation  $\sigma$  to the mean  $\mu$  :

$$c_v = \frac{\sigma}{\mu} \quad (\text{B.3})$$

The relative standard deviation (RSD), expressed as a percentage, is the absolute value of CV. The actual value of the RSD is independent of the unit in which the measurement has been taken, so it is a dimensionless number. For comparison between data sets with different units or widely different means, one should use the relative standard deviation instead of the standard deviation.

### B.3 Bandgap determination methods (EQE)

The bandgap of a device can be estimated with different methods:

- Absorption measurements, or indirectly by optical transmission measurements: taking the intercept of the  $(\alpha E)^2$  vs  $E$  curve. However, this method has shown inaccuracies because of the presence of secondary phases [411];
- The energy related to the wavelength of the photoluminescence (PL) peak and the electroluminescence (EL) peak of a semiconductor material can be used to estimate this semiconductor parameter. However, bandgap fluctuation and electrostatic potential fluctuation lead to band tailing in kesterite materials [213]. As a consequence peak broadening and a peak shift towards lower energy with respect to  $E_g$  are observed in room-temperature PL [23].
- Quantum efficiency measurements. For an ideal junction, the EQE can be approximated by:

$$\text{EQE} = 1 - \frac{\exp[-\alpha(\lambda)W(V)]}{1 + \alpha(\lambda)L_n} \quad (\text{B.4})$$

where  $\alpha(\lambda)$  is the absorption coefficient,  $W(V)$  the width of the space charge region and  $L_n$  the minority carrier diffusion length [166, 352]. Assuming a very short  $L_n$ , Equation B.4 reduces to:

$$\text{EQE} = 1 - \exp[-\alpha W(V)] \quad (\text{B.5})$$

Therefore the bandgap can be extracted from QE measurements based on the square root relationship of the absorption coefficient  $\alpha$  and the bandgap  $E_g$  for direct transitions [166, 412]:

$$\alpha(E) \propto \sqrt{E - E_g} \quad (\text{B.6})$$

where  $E$  is the photon energy. A plot of  $[E \times \ln(1 - \text{EQE})]^2$  against  $E$  can be used to extrapolate the bandgap  $E_g$  near the band edge. The bandgaps of absorber, TCO and buffer layers lie close to the inflection points, i.e. the extrema in the  $d\text{QE}/d\lambda$ -curve. Hence, another simple method for bandgap approximation consists in taking the inflection point at high wavelengths of the EQE curve [413]. A fit can be used to refine the result.

The methods used in literature for kesterite's bandgap estimation are summarized in Table B.1.

**Table B.1:** Bandgap determination methods.

Bandgap determination method	Reference
Transmission measurement	[411]
Photoluminescence at room temperature (RT-PL) or low temperature	[15, 61, 62, 411]
Inflection point of the QE curve	[13]
$[E \times \ln(1 - \text{EQE})]^2$ vs. $E$ near the band edge	[35, 179, 411]
$[E \times \text{EQE}]^2$ vs. $E$ or $\text{EQE}^2$ vs. $E$ near the band edge	[191]

The EQE curves of kesterite devices do not present a sharp band edge, making an accurate estimation of the bandgap by quantum efficiency difficult. As all methods suffer the same experimental imprecision, none should be considered superior, however, the derivative method is the most straightforward [413]. In this work, the bandgap is extracted from the EQE curve by taking the inflection point. However, because of “multiple” inflection points, it is not easy to find the maximum objectively, as shown in Figure B.4. For the 8.5% cell obtained with CdS 3, the most “natural” fitting is the a) whole peak fitting (method 1), giving a bandgap of 1.06 eV while for the 8.1% cell obtained with CdS 5, it is obvious that fitting d) the band-edge fitting, method 2 is more adapted. However, in order to compare the bandgaps of the cells, it is preferable to fit all curves in the same way. The fit b) with method 2 is challenging because it is subjective, so it may be

more easy to do the whole peak fit (method 1), as demonstrated for a) and c), in order to compare the bandgaps. Applying method 1, the bandgap might be overestimated, while using method 2, an underestimation is possible. Therefore, all the estimated bandgaps in this work (except when mentioned) might be overestimated.

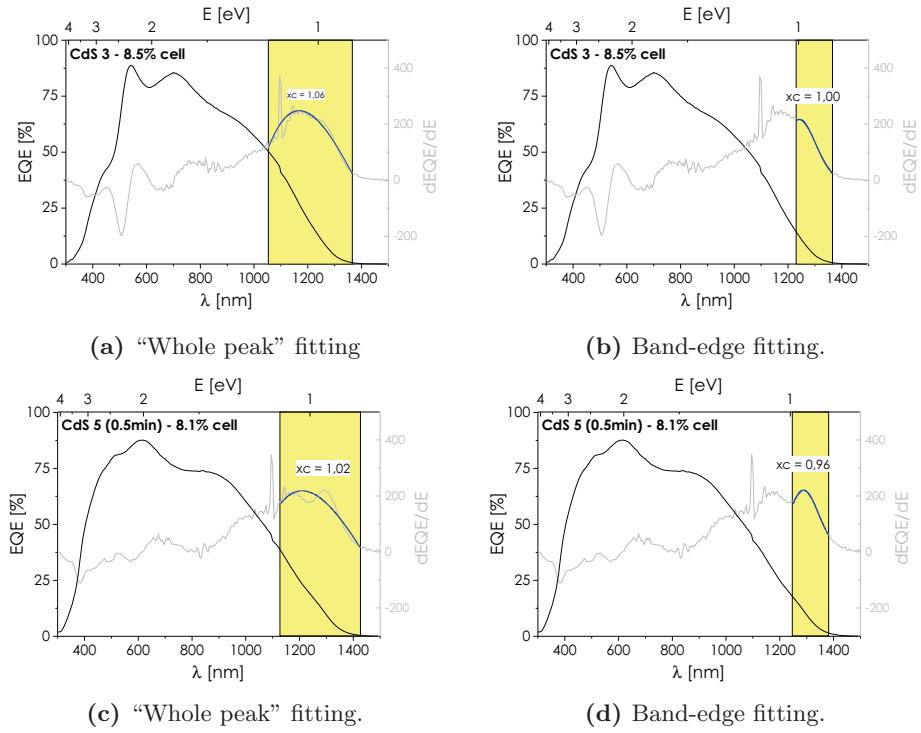


**Figure B.4:** Bandgap estimation by taking the inflection point of  $dEQE/dE$  vs  $E$  curves.

# Appendix C

## Safety classifications: risk phrases

R-phrases (short for Risk Phrases) are defined in Annex III of European Union Directive 67/548/EEC: Nature of special risks attributed to dangerous substances and preparations. The list was consolidated and republished in Directive 2001/59/EC, where translations into other EU languages may be found. R1 Explosive when dry

R2 Risk of explosion by shock, friction, fire or other sources of ignition

R3 Extreme risk of explosion by shock, friction, fire or other sources of ignition

R4 Forms very sensitive explosive metallic compounds

R5 Heating may cause an explosion

R6 Explosive with or without contact with air

R7 May cause fire

R8 Contact with combustible material may cause fire

R9 Explosive when mixed with combustible material

R10 Flammable

R11 Highly flammable

R12 Extremely flammable

R14 Reacts violently with water

R15 Contact with water liberates extremely flammable gases

R16 Explosive when mixed with oxidising substances

R17 Spontaneously flammable in air

R18 In use, may form flammable/explosive vapour-air mixture

R19 May form explosive peroxides

R20 Harmful by inhalation

R21 Harmful in contact with skin

R22 Harmful if swallowed

R23 Toxic by inhalation

R24 Toxic in contact with skin

R25 Toxic if swallowed

R26 Very toxic by inhalation

R27 Very toxic in contact with skin

R28 Very toxic if swallowed

R29 Contact with water liberates toxic gas

R30 Can become highly flammable in use

R31 Contact with acids liberates toxic gas

R32 Contact with acids liberates very toxic gas

R33 Danger of cumulative effects

R34 Causes burns

R35 Causes severe burns

R36 Irritating to eyes

R37 Irritating to respiratory system

R38 Irritating to skin  
R39 Danger of very serious irreversible effects  
R40 Limited evidence of a carcinogenic effect  
R41 Risk of serious damage to eyes  
R42 May cause sensitisation by inhalation  
R43 May cause sensitisation by skin contact  
R44 Risk of explosion if heated under confinement  
R45 May cause cancer  
R46 May cause inheritable genetic damage  
R48 Danger of serious damage to health by prolonged exposure  
R49 May cause cancer by inhalation  
R50 Very toxic to aquatic organisms  
R51 Toxic to aquatic organisms  
R52 Harmful to aquatic organisms  
R53 May cause long-term adverse effects in the aquatic environment  
R54 Toxic to flora  
R55 Toxic to fauna  
R56 Toxic to soil organisms  
R57 Toxic to bees  
R58 May cause long-term adverse effects in the environment  
R59 Dangerous for the ozone layer  
R60 May impair fertility  
R61 May cause harm to the unborn child  
R62 Possible risk of impaired fertility  
R63 Possible risk of harm to the unborn child  
R64 May cause harm to breast-fed babies  
R65 Harmful: may cause lung damage if swallowed  
R66 Repeated exposure may cause skin dryness or cracking  
R67 Vapours may cause drowsiness and dizziness  
R68 Possible risk of irreversible effects  
Risk combinations: R14/15 Reacts violently with water, liberating extremely flammable gases  
R15/29 Contact with water liberates toxic, extremely flammable gases  
R14/15/29 Reacts violently with water, liberating toxic, extremely flammable gases  
R20/21 Harmful by inhalation and in contact with skin  
R20/22 Harmful by inhalation and if swallowed  
R20/21/22 Harmful by inhalation, in contact with skin and if swallowed  
R21/22 Harmful in contact with skin and if swallowed  
R23/24 Toxic by inhalation and in contact with skin  
R23/25 Toxic by inhalation and if swallowed  
R23/24/25 Toxic by inhalation, in contact with skin and if swallowed  
R24/25 Toxic in contact with skin and if swallowed  
R26/27 Very toxic by inhalation and in contact with skin  
R26/28 Very toxic by inhalation and if swallowed  
R26/27/28 Very toxic by inhalation, in contact with skin and if swallowed  
R27/28 Very toxic in contact with skin and if swallowed  
R36/37 Irritating to eyes and respiratory system  
R36/38 Irritating to eyes and skin  
R36/37/38 Irritating to eyes, respiratory system and skin  
R37/38 Irritating to respiratory system and skin  
R39/23 Toxic: danger of very serious irreversible effects through inhalation  
R39/24 Toxic: danger of very serious irreversible effects in contact with skin  
R39/25 Toxic: danger of very serious irreversible effects if swallowed  
R39/23/24 Toxic: danger of very serious irreversible effects through inhalation and in contact with skin  
R39/23/25 Toxic: danger of very serious irreversible effects through inhalation and if swallowed  
R39/24/25 Toxic: danger of very serious irreversible effects in contact with skin and if swallowed  
R39/23/24/25 Toxic: danger of very serious irreversible effects through inhalation, in contact with skin and if swal-

---

lowed

R39/26 Very Toxic: danger of very serious irreversible effects through inhalation

R39/27 Very Toxic: danger of very serious irreversible effects in contact with skin

R39/28 Very Toxic: danger of very serious irreversible effects if swallowed

R39/26/27 Very Toxic: danger of very serious irreversible effects through inhalation and in contact with skin

R39/26/28 Very Toxic: danger of very serious irreversible effects through inhalation and if swallowed

R39/27/28 Very Toxic: danger of very serious irreversible effects in contact with skin and if swallowed

R39/26/27/28 Very Toxic: danger of very serious irreversible effects through inhalation, in contact with skin and if swallowed

R42/43 May cause sensitization by inhalation and skin contact

R45/46 May cause cancer and heritable genetic damage

R48/20 Harmful: danger of serious damage to health by prolonged exposure through inhalation

R48/21 Harmful: danger of serious damage to health by prolonged exposure in contact with skin

R48/22 Harmful: danger of serious damage to health by prolonged exposure if swallowed

R48/20/21 Harmful: danger of serious damage to health by prolonged exposure through inhalation and in contact with skin

R48/20/22 Harmful: danger of serious damage to health by prolonged exposure through inhalation and if swallowed

R48/21/22 Harmful: danger of serious damage to health by prolonged exposure in contact with skin and if swallowed

R48/20/21/22 Harmful: danger of serious damage to health by prolonged exposure through inhalation, in contact with skin and if swallowed

R48/23 Toxic: danger of serious damage to health by prolonged exposure through inhalation

R48/24 Toxic: danger of serious damage to health by prolonged exposure in contact with skin

R48/25 Toxic: danger of serious damage to health by prolonged exposure if swallowed

R48/23/24 Toxic: danger of serious damage to health by prolonged exposure through inhalation and in contact with skin

R48/23/25 Toxic: danger of serious damage to health by prolonged exposure through inhalation and if swallowed

R48/24/25 Toxic: danger of serious damage to health by prolonged exposure in contact with skin and if swallowed

R48/23/24/25 Toxic: danger of serious damage to health by prolonged exposure through inhalation, in contact with skin and if swallowed

R50/53 Very toxic to aquatic organisms, may cause long-term adverse effects in the aquatic environment

R51/53 Toxic to aquatic organisms, may cause long-term adverse effects in the aquatic environment

R52/53 Harmful to aquatic organisms, may cause long-term adverse effects in the aquatic environment

R68/20 Harmful: possible risk of irreversible effects through inhalation

R68/21 Harmful: possible risk of irreversible effects in contact with skin

R68/22 Harmful: possible risk of irreversible effects if swallowed

R68/20/21 Harmful: possible risk of irreversible effects through inhalation and in contact with skin

R68/20/22 Harmful: possible risk of irreversible effects through inhalation and if swallowed

R68/21/22 Harmful: possible risk of irreversible effects in contact with skin and if swallowed

R68/20/21/22 Harmful: possible risk of irreversible effects through inhalation, in contact with skin and if swallowed



# Bibliography

- [1] Technology Roadmap: Solar Photovoltaic Energy. Technical report, International Energy Agency (IEA), 2014. *5 citations pages xv, 2, 10, 11, and 145*
- [2] Europe’s solar market falls over 30 percent in 2014 as global solar installations continue to grow. <http://www.epia.org/news/press-releases>, 2015. *2 citations pages xv and 10*
- [3] Global Market Outlook for Solar Power 2015-2019. Technical report, SolarPower Europe (ex-EPIA (European Photovoltaic Industry Association)), 2015. *3 citations pages xv, 10, and 138*
- [4] Andrea Feltrin and Alex Freundlich. Material considerations for terawatt level deployment of photovoltaics. *Renewable Energy*, 33(2):180–185, February 2008. *4 citations pages xv, 2, 12, and 137*
- [5] Coby S Tao, Jiechao Jiang, and Meng Tao. Natural resource limitations to terawatt solar cell deployment. *ECS Trans.*, 33(17):3–11, 2011. *3 citations pages xv, 2, and 12*
- [6] Sébastien Delbos. Kesterite thin films for photovoltaics : a review. *EPJ Photovoltaics*, 3:35004, August 2012. *9 citations pages xv, 2, 11, 12, 17, 22, 23, 49, and 60*
- [7] Donald I. Bleiwas. Byproduct Mineral Commodities Used for the Production of Photovoltaic Cells. Technical report, U.S. Department of the Interior, U.S. Geological Survey (USGS), 2010. *3 citations pages xv, 13, and 14*
- [8] Mineral Commodity Summaries 2015. Technical report, U.S. Department of the Interior, U.S. Geological Survey (USGS), 2015. *4 citations pages xv, 13, 14, and 44*
- [9] Dong Han, Y. Y. Sun, Junhyeok Bang, Y. Y. Zhang, Hong-Bo Sun, Xian-Bin Li, and S. B. Zhang. Deep electron traps and origin of p-type conductivity in the earth-abundant solar-cell material  $\text{Cu}_2\text{ZnSnS}_4$ . *Physical review B*, 155206(87):1–5, 2013. *2 citations pages xv and 16*
- [10] Shiyu Chen, Aron Walsh, Xin-Gao Gong, and Su-Huai Wei. Classification of lattice defects in the kesterite  $\text{Cu}_2\text{ZnSnS}_4$  and  $\text{Cu}_2\text{ZnSnSe}_4$  earth-abundant solar cell absorbers. *Advanced materials*, 25(11):1522–39, March 2013. *8 citations pages xv, xxi, 16, 23, 25, 26, 49, and 133*
- [11] Clas Persson. Electronic and optical properties of  $\text{Cu}_2\text{ZnSnS}_4$  and  $\text{Cu}_2\text{ZnSnSe}_4$ . *Journal of Applied Physics*, 107(5):053710, 2010. *3 citations pages xv, 16, and 26*
- [12] Susanne Siebentritt and Susan Schorr. Kesterites — a challenging material for solar cells. *Progress in photovoltaics: research and applications*, 20(5, Special Issue: Adventures in Cu-Chalcogenide Solar Cells):512–519, 2012. *3 citations pages xv, 16, and 22*
- [13] Yun Seog Lee, Talia Gershon, Oki Gunawan, Teodor K. Todorov, Tayfun Gokmen, Yudistira Virgus, and Supratik Guha.  $\text{Cu}_2\text{ZnSnSe}_4$  Thin-Film Solar Cells by Thermal Co-evaporation with 11.6% Efficiency and Improved Minority Carrier Diffusion Length. *Advanced Energy Materials*, 5(7):1401372, 2015. *10 citations pages xv, xxi, 19, 20, 26, 76, 96, 99, 132, and 153*
- [14] Takuya Kato, Noriyuki Sakai, and Hiroki Sugimoto. Efficiency Improvement of  $\text{Cu}_2\text{ZnSn}(\text{S},\text{Se})_4$  Submodule with Graded Bandgap and Reduced Backside ZnS Segregation. In *Photovoltaic Specialist Conference (PVSC), 2014 IEEE 40th*, pages 0844 – 0846, Denver, CO, June 2014. IEEE. *4 citations pages xv, 8, 18, and 19*
- [15] S. Oueslati, G. Brammertz, M. Buffière, H. ElAnzeery, O. Touayar, C. Köble, J. Bekaert, M. Meuris, and J. Poortmans. Physical and electrical characterization of high-performance  $\text{Cu}_2\text{ZnSnSe}_4$  based thin film solar cells. *Thin Solid Films*, 582(E-MRS 2014 Spring Meeting, Symposium A, Thin-Film Chalcogenide Photovoltaic Materials):224–228, October 2015. *9 citations pages xv, xviii, xxi, 19, 20, 75, 76, 132, and 153*
- [16] Stephan Abermann. Non-vacuum processed next generation thin film photovoltaics: Towards marketable efficiency and production of CZTS based solar cells. *Solar Energy*, 94:37–70, August 2013. *13 citations pages xv, xxii, xxiv, 8, 20, 21, 22, 136, 137, 139, 140, 142, and 144*
- [17] Y.E. Romanyuk, C.M. Fella, A.R. Uhl, M. Werner, A.N. Tiwari, T. Schnabel, and E. Ahlswede. Recent trends in direct solution coating of kesterite absorber layers in solar cells. *Solar Energy Materials and Solar Cells*, 119:181–189, December 2013. *3 citations pages xv, 21, and 50*
- [18] D. Colombara, A. Crossay, L. Vauche, S. Jaime, M. Arasimowicz, P.-P. Grand, and P. J. Dale. Electrodeposition of Kesterite thin films for photovoltaic applications: Quo vadis? *Physica Status Solidi (a)*, 212(Special Issue on Advanced Materials and Nanotechnology for Photovoltaics):88–102, 2015. *5 citations pages xv, 21, 39, 42, and 50*



- [19] Laurence M. Peter. Electrochemical routes to earth-abundant photovoltaics: A minireview. *Electrochem. Commun.*, 50:88–92, 2015. 3 citations pages xv, 21, and 39
- [20] Chao Gao, Thomas Schnabel, Tobias Abzieher, Christoph Krämmer, Michael Powalla, Heinz Kalt, and Michael Hetterich.  $\text{Cu}_2\text{ZnSn}(\text{S},\text{Se})_4$  solar cells based on chemical bath deposited precursors. *Thin Solid Films*, 562:621–624, 2014. 2 citations pages xv and 21
- [21] Teodor K Todorov, Kathleen B Reuter, and David B Mitzi. High-efficiency solar cell with Earth-abundant liquid-processed absorber. *Advanced materials*, 22:1–4, May 2010. 4 citations pages xv, xviii, 21, and 76
- [22] Santanu Bag, Oki Gunawan, Tayfun Gokmen, Yu Zhu, Teodor K. Todorov, and David B. Mitzi. Low band gap liquid-processed CZTSe solar cell with 10.1% efficiency. *Energy & Environmental Science*, 5(5):7060, 2012. 2 citations pages xv and 21
- [23] Teodor K. Todorov, Jiang Tang, Santanu Bag, Oki Gunawan, Tayfun Gokmen, Yu Zhu, and David B. Mitzi. Beyond 11% Efficiency: Characteristics of State-of-the-Art  $\text{Cu}_2\text{ZnSn}(\text{S},\text{Se})_4$  Solar Cells. *Advanced Energy Materials*, 3(1):34–38, January 2012. 5 citations pages xv, xviii, 21, 76, and 153
- [24] D Aaron R Barkhouse, Oki Gunawan, Tayfun Gokmen, Teodor K Todorov, and David B Mitzi. Device characteristics of a 10.1% hydrazine-processed  $\text{Cu}_2\text{ZnSn}(\text{Se},\text{S})_4$  solar cell. *Progress in Photovoltaics: Research and Applications*, 20(1):6–11, 2012. 4 citations pages xv, xviii, 21, and 76
- [25] Wei Wang, Mark T. Winkler, Oki Gunawan, Tayfun Gokmen, Teodor K. Todorov, Yu Zhu, and David B. Mitzi. Device Characteristics of CZTSSe Thin-Film Solar Cells with 12.6% Efficiency. *Advanced Energy Materials*, 4(7):1301465, November 2013. 6 citations pages xv, xviii, 14, 19, 21, and 76
- [26] Jeehwan Kim, Homare Hiroi, Teodor K. Todorov, Oki Gunawan, Masaru Kuwahara, Tayfun Gokmen, Dhruv Nair, Marinus Hopstaken, Byungha Shin, Yun Seog Lee, Wei Wang, Hiroki Sugimoto, and David B. Mitzi. High Efficiency  $\text{Cu}_2\text{ZnSn}(\text{S},\text{Se})_4$  Solar Cells by Applying a Double  $\text{In}_2\text{S}_3/\text{CdS}$  Emitter. *Advanced Materials*, 26(44):7427–7431, August 2014. 11 citations pages xv, xxii, 8, 16, 19, 21, 26, 122, 128, 136, and 139
- [27] Thomas Schnabel, Tobias Abzieher, Theresa M Friedlmeier, and Erik Ahlswede. Solution-Based Preparation of  $\text{Cu}_2\text{ZnSn}(\text{S},\text{Se})_4$  for Solar Cells — Comparison of  $\text{SnSe}_2$  and Elemental Se as Chalcogen Source. *IEEE Journal of Photovoltaics*, 5(2):670–675, mar 2015. 5 citations pages xv, xviii, 19, 21, and 77
- [28] Stefan G. Haass, Matthias Diethelm, Melanie Werner, Benjamin Bissig, Yaroslav E. Romanyuk, and Ayodhya N. Tiwari. 11.2% Efficient Solution Processed Kesterite Solar Cell with a Low Voltage Deficit. *Advanced Energy Materials*, page 1500712, 2015. 3 citations pages xv, 19, and 21
- [29] Shafaat Ahmed, Kathleen B. Reuter, Oki Gunawan, Lian Guo, Lubomyr T. Romankiw, and Hariklia Deligianni. A High Efficiency Electrodeposited  $\text{Cu}_2\text{ZnSnS}_4$  Solar Cell. *Advanced Energy Materials*, 2(2):253–259, February 2012. 17 citations pages xv, xviii, 19, 21, 39, 41, 44, 45, 46, 47, 49, 50, 60, 66, 73, 74, and 92
- [30] Feng Jiang, Shigeru Ikeda, Takashi Harada, and Michio Matsumura. Pure Sulfide  $\text{Cu}_2\text{ZnSnS}_4$  Thin Film Solar Cells Fabricated by Preheating an Electrodeposited Metallic Stack. *Advanced Energy Materials*, 4(7), December 2013. 13 citations pages xv, xviii, 19, 21, 22, 39, 41, 44, 46, 47, 50, 73, and 74
- [31] Lian Guo, Yu Zhu, Oki Gunawan, Tayfun Gokmen, Vaughn R Deline, Shafaat Ahmed, Lubomyr T Romankiw, and Hariklia Deligianni. Electrodeposited  $\text{Cu}_2\text{ZnSnSe}_4$  thin film solar cell with 7 % power conversion efficiency. *Progress in photovoltaics: research and applications*, 22(1):58–68, jan 2013. 20 citations pages xv, xviii, xxi, 19, 21, 22, 39, 41, 44, 45, 46, 47, 50, 66, 73, 74, 86, 96, 99, and 132
- [32] Jong-Ok Jeon, Kee Doo Lee, Lee Seul Oh, Se-Won Seo, Doh-Kwon Lee, Honggon Kim, Jeung-Hyun Jeong, Min Jae Ko, Bongsoo Kim, Hae Jung Son, and Jin Young Kim. Highly Efficient Copper-Zinc-Tin-Selenide (CZTSe) Solar Cells by Electrodeposition. *ChemSusChem*, 7(4):1073–1077, April 2014. 11 citations pages xv, xviii, xxi, 19, 21, 22, 39, 40, 74, 75, and 132
- [33] Jonathan J. Scragg, Tomas Kubart, J. Timo Wätjen, Tove Ericson, Margareta K. Linnarsson, and Charlotte Platzer-Björkman. Effects of Back Contact Instability on  $\text{Cu}_2\text{ZnSnS}_4$  Devices and Processes. *Chemistry of Materials*, 25(15):3162–3171, August 2013. 6 citations pages xviii, 19, 20, 26, 73, and 79
- [34] M. Neuschitzer, Y. Sanchez, S. López-Marino, H. Xie, A. Fairbrother, M. Placidi, S. Haass, V. Izquierdo-Roca, A. Perez-Rodriguez, and E. Saucedo. Optimization of CdS buffer layer for high-performance  $\text{Cu}_2\text{ZnSnSe}_4$  solar cells and the effects of light soaking: elimination of crossover and red kink. *Progress in Photovoltaics: Research and Applications*, 2015. Available online at <http://dx.doi.org/10.1002/pip.2589>. 10 citations pages xviii, xxi, 19, 26, 73, 123, 125, 126, 127, and 132
- [35] Yanchun Yang, Gang Wang, Wangen Zhao, Qingwen Tian, Lijian Huang, and Daocheng Pan. Solution-Processed Highly Efficient  $\text{Cu}_2\text{ZnSnSe}_4$  Thin Film Solar Cells by Dissolution of Elemental Cu, Zn, Sn, and Se Powders. *Applied Materials & Interfaces*, 7:460–464, 2015. 5 citations pages xviii, 19, 21, 73, and 153
- [36] Dominik M. Berg and Philip J. Dale. Kesterites: Equilibria and Secondary Phase Identification. In *Copper Zinc Tin Sulfide-Based Thin-Film Solar Cells*, chapter 5. John Wiley & Sons, Ltd., first edition, 2015. Edited by Kentaro Ito. 4 citations pages xviii, 24, 72, and 78
- [37] Jiahua Tao, Junfeng Liu, Leilei Chen, Huiyi Cao, Xiankuan Meng, YingBin Zhang, Zhang Chuanjun, Lin Sun, Pingxiong Yang, and Junhao Chu. 7.1% efficient co-electroplated  $\text{Cu}_2\text{ZnSnS}_4$  thin film solar cells with sputtered CdS buffer layers. *Green Chem.*, 2015. Available online at <http://pubs.rsc.org/en/Content/ArticleLanding/2015/GC/C5GC02057C>. 6 citations pages xviii, 19, 40, 41, 73, and 74

- [38] Romain Bodeux, Fabien Mollica, and Sébastien Delbos. Growth of  $\text{Cu}_2\text{ZnSnSe}_4$  by cosputtering and reactive annealing atmosphere. *Solar Energy Materials and Solar Cells*, 132:67–73, January 2015. 7 citations pages xviii, 19, 20, 73, 74, 75, and 83
- [39] Gerardo Larramona, Stéphane Bourdais, Alain Jacob, Christophe Choné, Takuma Muto, Yan Cuccaro, Bruno Delatouche, Camille Moisan, Daniel Péré, and Gilles Dennler. Efficient  $\text{Cu}_2\text{ZnSnS}_4$  solar cells spray coated from a hydro-alcoholic colloid synthesized by instantaneous reaction. *RSC Advances*, 4(28):14655, 2014. 6 citations pages xviii, 19, 75, 76, 112, and 113
- [40] Thomas Unold, Justus Just, and Hans-Werner Schock. Coevaporation of CZTS Films and Solar Cells. In *Copper Zinc Tin Sulfide-Based Thin-Film Solar Cells*, chapter 10. John Wiley & Sons, Ltd., first edition, 2015. Edited by Kentaro Ito. 2 citations pages xviii and 77
- [41] Alex Redinger, Dominik M Berg, Phillip J. Dale, and Susanne Siebentritt. The Consequences of Kesterite Equilibria for Efficient Solar Cells. *Journal of the American Chemical Society*, 133(10):0–3, March 2010. 5 citations pages xviii, 24, 77, 78, and 108
- [42] Wilman Septina, Shigeru Ikeda, Takashi Harada, and Michio Matsumura. Fabrication of  $\text{Cu}_2\text{ZnSnSe}_4$  thin films from an electrodeposited Cu-Zn-Sn-Se/Cu-Sn-Se bilayer. *Physica Status Solidi (C)*, 10(7-8):1062–1066, August 2013. 5 citations pages xviii, 40, 41, 75, and 77
- [43] Vipul Kheraj, K.K. Patel, S.J. Patel, and D.V. Shah. Synthesis and characterisation of Copper Zinc Tin Sulphide (CZTS) compound for absorber material in solar-cells. *Journal of Crystal Growth*, 362:174–177, January 2013. 2 citations pages xviii and 77
- [44] Andrew Fairbrother, Lionel Fourdrinier, Xavier Fontané, Victor Izquierdo-Roca, Mirjana Dimitrievska, Alejandro Pérez-Rodríguez, and Edgardo Saucedo. Precursor Stack Ordering Effects in  $\text{Cu}_2\text{ZnSnSe}_4$  Thin Films Prepared by Rapid Thermal Processing. *The Journal of physical chemistry C*, 118(31):17291–17298, 2014. 6 citations pages xviii, 24, 77, 89, 90, and 141
- [45] A. D. Collord, H. Xin, and H. W. Hillhouse. Combinatorial Exploration of the Effects of Intrinsic and Extrinsic Defects in  $\text{Cu}_2\text{ZnSn(S,Se)}_4$ . *IEEE Journal of Photovoltaics*, 5(1):288–298, jan 2015. 5 citations pages xviii, 19, 76, 77, and 104
- [46] Tooru Tanaka, Takeshi Nagatomo, Daisuke Kawasaki, Mitsuhiro Nishio, Qixin Guo, Akihiro Wakahara, Akira Yoshida, and Hiroshi Ogawa. Preparation of  $\text{Cu}_2\text{ZnSnS}_4$  thin films by hybrid sputtering. *Journal of Physics and Chemistry of Solids*, 66(11):1978–1981, November 2005. 3 citations pages xviii, 20, and 77
- [47] P.M.P. Salomé, J. Malaquias, P.A. Fernandes, M.S. Ferreira, J.P. Leitão, A.F. da Cunha, J.C González, F.N. Matinaga, G.M. Ribeiro, and E.R. Viana. The influence of hydrogen in the incorporation of Zn during the growth of  $\text{Cu}_2\text{ZnSnS}_4$  thin films. *Solar Energy Materials and Solar Cells*, 95(12):3482–3489, December 2011. 2 citations pages xviii and 77
- [48] Liyong Yao, Jianping Ao, Ming-Jer Jeng, Jinlian Bi, Shoushuai Gao, Qing He, Zhiqiang Zhou, Guozhong Sun, Yun Sun, Liann-Be Chang, and Jian-Wun Chen. CZTSe solar cells prepared by electrodeposition of Cu/Sn/Zn stack layer followed by selenization at low Se pressure. *Nanoscale Research Letters*, 9(1):678, 2014. 7 citations pages xviii, 41, 44, 46, 47, 50, and 78
- [49] Andrew Fairbrother, Xavier Fontané, Victor Izquierdo-Roca, Marcel Placidi, Dioulde Sylla, Moises Espindola-Rodríguez, Simón López-Mariño, Fabian A Pulgarín, Osvaldo Vigil-Galán, Alejandro Pérez-Rodríguez, and Edgardo Saucedo. Secondary phase formation in Zn-rich  $\text{Cu}_2\text{ZnSnSe}_4$ -based solar cells annealed in low pressure and temperature conditions. *Progress in photovoltaics: research and applications*, 22(January):479–487, 2014. 6 citations pages xviii, 24, 63, 73, 78, and 84
- [50] Alex Redinger, Marina Mousel, Rabie Djemour, Levent Gütay, Nathalie Valle, and Susanne Siebentritt.  $\text{Cu}_2\text{ZnSnSe}_4$  thin film solar cells produced via co-evaporation and annealing including a  $\text{SnSe}_2$  capping layer. *Progress in photovoltaics: research and applications*, 22(1):51–57, 2013. 3 citations pages xviii, 20, and 78
- [51] Ana Kanevce, Ingrid Repins, and Su-Huai Wei. Impact of bulk properties and local secondary phases on the  $\text{Cu}_2(\text{Zn,Sn)}\text{Se}_4$  solar cells open-circuit voltage. *Solar Energy Materials and Solar Cells*, 133:119–125, February 2015. 4 citations pages xix, 24, 111, and 119
- [52] M. Bär, B. A. Schubert, B. Marsen, S. Krause, S. Pookpanratana, T. Unold, L. Weinhardt, C. Heske, and H. W. Schock. Impact of KCN etching on the chemical and electronic surface structure of  $\text{Cu}_2\text{ZnSnS}_4$  thin-film solar cell absorbers. *Applied Physics Letters*, 99(15):1–4, 2011. 2 citations pages xx and 112
- [53] K Timmo, M Altosaar, J Raudoja, M Grossberg, M Danilson, O Volobujeva, and E Mellikov. Chemical Etching of  $\text{Cu}_2\text{ZnSn(S,Se)}_4$  Monograin Powder. In *2010 35th IEEE Photovoltaic Specialists Conference*, pages 1982–1985, Honolulu, HI, June 2010. IEEE. 2 citations pages xx and 112
- [54] Haibing Xie, Yudania Sánchez, Simón López-Marino, Moisés Espíndola-rodríguez, Markus Neuschitzer, Dioulde Sylla, Andrew Fairbrother, Victor Izquierdo-Roca, Edgardo Saucedo, and Alejandro Pérez-Rodríguez. Impact of Sn(S,Se) Secondary Phases in  $\text{Cu}_2\text{ZnSn(S,Se)}_4$  Solar Cells: a Chemical Route for Their Selective Removal and Absorber Surface Passivation. *ACS applied materials & interfaces*, 6(15):12744–12751, July 2014. 6 citations pages xx, 112, 113, 114, 117, and 119
- [55] Simón López-Marino, Yudania Sánchez, Marcel Placidi, Andrew Fairbrother, Moisés Espindola-Rodríguez, Xavier Fontané, Víctor Izquierdo-Roca, Juan López-García, Lorenzo Calvo-Barrio, Alejandro Pérez-Rodríguez, and Edgardo Saucedo. ZnSe Etching of Zn-Rich  $\text{Cu}_2\text{ZnSnSe}_4$  : An Oxidation Route for Improved Solar-Cell Efficiency. *Chemistry - A European Journal*, 19(44):14814–14822, October 2013. 6 citations pages xx, 103, 112, 113, 114, and 119

- [56] Takuya Nakanishi and Kentaro Ito. Properties of chemical bath deposited CdS thin films. *Solar Energy Materials and Solar Cells*, 35:171–178, 1994. *2 citations pages xx and 120*
- [57] Hani Khallaf, Isaiah O. Oladeji, Guangyu Chai, and Lee Chow. Characterization of CdS thin films grown by chemical bath deposition using four different cadmium sources. *Thin Solid Films*, 516(21):7306–7312, 2008. *2 citations pages xx and 120*
- [58] J. M. Doña. Chemical Bath Deposition of CdS Thin Films: Electrochemical In Situ Kinetic Studies. *Journal of The Electrochemical Society*, 139(10):2810, 1992. *2 citations pages xx and 120*
- [59] Dongxiang Liao and Angus Rockett. Cd doping at the CuInSe<sub>2</sub>/CdS heterojunction. *Journal of Applied Physics*, 93(11):9380, 2003. *2 citations pages xx and 120*
- [60] I. L. Repins, J. V. Li, A. Kanevce, C. L. Perkins, K. X. Steirer, J. Pankow, G. Teeter, D. Kuciauskas, C. Beall, C. Dehart, J. Carapella, B. Bob, J. Park, and S. Wei. Effects of deposition termination on Cu<sub>2</sub>ZnSnSe<sub>4</sub> device characteristics. *Thin Solid Films*, 582(E-MRS 2014 Spring Meeting, Symposium A, Thin-Film Chalcogenide Photovoltaic Materials):184–187, 2015. *3 citations pages xxi, 19, and 132*
- [61] G. Brammertz, M. Buffière, S. Oueslati, H. ElAnzeery, K. Ben Messaoud, S. Sahayaraj, C. Köble, M. Meuris, and J. Poortmans. Characterization of defects in 9.7% efficient Cu<sub>2</sub>ZnSnSe<sub>4</sub>-CdS-ZnO solar cells. *Applied Physics Letters*, 103(16):163904, 2013. *7 citations pages xxi, 19, 22, 75, 112, 132, and 153*
- [62] Ingrid Repins, Carolyn Beall, Nirav Vora, Clay DeHart, Darius Kuciauskas, Pat Dippo, Bobby To, Jonathan Mann, Wan-Ching Hsu, Alan Goodrich, and Rommel Noufi. Co-evaporated Cu<sub>2</sub>ZnSnSe<sub>4</sub> films and devices. *Solar Energy Materials and Solar Cells*, 101:154–159, June 2012. *5 citations pages xxi, 19, 20, 132, and 153*
- [63] Byungha Shin, Yu Zhu, Nestor A. Bojarczuk, S. Jay Chey, and Supratik Guha. Control of an interfacial MoSe<sub>2</sub> layer in Cu<sub>2</sub>ZnSnSe<sub>4</sub> thin film solar cells: 8.9% power conversion efficiency with a TiN diffusion barrier. *Applied Physics Letters*, 101(5):053903, 2012. *6 citations pages xxi, 24, 76, 79, 80, and 132*
- [64] Marina Mousel, Torsten Schwarz, Rabie Djemour, Thomas P. Weiss, Jan Sendler, João C. Malaquias, Alex Redinger, Oana Cojocaru-Mirédin, Pyuck-Pa Choi, and Susanne Siebentritt. Cu-Rich Precursors Improve Kesterite Solar Cells. *Advanced Energy Materials*, 4(2), January 2014. *3 citations pages xxi, 19, and 132*
- [65] G. Brammertz, M. Buffière, Y. Mevel, Y. Ren, A. E. Zaghi, N. Lenaers, Y. Mols, C. Koeble, J. Vleugels, M. Meuris, and J. Poortmans. Correlation between physical, electrical, and optical properties of Cu<sub>2</sub>ZnSnSe<sub>4</sub> based solar cells. *Applied Physics Letters*, 102(013902), 2013. *2 citations pages xxi and 132*
- [66] G. Rey, A. Redinger, J. Sendler, T. P. Weiss, M. Thevenin, M. Guennou, B. El Adib, and S. Siebentritt. The band gap of Cu<sub>2</sub>ZnSnSe<sub>4</sub>: Effect of order-disorder. *Applied Physics Letters*, 105(11):112106, September 2014. *3 citations pages xxi, 25, and 133*
- [67] SunPower Launches X-Series Family of Solar Panels with World-Record Efficiencies of 21.5 Percent. <http://newsroom.sunpower.com/index.php?s=20295&item=122903>, 2013. *3 citations pages xxii, 8, and 136*
- [68] Yifeng Chen, Zhiqiang Feng, and Pierre Verlinden. Assessment of Module Efficiency and Manufacturing Cost for Industrial Crystalline Silicon and Thin Film Technologies. In *6th World Conference on Photovoltaic Energy Conversion*, Kyoto, Japan, 2014. *3 citations pages xxii, 8, and 136*
- [69] Martin A Green, Keith Emery, Yoshihiro Hishikawa, Wilhelm Warta, and Ewan D Dunlop. Solar cell efficiency tables (Version 46). *Progress in Photovoltaics: Research and Applications*, (23):805–812, 2015. *3 citations pages xxii, 8, and 136*
- [70] Philip Jackson, Dimitrios Hariskos, Roland Wuerz, Oliver Kiowski, Andreas Bauer, Theresa Magorian Friedlmeier, and Michael Powalla. Properties of Cu(In,Ga)Se<sub>2</sub> solar cells with new record efficiencies up to 21.7%. *physica status solidi (RRL) - Rapid Research Letters*, 9(1):28–31, 2015. *4 citations pages xxii, 8, 136, and 139*
- [71] Solar Frontier website. <http://www.solar-frontier.com/eng/solutions/products/index.html>, 2015. *6 citations pages xxii, 8, 14, 136, 139, and 146*
- [72] Miasolé. Miasolé Introduces the FLEX N Series Flexible PV Module for Standing Seam Metal Roofs. <http://miasole.com/en/news-downloads/news/#c1716>. *5 citations pages xxii, 8, 14, 136, and 139*
- [73] Lars Stolt. Success Factors for CIGS. In *3rd International Workshop on CIGS Solar Cell Technology*, Berlin, April 2012. *4 citations pages xxii, 8, 136, and 138*
- [74] Bernhard Dimmler. Thin Film Technology made by Manz. In *4th International Workshop on CIGS solar cell technology*, Berlin, April 2013. MANZ CIGS Technology GmbH. *4 citations pages xxii, 8, 136, and 138*
- [75] Ilka Luck. Competitiveness of CIGS technology in the light of recent PV developments - Part I: The state of the art in CIGS production. *Photovoltaics International*, pages 69–72, May 2014. *4 citations pages xxii, 8, 136, and 138*
- [76] Kelsey A W Horowitz and Michael Woodhouse. Cost and Potential of Monolithic CIGS Photovoltaic Modules. In *IEEE Photovoltaics Specialists Conference*, New Orleans, June 2015. *5 citations pages xxii, 8, 136, 138, and 140*
- [77] Cédric Broussillou. Definition and cost analysis of an industrial line (Confidential) - Deliverable 7.2 of SCALENANO project. Technical report, NEXCIS, July 2015. *8 citations pages xxii, xxiii, 8, 21, 136, 137, 138, and 139*

- [78] Price Index. Online at <http://www.pvxchange.com/priceindex/default.aspx?langTag=en-GB> (Accessed 2015-06-11). *4 citations pages xxii, 8, 12, and 136*
- [79] PV Technology Roadmap. Technical report, IHS Marketbuzz, 2015. *2 citations pages xxii and 136*
- [80] Ilka Luck. Competitiveness of CIGS technology in the light of recent PV developments - Part II: Cost-reduction potential in CIGS production. *Photovoltaics International*, pages 72–76, September 2014. *4 citations pages xxii, xxiii, 138, and 139*
- [81] Cédric Broussillou, Andreu Cabot, Alejandro Pérez-Rodríguez, and Ralf Kügler. Cost analysis of transfer of new processes developed in Scalenano to industrial manufacturing (Confidential) - Deliverable 7.4 of SCALE-NANO project. Technical report, NEXCIS, IREC, Merck, July 2015. *2 citations pages xxiii and 140*
- [82] World Population 2012. Technical report, United Nations (UN), 2012. *Cited page 2*
- [83] Antonio Luque and Steven S. Hegedus. *Handbook of Photovoltaic Science and Engineering - Second Edition*. WILEY, 2011. *5 citations pages 2, 4, 8, 9, and 136*
- [84] Christiana Honsberg and Stuart Bowden. PV CDROM, 2015. Online at <http://pveducation.org/>. *6 citations pages 2, 3, 4, 5, 6, and 7*
- [85] Kentaro Ito. An Overview of CZTS-Based Thin-Film Solar Cells. In *Copper Zinc Tin Sulfide-Based Thin-Film Solar Cells*, chapter 1. John Wiley & Sons, Ltd., 2015. Edited by Kentaro Ito. *2 citations pages 2 and 22*
- [86] First Solar Achieves World Record 18.6 % Thin Film Module Conversion Efficiency. <http://investor.firstsolar.com/releases.cfm?sect=all>, 2015. *Cited page 8*
- [87] Photovoltaics Report. Technical report, Fraunhofer ISE, updated: 26 August 2015. Available online at <https://www.ise.fraunhofer.de/en/news/news-archive/news-2012/fraunhofer-ise-publishes-photovoltaics-report>. *3 citations pages 7, 8, and 12*
- [88] Martin A. Green. Third generation photovoltaics: Solar cells for 2020 and beyond. *Physica E*, 14:65–70, 2002. *Cited page 8*
- [89] Robert F. Service. Devices team up to boost solar power. *SCIENCE*, 347:225, January 2015. *2 citations pages 8 and 15*
- [90] William Shockley and Hans J. Queisser. Detailed Balance Limit of Efficiency of p-n Junction Solar Cells. *Journal of Applied Physics*, 32(3):510, 1961. *3 citations pages 9, 16, and 26*
- [91] Research Cell Efficiency Records. <http://www.nrel.gov/ncpv/>, 2015. *Cited page 9*
- [92] This Month in Physics History April 25, 1954: Bell Labs Demonstrates the First Practical Silicon Solar Cell. *APS*, 18(4), 2009. *Cited page 9*
- [93] Renewable Power Generation Costs. Technical Report January, International Renewable Energy Agency (IRENA), 2015. *Cited page 10*
- [94] Global Market outlook for Photovoltaics. Technical report, European Photovoltaic Industry Association (EPIA), 2014. *Cited page 10*
- [95] The Future of Solar Energy. An interdisciplinary MIT study. Technical report, Massachusetts Institute of Technology (MIT), 2015. *3 citations pages 10, 12, and 136*
- [96] Tracking Clean Energy Progress 2014. Technical report, International Energy Agency (IEA), 2014. *Cited page 10*
- [97] Marika Edoff. Thin film solar cells: research in an industrial perspective. *Ambio*, 41(Supplement 2):112–118, January 2012. *2 citations pages 11 and 139*
- [98] Chiara Candelise, Jamie F. Spiers, and Robert J K Gross. Materials availability for thin film (TF) PV technologies development: A real concern? *Renewable and Sustainable Energy Reviews*, 15(Energy Reviews):4972–4981, 2011. *3 citations pages 11, 12, and 13*
- [99] Peck Yean Gan and ZhiDong Li. Quantitative study on long term global solar photovoltaic market. *Renewable and Sustainable Energy Reviews*, 46:88–99, 2015. *2 citations pages 12 and 136*
- [100] Report on Critical Raw Materials for the EU. Technical report, European Commission, 2014. *Cited page 12*
- [101] Indium - Cours Matière Première. [http://bourse.lesechos.fr/bourse/matieres\\_premieres/metaux.jsp](http://bourse.lesechos.fr/bourse/matieres_premieres/metaux.jsp). *Cited page 13*
- [102] Huiyong Liu, V. Avrutin, N. Izyumskaya, Ü Özgr, and H. Morkoç. Transparent conducting oxides for electrode applications in light emitting and absorbing devices. *Superlattices and Microstructures*, 48(5):458–484, 2010. *2 citations pages 13 and 129*
- [103] Anna Stamp, Patrick A. Wäger, and Stefanie Hellweg. Linking energy scenarios with metal demand modeling – The case of indium in CIGS solar cells. *Resources, Conservation & Recycling*, 93:156–167, 2014. *2 citations pages 14 and 146*
- [104] Teodor Todorov, Talia Gershon, Oki Gunawan, Charles Sturdevant, and Supratik Guha. Perovskite-kesterite monolithic tandem solar cells with high open-circuit voltage. *Applied Physics Letters*, 105(17):173902, October 2014. *Cited page 15*
- [105] Susan Schorr. The crystal structure of kesterite type compounds: A neutron and X-ray diffraction study. *Solar Energy Materials and Solar Cells*, 95(6):1482–1488, June 2011. *Cited page 17*

- [106] Ankur Khare, Burak Himmetoglu, Melissa Johnson, David J Norris, Matteo Cococcioni, and Eray S. Aydil. Calculation of the lattice dynamics and Raman spectra of copper zinc tin chalcogenides and comparison to experiments. *Journal of Applied Physics*, 111(8):083707, 2012. *Cited page 17*
- [107] Susan Schorr. Crystallographic Aspects of  $\text{Cu}_2\text{ZnSnS}_4$  (CZTS). In *Copper Zinc Tin Sulfide-Based Thin-Film Solar Cells*, chapter 3. John Wiley & Sons, Ltd., first edition, 2015. Edited by Kentaro Ito. *2 citations pages 17 and 25*
- [108] Johan Lindahl, Uwe Zimmermann, Piotr Szaniawski, Tobias Törndahl, Adam Hultqvist, Pedro Salomé, Charlotte Platzer-Björkman, and Marika Edoff. Inline  $\text{Cu}(\text{In,Ga})\text{Se}_2$  Co-evaporation for High-Efficiency Solar Cells and Modules. *IEEE Journal of Photovoltaics*, 3(3):1100–1105, 2013. *2 citations pages 17 and 20*
- [109] M. Powalla, M. Cemernjak, J. Eberhardt, F. Kessler, R. Kniese, H. D. Mohring, and B. Dimmler. Large-area CIGS modules: Pilot line production and new developments. *Solar Energy Materials and Solar Cells*, 90(18-19):3158–3164, 2006. *Cited page 17*
- [110] Joop van Deelen, Marco Barink, Lennaert Klerk, Pim Voorthuizen, and Arjan Hovestad. Efficiency loss prevention in monolithically integrated thin film solar cells by improved front contact. *Progress in Photovoltaics: Research and Applications*, 23(4):498–506, 2015. *3 citations pages 17, 129, and 139*
- [111] Axel Neisser, Christoph Waldauf, Timo Holopainen, Kaia Ernits, Sebastian Moser, and Dieter Meissner. Flexible monograin membrane photovoltaic modules - roadmap to production. In *28th European Photovoltaic Solar Energy Conference and Exhibition*, 2013. *2 citations pages 17 and 19*
- [112] E. M. Mkawi, K. Ibrahim, M. K. M. Ali, and Abdussalam Salhin Mohamed. Dependence of Copper Concentration on the Properties of  $\text{Cu}_2\text{ZnSnS}_4$  Thin Films Prepared by Electrochemical Method. *International Journal of Electrochemical Science*, 8:359–368, 2013. *2 citations pages 17 and 42*
- [113] Simón López-Marino, Markus Neuschitzer, Yudania Sánchez, Andrew Fairbrother, Moisés Espindola-Rodríguez, Juan López-García, Marcel Placidi, Lorenzo Calvo-Barrio, Alejandro Pérez-Rodríguez, and Edgardo Saucedo. Earth-abundant absorber based solar cells onto low weight stainless steel substrate. *Solar Energy Materials and Solar Cells*, 130:347–353, November 2014. *2 citations pages 17 and 84*
- [114] M. Farinella, R. Inguanta, T. Spanò, P. Livreri, S. Piazza, and C. Sunseri. Electrochemical deposition of CZTS thin films on flexible substrate. *Energy Procedia*, 44(May 2013):105–110, 2014. *2 citations pages 17 and 40*
- [115] N. Naghavi, D. Abou-Ras, N. Allsop, N. Barreau, S. Bücheler, A. Ennaoui, C. H. Fischer, C. Guillen, D. Hariskos, J. Herrero, R. Klenk, K. Kushiya, D. Lincot, R. Menner, T. Nakada, C. Platzer-Björkman, S. Spiering, A. N. Tiwari, and T. Törndahl. Buffer layers and transparent conducting oxides for chalcopyrite  $\text{Cu}(\text{In,Ga})(\text{S,Se})_2$  based thin film photovoltaics: Present status and current developments. *Progress in Photovoltaics: Research and Applications*, 18(April):411–433, 2010. *3 citations pages 17, 120, and 121*
- [116] Carolin M. Fella, Yaroslav E. Romanyuk, and Ayodhya N. Tiwari. Technological status of  $\text{Cu}_2\text{ZnSn}(\text{S,Se})_4$  thin film solar cells. *Solar Energy Materials and Solar Cells*, 119:276–277, December 2013. *Cited page 18*
- [117] Grayson M Ford, Qijie Guo, Rakesh Agrawal, and Hugh W Hillhouse. Earth Abundant Element  $\text{Cu}_2\text{Zn}(\text{Sn}_{1-x}\text{Ge}_x)\text{S}_4$  Nanocrystals for Tunable Band Gap Solar Cells: 6.8% Efficient Device Fabrication. *Chemistry of Materials*, (23):2626–2629, 2011. *Cited page 18*
- [118] Qijie Guo, Grayson M. Ford, Wei-Chang Yang, Charles J. Hages, Hugh W. Hillhouse, and Rakesh Agrawal. Enhancing the performance of CZTSSe solar cells with Ge alloying. *Solar Energy Materials and Solar Cells*, 105:132–136, October 2012. *Cited page 18*
- [119] Santanu Bag, Oki Gunawan, Tayfun Gokmen, Yu Zhu, and David B. Mitzi. Hydrazine-Processed Ge-Substituted CZTSe Solar Cells. *Chemistry of Materials*, 24(23):4588–4593, December 2012. *Cited page 18*
- [120] Shinho Kim, Kang Min Kim, Hitoshi Tampo, Hajime Shibata, Koji Matsubara, and Shigeru Niki. Ge-incorporated  $\text{Cu}_2\text{ZnSnSe}_4$  thin-film solar cells with efficiency greater than 10%. *Solar Energy Materials and Solar Cells*, 144:488–492, 2016. *Cited page 18*
- [121] Sergio Giraldo, Markus Neuschitzer, Thomas Thersleff, Simón López-Marino, Yudania Sánchez, Haibing Xie, Mónica Colina, Marcel Placidi, Paul Pistor, Victor Izquierdo-Roca, Klaus Leifer, Alejandro Pérez-Rodríguez, and Edgardo Saucedo. Large Efficiency Improvement in  $\text{Cu}_2\text{ZnSnSe}_4$  Solar Cells by Introducing a Superficial Ge Nanolayer. *Advanced Energy Materials*, 2015. Available online at [10.1002/aenm.201501070](https://doi.org/10.1002/aenm.201501070). *Cited page 18*
- [122] Zhenghua Su, Joel Ming Rui Tan, Xianglin Li, Xin Zeng, Sudip Kumar Batabyal, and Lydia Helena Wong. Cation substitution of solution-processed  $\text{Cu}_2\text{ZnSnS}_4$  thin film solar cell with over 9% efficiency. *Advanced Energy Materials*, jul 2015. Available online at <http://dx.doi.org/10.1002/aenm.201500682>. *Cited page 18*
- [123] Takuya Kato, Homare Hiroi, Noriyuki Sakai, and Hiroki Sugimoto. Buffer/Absorber Interface Study on  $\text{Cu}_2\text{ZnSnS}_4$  and  $\text{Cu}_2\text{ZnSnSe}_4$  Based Solar Cells: Band Alignment and Its Impact on the Solar Cell Performance. In *28th European Photovoltaic Solar Energy Conference and Exhibition*, pages 2125–2127. WIP, 2013. *4 citations pages 18, 19, 20, and 121*
- [124] Takuya Kato, Homare Hiroi, Noriyuki Sakai, Satoshi Muraoka, and Hiroki Sugimoto. Characterization of front and back interfaces on CZTS thin-film solar cells. In *27th European Photovoltaic Solar Energy Conference and Exhibition*, pages 2236–2239, Frankfurt, 2012. *6 citations pages 18, 19, 24, 26, 93, and 121*
- [125] Homare Hiroi, Noriyuki Sakai, Takuya Kato, and Hiroki Sugimoto. High Voltage  $\text{Cu}_2\text{ZnSnS}_4$  Submodules by Hybrid Buffer Layer. *Photovoltaic Specialists Conference (PVSC), 2013 IEEE 39th*, pages 0863–0866, jun 2013. *4 citations pages 19, 121, 122, and 128*

- [126] Vardaan Chawla and Bruce Clemens. Effect of Composition on High Efficiency CZTSSe Devices Fabricated Using Co-sputtering of Compound Targets. In *Photovoltaic Specialists Conference (PVSC), 2012 38th IEEE*, pages 002990 – 002992, Austin, Texas, 2012. IEEE. *2 citations pages 19 and 23*
- [127] Hiroki Sugimoto, Christopher Liao, Homare Hiroi, Noriyuki Sakai, and Takuya Kato. Lifetime Improvement for High Efficiency  $\text{Cu}_2\text{ZnSnS}_4$  Submodules. In *Photovoltaic Specialists Conference (PVSC), 2013 IEEE 39th*, pages 3208–3211, Tampa, FL, June 2013. IEEE. *Cited page 19*
- [128] Myeng Gil Gang, Seung Wook Shin, Chang Woo Hong, K.V. Gurav, Jihye Gwak, Jaeho Yun, Jeong Yong Lee, and Jin Hyeok Kim. Sputtering processed highly efficient  $\text{Cu}_2\text{ZnSn}(\text{S},\text{Se})_4$  solar cells by a low-cost, simple, green, and up-scalable strategy. *Green Chem.*, 2015. Available online at <http://pubs.rsc.org/en/Content/ArticleLanding/2015/GC/C5GC02417J>. *Cited page 19*
- [129] Gee Yeong Kim, Dae-Ho Son, Trang Thi Thu Nguyen, Seokhyun Yoon, Minsu Kwon, Chan-Wook Jeon, Dae-Hwan Kim, Jin-Kyu Kang, and William Jo. Enhancement of photo-conversion efficiency in  $\text{Cu}_2\text{ZnSn}(\text{S},\text{Se})_4$  thin-film solar cells by control of ZnS precursor-layer thickness. *Progress in Photovoltaics: Research and Applications*, 2015. Available online at <http://dx.doi.org/10.1002/pip.2693>. *Cited page 19*
- [130] Jianjun Li, Yi Zhang, Wei Zhao, Dahyun Nam, Hyeonsik Cheong, Li Wu, Zhiqiang Zhou, and Yun Sun. A Temporary Barrier Effect of the Alloy Layer During Selenization: Tailoring the Thickness of  $\text{MoSe}_2$  for Efficient  $\text{Cu}_2\text{ZnSnSe}_4$  Solar Cells. *Advanced Energy Materials*, 1402178:1–9, 2015. *2 citations pages 19 and 79*
- [131] Ye Feng, Bing Yu, Guanming Cheng, Ling Yin, Tsz-Ki Lau, Zhaohui Li, Qiuming Song, Chunlei Yang, and Xudong Xiao. Searching for fabrication route of efficient  $\text{Cu}_2\text{ZnSnS}_4$  solar cells by post-sulfuration of co-sputtered Sn-enriched precursors. *Journal of Materials Chemistry C*, 2015. Available online at <http://pubs.rsc.org/en/Content/ArticleLanding/2015/TC/C5TC02486B>. *2 citations pages 19 and 75*
- [132] Byungha Shin, Oki Gunawan, Yu Zhu, Nestor A. Bojarczuk, S. Jay Chey, and Supratik Guha. Thin film solar cell with 8.4 % power conversion efficiency using an earth-abundant  $\text{Cu}_2\text{ZnSnS}_4$  absorber. *Progress in photovoltaics: research and applications*, 21:72–76, 2013. *4 citations pages 19, 20, 76, and 92*
- [133] J. Márquez, M. Neuschitzer, M. Dimitrievska, R. Gunder, S. Haass, M. Werner, Y.E. Romanyuk, Susan Schorr, N.M. Pearsall, and I. Forbes. Systematic compositional changes and their influence on lattice and optoelectronic properties of  $\text{Cu}_2\text{ZnSnSe}_4$  kesterite solar cells. *Solar Energy Materials and Solar Cells*, 144:579–585, 2016. *Cited page 19*
- [134] Tove Ericson, Jonathan J Scragg, Adam Hultqvist, Jörn Timo Wätjen, Piotr Szaniawski, Tobias Torndahl, and Charlotte Platzer-björkman. Zn(O,S) Buffer Layers and Thickness Variations of CdS Buffer for  $\text{Cu}_2\text{ZnSnS}_4$  Solar Cells. *IEEE Journal of Photovoltaics*, 4(1):465–469, jan 2014. *2 citations pages 19 and 122*
- [135] Kee-Jeong Yang, Jun-Hyoung Sim, Dae-Ho Son, Dae-Hwan Kim, Gee Yeong Kim, William Jo, Soomin Song, JunHo Kim, Dahyun Nam, Hyeonsik Cheong, and Jin-Kyu Kang. Effects of the compositional ratio distribution with sulfurization temperatures in the absorber layer on the defect and surface electrical characteristics of  $\text{Cu}_2\text{ZnSnS}_4$  solar cells. *Progress in Photovoltaics: Research and Applications*, 2015. Available online at <http://dx.doi.org/10.1002/pip.2619>. *2 citations pages 19 and 75*
- [136] Chung-Hao Cai, Shih-Yuan Wei, Wei-Chih Huang, Jeff Lin, Tzu-Hsuan Yeh, and Chih-Huang Lai. Efficiency enhancement by adding SnS powder during selenization for  $\text{Cu}_2\text{ZnSn}(\text{S},\text{Se})_4$  thin film solar cells. *Solar Energy Materials and Solar Cells*, 145(3):296–302, 2016. *2 citations pages 19 and 78*
- [137] Fangqin Zeng, Kaiwen Sun, Li Gong, Liangxing Jiang, Fangyang Liu, Yanqing Lai, and Jie Li. Back contact-absorber interface modification by inserting carbon intermediate layer and conversion efficiency improvement in  $\text{Cu}_2\text{ZnSn}(\text{S},\text{Se})_4$  solar cell. *Phys. Status Solidi RRL*, 9(12):687–691, 2015. *2 citations pages 19 and 79*
- [138] Solange Temgoua, Romain Bodeux, Negar Naghavi, and Sébastien Delbos. Effects of  $\text{SnSe}_2$  secondary phases on the efficiency of  $\text{Cu}_2\text{ZnSn}(\text{S}_x\text{Se}_{1-x})_4$  based solar cells. *Thin Solid Films*, 582:215–219, may 2015. *4 citations pages 19, 23, 24, and 117*
- [139] Louis Grenet, Sergio Bernardi, David Kohen, Christophe Lepoittevin, Sébastien Noël, Nicolas Karst, Arnaud Brioude, Simon Perraud, and Henri Mariette.  $\text{Cu}_2\text{ZnSn}(\text{S}_{1-x}\text{Se}_x)_4$  based solar cell produced by selenization of vacuum deposited precursors. *Solar Energy Materials and Solar Cells*, 101:11–14, 2012. *Cited page 19*
- [140] Louis Grenet, Pauline Grondin, Karol Coumert, Nicolas Karst, Fabrice Emieux, Frédéric Roux, Raphaël Fillon, Giovanni Altamura, Hélène Fournier, Pascal Faucherand, and Simon Perraud. Experimental evidence of light soaking effect in Cd-free  $\text{Cu}_2\text{ZnSn}(\text{S},\text{Se})_4$ -based solar cells. *Thin Solid Films*, 564:375–378, 2014. *3 citations pages 19, 122, and 127*
- [141] Sambhaji M. Pawar, Akbar I. Inamdar, Kishor V. Gurav, Seung Wook Shin, Jihye Gwak, Yongcheol Jo, JaeHo Yun, Hisun Pak, Sehan Kwon, Hyungsang Kim, Jin Hyeok Kim, and Hyunsik Im. Fabrication of  $\text{Cu}_2\text{ZnSn}(\text{S}_x\text{Se}_{1-x})_4$  thin film solar cell by single step sulfo-selenization of stacked metallic precursors. *Current Applied Physics*, 15(2):59–63, 2015. *Cited page 19*
- [142] Homare Hiroi, Jeehwan Kim, Oki Gunawan, Tayfun Gokmen, Masaru Kuwahara, Teodor K Todorov, Dhruv Nair, Yun Seog Lee, Marinus Hopstaken, Yu Zhu, David B Mitzi, and Hiroki Sugimoto. Enhancement of Carrier Collection in  $\text{Cu}_2\text{ZnSn}(\text{SeS})_4$  Solar Cell With Hybrid Buffer Layer. In *29th European Photovoltaic Solar Energy Conference and Exhibition*, pages 1473 – 1476. WIP, 2014. *2 citations pages 19 and 122*
- [143] Hao Xin, John K. Katahara, Ian L. Braly, and Hugh W. Hillhouse. 8% Efficient  $\text{Cu}_2\text{ZnSn}(\text{S},\text{Se})_4$  solar cells from redox equilibrated simple precursors in DMSO. *Advanced Energy Materials*, 4:1–5, 2014. *3 citations pages 19, 21, and 76*

- [144] M. Werner, C.M. Sutter-Fella, Y.E. Romanyuk, and A.N. Tiwari. 8.3% efficient  $\text{Cu}_2\text{ZnSn}(\text{S,Se})_4$  solar cells processed from sodium-containing solution precursors in a closed reactor. *Thin Solid Films*, 582:308–312, 2014. *Cited page 19*
- [145] Thomas Schnabel, Manuel Löw, and Erik Ahlswede. Solution-processed  $\text{Cu}_2\text{ZnSn}(\text{S,Se})_4$  solar cells - various impacts on morphology and performance. *2013 IEEE 39th Photovoltaic Specialists Conference (PVSC)*, June 2013. *Cited page 19*
- [146] Thomas Schnabel, Manuel Löw, and Erik Ahlswede. Vacuum-free preparation of 7.5% efficient  $\text{Cu}_2\text{ZnSn}(\text{S,Se})_4$  solar cells based on metal salt precursors. *Solar Energy Materials and Solar Cells*, 117:324–328, October 2013. *Cited page 19*
- [147] Craig Leidholm, Charlie Hotz, Alison Breeze, Chris Sunderland, Wooseok Ki, and Don Zehner. Final Report : Sintered CZTS Nanoparticle Solar Cells on Metal Foil. Technical report, NREL, 2012. *2 citations pages 19 and 21*
- [148] Qijie Guo, Grayson M Ford, Wei-Chang Yang, Bryce C Walker, Eric a Stach, Hugh W Hillhouse, and Rakesh Agrawal. Fabrication of 7.2% efficient CZTSSe solar cells using CZTS nanocrystals. *Journal of the American Chemical Society*, 132(49):17384–6, December 2010. *Cited page 19*
- [149] Caleb K. Miskin, Wei-Chang Yang, Charles J. Hages, Nathaniel J. Carter, Chinmay S. Joglekar, Eric A. Stach, and Rakesh Agrawal. 9.0% efficient  $\text{Cu}_2\text{ZnSn}(\text{S,Se})_4$  solar cells from selenized nanoparticle inks. *Progress in Photovoltaics: Research and Applications*, 23(5):654–659, feb 2014. *2 citations pages 19 and 21*
- [150] Gerardo Larramona, Stéphane Bourdais, Alain Jacob, Christophe Choné, Takuma Muto, Yan Cuccaro, Bruno Delatouche, Camille Moisan, Daniel Péré, and Gilles Dennler. 8.6% Efficient CZTSSe Solar Cells Sprayed from Water Ethanol CZTS Colloidal Solutions. *The Journal of Physical Chemistry Letters*, 5:3763–3767, 2014. *4 citations pages 19, 21, 22, and 76*
- [151] Hsin-Sheng Duan, Wenbing Yang, Brion Bob, Chia-Jung Hsu, Bao Lei, and Yang Yang. The Role of Sulfur in Solution-Processed  $\text{Cu}_2\text{ZnSn}(\text{S,Se})_4$  and its Effect on Defect Properties. *Advanced Functional Materials*, 23(11):1466–1471, March 2013. *Cited page 19*
- [152] Wan-ching Hsu, Huanping Zhou, Song Luo, Tze-Bin Song, Yao-tsung Hsieh, Hsin-sheng Duan, Shenglin Ye, Wenbing Yang, Chia-Jung Hsu, Chengyang Jiang, Brion Bob, and Yang Yang. Spatial Element Distribution Control in a Fully Solution-Processed Nanocrystals-Based 8.6%  $\text{Cu}_2\text{ZnSn}(\text{S,Se})_4$  Device. *ACS NANO*, 8(9):9164–9172, 2014. *2 citations pages 19 and 21*
- [153] Yanyan Cao, Michael S Denny, Jonathan V Caspar, William E Farneth, Qijie Guo, Alex S Ionkin, Lynda K Johnson, Meijun Lu, Irina Malajovich, Daniela Radu, H David Rosenfeld, Kaushik Roy Choudhury, and Wei Wu. High-efficiency solution-processed  $\text{Cu}_2\text{ZnSn}(\text{S,Se})_4$  thin-film solar cells prepared from binary and ternary nanoparticles. *Journal of the American Chemical Society*, 134(38):15644–7, September 2012. *2 citations pages 19 and 21*
- [154] Dieter Meissner, Enn Mellikov, Mare Altosaar, Thomas Badegruber, Mati Danilson, Kaia Ernits, Maarja Grossberg, Andri Jagomägi, Marit Kauk, Jüri Krustok, Franz Lehner, Katri Muska, Maris Pilvet, Jaan Raudoja, Wolfgang Ressler, Kristi Timmo, Tiit Varema, and Olga Volobujeva. 50 years of Monograin Solar Cells - Time to go to Market. In *216th ECS Meeting*. The Electrochemical Society, 2009. *Cited page 19*
- [155] M. Kauk, K. Muska, M. Altosaar, J. Raudoja, M. Pilvet, T. Varema, K. Timmo, and O. Volobujeva. Effects of sulphur and tin disulphide vapour treatments of  $\text{Cu}_2\text{ZnSn}(\text{S,Se})_4$  absorber materials for monograin solar cells. *Energy Procedia*, 10:197–202, 2011. *Cited page 19*
- [156] Crystalsol sets European cell efficiency record for CZTS based photovoltaic cells. <http://www.crystalsol.com/>, 2013. *Cited page 19*
- [157] Mai Nguyen, Kaia Ernits, Kong Fai Tai, Chin Fan Ng, Stevin Snellius Pramana, Wardhana A. Sasangka, Sudip K. Batabyal, Timo Holopainen, Dieter Meissner, Axel Neisser, and Lydia H. Wong. ZnS buffer layer for  $\text{Cu}_2\text{ZnSn}(\text{S,Se})_4$  monograin layer solar cell. *2010 35th IEEE Photovoltaic Specialists Conference*, 111:344–349, 2010. *Cited page 19*
- [158] Fangyang Liu, Fangqin Zeng, Ning Song, Liangxing Jiang, Zili Han, Zhenghua Su, Chang Yan, Xiaoming Wen, Xiaojing Hao, and Yexiang Liu. Kesterite  $\text{Cu}_2\text{ZnSn}(\text{S,Se})_4$  Solar Cells with beyond 8% Efficiency by a Sol-gel and Selenization Process. *ACS Applied Materials & Interfaces*, 7:14376–14383, 2015. *Cited page 19*
- [159] Feng Jiang, Shigeru Ikeda, Zeguo Tang, Takashi Minemoto, Wilman Septina, Takashi Harada, and Michio Matsumura. Impact of alloying duration of an electrodeposited Cu/Sn/Zn metallic stack on properties of  $\text{Cu}_2\text{ZnSnS}_4$  absorbers for thin-film solar cells. *Progress in Photovoltaics: Research and Applications*, 2015. Available online at <http://dx.doi.org/10.1002/pip.2638>. *6 citations pages 19, 41, 44, 46, 47, and 50*
- [160] Yanchun Yang, Xiaojiao Kang, Lijian Huang, Song Wei, and Daocheng Pan. A Facile and Low-Cost Sodium-Doping Method for High-Efficiency  $\text{Cu}_2\text{ZnSnSe}_4$  Thin Film Solar Cells. *The Journal of Physical Chemistry C*, 2015. Available online at <http://pubs.acs.org/doi/10.1021/acs.jpcc.5b06381>. *Cited page 19*
- [161] Qingwen Tian, Yong Cui, Gang Wang, and Daocheng Pan. A robust and low-cost strategy to prepare  $\text{Cu}_2\text{ZnSnS}_4$  precursor solution and its application in  $\text{Cu}_2\text{ZnSn}(\text{S,Se})_4$  solar cells. *RSC Adv.*, 5:4184–4190, 2015. *2 citations pages 19 and 21*
- [162] Kyoohee Woo, Youngwoo Kim, Wooseok Yang, Kyujin Kim, Inhyuk Kim, Yunjung Oh, Jin Young Kim, and Jooho Moon. Band-gap-graded  $\text{Cu}_2\text{ZnSn}(\text{S}_{1-x},\text{Se}_x)_4$  Solar Cells Fabricated by an Ethanol-based, Particulate Precursor Ink Route. *Scientific reports*, 3:3069, January 2013. *2 citations pages 19 and 21*

- [163] David B Mitzi, Oki Gunawan, Teodor K Todorov, and D Aaron R Barkhouse. Prospects and performance limitations for Cu-Zn-Sn-S-Se photovoltaic technology. *Philosophical transactions of the Royal Society A*, 371(July), 2013. *2 citations pages 20 and 139*
- [164] Kentaro Ito and Tatsuo Nakazawa. Electrical and Optical Properties of Stannite-Type Quaternary Semiconductor Thin Films. *Japanese Journal of Applied Physics*, 27(1956):26–27, 1988. *Cited page 20*
- [165] Hironori Katagiri, Kazuo Jimbo, Win Shwe Maw, Koichiro Oishi, Makoto Yamazaki, Hideaki Araki, and Akiko Takeuchi. Development of CZTS-based thin film solar cells. *Thin Solid Films*, 517(7):2455–2460, February 2009. *Cited page 20*
- [166] G. Zoppi, I. Forbes, R. W. Miles, P. J. Dale, J. J. Scragg, and L. M. Peter.  $\text{Cu}_2\text{ZnSnSe}_4$  thin film solar cells produced by selenisation of magnetron sputtered precursors. *Progress in Photovoltaics: Research and Applications*, 17(5):315–319, 2009. *2 citations pages 20 and 153*
- [167] Ingrid L. Repins, Manuel J. Romero, Jian V. Li, Su-Huai Wei, Darius Kuciauskas, Chun-Sheng Jiang, Carolyn Beall, Clay DeHart, Jonathan Mann, Wan-Ching Hsu, Glenn Teeter, Al Goodrich, and Rommel Noufi. Kesterite Successes, Ongoing Work, and Challenges: A Perspective From Vacuum Deposition. *IEEE Journal of Photovoltaics*, 3(1):439–445, January 2013. *2 citations pages 20 and 22*
- [168] Michael Graetzel, René A. J. Janssen, David B. Mitzi, and Edward H. Sargent. Materials interface engineering for solution-processed photovoltaics. *Nature*, 488(7411):304–12, August 2012. *3 citations pages 21, 22, and 121*
- [169] Huanping Zhou, Wan-Ching Hsu, Hsin-Sheng Duan, Brion Bob, Wenbing Yang, Tze-Bin Song, Chia-Jung Hsu, and Yang Yang. CZTS nanocrystals: a promising approach for next generation thin film photovoltaics. *Energy & Environmental Science*, 6(10):2822, 2013. *2 citations pages 21 and 22*
- [170] Jianmin Li, Guilin Chen, Cong Xue, Xin Jin, Weifeng Liu, and Changfei Zhu.  $\text{Cu}_2\text{ZnSnS}_{4-x}\text{Se}_x$  solar cells fabricated with precursor stacked layer ZnS/Cu/SnS by a CBD method. *Solar Energy Materials and Solar Cells*, 137:131–137, 2015. *Cited page 21*
- [171] Seongyeon Kim and Junho Kim. Effect of selenization on sprayed  $\text{Cu}_2\text{ZnSnSe}_4$  thin film solar cell. *Thin Solid Films*, 547:178–180, 2013. *2 citations pages 21 and 122*
- [172] M Espindola Rodriguez, D Sylla, Y Sanchez, S López-Marino, X Fontané, J López-García, M Placidi, A Pérez-Rodríguez, O Vigil-Galán, and E Saucedo. Pneumatically sprayed  $\text{Cu}_2\text{ZnSnS}_4$  films under Ar and Ar- $\text{H}_2$  atmosphere. *Journal of Physics D: Applied Physics*, 47(24):245101, 2014. *2 citations pages 21 and 24*
- [173] O Vigil-Galán, Maykel Courel, M Espindola-Rodríguez, D Jiménez-Olarte, M. Aguilar-Frutis, and E. Saucedo. Electrical properties of sprayed  $\text{Cu}_2\text{ZnSnS}_4$  thin films and its relation with secondary phase formation and solar cell performance. *Solar Energy Materials and Solar Cells*, 132:557–562, 2015. *Cited page 21*
- [174] Hariklia (Lili) Deligianni, Shafaat Ahmed, and Lubomyr T Romankiw. The Next Frontier : Electrodeposition for Solar Cell Fabrication. *The Electrochemical Society Interface*, pages 47–53, 2011. *Cited page 21*
- [175] Alex Polizzotti, Ingrid Repins, Rommel Noufi, Su-Huai Wei, David Mitzi, and David Mitzi. The State and Future Prospects of Kesterite Photovoltaics. *Energy & Environmental Science*, 6(207890):3171–3182, 2013. *2 citations pages 22 and 139*
- [176] Susanne Siebentritt. Why are kesterite solar cells not 20% efficient? *Thin Solid Films*, 535:1–4, May 2013. *3 citations pages 22, 23, and 24*
- [177] Talia Gershon, Tayfun Gokmen, Oki Gunawan, Richard Haight, Supratik Guha, and Byungha Shin. Understanding the relationship between  $\text{Cu}_2\text{ZnSn}(\text{S},\text{Se})_4$  material properties and device performance. *MRS Communications*, 4(04):159–170, November 2014. *4 citations pages 22, 23, 26, and 49*
- [178] Mukesh Kumar, Ashish Dubey, Nirmal Adhikari, Swaminathan Venkatesan, and Qiquan Qiao. Strategic review of secondary phases, defects and defect-complexes in kesterite CZTS-Se solar cells. *Energy Environ. Sci.*, 2015. *2 citations pages 22 and 24*
- [179] David B. Mitzi, Oki Gunawan, Teodor K. Todorov, Kejia Wang, and Supratik Guha. The path towards a high-performance solution-processed kesterite solar cell. *Solar Energy Materials and Solar Cells*, 95(6):1421–1436, June 2011. *8 citations pages 22, 23, 49, 60, 111, 121, 132, and 153*
- [180] Alex Redinger and Susanne Siebentritt. Loss Mechanisms in Kesterite Solar Cells. In *Copper Zinc Tin Sulfide-Based Thin-Film Solar Cells*, chapter 16. John Wiley & Sons, Ltd., first edition, 2015. Edited by Kentaro Ito. *2 citations pages 22 and 121*
- [181] Oki Gunawan, Teodor K. Todorov, and David B. Mitzi. Loss mechanisms in hydrazine-processed  $\text{Cu}_2\text{ZnSn}(\text{Se},\text{S})_4$  solar cells. *Applied Physics Letters*, 97(23):233506, 2010. *Cited page 23*
- [182] Oki Gunawan, Tayfun Gokmen, and David B. Mitzi.  $\text{Suns-V}_{OC}$  characteristics of high performance kesterite solar cells. *Journal of Applied Physics*, 116(8):084504, August 2014. *2 citations pages 23 and 26*
- [183] I.V. Dudchak and L V Piskach. Phase equilibria in the  $\text{Cu}_2\text{SnSe}_3$ – $\text{SnSe}_2$ – $\text{ZnSe}$  system. *Journal of Alloys and Compounds*, 351:145–150, 2003. *Cited page 23*
- [184] I.D. Oleksyuk, I.V. Dudchak, and L.V. Piskach. Phase equilibria in the  $\text{Cu}_2\text{S}$ – $\text{ZnS}$ – $\text{SnS}_2$  system. *Journal of Alloys and Compounds*, 368(1-2):135–143, April 2004. *Cited page 23*
- [185] G. Marcano, C. Rincón, L. M. De Chalbaud, D. B. Bracho, and G. Sánchez Pérez. Crystal growth and structure, electrical, and optical characterization of the semiconductor  $\text{Cu}_2\text{SnSe}_3$ . *Journal of Applied Physics*, 90(4):1847, 2001. *Cited page 24*



- [186] Pedro M. P. Salomé, Paulo A. Fernandes, Joaquim P. Leitão, Marta G. Sousa, Jennifer P. Teixeira, and António F. da Cunha. Secondary crystalline phases identification in  $\text{Cu}_2\text{ZnSnSe}_4$  thin films: contributions from Raman scattering and photoluminescence. *Journal of Materials Science*, 49:7425–7436, 2014. Cited page 24
- [187] A.R. Balu, V.S. Nagarethinam, M.G. Syed Basheer Ahamed, A. Thayumanavan, K.R. Murali, C. Sanjeeviraja, V. Swaminathan, and M. Jayachandran. Influence of thickness on the microstructural, optoelectronic and morphological properties of nanocrystalline ZnSe thin films. *Materials Science and Engineering: B*, 171:93–98, July 2010. Cited page 24
- [188] Dominik M Berg, Rabie Djemour, Levent Gütay, Guillaume Zoppi, Susanne Siebentritt, and Phillip J. Dale. Thin film solar cells based on the ternary compound  $\text{Cu}_2\text{SnS}_3$ . *Thin Solid Films*, 520(19):6291–6294, July 2012. Cited page 24
- [189] Xinlong Yan, Elizebeth Michael, Sridhar Komarneni, Jeffrey R. Brownson, and Zi-Feng Yan. Microwave-and conventional-hydrothermal synthesis of CuS, SnS and ZnS: Optical properties. *Ceramics International*, (39):4757–4763, July 2013. Cited page 24
- [190] S. Sohila, M. Rajalakshmi, Chanchal Ghosh, A.K. Arora, and C. Muthamizhchelvan. Optical and Raman scattering studies on SnS nanoparticles. *Journal of Alloys and Compounds*, 509(19):5843–5847, May 2011. Cited page 24
- [191] Hendrik Flammersberger. *Experimental study of  $\text{Cu}_2\text{ZnSnS}_4$  thin films for solar cells*. PhD thesis, Uppsala University, 2010. 4 citations pages 24, 49, 74, and 153
- [192] Marina Mousel, Alex Redinger, Rabie Djemour, Monika Arasimowicz, Nathalie Valle, Phillip J. Dale, and Susanne Siebentritt. HCl and  $\text{Br}_2$ -MeOH etching of  $\text{Cu}_2\text{ZnSnSe}_4$  polycrystalline absorbers. *Thin Solid Films*, 535:83–87, May 2013. 4 citations pages 23, 112, 113, and 119
- [193] Nirav Vora, Jeffrey Blackburn, Ingrid Repins, Carolyn Beall, Bobby To, Joel Pankow, Glenn Teeter, Matthew Young, and Rommel Noufi. Phase identification and control of thin films deposited by co-evaporation of elemental Cu, Zn, Sn, and Se. *Journal of Vacuum Science & Technology A: Vacuum, Surfaces, and Films*, 30(5):051201, 2012. 3 citations pages 23, 24, and 104
- [194] H Yoo, R Lechner, S Jost, J Palm, A Verger, A Lelarge, V Moreau, C Papret, and R Hock. The Effect of Secondary Phases on  $\text{Cu}_2\text{ZnSn(S,Se)}_4$  based Solar Cell. *Photovoltaic Specialist Conference (PVSC), 2014 IEEE 40th*, pages 2431–2435, 2014. 3 citations pages 23, 24, and 103
- [195] Wan-Ching Hsu, Ingrid Repins, Carolyn Beall, Clay DeHart, Glenn Teeter, Bobby To, Yang Yang, and Rommel Noufi. The effect of Zn excess on kesterite solar cells. *Solar Energy Materials and Solar Cells*, 113:160–164, June 2013. 6 citations pages 23, 24, 93, 95, 111, and 118
- [196] Diego Colombara, Erika Victoria Christiane Robert, Alexandre Crossay, Aidan Taylor, Mael Guennou, Monika Arasimowicz, Joao Corujo Branco Malaquias, Rabie Djemour, and Phillip J. Dale. Quantification of surface ZnSe in  $\text{Cu}_2\text{ZnSnSe}_4$ -based solar cells by analysis of the spectral response. *Solar Energy Materials and Solar Cells*, 123:220–227, April 2014. 6 citations pages 23, 95, 103, 112, 115, and 118
- [197] M. Ganchev, J. Iljina, L. Kaupmees, T. Raadik, O. Volobujeva, A. Mere, M. Altosaar, J. Raudoja, and E. Mellikov. Phase composition of selenized  $\text{Cu}_2\text{ZnSnSe}_4$  thin films determined by X-ray diffraction and Raman spectroscopy. *Thin Solid Films*, 519(21):7394–7398, August 2011. 2 citations pages 24 and 103
- [198] Alex Redinger, Katja Hönes, Xavier Fontané, Victor Izquierdo-Roca, Edgardo Saucedo, Nathalie Valle, Alejandro Pérez-Rodríguez, and Susanne Siebentritt. Detection of a ZnSe secondary phase in coevaporated  $\text{Cu}_2\text{ZnSnSe}_4$  thin films. *Applied Physics Letters*, 98(10):101907, 2011. 2 citations pages 24 and 102
- [199] Carolin M. Fella, Alexander R. Uhl, Ceri Hammond, Ive Hermans, Yaroslav E. Romanyuk, and Ayodhya N. Tiwari. Formation mechanism of  $\text{Cu}_2\text{ZnSnSe}_4$  absorber layers during selenization of solution deposited metal precursors. *Journal of Alloys and Compounds*, 567:102–106, August 2013. 3 citations pages 24, 71, and 76
- [200] H. Yoo, R.A. Wibowo, A. Hölzing, R. Lechner, J. Palm, S. Jost, M. Gowtham, F. Sorin, B. Louis, and R. Hock. Investigation of the solid state reactions by time-resolved X-ray diffraction while crystallizing kesterite  $\text{Cu}_2\text{ZnSnSe}_4$  thin films. *Thin Solid Films*, 535:73–77, May 2013. 4 citations pages 24, 71, 103, and 104
- [201] Jonathan J Scragg, J Timo Wätgen, Marika Edo, Tove Ericson, Tomas Kubart, and Charlotte Platzer-Björkman. A Detrimental Reaction at the Molybdenum Back Contact in  $\text{Cu}_2\text{ZnSn(S,Se)}_4$  Thin-Film Solar Cells. *Journal of the American Chemical Society*, 134:19330–19333, 2012. 2 citations pages 24 and 79
- [202] Xavier Fontane, Victor Izquierdo-Roca, Andrew Fairbrother, Moises Espindola-Rodriguez, Marcel Placidi, Tariq Jawhari, Edgardo Saucedo, and Alejandro Perez-Rodriguez. Selective Detection of Secondary Phases in  $\text{Cu}_2\text{ZnSn(S,Se)}_4$  Based Absorbers by Pre-Resonant Raman Spectroscopy. In *Photovoltaic Specialists Conference (PVSC), 2013 IEEE 39th*, pages 2581–2584, June 2013. 2 citations pages 24 and 102
- [203] Dominik M Berg, Monika Arasimowicz, Rabie Djemour, Levent Gütay, Susanne Siebentritt, Susan Schorr, Xavier Fontané, Victor Izquierdo-Roca, Alejandro Pérez-Rodríguez, and Phillip J Dale. Discrimination and detection limits of secondary phases in  $\text{Cu}_2\text{ZnSnS}_4$  using X-ray diffraction and Raman spectroscopy. *Thin Solid Films*, 569:113–123, 2014. 2 citations pages 24 and 86
- [204] Andrew Fairbrother, Victor Izquierdo-Roca, Xavier Fontané, Maria Ibáñez, Andreu Cabot, Edgardo Saucedo, and Alejandro Pérez-Rodríguez. ZnS grain size effects on near-resonant Raman scattering: optical non-destructive grain size estimation. *CrystEngComm*, (16):4120–4125, 2014. Cited page 24
- [205] O. Vigil-Galán, M. Espindola-Rodríguez, Maykel Courel, X. Fontané, D. Sylla, V. Izquierdo-Roca, A. Fairbrother, E. Saucedo, and A. Pérez-Rodríguez. Secondary phases dependence on composition ratio in sprayed  $\text{Cu}_2\text{ZnSnS}_4$  thin films and its impact on the high power conversion efficiency. *Solar Energy Materials and Solar Cells*, 117:246–250, October 2013. Cited page 24

- [206] Rabie Djemour, Marina Mousel, Alex Redinger, Levent Gütay, Alexandre Crossay, Diego Colombara, Phillip J. Dale, and Susanne Siebentritt. Detecting ZnSe secondary phase in  $\text{Cu}_2\text{ZnSnSe}_4$  by room temperature photoluminescence. *Applied Physics Letters*, 102(22):222108, 2013. 6 citations pages 24, 41, 44, 45, 46, and 47
- [207] A. Weber, R. Mainz, and H. W. Schock. On the Sn loss from thin films of the material system Cu–Zn–Sn–S in high vacuum. *Journal of Applied Physics*, 107(1):013516, 2010. 2 citations pages 24 and 77
- [208] Jonathan J. Scragg, Tove Ericson, Tomas Kubart, Marika Edo, and Charlotte Platzer-Björkman. Chemical Insights into the Instability of  $\text{Cu}_2\text{ZnSnS}_4$  Films during Annealing. *Chemistry of Materials*, 23(20):4625–4633, 2011. 3 citations pages 24, 78, and 80
- [209] Shiyu Chen, Lin-Wang Wang, Aron Walsh, X. G. Gong, and Su-Huai Wei. Abundance of  $\text{Cu}_{\text{Zn}} + \text{Sn}_{\text{Zn}}$  and  $2\text{Cu}_{\text{Zn}} + \text{Sn}_{\text{Zn}}$  defect clusters in kesterite solar cells. *Applied Physics Letters*, 101(22):223901, 2012. Cited page 25
- [210] Jonathan J. S. Scragg, Léo Choubrac, Alain Lafond, Tove Ericson, and Charlotte Platzer-Björkman. A low-temperature order-disorder transition in  $\text{Cu}_2\text{ZnSnS}_4$  thin films. *Applied Physics Letters*, 104(4):041911, January 2014. Cited page 25
- [211] R. Caballero, E. Garcia-Llamas, J.M. Merino, M. León, I. Babichuk, V. Dzhagan, V. Strelchuk, and M. Valakh. Non-stoichiometry effect and disorder in  $\text{Cu}_2\text{ZnSnS}_4$  thin films obtained by flash evaporation: Raman scattering investigation. *Acta Materialia*, 65:412–417, February 2014. Cited page 25
- [212] Christoph Krämmmer, Christian Huber, Christian Zimmermann, Mario Lang, Thomas Schnabel, Tobias Abzieher, Erik Ahlswede, Heinz Kalt, and Michael Hetterich. Reversible order-disorder related band gap changes in  $\text{Cu}_2\text{ZnSn}(\text{S},\text{Se})_4$  via post-annealing of solar cells measured by electroreflectance. *Applied Physics Letters*, 105(26):262104, 2014. Cited page 25
- [213] Tayfun Gokmen, Oki Gunawan, Teodor K. Todorov, and David B. Mitzi. Band tailing and efficiency limitation in kesterite solar cells. *Applied Physics Letters*, 103(10):103506, 2013. 3 citations pages 26, 143, and 153
- [214] Oki Gunawan, Tayfun Gokmen, Charles W Warren, J David Cohen, Teodor K. Todorov, D Aaron R Barkhouse, Santanu Bag, Jiang Tang, Byungha Shin, and David B Mitzi. Electronic properties of the  $\text{Cu}_2\text{ZnSn}(\text{S},\text{Se})_4$  absorber layer in solar cells as revealed by admittance spectroscopy and related methods. *Applied Physics Letters*, 253905(100):1–4, 2012. Cited page 26
- [215] Chang Yan, Fangyang Liu, Ning Song, Boon K. Ng, John a. Stride, Anton Tadich, and Xiaojing Hao. Band alignments of different buffer layers ( $\text{CdS}$ ,  $\text{Zn}(\text{O},\text{S})$ , and  $\text{In}_2\text{S}_3$ ) on  $\text{Cu}_2\text{ZnSnS}_4$ . *Applied Physics Letters*, 104(17):173901, April 2014. 3 citations pages 26, 121, and 122
- [216] Electrochemical Engineering. In *Encyclopedia of Electrochemistry*. 2007. Edited by Macdonald, Digby D. and Schmuki, Patrik. Cited page 31
- [217] Helen H. Lou and Yinlun Huang. Electroplating. *Encyclopedia of chemical processing*, 1:839–848, 1978. Cited page 31
- [218] Morton Schwartz. Deposition from aqueous solutions: an overview. In *Handbook of Deposition Technologies for Films and Coatings*, pages 506–616. 1994. 2 citations pages 31 and 33
- [219] Sébastien Delbos. *Turbulence controlled Cu-In-Se electrodeposition for solar cell production*. PhD thesis, Université Paris 6 - Pierre et Marie Curie, 2008. 3 citations pages 32, 35, and 36
- [220] Douglas A Skoog, Donald M West, F James Holler, and Stanley R Crouch. *Fundamentals of Analytical Chemistry*. Thomson Brooks/Cole, eight edition, 2004. 2 citations pages 33 and 34
- [221] C.H Siah, N. Aziz, Z. Samad, N. Noordin, M.N. Idris, and M.A. Miskam. A Review Of The Fundamentals Studies For The Electroplating Process. *eprints.usm.my*, pages 887–892, 2002. Cited page 36
- [222] Gregory J. Wilson and Paul R. McHugh. Unsteady Numerical Simulation of the Mass Transfer within a Reciprocating Paddle Electroplating Cell. *Journal of The Electrochemical Society*, 152(6):C356, 2005. Cited page 36
- [223] Jonathan J. Scragg. *Copper Zinc Tin Sulfide Thin Films for Photovoltaics*. Springer Berlin Heidelberg, 2011. 8 citations pages 37, 38, 41, 42, 44, 49, 77, and 89
- [224] Daniel Lincot. Electrodeposition of semiconductors. *Thin Solid Films*, 487:40–48, 2005. Cited page 38
- [225] D. Cunningham, M. Rubcich, and D. Skinner. Cadmium telluride PV module manufacturing at BP solar. *Progress in Photovoltaics: Research and Applications*, (10):159–168, 2002. Cited page 38
- [226] D. Lincot, J.F. Guillemoles, S. Taunier, D. Guimard, J. Six-Kurdi, A. Chaumont, O. Roussel, O. Ramdani, C. Hubert, J.P. Fauvarque, N. Bodereau, L. Parissi, P. Panheleux, P. Fanouillere, N. Naghavi, P.P. Grand, M. Benfarah, P. Mogensen, and O. Kerrec. Chalcopyrite thin film solar cells by electrodeposition. *Solar Energy*, 77(6):725–737, December 2004. Cited page 38
- [227] S. Taunier, J. Six-Kurdi, P. P. Grand, a. Chomont, O. Ramdani, L. Parissi, P. Panheleux, N. Naghavi, C. Hubert, M. Ben-Farah, J. P. Fauvarque, J. Connolly, O. Roussel, P. Mogensen, E. Mahé, J. F. Guillemoles, D. Lincot, and O. Kerrec.  $\text{Cu}(\text{In},\text{Ga})(\text{S},\text{Se})_2$  solar cells and modules by electrodeposition. *Thin Solid Films*, 480-481:526–531, 2005. Cited page 38
- [228] B M Basol, M Pinarbasi, S Aksu, J Freitag, P Gonzalez, T Johnson, Y Matus, B Metin, M Narasimhan, D Nayak, G Norsworthy, D Soltz, J Wang, T Wang, and H Zolla. Status of Electroplating based CIGS technology development. In *34th IEEE PVSC*, pages 2310–2315, 2009. Cited page 38

- [229] C. Broussillou, T. Goislard de Monsabert, F. Bahi, J. Houles, J. Rousset, M. Paire, F. Tsin, and L. Parissi. Efficiency Enhancement of Electrodeposition-Based CIGS PV: 14% Module & 17,3% Cell. In *Photovoltaic Technical Conference - Advanced Materials and Processes to Innovative Applications*, Aix-en-Provence, France, May 2015. *2 citations pages 38 and 130*
- [230] Cedric Broussillou, Cedric Viscogliosi, Alexandre Rogee, Pierre-Philippe Grand, Sylvie Bodnar, Christophe Debauche, Jean-Louis Allary, Bertrand Bertrand, Cyrille Guillou, Ludovic Parissi, and Stephane Coletti. Statistical Process Control for Cu(In,Ga)(S,Se)<sub>2</sub> electrodeposition-based manufacturing process of 60 × 120 cm<sup>2</sup> modules up to 14,0% efficiency. In *PVSC-42*, New Orleans, USA, 2015. *Cited page 38*
- [231] Jonathan J. Scragg, Philip J. Dale, Laurence M. Peter, Guillaume Zoppi, and Ian Forbes. New routes to sustainable photovoltaics: evaluation of Cu<sub>2</sub>ZnSnS<sub>4</sub> as an alternative absorber material. *Physica Status Solidi (B)*, 245(9):1772–1778, September 2008. *7 citations pages 38, 41, 44, 45, 46, 47, and 73*
- [232] J.J. Scragg, P.J. Dale, and L.M. Peter. Synthesis and characterization of Cu<sub>2</sub>ZnSnS<sub>4</sub> absorber layers by an electrodeposition-annealing route. *Thin Solid Films*, 517(7):2481–2484, February 2009. *3 citations pages 38, 45, and 46*
- [233] Jonathan J. Scragg, Dominik M Berg, and Phillip J. Dale. A 3.2% efficient Kesterite device from electrodeposited stacked elemental layers. *Journal of Electroanalytical Chemistry*, 646(1-2):52–59, July 2010. *9 citations pages 38, 41, 42, 44, 45, 46, 47, 73, and 112*
- [234] Hideaki Araki, Yuki Kubo, Aya Mikaduki, Kazuo Jimbo, Win Shwe Maw, Hironori Katagiri, Makoto Yamazaki, Koichiro Oishi, and Akiko Takeuchi. Preparation of Cu<sub>2</sub>ZnSnS<sub>4</sub> thin films by sulfurizing electroplated precursors. *Solar Energy Materials and Solar Cells*, 93(6-7):996–999, June 2009. *5 citations pages 38, 41, 44, 46, and 47*
- [235] Hideaki Araki, Yuki Kubo, Kazuo Jimbo, Win Shwe Maw, Hironori Katagiri, Makoto Yamazaki, Koichiro Oishi, and Akiko Takeuchi. Preparation of Cu<sub>2</sub>ZnSnS<sub>4</sub> thin films by sulfurization of co-electroplated Cu-Zn-Sn precursors. *Physica Status Solidi (C)*, 6(5):1266–1268, May 2009. *2 citations pages 39 and 40*
- [236] A. Ennaoui, M. Lux-Steiner, A. Weber, D. Abou-Ras, I. Kötschau, H.-W. Schock, R. Schurr, A. Hölzling, S. Jost, R. Hock, T. Voß, J. Schulze, and A. Kirbs. Cu<sub>2</sub>ZnSnS<sub>4</sub> thin film solar cells from electroplated precursors: Novel low-cost perspective. *Thin Solid Films*, 517(7):2511–2514, February 2009. *3 citations pages 39, 40, and 75*
- [237] Gee Yeong Kim, William Jo, Kee Doo Lee, Hee-Su Choi, Jin Young Kim, Hae-Young Shin, Trang Thi Thu Nguyen, Seokhyun Yoon, Beom Soo Joo, Minseon Gu, and Moonsoo Han. Optical and surface probe investigation of secondary phases in Cu<sub>2</sub>ZnSnS<sub>4</sub> films grown by electrochemical deposition. *Solar Energy Materials and Solar Cells*, 139:10–18, 2015. *2 citations pages 39 and 112*
- [238] Kee Doo Lee, Se-Won Seo, Doh-Kwon Lee, Honggon Kim, Jeung-Hyun Jeong, Min Jae Ko, BongSoo Kim, Dong Hwan Kim, and Jin Young Kim. Preparation of Cu<sub>2</sub>ZnSnS<sub>4</sub> thin films via electrochemical deposition and rapid thermal annealing. *Thin Solid Films*, 546(The proceedings of International Union of the Materials Research Society -International Conference in Asia 2012- IUMRS-ICA 2012):294–298, 2013. *2 citations pages 39 and 112*
- [239] C. Gougoud, D. Rai, S. Delbos, E. Chassaing, and D. Lincot. Electrochemical Studies of One-Step Electrodeposition of Cu-Sn-Zn Layers from Aqueous Electrolytes for Photovoltaic Applications. *Journal of the Electrochemical Society*, 160(10):D485–D494, September 2013. *3 citations pages 39, 40, and 73*
- [240] YongZheng Zhang, Cheng Liao, Kai Zong, Hao Wang, JingBing Liu, Tao Jiang, JunFeng Han, GuoQiang Liu, Liang Cui, QinYan Ye, Hui Yan, and WoonMing Lau. Cu<sub>2</sub>ZnSnSe<sub>4</sub> thin film solar cells prepared by rapid thermal annealing of co-electroplated Cu-Zn-Sn precursors. *Solar Energy*, 94:1–7, August 2013. *3 citations pages 39, 40, and 73*
- [241] Yi Li, Tengfei Yuan, Liangxing Jiang, Zhenghua Su, and Fangyang Liu. Growth and characterization of Cu<sub>2</sub>ZnSnS<sub>4</sub> photovoltaic thin films by electrodeposition and sulfurization. *Journal of Alloys and Compounds*, 610:331–336, 2014. *3 citations pages 39, 40, and 75*
- [242] E M Mkawi, K Ibrahim, M K M Ali, M A Farrukh, A S Mohamed, and Nageh K Allam. Effect of complexing agents on the electrodeposition of Cu-Zn-Sn metal precursors and corresponding Cu<sub>2</sub>ZnSnS<sub>4</sub>-based solar cells. *Journal of Electroanalytical Chemistry*, 735:129–135, 2014. *2 citations pages 39 and 75*
- [243] E. M. Mkawi, K. Ibrahim, M. K. M. Ali, K. M. A. Saron, M. A. Farrukh, and Nageh K. Allam. Influence of substrate temperature on the properties of electrodeposited kesterite Cu<sub>2</sub>ZnSnS<sub>4</sub> (CZTS) thin films for photovoltaic applications. *Journal of Materials Science: Materials in Electronics*, 26(1):222–228, 2014. *Cited page 39*
- [244] E. M. Mkawi, K. Ibrahim, M. K. M. Ali, M. A. Farrukh, and A. S. Mohamed. Dependence of the properties of copper zinc tin sulfide thin films prepared by electrochemical deposition on sulfurization temperature. *Journal of Materials Science: Materials in Electronics*, 25(2):857–863, 2014. *Cited page 39*
- [245] R. Kondrotas, R. Juškenas, A. Naujokaitis, A. Selskis, R. Giraitis, Z. Mockus, S. Kanapeckaitė, G. Niaura, H. Xie, Y. Sánchez, and E. Saucedo. Characterization of Cu<sub>2</sub>ZnSnSe<sub>4</sub> solar cells prepared from electrochemically co-deposited Cu-Zn-Sn alloy. *Solar Energy Materials and Solar Cells*, 132:21–28, January 2015. *4 citations pages 39, 40, 50, and 73*
- [246] Remigijus Juškenas, Stasė Kanapeckaitė, Violeta Karpavičienė, Zenius Mockus, Vidas Pakštas, Aušra Selskienė, Raimondas Giraitis, and Gediminas Niaura. A two-step approach for electrochemical deposition of Cu-Zn-Sn and Se precursors for CZTSe solar cells. *Solar Energy Materials and Solar Cells*, 101:277–282, June 2012. *3 citations pages 39, 42, and 72*

- [247] Tubshin Hreid, Jianjun Li, Yi Zhang, Henry J. Spratt, Hongxia Wang, and Geoffrey Will. Effects of metal ions concentration on electrodeposited CuZnSn film and its application in kesterite  $\text{Cu}_2\text{ZnSnS}_4$  solar cells. *RSC Adv.*, (5):65114–65122, 2015. *Cited page 39*
- [248] Ji Li, Tuteng Ma, Ming Wei, Weifeng Liu, Guoshun Jiang, and Changfei Zhu. The  $\text{Cu}_2\text{ZnSnSe}_4$  thin films solar cells synthesized by electrodeposition route. *Applied Surface Science*, 258(17):6261–6265, June 2012. *2 citations pages 39 and 75*
- [249] Xin-kuai He, Bai-zhen Chen, Geng-sheng Hu, Ling-feng Deng, Ning-bo Zhou, and Wen-zeng Tian. Process of electroless plating Cu-Sn-Zn ternary alloy. *Transactions of Nonferrous Metals Society of China*, (16):223–228, 2006. *Cited page 40*
- [250] Yingjun Wang, Jianbing Ma, Ping Liu, Yongsheng Chen, Rui Li, Jinhua Gu, Jingxiao Lu, Shi-e Yang, and Xiaoyong Gao.  $\text{Cu}_2\text{ZnSnS}_4$  films deposited by a co-electrodeposition-annealing route. *Materials Letters*, 77:13–16, 2012. *Cited page 40*
- [251] K.V. Gurav, S.M. Pawar, Seung Wook Shin, M.P. Suryawanshi, G.L. Agawane, P.S. Patil, Jong-Ha Moon, J.H. Yun, and Jin Hyeok Kim. Electrosynthesis of CZTS films by sulfurization of CZT precursor: Effect of soft annealing treatment. *Applied Surface Science*, 283:74–80, October 2013. *2 citations pages 40 and 50*
- [252] Lorenzo Rovelli, S David Tilley, and Kevin Sivula. Optimization and stabilization of electrodeposited  $\text{Cu}_2\text{ZnSnS}_4$  photocathodes for solar water reduction. *ACS applied materials & interfaces*, 5(16):8018–24, August 2013. *2 citations pages 40 and 42*
- [253] Ibrahim Khalil, Roberto Bernasconi, and Luca Magagnin. CZTS layers for solar cells by an electrodeposition-annealing route. *Electrochimica Acta*, (145):154–158, 2014. *Cited page 40*
- [254] Ke Cheng, Jian Meng, Xiaoyun Wang, Yuqian Huang, Jingjing Liu, Ming Xue, and Zuliang Du. Low-cost  $\text{Cu}_2\text{ZnSnS}_4$  thin films prepared from single step electrodeposited Cu/Zn/Sn alloy precursor films. *Materials Chemistry and Physics*, 163:24–29, August 2015. *Cited page 40*
- [255] M. Jeon, Y. Tanaka, T. Shimizu, and S. Shingubara. Formation and characterization of single-step electrodeposited  $\text{Cu}_2\text{ZnSnS}_4$  thin films: Effect of complexing agent volume. *Energy Procedia*, 10:255–260, January 2011. *Cited page 40*
- [256] Minsung Jeon, Tomohiro Shimizu, and Shoso Shingubara.  $\text{Cu}_2\text{ZnSnS}_4$  thin films and nanowires prepared by different single-step electrodeposition method in quaternary electrolyte. *Materials Letters*, 65(15-16):2364–2367, August 2011. *Cited page 40*
- [257] Sambhaji M Pawar, Bharati S Pawar, Kishor V Gurav, Do Won Bae, Se Han Kwon, Sanjay S Kolekar, and Jin Hyeok Kim Á. Fabrication of  $\text{Cu}_2\text{ZnSnS}_4$  Thin Film Solar Cell Using Single Step Electrodeposition Method. *Japanese Journal of Applied Physics*, 51:10NC27, 2012. *Cited page 40*
- [258] Kai Yang and Masaya Ichimura. Fabrication of Cu-Zn-Sn-SO thin films by the electrochemical deposition method and application to heterojunction cells. *International Journal of Photoenergy*, 2012:154704, 2012. *Cited page 40*
- [259] J. Iljina, R. Zhang, M. Ganchev, T. Raadik, O. Volobujeva, M. Altosaar, R. Traksmaa, and E. Mellikov. Formation of  $\text{Cu}_2\text{ZnSnS}_4$  absorber layers for solar cells by electrodeposition-annealing route. *Thin Solid Films*, 537:85–89, 2013. *Cited page 40*
- [260] Jie Ge, Jinchun Jiang, Pingxiong Yang, Cheng Peng, Zhipeng Huang, Shaohua Zuo, Lihong Yang, and Junhao Chu. A 5.5% efficient co-electrodeposited ZnO/CdS/ $\text{Cu}_2\text{ZnSnS}_4$ /Mo thin film solar cell. *Solar Energy Materials and Solar Cells*, 125:20–26, 2014. *2 citations pages 40 and 41*
- [261] Balakrishna Ananthoju, Farjana J. Sonia, Ajay Kushwaha, D. Bahadur, N. V. Medhekar, and M. Aslam. Improved structural and optical properties of  $\text{Cu}_2\text{ZnSnS}_4$  thin films via optimized potential in single bath electrodeposition. *Electrochimica Acta*, 137:154–163, 2014. *Cited page 40*
- [262] Seul Gi Lee, Jongmin Kim, Huyn Suk Woo, Yongcheol Jo, a.I. I. Inamdar, S.M. M. Pawar, Hyung Sang Kim, Woong Jung, and Hyun Sik Im. Structural, morphological, compositional, and optical properties of single step electrodeposited  $\text{Cu}_2\text{ZnSnS}_4$  (CZTS) thin films for solar cell application. *Current Applied Physics*, 14(3):254–258, March 2014. *Cited page 40*
- [263] M. Valdes, M. Modibedi, M. Mathe, T. Hillie, and M. Vazquez. Electrodeposited  $\text{Cu}_2\text{ZnSnS}_4$  thin films. *Electrochimica Acta*, 128:393–399, 2014. *Cited page 40*
- [264] Jiahua Tao, Jun He, Kezhi Zhang, Junfeng Liu, Yuchen Dong, Lin Sun, Pingxiong Yang, and Junhao Chu. Effect of deposition potential on the properties of  $\text{Cu}_2\text{ZnSnS}_4$  films for solar cell applications. *Materials Letters*, 135:8–10, 2014. *2 citations pages 40 and 41*
- [265] Tulshi Shiyani, Malkesh Patel, Indrajeet Mukhopadhyay, and Abhijit Ray. Effect of Annealing on Structural Properties of Electrodeposited CZTS Thin Films. *IETE Technical Review*, 2015. Available online at <http://dx.doi.org/10.1080/02564602.2015.1045044>. *Cited page 40*
- [266] E. M. Mkawi, K. Ibrahim, M. K M Ali, M. A. Farrukh, and A. S. Mohamed. Influence of triangle wave pulse on the properties of  $\text{Cu}_2\text{ZnSnS}_4$  thin films prepared by single step electrodeposition. *Solar Energy Materials and Solar Cells*, 130:91–98, 2014. *Cited page 40*
- [267] B.S. Pawar, S.M. Pawar, S.W. Shin, D.S. Choi, C.J. Park, S.S. Kolekar, and J.H. Kim. Effect of complexing agent on the properties of electrochemically deposited  $\text{Cu}_2\text{ZnSnS}_4$  (CZTS) thin films. *Applied Surface Science*, 257(5):1786–1791, December 2010. *Cited page 40*

- [268] K V Gurav, S W Shin, U M Patil, M P Suryawanshi, S M Pawar, M G Gang, S A Vanalakar, J H Yun, and J H Kim. Improvement in the properties of CZTSSe thin films by selenizing single-step electrodeposited CZTS thin films. *Journal of Alloys and Compounds*, 631:178–182, 2015. *Cited page 40*
- [269] Wilman Septina, Shigeru Ikeda, Akio Kyoraiseki, Takashi Harada, and Michio Matsumura. Formation and characterization of thin film kesterites prepared from a single-step electrodeposited Cu-Zn-Sn-Se precursor film. *27th European Photovoltaic Solar Energy Conference and Exhibition*, pages 2787–2789, 2012. *Cited page 40*
- [270] Wilman Septina, Shigeru Ikeda, Akio Kyoraiseki, Takashi Harada, and Michio Matsumura. Single-step electrodeposition of a microcrystalline  $\text{Cu}_2\text{ZnSnSe}_4$  thin film with a kesterite structure. *Electrochimica Acta*, 88:436–442, 2013. *Cited page 40*
- [271] Wilman Septina. *Studies on Electrochemical Syntheses of Semiconductor Thin Films for Photovoltaic Applications*. PhD thesis, Osaka University, 2013. *Cited page 40*
- [272] Jie Ge, Junhao Chu, Yanfa Yan, Jinchun Jiang, and Pingxiong Yang. Co-electroplated Kesterite Bifacial Thin-film Solar Cells: a Study of Sulfurization Temperature. *ACS Applied Materials & Interfaces*, (7):10414–10428, 2015. *Cited page 41*
- [273] Yixin Lin, Shigeru Ikeda, Wilman Septina, Yoshihito Kawasaki, Takashi Harada, and Michio Matsumura. Mechanistic aspects of preheating effects of electrodeposited metallic precursors on structural and photovoltaic properties of  $\text{Cu}_2\text{ZnSnS}_4$  thin films. *Solar Energy Materials and Solar Cells*, 120:218–225, January 2014. *9 citations pages 41, 42, 44, 46, 47, 50, 64, 66, and 74*
- [274] Monika Arasimowicz. *Phase Segregation in  $\text{Cu}_2\text{ZnSnSe}_4$  Thin Films for Photovoltaic Applications: the effects of precursor microstructure and selenium activity during selenization of electrodeposited metallic precursors*. PhD thesis, Université du Luxembourg, 2014. *10 citations pages 41, 42, 44, 45, 46, 47, 50, 51, 67, and 73*
- [275] Monika Arasimowicz, Maxime Thevenin, and Phillip J. Dale. The Effect of Soft Pre-Annealing of Differently Stacked Cu-Sn-Zn Precursors on the Quality of  $\text{Cu}_2\text{ZnSnSe}_4$  Absorbers. *Mater. Res. Soc. Symp. Proc.*, 1538:123–129, 2013. *3 citations pages 41, 42, and 50*
- [276] Dominik Matthias Berg. *Kesterite Equilibrium Reaction and the Discrimination of Secondary Phases from  $\text{Cu}_2\text{ZnSnS}_4$* . PhD thesis, Université du Luxembourg, 2012. *Cited page 41*
- [277] Raghu N Bhattacharya. 3.6 % -CZTSS Device Fabricated From Ionic Liquid Electrodeposited Sn Layer. *The Open Surface Science Journal*, (5):21–24, 2013. *2 citations pages 41 and 42*
- [278] Raghu N Bhattacharya and J Y Kim. Cu-Zn-Sn-S Thin Films from Electrodeposited Metallic Precursor Layers. *The Open Surface Science Journal*, (4):19–24, 2012. *6 citations pages 41, 42, 44, 45, 46, and 47*
- [279] E M Mkawi, K Ibrahim, M K M Ali, M A Farrukh, and Nageh K Allam. Influence of precursor thin films stacking order on the properties of  $\text{Cu}_2\text{ZnSnS}_4$  thin films fabricated by electrochemical deposition method. *Superlattices and Microstructures*, (76):339–348, 2014. *7 citations pages 41, 42, 44, 45, 46, 47, and 75*
- [280] Guijun Ma, Tsutomu Minegishi, Daisuke Yokoyama, Jun Kubota, and Kazunari Domen. Photoelectrochemical hydrogen production on  $\text{Cu}_2\text{ZnSnS}_4$ /Mo-mesh thin-film electrodes prepared by electroplating. *Chemical Physics Letters*, 501(4-6):619–622, January 2011. *2 citations pages 42 and 44*
- [281] Xiancong He, Honglie Shen, Jinhong Pi, Chuanxiang Zhang, and Yu Hao. Synthesis of  $\text{Cu}_2\text{ZnSnS}_4$  films from sequentially electrodeposited Cu-Sn-Zn precursors and their structural and optical properties. *Journal of Materials Science: Materials in Electronics*, 24(11):4578–4584, August 2013. *2 citations pages 42 and 44*
- [282] Rachmat Adhi Wibowo, Raad Hamid, Thomas Maier, and Theodoros Dimopoulos. Galvanostatically-electrodeposited Cu-Zn-Sn multilayers as precursors for crystallising kesterite  $\text{Cu}_2\text{ZnSnS}_4$  thin films. *Thin Solid Films*, 582:239–244, 2015. *2 citations pages 42 and 44*
- [283] Chia-Ying Su, Chiu-Yen Chiu, and Jyh-Ming Ting.  $\text{Cu}_2\text{ZnSnS}_4$  absorption layers with controlled phase purity. *Scientific Reports*, 5:9291, 2015. *2 citations pages 42 and 64*
- [284] Prashant K. Sarswat, Michael Snure, Michael L. Free, and Ashutosh Tiwari. CZTS thin films on transparent conducting electrodes by electrochemical technique. *Thin Solid Films*, 520(6):1694–1697, January 2012. *2 citations pages 42 and 45*
- [285] E.M. Mkawi, K. Ibrahim, M.K.M. Ali, M.A. Farrukh, and Abdussalam Salhin Mohamed. Synthesized and Characterization of  $\text{Cu}_2\text{ZnSnS}_4$  (CZTS) Thin Films Deposited by Electrodeposition Method. *Applied Mechanics and Materials*, 343:85–89, 2013. *Cited page 42*
- [286] J. Iljina, O. Volobujeva, T. Raadik, N. Revathi, J. Raudoja, M. Loorits, R. Traksmaa, and E. Mellikov. Selenisation of sequentially electrodeposited Cu-Zn and Sn precursor layers. *Thin Solid Films*, 535:14–17, May 2013. *Cited page 42*
- [287] J. Lehner, M. Ganchev, M. Loorits, N. Revathi, T. Raadik, J. Raudoja, M. Grossberg, E. Mellikov, and O. Volobujeva. Structural and compositional properties of CZTS thin films formed by rapid thermal annealing of electrodeposited layers. *Journal of Crystal Growth*, 380:236–240, October 2013. *Cited page 42*
- [288] M. Ganchev, L. Kaupmees, J. Iliyana, J. Raudoja, O. Volobujeva, H. Dikov, M. Altosaar, E. Mellikov, and T. Varema. Formation of thin films by selenization of electrodeposited stacked binary alloy layers. *Energy Procedia*, 2(1):65–70, August 2010. *Cited page 42*

- [289] Tengfei Yuan, Yi Li, Ming Jia, Yanqing Lai, Jie Li, Fangyang Liu, and Yexiang Liu. Fabrication of  $\text{Cu}_2\text{ZnSnS}_4$  thin film solar cells by sulfurization of electrodeposited stacked binary Cu–Zn and Cu–Sn alloy layers. *Materials Letters*, 155:44–47, 2015. *Cited page 42*
- [290] Raghu N Bhattacharya. Fabrication of ionic liquid electrodeposited Cu–Sn–Zn–S–Se thin films and method of making (Patent US 2013/0168825 A1), 2013. *5 citations pages 42, 44, 45, 46, and 47*
- [291] Marc Steichen, Neil R Brooks, Monika Arasimowicz, João Malaquias, Phillip J Dale, and Luc Van Meervelt. Liquid Metal Salts: High Current Density Electrodeposition of Cu–Sn–Zn Metal Stacks from Ionic Liquids for Kesterite based Thin Film Photovoltaics. In *224th ECS Meeting*, 2013. *Cited page 42*
- [292] Magida Fawaz. Développement par électrodépôt de précurseurs à base de kesterite compatibles avec un procédé industriel (Confidential). Technical report, NEXCIS, 2012. *7 citations pages 43, 46, 47, 48, 52, 60, and 147*
- [293] Jack W. Dini and Dexter D. Snyder. Electrodeposition of copper. In Mordechai Schlesinger and Milan Paunovic, editors, *Modern Electroplating, Fifth Edition*, pages 33–78. John Wiley & Sons, Inc., 2010. *2 citations pages 44 and 45*
- [294] Raghu N. Bhattacharya. CIGS-based solar Cells prepared from electrodeposited stacked Cu/In/Ga Layers. *Solar Energy Materials and Solar Cells*, 113:96–99, 2013. *2 citations pages 44 and 45*
- [295] Hideaki Araki, Yuki Kubo, Aya Mikaduki, Kazuo Jimbo, Win Shwe Maw, Hironori Katagiri, Makoto Yamazaki, Koichiro Oishi, and Akiko Takeuchi. Preparation of  $\text{Cu}_2\text{ZnSnS}_4$  thin films by sulfurizing electroplated precursors. *Solar Energy Materials and Solar Cells*, 93(6-7):996–999, June 2009. *Cited page 44*
- [296] L. L. Barbosa, M. R. H de Almeida, R. M. Carlos, M. Yonashiro, G. M. Oliveira, and Ivani A. Carlos. Study and development of an alkaline bath for copper deposition containing sorbitol as complexing agent and morphological characterization of the copper film. *Surface and Coatings Technology*, 192(2-3):145–153, 2005. *Cited page 45*
- [297] Pierre-Philippe Grand, Jesus Salvador Jaime-Ferrer, Emmanuel Roche, Hariklia Deligianni, Raman Vaidyanathan, Kathleen B. Reuter, Qiang Huang, Lubomyr T. Romankiw, Maurice Mason, and Donna S. Zupanski-Nielsen. Improved interface between a I-III-VI2 material layer and a molybdenum substrate (Patent WO 2012/089558 A1), 2012. *2 citations pages 45 and 52*
- [298] Fa-Xin Xiao, Xiao-Ni Shen, Feng-Zhang Ren, and Alex A. Volinsky. Additive effects on tin electrodeposition in acid sulfate electrolytes. *International Journal of Minerals, Metallurgy, and Materials*, 20(5):472–478, May 2013. *2 citations pages 45 and 46*
- [299] Pourbaix. *Atlas of Electrochemical Equilibria in Aqueous Solutions*. 1974. *Cited page 45*
- [300] G. Rozovskis, Z. Mockus, V Pautienien, and A. Survila. Electrochemical determination of Sn(IV)/Sn(II) ratio in tin sol formed in copper–tin sulphate solution containing laprol 2402C. *Electrochemistry Communications*, 4(1):76–79, January 2002. *Cited page 45*
- [301] F. I. Danilov, T. E. Butyrina, V. S. Protsenko, and E. A. Vasil’eva. Oxidation of Sn(II) in methanesulfonate electrolytes in presence of antioxidants. *Russian Journal of Applied Chemistry*, 83(4):752–754, 2010. *Cited page 45*
- [302] R. Sekar, C. Eagammai, and Sobha Jayakrishnan. Effect of additives on electrodeposition of tin and its structural and corrosion behaviour. *Journal of Applied Electrochemistry*, 40(1):49–57, July 2009. *Cited page 46*
- [303] C.T.J. Low and F.C. Walsh. The stability of an acidic tin methanesulfonate electrolyte in the presence of a hydroquinone antioxidant. *Electrochimica Acta*, 53(16):5280–5286, June 2008. *Cited page 46*
- [304] Stuart Meibuhr, Ernest Yeager, Akiya Kozawa, and Frank Hovorka. The Electrochemistry of Tin. I. Effects of Nonionic Addition Agents on Electrodeposition from Stannous Sulfate Solutions. *Journal of The Electrochemical Society*, 110(3):190–201, 1963. *Cited page 46*
- [305] René Winand. Chapter 10 : Electrodeposition of Zinc and Zinc Alloys. In *Modern Electroplating, Fifth Edition*, pages 285–307. John Wiley & Sons, Inc., 2010. Edited by Schlesinger, Mordechai and Paunovic, Milan. *Cited page 47*
- [306] José Luis Ortiz-Aparicio, Yunny Meas, Gabriel Trejo, Raúl Ortega, Thomas W. Chapman, and Eric Chainet. Effects of organic additives on zinc electrodeposition from alkaline electrolytes. *Journal of Applied Electrochemistry*, 43(3):289–300, December 2012. *Cited page 47*
- [307] Louis Lacourcelle. *Traité de Galvanotechnique*. 1996. *Cited page 47*
- [308] S. M. Pawar, A. I. Inamdar, B. S. Pawar, K. V. Gurav, S. W. Shin, Xiao Yanjun, S. S. Kolekar, Jung Ho Lee, Jin Hyeok Kim, and Hyunsik Im. Synthesis of  $\text{Cu}_2\text{ZnSnS}_4$  (CZTS) absorber by rapid thermal processing (RTP) sulfurization of stacked metallic precursor films for solar cell applications. *Materials Letters*, 118:76–79, 2014. *2 citations pages 49 and 73*
- [309] S. M. Pawar, A. I. Inamdar, K. V. Gurav, S. W. Shin, Yongcheol Jo, Jongmin Kim, Hyunsik Im, and Jin Hyeok Kim. Growth of void free  $\text{Cu}_2\text{ZnSnS}_4$  (CZTS) thin films by sulfurization of stacked metallic precursor films. *Vacuum*, 104:57–60, 2014. *Cited page 50*
- [310] Phillip J. Dale, Monika Arasimowicz, Diego Colombara, Alexandre Crossay, Erika Robert, and Aidan A Taylor. Is it Possible to Grow Thin Films of Phase Pure Kesterite Semiconductor? A ZnSe case study. *Mater. Res. Soc. Symp. Proc.*, 1538:83–94, 2013. *Cited page 50*

- [311] S. Fürtauer, D. Li, D. Cupid, and H. Flandorfer. The Cu–Sn phase diagram, Part I: New experimental results. *Intermetallics*, 34:142–147, March 2013. *Cited page 50*
- [312] Chin-yi Chou and Sinn-wen Chen. Phase equilibria of the Sn–Zn–Cu ternary system. *Acta Materialia*, 54(9):2393–2400, May 2006. *2 citations pages 50 and 65*
- [313] Yu-Chih Huang, Sinn-Wen Chen, Chin-Yi Chou, and Wojciech Gierlotka. Liquidus projection and thermodynamic modeling of Sn–Zn–Cu ternary system. *Journal of Alloys and Compounds*, 477(1-2):283–290, May 2009. *Cited page 50*
- [314] Tetiana Olar, Markus Neuschitzer, and José Marquez. Waste management of Cu–Zn–Sn electrodeposition bath (Confidential). Technical report, Nexcis, KESTCELLS, June 2015. *2 citations pages 58 and 68*
- [315] Remigijus Juskeenas, V Pakštas, A Sudavičius, V Kapočius, and V Karpavičienė. Formation of intermetallic phases during ageing of Zn electroplate on the Cu substrate. *Applied Surface Science*, 229:402–408, May 2004. *Cited page 64*
- [316] H. Yoo, R.A. Wibowo, G. Manoharan, R. Lechner, S. Jost, A. Verger, J. Palm, and R. Hock. The formation mechanism of secondary phases in  $\text{Cu}_2\text{ZnSnSe}_4$  absorber layer. *Thin Solid Films*, 582: E-MRS 2014 Spring Meeting, Symposium A, Thin-Film Chalcogenide Photovoltaic Materials:245–248, May 2015. *Cited page 71*
- [317] R. Schurr, A. Hölzing, S. Jost, R. Hock, T. Voß, J. Schulze, A. Kirbs, A. Ennaoui, M. Lux-Steiner, A. Weber, I. Kötschau, and H.-W. Schock. The crystallisation of  $\text{Cu}_2\text{ZnSnS}_4$  thin film solar cell absorbers from co-electroplated Cu–Zn–Sn precursors. *Thin Solid Films*, 517(7):2465–2468, February 2009. *Cited page 71*
- [318] Rachmat Adhi Wibowo, Stefan A. Moeckel, Hyesun Yoo, Christina Hetzner, Astrid Hoelzing, Peter Wellmann, and Rainer Hock. Intermetallic compounds dynamic formation during annealing of stacked elemental layers and its influences on the crystallization of  $\text{Cu}_2\text{ZnSnSe}_4$  films. *Materials Chemistry and Physics*, 142(1):311–317, October 2013. *Cited page 71*
- [319] Andrew Fairbrother, Xavier Fontané, Victor Izquierdo-Roca, Moises Espíndola-Rodríguez, Simon López-Marino, Marcel Placidi, Lorenzo Calvo-Barrio, Alejandro Pérez-Rodríguez, and Edgardo Saucedo. On the formation mechanisms of Zn-rich  $\text{Cu}_2\text{ZnSnS}_4$  films prepared by sulfurization of metallic stacks. *Solar Energy Materials and Solar Cells*, 112:97–105, May 2013. *4 citations pages 71, 73, 76, and 92*
- [320] R. Lechner, S. Jost, J. Palm, M. Gowtham, F. Sorin, B. Louis, H. Yoo, R.A. Wibowo, and R. Hock.  $\text{Cu}_2\text{ZnSn}(\text{S},\text{Se})_4$  solar cells processed by rapid thermal processing of stacked elemental layer precursors. *Thin Solid Films*, 535:5–9, May 2013. *Cited page 72*
- [321] Sunwook Hwang, Dae-Hwan Kim, Dae-Ho Son, Kee-Jeong Yang, Dahyun Nam, Hyeonsik Cheong, Jin-Kyu Kang, and Su-il In. Effects of a pre-annealing treatment (PAT) on  $\text{Cu}_2\text{ZnSn}(\text{S},\text{Se})_4$  thin films prepared by rapid thermal processing (RTP) selenization. *Solar Energy Materials and Solar Cells*, 143:218–225, 2015. *2 citations pages 72 and 94*
- [322] Sebastien Delbos, Marya Benmoussa, Romain Bodeux, Corentin Gougau, and Negar Naghavi. Chemical deposition of selenium layers for selenization of sputtered and electrodeposited Cu–Zn–Sn metallic layers for photovoltaic application. *Thin Solid Films*, 589(September):508–513, 2015. *Cited page 72*
- [323] R.B.V. Chalapathy, Gwang Sun Jung, and Byung Tae Ahn. Fabrication of  $\text{Cu}_2\text{ZnSnS}_4$  films by sulfurization of Cu/ZnSn/Cu precursor layers in sulfur atmosphere for solar cells. *Solar Energy Materials and Solar Cells*, 95(12):3216–3221, December 2011. *Cited page 73*
- [324] Simón López-Marino, Marcel Placidi, Amador Pérez-Tomás, Jordi Llobet, Victor Izquierdo-Roca, Xavier Fontané, Andrew Fairbrother, Moises Espíndola-Rodríguez, Diouldé Sylla, Alejandro Pérez-Rodríguez, and Edgardo Saucedo. Inhibiting the absorber/Mo-back contact decomposition reaction in  $\text{Cu}_2\text{ZnSnSe}_4$  solar cells: the role of a ZnO intermediate nanolayer. *Journal of Materials Chemistry A*, 1(29):8338, 2013. *2 citations pages 73 and 79*
- [325] O. Volobujeva, S. Bereznev, J. Raudoja, K. Otto, M. Pilvet, and E. Mellikov. Synthesis and characterisation of  $\text{Cu}_2\text{ZnSnSe}_4$  thin films prepared via a vacuum evaporation-based route. *Thin Solid Films*, 535:48–51, May 2013. *Cited page 74*
- [326] Ando D. Kuypers, Raymond J.W. Knaapen, Mirjam Theelen, Marc Meuris, Maarten van der Vleuten, and Wiro Zijlmans. Cost-efficient equipment for CIGS production. *Photovoltaics International*, pages 61–69, May 2013. *3 citations pages 75, 141, and 142*
- [327] Arun Khalkar, Kwang-soo Lim, Seong-man Yu, Dong-wook Shin, Tae-sik Oh, and Ji-beom Yoo. Effects of Sulfurization Pressure on the Conversion Efficiency of Cosputtered  $\text{Cu}_2\text{ZnSnS}_4$  Thin Film Solar Cells. *International Journal of Photoenergy*, 2015(750846):1–7, 2015. *Cited page 75*
- [328] Patrice Bras, Jan Sterner, and Charlotte Platzer-Björkman. Influence of hydrogen sulfide annealing on copper–zinc–tin–sulfide solar cells sputtered from a quaternary compound target. *Thin Solid Films*, 582: E-MRS 2014 Spring Meeting, Symposium A, Thin-Film Chalcogenide Photovoltaic Materials:233–238, May 2015. *Cited page 75*
- [329] K. Wang, O. Gunawan, T. Todorov, B. Shin, S. J. Chey, N. A. Bojarczuk, D. Mitzi, and S. Guha. Thermally evaporated  $\text{Cu}_2\text{ZnSnS}_4$  solar cells. *Applied Physics Letters*, 97(14):143508, 2010. *Cited page 76*
- [330] Kejia Wang, Byungha Shin, Kathleen B. Reuter, Teodor Todorov, David B. Mitzi, and Supratik Guha. Structural and elemental characterization of high efficiency  $\text{Cu}_2\text{ZnSnS}_4$  solar cells. *Applied Physics Letters*, 98(5):051912, 2011. *Cited page 76*

- [331] Wooseok Ki and Hugh W. Hillhouse. Earth-Abundant Element Photovoltaics Directly from Soluble Precursors with High Yield Using a Non-Toxic Solvent. *Advanced Energy Materials*, 1(5):732–735, October 2011. Cited page 76
- [332] Yoonjung Hwang, Bo-in Park, Byung-seok Lee, Jin Young Kim, Jeung-hyun Jeong, Honggon Kim, Min Jae Ko, Bongsoo Kim, Hae Jung Son, Seung Yong Lee, Jae-seung Lee, Jong-ku Park, So-hye Cho, and Doh-kwon Lee. Influences of Extended Selenization on  $\text{Cu}_2\text{ZnSnSe}_4$  Solar Cells Prepared from Quaternary Nanocrystal Ink. *The Journal of physical chemistry C*, 118:27657–27663, 2014. 2 citations pages 76 and 79
- [333] Alfons Weber. *Growth of thin films of the material system Cu-Zn-Sn-S*. PhD thesis, Friedrich-Alexander-Universität Erlangen-Nürnberg (FAU), 2009. Cited page 77
- [334] Dominik M. Berg, Alexandre Crossay, Jérôme Guillot, Victor Izquierdo-Roca, Alejandro Pérez-Rodríguez, Shafaat Ahmed, Hariklia Deligianni, Susanne Siebentritt, and Phillip J. Dale. Simplified formation process for  $\text{Cu}_2\text{ZnSnS}_4$ -based solar cells. *Thin Solid Films*, 573:148–158, 2014. Cited page 78
- [335] G. Altamura, L. Grenet, C. Roger, F. Roux, V. Reita, R. Fillon, H. Fournier, S. Perraud, and H. Mariette. Alternative back contacts in kesterite  $\text{Cu}_2\text{ZnSn}(\text{S}_{1-x}\text{Se}_x)_4$  thin film solar cells. *J. Renewable Sustainable Energy*, 6(1):011401, 2014. Cited page 78
- [336] Cédric Broussillou. *Relations traitement thermique - phases - adhérence dans les couches minces constituant les cellules photovoltaïques  $\text{CuIn}(\text{S}_x\text{Se}_{1-x})_2$  Electrodéposées (CISEL)*. PhD thesis, Mines ParisTech, 2011. 3 citations pages 79, 82, and 83
- [337] Dong-Hau Kuo, Jin-Tung Hsu, and Albert Daniel Saragih. Effects of the metallic target compositions on the absorber properties and the performance of  $\text{Cu}_2\text{ZnSnSe}_4$  solar cell devices fabricated on TiN-coated Mo/glass substrates. *Materials Science and Engineering: B*, 186:94–100, 2014. Cited page 79
- [338] Giovanni Altamura, Mingqing Wang, and Kwang-Leong Choy. Improving efficiency of electrostatic spray-assisted vapor deposited  $\text{Cu}_2\text{ZnSn}(\text{S},\text{Se})_4$  solar cells by modification of Mo/absorber interface. *Thin Solid Films*, 597:19–24, 2015. Cited page 79
- [339] Fangyang Liu, Kaiwen Sun, Wei Li, Chang Yan, Hongtao Cui, Liangxing Jiang, Xiaojing Hao, and Martin A. Green. Enhancing the  $\text{Cu}_2\text{ZnSnS}_4$  solar cell efficiency by back contact modification: Inserting a thin  $\text{TiB}_2$  intermediate layer at  $\text{Cu}_2\text{ZnSnS}_4/\text{Mo}$  interface. *Applied Physics Letters*, 104(5):051105, 2014. Cited page 79
- [340] Hongtao Cui, Xiaolei Liu, Fangyang Liu, Xiaojing Hao, Ning Song, and Chang Yan. Boosting  $\text{Cu}_2\text{ZnSnS}_4$  solar cells efficiency by a thin Ag intermediate layer between absorber and back contact. *Applied Physics Letters*, 104(4):041115, 2014. Cited page 79
- [341] Hongtao Cui, Chang-yeh Lee, Wei Li, Xiaolei Liu, Xiaoming Wen, and Xiaojing Hao. Improving Efficiency of Evaporated  $\text{Cu}_2\text{ZnSnS}_4$  Thin Film Solar Cells by a Thin Ag Intermediate Layer between Absorber and Back Contact. *International Journal of Photoenergy*, 2015:170507, 2015. Cited page 79
- [342] Zhengfu Tong, Kun Zhang, Kaiwen Sun, Chang Yan, Fangyang Liu, Liangxing Jiang, Yanqing Lai, Xiaojing Hao, and Jie Li. Modification of absorber quality and Mo-back contact by a thin Bi intermediate layer for kesterite  $\text{Cu}_2\text{ZnSnS}_4$  solar cells. *Solar Energy Materials and Solar Cells*, 144:537–543, 2016. Cited page 79
- [343] Stephanie Angle and Ludovic Parissi. Interface between a I/III/VI<sub>2</sub> layer and a back contact layer in a photovoltaic cell (Patent US2014/0315346 A1), 2014. Cited page 81
- [344] Ankur Khare, Burak Himmetoglu, Matteo Cococcioni, and Eray S Aydil. First principles calculation of the electronic properties and lattice dynamics of  $\text{Cu}_2\text{ZnSn}(\text{S}_{1-x}\text{Se}_x)_4$ . *Journal of Applied Physics*, 111:123704, 2012. Cited page 86
- [345] X. Fontane, L. Calvo-Barrio, V. Izquierdo-Roca, E. Saucedo, A. Perez-Rodríguez, J. R. Morante, D. M. Berg, P. J. Dale, and S. Siebentritt. In-depth resolved Raman scattering analysis for the identification of secondary phases: Characterization of  $\text{Cu}_2\text{ZnSnS}_4$  layers for solar cell applications. *Applied Physics Letters*, 98(18):181905, 2011. Cited page 86
- [346] Markus Neuschitzer, Yudania Sanchez, Tetiana Olar, Thomas Thersleff, Simon Lopez-Marino, Florian Oliva, Moisés Espindola-Rodríguez, Haibing Xie, Marcel Placidi, Victor Izquierdo-Roca, Iver Lauermann, Klaus Leifer, Alejandro Pérez-Rodríguez, and Edgardo Saucedo. The complex surface chemistry of kesterites: Cu/Zn re-ordering after low temperature post deposition annealing and its role in high performance devices. *Chemistry of Materials*, 27:5279–5287, 2015. 2 citations pages 86 and 114
- [347] Sree Satya Kanth Bendapudi. *Novel Film Formation Pathways for  $\text{Cu}_2\text{ZnSnSe}_4$  for Solar Cell Applications*. PhD thesis, University of South Florida, 2011. Cited page 90
- [348] M G Sousa, A F Cunha, P M P Salomé, P A Fernandes, J P Teixeira, and J P Leitão.  $\text{Cu}_2\text{ZnSnS}_4$  absorber layers obtained through sulphurization of metallic precursors : Graphite box versus sulphur flux. *Thin Solid Films*, 535:27–30, 2013. Cited page 90
- [349] Homare Hiroi, Noriyuki Sakai, and Hiroki Sugimoto. Development of high efficiency  $\text{Cu}_2\text{ZnSnS}_4$  solar cells and modules. In *26th European Photovoltaic Solar Energy Conference and Exhibition*, pages 2448–2451, 2011. Cited page 92
- [350] Andrew Fairbrother, Eric García-Hemme, Victor Izquierdo-Roca, Xavier Fontané, Fabián A. Pulgarín-Agudelo, Osvaldo Vigil-Galán, Alejandro Pérez-Rodríguez, and Edgardo Saucedo. Development of a selective chemical etch to improve the conversion efficiency of Zn-rich  $\text{Cu}_2\text{ZnSnS}_4$  solar cells. *Journal of the American Chemical Society*, 134(19):8018–8021, May 2012. 3 citations pages 93, 112, and 113



- [351] Jörn Timo Wätjen, Jessica Engman, Marika Edoff, and Charlotte Platzer-Björkman. Direct evidence of current blocking by ZnSe in  $\text{Cu}_2\text{ZnSnSe}_4$  solar cells. *Applied Physics Letters*, 100:173510, 2012.  
*2 citations pages 95 and 103*
- [352] Steven S. Hegedus and William N. Shafarman. Thin-film solar cells: device measurements and analysis. *Progress in Photovoltaics: Research and Applications*, 12(23):155–176, March 2004.  
*2 citations pages 95 and 153*
- [353] Ingrid Repins, Nirav Vora, Carolyn Beall, Su-huai Wei, Yanfa Yan, Manuel Romero, Glenn Teeter, Hui Du, Bobby To, Matt Young, and Rommel Noufi. Kesterites and Chalcopyrites : A Comparison of Close Cousins. In *MRS Proceedings*, volume 1324 Symposium - D - Compound Semiconductors for Energy Applications and Environmental Sustainability, San Francisco, California, 2011. Cambridge University Press (CUP).  
*Cited page 99*
- [354] Mehmet Eray, Vardaan Chawla, Ingrid Repins, and Michael A Scarpulla. Interplay between surface preparation and device performance in CZTSSe solar cells : Effects of KCN and  $\text{NH}_4\text{OH}$  etching. *Solar Energy Materials and Solar Cells*, 136:78–85, 2015.  
*2 citations pages 111 and 112*
- [355] Björn-Arvid Schubert, Björn Marsen, Sonja Cinque, Thomas Unold, Reiner Klenk, Susan Schorr, and Hanswerner Schock.  $\text{Cu}_2\text{ZnSnS}_4$  thin film solar cells by fast coevaporation. *Progress in Photovoltaics: Research and Applications*, 19:93–96, 2011.  
*Cited page 112*
- [356] Gee Yeong Kim, Ju Ri Kim, William Jo, Kee Doo Lee, Jin Young Kim, Trang Thi Thu Nguyen, and Seokhyun Yoon. Effects of  $\text{Cu}_{2-x}\text{S}$  phase removal on surface potential of  $\text{Cu}_2\text{ZnSnS}_4$  thin-films grown by electroplating. *Current Applied Physics*, 14(12):1665–1668, 2014.  
*Cited page 112*
- [357] Trang Thi Thu Nguyen, Hae-Young Shin, Gee Yeong Kim, Ju Ri Kim, William Jo, Seokhyun Yoon, Ki Doo Lee, and Jin Young Kim. Raman scattering studies of  $\text{Cu}_2\text{ZnSnS}_4$  thin films: Local distribution of the secondary phase  $\text{Cu}_{2-x}\text{S}$  and the effect of KCN etching on  $\text{Cu}_{2-x}\text{S}$ . *Journal of the Korean Physical Society*, 66(1):117–122, 2015.  
*Cited page 112*
- [358] Tooru Tanaka, Tatsuya Sueishi, Katsuhiko Saito, Qixin Guo, Mitsuhiro Nishio, Kin M Yu, and Wladek Walukiewicz. Existence and removal of  $\text{Cu}_2\text{Se}$  second phase in coevaporated  $\text{Cu}_2\text{ZnSnSe}_4$  thin films. *Journal of Applied Physics*, 111(5):053522, 2012.  
*Cited page 112*
- [359] M. Buffiere, G. Brammertz, A.-A. El Mel, N. Lenaers, Yi Ren, A. E. Zaghi, Y. Mols, C. Koeble, J. Vleugels, M. Meuris, and J. Poortmans. Recombination Stability in Polycrystalline  $\text{Cu}_2\text{ZnSnSe}_4$  Thin Films. *Photovoltaic Specialists Conference (PVSC), 2013 IEEE 39th*, pages 1941 – 1944, 2013.  
*Cited page 112*
- [360] Marie Buffière, Guy Brammertz, Sylvester Sahayaraj, Maria Batuk, Samira Khelifi, Denis Mangin, Abdel-Aziz El Mel, Ludovic Arzel, Joke Hadermann, Marc Meuris, and Jef Poortmans. KCN Chemical Etch for Interface Engineering in  $\text{Cu}_2\text{ZnSnSe}_4$  Solar Cells. *ACS Applied Materials & Interfaces*, 7:14690–14698, 2015.  
*Cited page 112*
- [361] Marie Buffière, Abdel-Aziz El Mel, Nick Lenaers, Guy Brammertz, Armin E. Zaghi, Marc Meuris, and Jef Poortmans. Surface Cleaning and Passivation Using  $(\text{NH}_4)_2\text{S}$  Treatment for  $\text{Cu}(\text{In,Ga})\text{Se}_2$  Solar Cells: A Safe Alternative to KCN. *Advanced Energy Materials*, 5:1401689, March 2015.  
*Cited page 112*
- [362] K. Timmo, M. Altosaar, J. Raudoja, K. Muska, M. Pilvet, M. Kauk, T. Varema, M. Danilson, O. Volobujeva, and E. Mellikov. Sulfur-containing  $\text{Cu}_2\text{ZnSnSe}_4$  monograin powders for solar cells. *Solar Energy Materials and Solar Cells*, 94(11):1889–1892, November 2010.  
*Cited page 112*
- [363] Y. Ogawa, A. Jäger-Waldau, T.H. Hua, Y. Hashimoto, and K. Ito. Influence of KCN treatment on  $\text{CuInS}_2$  thin films. *Applied Surface Science*, 92:232–236, 1996.  
*Cited page 112*
- [364] Yasuhiro Hashimoto, Naoki Kohara, Takayuki Negami, Mikihiko Nishitani, and Takahiro Wada. Surface Characterization of Chemically Treated  $\text{Cu}(\text{In,Ga})\text{Se}_2$  Thin Films. *Japanese Journal of Applied Physics*, 35:4760–4764, 1996.  
*Cited page 112*
- [365] Marcus Bär, Joachim Klaer, Lothar Weinhardt, Regan G. Wilks, Stefan Krause, Monika Blum, Wanli Yang, Clemens Heske, and Hans Werner Schock.  $\text{Cu}_{2-x}\text{S}$  surface phases and their impact on the electronic structure of  $\text{CuInS}_2$  thin films - A hidden parameter in solar cell optimization. *Advanced Energy Materials*, 3(6):777–781, 2013.  
*Cited page 112*
- [366] M. Werner, C. M. Sutter-Fella, H. Hagendorfer, Y. E. Romanyuk, and A. N. Tiwari.  $\text{Cu}_2\text{ZnSn}(\text{S,Se})_4$  solar cell absorbers processed from Na-containing solutions in DMSO. *Physica Status Solidi (a)*, 212(1):116–120, 2015.  
*Cited page 112*
- [367] M. Bär, B.-A. Schubert, B. Marsen, R. G. Wilks, S. Pookpanratana, M. Blum, S. Krause, T. Unold, W. Yang, L. Weinhardt, C. Heske, and H.-W. Schock. Cliff-like conduction band offset and KCN-induced recombination barrier enhancement at the  $\text{CdS}/\text{Cu}_2\text{ZnSnS}_4$  thin-film solar cell heterojunction. *Applied Physics Letters*, 99(22):222105, 2011.  
*2 citations pages 112 and 121*
- [368] B. Canava, J. F. Guillemoles, J. Vigneron, D. Lincot, and A. Etcheberry. Chemical elaboration of well defined  $\text{Cu}(\text{In,Ga})\text{Se}_2$  surfaces after aqueous oxidation etching. *Journal of Physics and Chemistry of Solids*, 64(9-10):1791–1796, 2003.  
*Cited page 113*
- [369] Raúl Ortega-Borges and Daniel Lincot. Mechanism of Chemical Bath Deposition of Cadmium Sulfide Thin Films in the Ammonia-Thiourea System. *Journal of The Electrochemical Society*, 140(12):3464, 1993.  
*Cited page 120*

- [370] Daisuke Hironiwa, Ryo Takai, Jakapan Chantana, Noriyuki Sakai, Takuya Kato, Hiroki Sugimoto, and Takashi Minemoto. Effect of ammonia etching on structural and electrical properties of  $\text{Cu}_2\text{ZnSn}(\text{S},\text{Se})_4$  absorbers. *Applied Surface Science*, 353:209–213, 2015. *Cited page 120*
- [371] Nobuki Matsuo, Daisuke Hironiwa, Jakapan Chantana, Noriyuki Sakai, Takuya Kato, Hiroki Sugimoto, and Takashi Minemoto. Evaluation of sputtering damage in  $\text{Cu}_2\text{ZnSn}(\text{S},\text{Se})_4$  solar cells with CdS and  $(\text{Cd},\text{Zn})\text{S}$  buffer layers by photoluminescence measurement. *Japanese Journal of Applied Physics*, 042302(54):1–5, 2015. *2 citations pages 120 and 122*
- [372] E.M. Mkawi, K. Ibrahim, M.K.M. Ali, M.A. Farrukh, and A.S. Mohamed. Electrodeposited ZnS Precursor Layer with Improved Electrooptical Properties for Efficient  $\text{Cu}_2\text{ZnSnS}_4$  Thin-Film Solar Cells. *Journal of Electronic Materials*, 44:3380–3387, October 2015. *2 citations pages 120 and 122*
- [373] Daisuke Hironiwa, Nobuki Matsuo, Noriyuki Sakai, Takuya Katou, Hiroki Sugimoto, Jakapan Chantana, Zeguo Tang, and Takashi Minemoto. Sputtered  $(\text{Zn},\text{Mg})\text{O}$  buffer layer for band offset control in  $\text{Cu}_2\text{ZnSn}(\text{S},\text{Se})_4$  solar cells. *Japanese Journal of Applied Physics*, 53:106502, 2014. *2 citations pages 120 and 122*
- [374] Adam Hultqvist. *Cadmium Free Buffer Layers and the Influence of their Material Properties on the Performance of  $\text{Cu}(\text{In},\text{Ga})\text{Se}_2$  Solar Cells*. PhD thesis, Uppsala University, 2010. *Cited page 120*
- [375] Daisuke Hironiwa, Nobuki Matsuo, Jakapan Chantana, Noriyuki Sakai, Takuya Kato, Hiroki Sugimoto, and Takashi Minemoto. Annealing effect on  $\text{Cu}_2\text{ZnSn}(\text{S},\text{Se})_4$  solar cell with  $\text{Zn}_{1-x}\text{Mg}_x\text{O}$  buffer layer. *Physica Status Solidi (a)*, 2015. Available online at <http://doi.wiley.com/10.1002/pssa.201532217>. *2 citations pages 120 and 122*
- [376] D Aaron R Barkhouse, Richard Haight, Noriyuki Sakai, Homare Hiroi, Hiroki Sugimoto, and David B Mitzi. Cd-free buffer layer materials on  $\text{Cu}_2\text{ZnSn}(\text{S}_x\text{Se}_{1-x})_4$ : Band alignments with ZnO, ZnS, and  $\text{In}_2\text{S}_3$ . *Applied Physics Letters*, 193904(100):1–5, 2012. *3 citations pages 120, 121, and 122*
- [377] Richard Haight, Aaron Barkhouse, Oki Gunawan, Byungha Shin, Matt Copel, Marinus Hopstaken, and David B. Mitzi. Band alignment at the  $\text{Cu}_2\text{ZnSn}(\text{S}_x\text{Se}_{1-x})_4/\text{CdS}$  interface. *Applied Physics Letters*, 98(25):253502, 2011. *Cited page 121*
- [378] A Santoni, F Biccari, C Malerba, M Valentini, R Chierchia, and A Mittiga. Valence band offset at the CdS/ $\text{Cu}_2\text{ZnSnS}_4$  interface probed by x-ray photoelectron spectroscopy. *Journal of Physics D: Applied Physics*, 46(17):175101, 2013. *Cited page 121*
- [379] Lingyan Lin, Jinling Yu, Shuying Cheng, Peimin Lu, Yunfeng Lai, Sile Lin, and Pengyi Zhao. Band alignment at the  $\text{In}_2\text{S}_3/\text{Cu}_2\text{ZnSnS}_4$  heterojunction interface investigated by X-ray photoemission spectroscopy. *Applied Physics A*, pages 2173–2177, 2014. *Cited page 121*
- [380] Norio Terada, Sho Yoshimoto, Kosuke Chochi, Takayuki Fukuyama, Masahiro Mitsunaga, Hitoshi Tampo, Hajime Shibata, Koji Matsubara, Shigeru Niki, Noriyuki Sakai, Takuya Katou, and Hiroki Sugimoto. Characterization of electronic structure of  $\text{Cu}_2\text{ZnSn}(\text{S}_x\text{Se}_{1-x})_4$  absorber layer and CdS/ $\text{Cu}_2\text{ZnSn}(\text{S}_x\text{Se}_{1-x})_4$  interfaces by in-situ photoemission and inverse photoemission spectroscopies. *Thin Solid Films*, 582:166–170, 2015. *Cited page 121*
- [381] Zi-Yuan Dong, Yong-Feng Li, Bin Yao, Zhan-Hui Ding, Gang Yang, Rui Deng, Xuan Fang, Zhi-Peng Wei, and Lei Liu. An experimental and first-principles study on band alignments at interfaces of  $\text{Cu}_2\text{ZnSnS}_4/\text{CdS}/\text{ZnO}$  heterojunctions. *Journal of Physics D: Applied Physics*, 47(7):075304, 2014. *Cited page 121*
- [382] Gang Yang, Yong-Feng Li, Bin Yao, Zhan-Hui Ding, Rui Deng, Jie-Ming Qin, Fang Fang, Xuan Fang, Zhi-Peng Wei, and Lei Liu. Band alignments at interface of  $\text{Cu}_2\text{ZnSnS}_4/\text{ZnO}$  heterojunction: An X-ray photoelectron spectroscopy and first-principles study. *Journal of Alloys and Compounds*, 628:293–297, 2015. *Cited page 121*
- [383] S Y Chen, Aron Walsh, J H Yang, X G Gong, L Sun, P X Yang, J H Chu, and S H Wei. Compositional dependence of structural and electronic properties of  $\text{Cu}_2\text{ZnSn}(\text{S},\text{Se})_4$  alloys for thin film solar cells. *Physical Review B*, 83(March):125201, 2011. *Cited page 121*
- [384] Wujisiguleng Bao and Masaya Ichimura. Band Offsets at the ZnO/ $\text{Cu}_2\text{ZnSnS}_4$  Interface Based on the First Principles Calculation. *Japanese Journal of Applied Physics*, 52:061203, 2013. *Cited page 121*
- [385] A Nagoya, R Asahi, and G Kresse. First-principles study of  $\text{Cu}_2\text{ZnSnS}_4$  and the related band offsets for photovoltaic applications. *Journal of physics. Condensed matter: an Institute of Physics journal*, 23(40):404203, October 2011. *Cited page 121*
- [386] K. Xerxes Steirer, Rebekah L. Garris, Jian V. Li, Michael J. Dzara, Paul F. Ndione, Kannan Ramanathan, Ingrid Repins, Glenn Teeter, and Craig L. Perkins. Co-solvent enhanced zinc oxysulfide buffer layers in Kesterite copper zinc tin selenide solar cells. *Phys. Chem. Chem. Phys.*, 17(23):15355–15364, 2015. *2 citations pages 121 and 122*
- [387] Chang Yan, Fangyang Liu, Kaiwen Sun, Ning Song, John A. Stride, Fangzhou Zhou, Xiaojing Hao, and Martin Green. Boosting the efficiency of pure sulfide CZTS solar cells using the In/Cd-based hybrid buffers. *Solar Energy Materials and Solar Cells*, 144:700–706, 2016. *Cited page 122*
- [388] Dhruba B. Khadka, SeongYeon Kim, and JunHo Kim. A Nonvacuum Approach for Fabrication of  $\text{Cu}_2\text{ZnSnSe}_4/\text{In}_2\text{S}_3$  Thin Film Solar Cell and Optoelectronic Characterization. *The Journal of Physical Chemistry C*, 119(22):12226–12235, 2015. *Cited page 122*

- [389] Jongmin Kim, C. Park, S. M. Pawar, Akbar I. Inamdar, Yongcheol Jo, J. Han, Jinpyo Hong, Young S. Park, D. Y. Kim, W. Jung, Hyungsang Kim, and Hyunsik Im. Optimization of sputtered ZnS buffer for  $\text{Cu}_2\text{ZnSnS}_4$  thin film solar cells. *Thin Solid Films*, 566:88–92, 2014. *Cited page 122*
- [390] Myo Than Htay, Yoshio Hashimoto, Noritaka Momose, Kouichi Sasaki, Hiroshi Ishiguchi, Shigeo Igarashi, Kazuki Sakurai, and Kentaro Ito. A cadmium-free  $\text{Cu}_2\text{ZnSnS}_4/\text{ZnO}$  heterojunction solar cell prepared by practicable processes. *Japanese Journal of Applied Physics*, 50(3):1–4, 2011. *2 citations pages 122 and 128*
- [391] Mai Nguyen, Kaia Ernits, Kong Fai Tai, Chin Fan Ng, Stevin Snellius Pramana, Wardhana A. Sasangka, Sudip K. Batabyal, Timo Holopainen, Dieter Meissner, Axel Neisser, and Lydia H. Wong. ZnS buffer layer for  $\text{Cu}_2\text{ZnSn}(\text{S},\text{Se})_4$  monograin layer solar cell. *Solar Energy*, 111:344–349, 2015. *Cited page 122*
- [392] C. Platzer-Björkman, C. Frisk, J. K. Larsen, T. Ericson, S.-Y. Li, J. J. S. Scragg, J. Keller, F. Larsson, and T. Törndahl. Reduced interface recombination in  $\text{Cu}_2\text{ZnSnS}_4$  solar cells with atomic layer deposition  $\text{Zn}_{1-x}\text{Sn}_x\text{O}_y$  buffer layers. *Applied Physics Letters*, 107(24):243904, 2015. *Cited page 122*
- [393] Daisuke Hironiwa, Jakapan Chantana, Noriyuki Sakai, Takuya Kato, Hiroki Sugimoto, and Takashi Minemoto. Application of multi-buffer layer of  $(\text{Zn},\text{Mg})\text{O}/\text{CdS}$  in  $\text{Cu}_2\text{ZnSn}(\text{S},\text{Se})_4$  solar cells. *Current Applied Physics*, 15(3):383–388, 2015. *Cited page 122*
- [394] Homare Hiroi, Jeehwan Kim, Masaru Kuwahara, Teodor K Todorov, Dhruv Nair, Marinus Hopstaken, Yu Zhu, Oki Gunawan, David B. Mitzi, and Hiroki Sugimoto. Over 12 % efficiency  $\text{Cu}_2\text{ZnSn}(\text{SeS})_4$  solar cell via hybrid buffer layer. In *Photovoltaic Specialist Conference (PVSC), 2014 IEEE 40th*, pages 0030 – 0032, Denver, CO, June 2014. IEEE. *2 citations pages 122 and 128*
- [395] Miguel A Contreras, Manuel J Romero, Bobby To, F Hasoon, R Noufi, S Ward, and K Ramanathan. Optimization of CBD CdS process in high-efficiency  $\text{Cu}(\text{In},\text{Ga})\text{Se}_2$ -based solar cells. *Thin Solid Films*, 403-404:204–211, 2002. *Cited page 125*
- [396] Negar Naghavi, Solange Temgoua, Thibaud Hildebrandt, Jean-françois Guillemoles, and Daniel Lincot. Impact of oxygen concentration during the deposition of window layers on lowering the metastability effects in  $\text{Cu}(\text{In},\text{Ga})\text{Se}_2/\text{CBD Zn}(\text{S},\text{O})$  based solar cell. *Progress in Photovoltaics: Research and Applications*, 2015. <http://dx.doi.org/10.1002/pip.2626>. *2 citations pages 125 and 126*
- [397] M Buffière, G Brammertz, S Oueslati, H El Anzeery, J Bekaert, K Ben Messaoud, C Köble, S Khelifi, M Meuris, and J Poortmans. Spectral current-voltage analysis of kesterite solar cells. *Journal of Physics D: Applied Physics*, 47(17):175101, April 2014. *Cited page 125*
- [398] Mark T. Winkler, Wei Wang, Oki Gunawan, Harold J. Hovel, Teodor K. Todorov, and David B. Mitzi. Optical designs that improve the efficiency of  $\text{Cu}_2\text{ZnSn}(\text{S},\text{Se})_4$  solar cells. *Energy & Environmental Science*, 7:1029–1036, 2014. *Cited page 129*
- [399] Standard Test Method for Electrical Performance of Photovoltaic Cells Using Reference Cells Under Simulated Sunlight. Technical report, ASTM International, 2009. *Cited page 130*
- [400] Volker Probst, Immo Koetschau, Emmerich Novak, Axel Jasenek, Heinz Eschrich, Frank Hergert, Thomas Hahn, Martin Schütze, Rudolf Thyen, Jochen Feichtinger, and Bernd Walther. A New Sequential Absorber Formation Technology for High Performance CIGS<sub>Se</sub> Module Fabrication on Industrial Scale. In *5th International Workshop on CIGS Solar Cell Technology*, pages 1–18, Berlin, April 2014. BOSCH Solar CISTech GmbH. *Cited page 138*
- [401] Rommel Noufi and Ken Zweibel. High-efficiency CdTe and CIGS thin-film solar cells: Highlights and challenges. *Conference Record of the 2006 IEEE 4th World Conference on Photovoltaic Energy Conversion, WCPEC-4*, 1(May):317–320, 2007. *Cited page 139*
- [402] Arnulf Jäger-Waldau. Market Challenges for CZTS-Based Thin-Film Solar Cells. In *Copper Zinc Tin Sulfide-Based Thin-Film Solar Cells*, chapter 2. John Wiley & Sons, Ltd., first edition, 2015. Edited by Kentaro Ito. *Cited page 139*
- [403] Cédric Broussillou. Extension of the study to the implementation of alternative scalable processes (Confidential) - Deliverable 7.3 of SCALENANO project. Technical report, NEXCIS, July 2015. *Cited page 140*
- [404] First solar website. <http://www.firstsolar.com/>, 2015. *Cited page 146*
- [405] Xiandeng Hou and Bradley T Jones. Inductively Coupled Plasma / Optical Emission Spectrometry. In *Encyclopedia of Analytical Chemistry*, pages 9468–9485. 2000. *Cited page 151*
- [406] Philip J Potts and Peter C Webb. X-ray fluorescence spectrometry. *Journal of Geochemical Exploration*, 44:251–296, 1992. *2 citations pages 151 and 152*
- [407] How Handheld XRF Works: A Step-by-Step Guide. <https://www.bruker.com/fr/products/x-ray-diffraction-and-elemental-analysis/handheld-xrf/how-xrf-works.html>. *Cited page 151*
- [408] XRF - X-ray Fluorescence analysis explained. <http://www.oxford-instruments.com/businesses/industrial-products/industrial-analysis/xrf>. *Cited page 151*
- [409] Philip J. Potts, Andrew T. Ellis, Mike Holmes, Peter Kregsamer, Christina Strelly, Margaret West, and Peter Wobrauschek. X-ray fluorescence spectrometry. *Journal of Analytical Atomic Spectrometry*, 15(10):1417–1442, 2000. *Cited page 152*
- [410] Roberto Cesareo. X-Ray Fluorescence Spectrometry. In *Encyclopedia of Industrial Chemistry*, volume 39, pages 595–631. 2012. *Cited page 152*

- [411] SeJin Ahn, Sunghun Jung, Jihye Gwak, Ara Cho, Keeshik Shin, Kyunghoon Yoon, Doyoung Park, Hyonsik Cheong, and Jae Ho Yun. Determination of band gap energy ( $E_g$ ) of  $\text{Cu}_2\text{ZnSnSe}_4$  thin films: On the discrepancies of reported band gap values. *Applied Physics Letters*, 97(2):021905, 2010. *Cited page 153*
- [412] Henning Helmers, Christian Karcher, and Andreas W. Bett. Bandgap determination based on electrical quantum efficiency. *Applied Physics Letters*, 103(3):032108, 2013. *Cited page 153*
- [413] Jonas Lähnemann. *Spectrally Resolved Current Losses in  $\text{Cu(In,Ga)Se}_2$  Thin-film Solar Cells*. PhD thesis, Freie Universität Berlin (FUB), 2008. *Cited page 153*



# List of Publications

- L. Vauche, L. Risch, Y. Sánchez, M. Dimitrievska, M. Pasquinelli, T. Goislard de Monsabert, P.-P. Grand, S. Jaime-Ferrer, and E. Saucedo, 8.2% Pure Selenide Kesterite Thin Film Solar Cells from Large Area Electrodeposited Precursors, *Progress in Photovoltaics: Research and Applications* vol. 24, no. 1, pp. 38 – 51, Jan. 2016, available at <http://onlinelibrary.wiley.com/doi/10.1002/pip.2643/abstract>.
- D. Colombara, A. Crossay, L. Vauche, S. Jaime, M. Arasimowicz, P.-P. Grand, and P. J. Dale, Electrodeposition of Kesterite thin films for photovoltaic applications: Quo vadis?, *Physica Status Solidi (a)* vol. 212, Special Issue on Advanced Materials and Nanotechnology for Photovoltaics, pp. 88 – 102, Jan. 2015, available at <http://onlinelibrary.wiley.com/doi/10.1002/pssa.201431364/abstract>.
- L. Vauche, J. Dubois, A. Laparre, M. Pasquinelli, S. Bodnar, P.-P. Grand, and S. Jaime, Rapid thermal processing annealing challenges for large scale  $\text{Cu}_2\text{ZnSnS}_4$  thin films, *Physica Status Solidi (a)*, vol. 212, Special Issue on Advanced Materials and Nanotechnology for Photovoltaics, pp. 103 – 108, Jan. 2015, available at <http://onlinelibrary.wiley.com/doi/10.1002/pssa.201431387/abstract>.
- L. Vauche, J. Dubois, A. Laparre, F. Mollica, R. Bodeux, S. Delbos, C. M. Ruiz, M. Pasquinelli, F. Bahi, T. Goislard de Monsabert, S. Jaime, S. Bodnar, P.-P. Grand, T. G. de Monsabert, S. Jaime, S. Bodnar, and P.-P. Grand,  $\text{Cu}_2\text{ZnSnSe}_4$  thin film solar cells above 5% conversion efficiency from electrodeposited Cu Sn Zn precursors, *Physica Status Solidi (a)*, vol. 211, no. 9, pp. 2082 – 2085, September 2014, available at <http://onlinelibrary.wiley.com/doi/10.1002/pssa.201300630/abstract>.



# List of Figures

2	(a) Représentation schématique et (b) diagramme de bandes de la structure d'un dispositif photovoltaïque à base de kesterite. . . . .	xv
3	Représentation schématique des stratégies d'électrodépôt de kesterite . . . . .	xvi
4	Vue générale du procédé d'électrodépôt de Cu/Sn/Zn. . . . .	xvii
5	Représentation schématique en coupe du précurseur, juste après électro-dépôt ou après traitement thermique basse température, ainsi que leur évolution naturelle. . . . .	xvii
6	Résumé de l'évolution des performances des cellules kesterite: optimisation de différentes étapes. . . . .	xxii
7	Cost comparison of $\text{CuIn}_x\text{Ga}_{1-x}(\text{S,Se})_2$ (CIGS) and $\text{Cu}_2\text{ZnSn}(\text{S,Se})_4$ (CZTSSe) absorbers with ED, PVD or printing processes . . . . .	xxiii
I.1	Solar radiation at the earth's surface . . . . .	3
I.2	Schematic of a semiconductor electronic band structure . . . . .	4
I.3	P-N junction band diagram under illumination . . . . .	5
I.4	Schematic of a solar cell . . . . .	5
I.5	I-V curve of a solar cell under illumination . . . . .	6
I.6	Solar cell circuit with parasitic resistances . . . . .	7
I.7	Best laboratory solar cell efficiencies . . . . .	9
I.8	Global cumulative installed solar photovoltaic capacity, 2000-2014 . . . . .	10
I.9	IEA scenarios for the global electricity mix in 2050 . . . . .	11
I.10	PV Outlook: module price and PV technologies market share evolution . . . . .	12
I.11	Indium prices according to London Metal Exchange 2005-2015 . . . . .	13
I.12	CZTS, CZTSe and CIGS absorption coefficients . . . . .	16
I.13	Kesterite crystalline structure . . . . .	17
I.14	(a) Schematic representation and (b) band diagram of a kesterite-based device structure. . . . .	18
I.15	SEM cross sectional images of vacuum-processed kesterite-based solar cells . . . . .	20
I.16	SEM cross sectional images of solution-processed kesterite-based solar cells . . . . .	21
I.17	SEM cross sectional images of ED-processed kesterite-based solar cells . . . . .	22
I.18	CIGS and CZTS power conversion efficiency trend. . . . .	22
I.19	$V_{OC}$ vs bandgap . . . . .	22
I.20	Kesterite phase diagram . . . . .	23
I.21	Cu-Zn order-disorder in CZTSe . . . . .	25
II.1	Scheme of a two-electrode electrochemical cell for the reduction of metal ion into a metal atom . . . . .	32
II.2	Standard reduction potentials of Cu, Sn, Zn . . . . .	34
II.3	Schematic illustration of stacked precursor uniformity . . . . .	37
II.4	Schematic representations of the three main kesterite precursor electrodeposition approaches . . . . .	38
II.5	SEM images of Cu-Sn-Zn precursors produced by co-electrodeposition . . . . .	40
II.6	SEM images of Cu-Sn-Zn-S and Cu-Sn-Zn-Se precursors produced by quaternary electrodeposition . . . . .	40
II.7	SEM images of electrodeposited Cu/Sn/Zn and Cu/Sn/Zn/Sn stacks . . . . .	42
II.8	Schema of Cu seed layer . . . . .	45
II.9	Schematic illustration (cross-section) of volume expansion. . . . .	49



II.10	Three types of microstructure developed after low-temperature annealing of electrodeposited Cu-Sn-Zn stacks . . . . .	51
II.11	Overview of the electrodeposition sequence. . . . .	52
II.12	$15 \times 15 \text{ cm}^2$ electrodeposition set-up . . . . .	54
II.13	Concentration of Cu electrolyte components and impurities traced for one year . .	56
II.14	Concentration of Sn electrolyte components and impurities traced for one year . .	57
II.15	Tin bath stability issue illustrated by images of (a) new and (b) 1 year aged baths.	57
II.16	SEM images of a Cu/Sn sample and a CZTSe absorber produced using an aged Sn electrolyte . . . . .	57
II.17	Estimation of $\text{Sn}^{\text{II}}$ loss rate by $\text{Sn}^{\text{IV}}$ colloid formation . . . . .	58
II.18	Concentration of Sn electrolyte components traced for one year . . . . .	59
II.19	Concentration of Zn electrolyte components and impurities traced for 1 or 2 years	59
II.20	Thickness and uniformity (RSD) of a $15 \times 15 \text{ cm}^2$ electrodeposited Cu/Sn/Zn precursor . . . . .	60
II.21	Cu deposition parameters . . . . .	61
II.22	Sn deposition parameters . . . . .	62
II.23	Zn deposition parameters . . . . .	62
II.24	Thickness and uniformity (RSD) of a $15 \times 15 \text{ cm}^2$ Cu/Sn/Zn precursor with a copper layer deposited by PVD and electrodeposited Sn and Zn layers . . . . .	63
II.25	Electrodeposited (a) Cu, (b) Sn and (c) Zn SEM surface images. . . . .	64
II.26	SEM and GDOES of the electrodeposited precursor, initially and after a few days	64
II.27	XRD pattern of electrodeposited precursor . . . . .	65
II.28	Surface SEM image of a precursor alloyed at $230^\circ\text{C}$ . . . . .	65
II.29	SEM and GDOES of the $200^\circ\text{C}$ pre-alloyed precursor . . . . .	65
II.30	XRD pattern of alloyed precursor . . . . .	66
II.31	Tof-SIMS profile of (a) electrodeposited and (b) pre-alloyed precursor. . . . .	66
II.32	Schematic of precursor structure, as-electrodeposited and pre-alloyed, and its evolution with natural ageing. . . . .	67
III.1	Conversion of a Cu-Sn-Zn metallic precursor into a absorber layer by annealing. .	71
III.2	An arrow diagram for the possible phase formation during annealing. . . . .	72
III.3	Confined chalcogen (CC) system . . . . .	73
III.4	Three or two-zone furnace, an independant chalcogen source (IC) system . . . . .	74
III.5	$\text{H}_2\text{Se}$ or $\text{H}_2\text{S}$ furnace, an independent chalcogen source (IC) system. . . . .	75
III.6	Saturating vapor pressure for Cu, Zn, Sn, S, Se and compounds . . . . .	77
III.7	Metal composition ternary phase diagram of a Cu-Sn-Zn-S(e) system. . . . .	79
III.8	Experimentals overview . . . . .	81
III.9	SEM images of evaporated and VTD deposited Se capping layers on Cu-Sn-Zn precursors. . . . .	81
III.10	System CC-NEXCIS, a $15 \times 15 \text{ cm}^2$ RTP system . . . . .	82
III.11	System IC-IRDEP, a three-zone RTP . . . . .	83
III.12	System CC-IRDEP, graphite box in tubular furnace . . . . .	84
III.13	System CC-IREC, graphite box in tubular furnace . . . . .	85
III.14	Temperature profiles for sulfurization in CC-NEXCIS system . . . . .	88
III.15	Precursor and CZTS absorber composition depending on the annealing ramp. . .	89
III.16	Images of Cu-Zn-Sn-S sample and glass cover after annealing (A) . . . . .	89
III.17	Images of Cu-Zn-Sn-S sample and glass cover, Sn XRF mapping after annealing (B)	90
III.18	Influence of the background pressure on sulfur incorporation . . . . .	90
III.19	SEM images of CZTS absorbers after annealings (A) and (B) . . . . .	91
III.20	Surface SEM image of an absorber obtained with annealing (B). . . . .	91
III.21	SEM and GDOES of a Cu-Zn-Sn-S film after pre-alloying (C) . . . . .	92
III.22	SEM and GDOES of a CZTS absorber after pre-alloying (C) + annealing (B) . .	92
III.23	J-V and EQE of best CZTS devices from CC-NEXCIS annealing . . . . .	92
III.24	Temperature profiles for selenization in the CC-NEXCIS annealing system . . . .	93
III.25	Precursor and CZTSe absorber film composition after selenization in CC-NEXCIS	94

III.26 Images of a Cu-Zn-Sn-Se sample, glass cover and Zn XRF mapping after annealing (D) . . . . .	95
III.27 SEM and GDOES of CZTSe absorber with annealing (D) in CC-NEXCIS . . . . .	95
III.28 J-V and EQE of best CZTSe in CC-NEXCIS system . . . . .	96
III.29 Precursor and CZTSe absorber composition after annealing in systems IC-IRDEP and CC-IRDEP . . . . .	97
III.30 Uniformity of an absorber annealed in IC-IRDEP system. . . . .	97
III.31 Uniformity of an absorber annealed in CC-IRDEP system (2 samples configuration). . . . .	97
III.32 SEM and SIMS of CZTSe absorbers annealed in IC- and CC-IRDEP systems. . . . .	98
III.33 XRD pattern of absorbers annealed in atmospheric systems IC- and CC-IRDEP. . . . .	99
III.34 SEM and SIMS of CZTSe absorbers annealed in IC- and CC-IRDEP systems from Se-capped precursors . . . . .	99
III.35 EQE of CZTSe devices prepared with absorbers annealed in systems IC-IRDEP and CC-IRDEP with uncovered and Se-capped precursors. . . . .	100
III.36 Precursor and CZTSe absorber film composition after annealing in CC-IREC system . . . . .	101
III.37 Image of an absorber annealed in system CC-IREC. . . . .	101
III.38 SEM and GDOES of a CZTSe absorber after annealing in system CC-IREC . . . . .	102
III.39 SEM surface of a Zn-rich absorber, partly covered with small ZnSe grains . . . . .	102
III.40 Raman spectra of a Zn-rich absorber . . . . .	103
III.41 Ternary diagram showing the detection zones for ZnSe secondary phase by SEM . . . . .	103
III.42 SEM surface of a Sn-rich absorber, partly covered with small Sn-Se grains . . . . .	103
III.43 XRD patterns and Raman spectra of Sn-rich absorbers . . . . .	104
III.44 Ternary diagram showing the Sn-Se (SnSe, SnSe <sub>2</sub> ) secondary phases presence composition regions, as detected by SEM, XRD and Raman spectroscopy at 785 nm. . . . .	105
III.45 Detection of secondary phases at the back contact by SEM in a Sn-rich absorber and by Raman spectroscopy in a Zn-rich absorber . . . . .	106
III.46 Ternary diagrams showing the (a) zones of secondary phases presence and (b) average power conversion efficiency in dependence of absorber composition. Orange and blue zones present large amounts of SnSe/SnSe <sub>2</sub> and ZnSe secondary phases, respectively. In the green area, the amount of secondary phases is limited when the composition is closer from stoichiometry but increases when the copper content decreases. . . . .	107
IV.1 Schematic of etching principle . . . . .	111
IV.2 SEM and Raman spectra of Zn-rich absorbers before and after removal of the ZnSe secondary phase from the surface by (i) acidic KMnO <sub>4</sub> followed by Na <sub>2</sub> S etching . . . . .	115
IV.3 SEM and Raman spectra of Sn-rich absorbers before and after removal of Sn-Se (SnSe, SnSe <sub>2</sub> ) secondary phases from the surface by (ii) (NH <sub>4</sub> ) <sub>2</sub> S etching . . . . .	115
IV.4 Surface SEM images showing the removal of ZnSe and Sn-Se (SnSe, SnSe <sub>2</sub> ) secondary phases from the surface of a Sn-rich and Zn-rich absorber by (iii) acidic KMnO <sub>4</sub> followed by Na <sub>2</sub> S etching + (NH <sub>4</sub> ) <sub>2</sub> S etching. . . . .	116
IV.5 Ternary diagram illustrating the composition of unetched and etched absorbers . . . . .	116
IV.6 Normalized EQE in the low wavelength region of CZTSe-based devices for different etchings . . . . .	118
IV.7 J-V, EQE at 0V and under reverse bias of device made with Sn-rich absorbers unetched and etched by (ii) . . . . .	119
IV.8 Band alignment at the kesterite/buffer layer heterointerface . . . . .	121
IV.9 Optoelectronic parameters extracted from J-V curves of devices made with different CdS layers . . . . .	124
IV.10 Normalized external quantum efficiency in the low wavelength region with different CdS layers. . . . .	125
IV.11 SEM and EDX of devices made with different CdS layers . . . . .	125
IV.12 J-V curves of devices prepared with different CdS layers using four different optical band pass filters (400, 515, 550 and 780 nm). . . . .	126

LIST OF FIGURES

---

IV.13	J-V curves of devices prepared with different CdS layers using four different optical band pass filters (400, 515, 550 and 780 nm), after 5 min of light-soaking. . . . .	126
IV.14	Optoelectronic parameters extracted from J-V curves of devices made with different In <sub>2</sub> S <sub>3</sub> and ZnS layers . . . . .	127
IV.15	EQE of devices prepared with different buffer layers . . . . .	128
IV.16	J-V curve of a CZTSe/In <sub>2</sub> S <sub>3</sub> based device measured after light-soaking (LS). . . . .	128
IV.17	J-V curve of the CZTSe 9.1% record cell, measured after 30 min light soaking. . . . .	130
IV.18	Ternary diagrams illustrating $\eta$ , $V_{OC}$ , $J_{SC}$ and FF in dependence of absorber composition . . . . .	131
IV.19	Bandgap (eV) extracted from the EQE curve versus absorber composition. . . . .	133
IV.20	Summary of the device improvement evolution and the optimized steps. . . . .	133
V.1	Total cost of ownership. . . . .	138
V.2	Cost comparison of CuIn <sub>x</sub> Ga <sub>1-x</sub> (S,Se) <sub>2</sub> (CIGS) and Cu <sub>2</sub> ZnSn(S,Se) <sub>4</sub> (CZTSSe) absorbers with ED, PVD or printing processes . . . . .	140
B.1	Electrodeposition in Hull cell . . . . .	147
B.2	X-ray fluorescence principle . . . . .	151
B.3	Schema of the points measured by XRF on a sample of a given area. . . . .	152
B.4	Bandgap estimation by taking the inflection point of dEQE/dE vs E curves. . . . .	154

# List of Tables

1	Composition et prix des bains chimiques choisis pour l'électrodépôt de Cu, Sn et Zn	xvi
2	Systèmes de traitement thermique	xviii
3	Résultats principaux pour les différents systèmes de traitement thermique.	xix
4	Paramètres opto-électroniques des cellules $\text{Cu}_2\text{ZnSnSe}_4$ (CZTSe) devices dans ce travail.	xxi
5	Paramètres opto-électroniques des cellules $\text{Cu}_2\text{ZnSnSe}_4$ (CZTSe) devices dans la littérature	xxi
6	Comparaison des technologies PV silicium, couches minces CIGS and kesterite	xxii
I.1	PV Technologies	8
I.2	Commercial PV Technologies	8
I.3	Photovoltaics in the global electricity mix in 2050.	11
I.4	World production and price of Cd, Cu, Ga, In, S, Se, Sn, Te, Zn metals	13
I.5	Metals amount required to produce 880 GW of CIGS or CZTSSe cells	14
I.6	Selection of CZTS, CZTSe and CZTSSe solar cell devices with efficiency over 7%	19
I.7	Kesterite main secondary phases and their bandgaps.	24
II.1	Electrolyte components of interest	36
II.2	Kesterite electrodeposited by Cu-Sn-Zn metal alloy route	39
II.3	Kesterite by Cu-Sn-Zn-S or Cu-Sn-Zn-Se quaternary electrodeposition	41
II.4	Kesterite by stacked elemental layer approach	41
II.5	Comparison of different ED routes vs specifications for thin films deposition.	42
II.6	Specifications for an industry-compatible electrodeposition process.	43
II.7	Copper deposition parameters for kesterite fabrication by the SEL approach	44
II.8	ENTHONE's copper commercial chemistry used in this thesis.	45
II.9	Tin deposition parameters for kesterite fabrication by the SEL approach	46
II.10	Comparison of different ENTHONE's commercial Sn chemistries	46
II.11	Zinc deposition parameters for kesterite fabrication by the SEL approach	47
II.12	Comparison of different ENTHONE's commercial Zn chemistries	48
II.13	Summary: selected electrolytes, composition and price	48
II.14	Low temperature thermal treatments in literature	50
II.15	Initial electrolyte composition	52
II.16	Bath characterization methods	53
II.17	Additive consumption rate	53
II.18	Initial optimum parameters for Cu/Sn/Zn electrodeposition at $15 \times 15 \text{ cm}^2$ size	60
II.19	Deposition durations and resulting film thicknesses	63
II.20	Specifications for an industry-compatible electrodeposition process	68
III.1	Graphite box in literature	73
III.2	Sealed ampoule or quartz tube in literature	74
III.3	Three or two-zone tube furnace in literature	75
III.4	$\text{H}_2\text{S}$ / $\text{H}_2\text{Se}$ in literature	75
III.5	Hot plate annealing in literature	76
III.6	Thermal treatment systems	82
III.7	Device finishing standard procedure, by institute	86
III.8	Relative standard deviation (RSD) of the CZTS absorber composition	89

LIST OF TABLES

---

III.9	RSD in CZTSe absorber composition . . . . .	94
III.10	RSD of CZTSe absorbers annealed in IC- and CC-IRDEP . . . . .	96
III.11	CZTSe devices optoelectronic parameters, annealing in IC- and CC-IRDEP systems from bare and Se-capped precursors . . . . .	100
III.12	RSD of CZTSe absorbers composition, annealed in CC-IREC system. . . . .	101
III.13	CZTSe kesterite devices optoelectronic parameters for different absorber composition, after annealing in system CC-IREC . . . . .	107
III.14	Main annealing results for different thermal treatment systems. . . . .	108
IV.1	Wet chemical etchings in literature. . . . .	112
IV.2	Kesterite devices optoelectronic parameters for different absorber composition and etching: (i) ZnSe, (ii) SnSe and (iii) ZnSe + SnSe etching . . . . .	117
IV.3	Evolution of kesterite devices J-V parameters after (i), (ii) (iii) etching for different absorber compositions . . . . .	117
IV.4	Buffer layer bandgaps . . . . .	120
IV.5	Conduction band offsets at kesterite / buffer layer interface. . . . .	121
IV.6	Performance characteristics of Cd-free solar cells (versus CdS reference in parenthesis) in literature . . . . .	122
IV.7	Buffer layers and their CBD deposition parameters. . . . .	123
IV.8	Optoelectronic parameters of high-efficiency pure selenium $\text{Cu}_2\text{ZnSnSe}_4$ (CZTSe) devices in this work . . . . .	132
IV.9	Optoelectronic parameters of high-efficiency pure selenium $\text{Cu}_2\text{ZnSnSe}_4$ (CZTSe) devices in literature . . . . .	132
V.1	Comparison of Si, CIGS and kesterite PV technologies . . . . .	136
V.2	CIGS estimated module cost depending on hypotheses . . . . .	138
V.3	Thermal treatment systems . . . . .	141
A.1	Worldwide installed peak capacity (TW) in 2050. . . . .	145
A.2	Surface covered by PV ( $\text{km}^2$ ) in 2050. . . . .	146
A.3	Part of thin film technologies in 2050, depending on the PV deployment scenario and the part of thin films in the market share. . . . .	146
B.1	Bandgap determination methods. . . . .	153

## Résumé

Dans un contexte général d'augmentation de la demande énergétique et de préoccupation croissante face au réchauffement climatique et à la limitation des ressources naturelles, l'utilisation d'énergie solaire devrait augmenter. L'avenir des différentes technologies photovoltaïques dépend évidemment de leur rendement de conversion photovoltaïque et de leur coût (ces deux paramètres peuvent être ramenés au coût par watt) mais aussi de la disponibilité des ressources. La kesterite,  $\text{Cu}_2\text{ZnSnS}_4$  (CZTS),  $\text{Cu}_2\text{ZnSnSe}_4$  (CZTSe) ou  $\text{Cu}_2\text{ZnSn}(\text{S},\text{Se})_4$  (CZTSSe), composée d'éléments abondants dans la croûte terrestre, et pouvant être fabriquée en couches minces avec des procédés à bas coûts, se positionne en candidat prometteur pour la conversion d'énergie solaire à grande échelle.

Dans cette thèse, l'électro-dépôt, un procédé compatible avec des exigences industrielles de production de masse à bas coût et de sécurité, est utilisé pour déposer un précurseur de cuivre, étain et zinc sur des substrats de  $15 \times 15 \text{ cm}^2$ , de composition et épaisseur contrôlables. Ce précurseur est ensuite converti en semiconducteur par traitement thermique en présence de soufre ou de sélénium. Les couches ainsi formées de Cu-Zn-Sn-S ou Cu-Zn-Sn-Se, doivent être uniformes et présenter les propriétés appropriées (phases, composition, morphologie) pour la fabrication de cellules solaires à haut rendement. Le procédé de fabrication de la cellule solaire complète, notamment les étapes qui interviennent dans la formation de la jonction p-n (décapage chimique et dépôt de couche tampon) est également optimisé pour maximiser les rendements. À l'issue de ces optimisations, un rendement de 9.1% est obtenu pour une cellule solaire CZTSe, un nouveau record pour les cellules solaires à base de kesterite fabriquées par électro-dépôt.

## Abstract

Facing growing energy demand and increasing concerns about climate change and finite energy sources, solar energy use should increase. The future of the different photovoltaic technologies obviously depends on their power conversion efficiency and cost (summarized by the ratio cost per watt), but also on the elements availability. Thin films of earth-abundant kesterite,  $\text{Cu}_2\text{ZnSnS}_4$  (CZTS),  $\text{Cu}_2\text{ZnSnSe}_4$  (CZTSe) or  $\text{Cu}_2\text{ZnSn}(\text{S},\text{Se})_4$  (CZTSSe), which can be manufactured with low-cost processes, are promising candidates for solar energy conversion at large scale.

In this thesis, a copper tin and zinc precursor of controllable composition and thickness is electrodeposited on  $15 \times 15 \text{ cm}^2$  substrates. Electrodeposition is a process compatible with high throughput low-cost and safety industry requirements. The precursor is converted into a semiconductor by thermal treatments in presence of sulfur or selenium. The resulting Cu-Zn-Sn-S or Cu-Zn-Sn-Se layers should be uniform and have adequate properties (phases, composition and morphology) to produce high efficient solar cells. Full device processing, including the p-n junction formation steps (wet chemical etching and buffer layer deposition) is also investigated in order to maximize device efficiency. The best CZTSe solar cell exhibits a 9.1% power conversion efficiency, setting a new record for kesterite solar cells produced by electrodeposition.